Heterogeneous catalysis using supported metal nanoparticles for environmental applications

Thesis submitted in accordance with the regulations of the University of Cardiff for the degree of

Doctor of Philosophy

By

Khaled Fadhi F. Alshammari

School of Chemistry
Cardiff University

2018

Declaration

This work has not been submitted in substance for any other degree or award at ths or any other university or place of learning, nor is being submitted concurrently in candidature for any degree or other award.

Signed………………………………………… (candidate)   Date ……………………....

Statement 1

This thesis is being submitted in partial fulfilment of the requirements for the degree of ……PhD……….. (insert MCh, MD, MPhil, PhD, etc, as appropriate).

Signed………………………………………… (candidate)   Date ……………………....

Statement 2

This thesis is the result of my own independent work/investigation, except where otherwise stated, and the thesis has not been edited by a third party beyond what is permitted by Cardiff University's Policy on the Use of Third-Party Editors by Research Degree Students. Other sources are acknowledged by explicit references. The views expressed are my own.

Signed………………………………………… (candidate)   Date ……………………....

Statement 3

I hereby give consent for my thesis, if accepted, to be available online in the University's Open Access repository and for inter-library loan, and for the title and summary to be made available to outside organisations.

Signed………………………………………… (candidate)   Date ……………………....

Statement 4: Previously Approved Bar on Access.

I hereby give consent for my thesis, if accepted, to be available online in the University's Open Access repository and for inter-library loans **after expiry of a bar on access previously approved by the Academic Standards and Quality Committee.**

Signed………………………………………… (candidate)   Date ……………………....

To my parents

To my wife

To my daughter and sons

To my brothers and sisters

Table of Contents

List of Figures

List of Tables

Acknowledgements

Publications

Khaled Al shammari, Nikolaos Dimitratos and Graham Hutchings, *Reduction of 4-Nitrophenol using supported gold nanoparticles*, Poster day in Cardiff Catalysis Institute Conference, School of Chemistry, Cardiff University, Cardiff, UK, 10-11th January 2017

Khaled Al shammari, Nikolaos Dimitratos and Graham Hutchings, *Synergistic effect on AuPd bimetallic catalyst during reduction of 4-Nitrophenol*, Poster day in 16th Annual Cardiff Chemistry Conference, Cardiff Catalysis Institute, School of Chemistry, Cardiff University, Cardiff, UK, 15-16th May 2017.

Davide Motta; Felipe Sanchez; **Khaled Al shammari**; Maddie Hewitt; Lidia E. Chinchilla; Gianluigi A. Botton; David Morgan; Tommaso Tabanelli; Alberto Villa; Ceri Hammond; Nikolaos Dimitratos, *Preformed Au colloidal nanoparticles immobilised on NiO as highly efficient heterogeneous catalysts for reduction of 4-nitrophenol to 4-aminophenol. **Accepted manuscript**, Journal of Hazardous Materials, June **2018**.*

Abstract

In this study, monometallic and a series of bimetallic nanoparticles, composed of Au, Ag and Pd supported on different types of metal oxides (e.g. TiO_2, CuO and NiO) have been synthesised *via* a sol-immobilization approach using PVA and $NaBH_4$ as capping and reducing agents, respectively. The activity of these supported nanoparticles has been evaluated towards the reduction of 4-nitrophenol (4-NP) to 4-aminophenol (4-AP), as a model reaction. The effect of using different reducing agents (such as $NaBH_4$, formic acid and hydrous hydrazine) was also studied. The reaction parameters were also optimised under kinetic regime control. The catalysts showed promising activity towards the reduction of 4-NP to 4-AP with the highest activity and re-usability (up to 5 cycles) observed for the bimetallic AgPd supported alloyed nanoparticles particularly with an optimum molar ratio of Ag:Pd = 25:75.

The successful synthesis of the targeted active components together with the structure-activity correlations have been probed by using different bulk and surface characterization techniques including; powder x-ray diffraction (XRD), MP-AES, X-ray photoelectron spectroscopy (XPS), scanning electron microscopy (SEM), transmission electron microscopy (TEM), HAADF-STEM, and S_{BET} surface area measurements. The results clearly demonstrated the successful preparation of mono- and bimetallic supported heterogenous systems *via* sol-immobilization route with high distribution and confinement of the supported nanoparticles onto the supports as evidenced by TEM and XRD analysis. Amongst all heterogenous systems, bimetallic $Ag_{0.25}Pd_{0.75}/TiO_2$ and $Au_{0.5}Pd_{0.5}/TiO_2$ catalysts showed the highest activity over other molar ratios. The results clearly proved that the observed activity of the supported nanoparticles is mainly depending on the degree of metal-metal interactions together with the strong metal-support interactions as well as the small particle sizes offered by the sol-immobilization method. This would help and facilitate the electron transfer from metal-to-metal at the metal/metal interfaces and hence the promote the synergistic effect between the two metals which eventually ended with an acceleration for the reaction.

Chapter 1

Introduction

1.1. Introduction

1.1.1. History of catalysis

The conversion of alcohol to ether catalysed by sulphuric acid in 1552 by Valerius Cordus who the first recorded instance of an inorganic catalysis reaction [1]. Over two centuries later, in 1781, Antoine Augustin Parmentier recorded that when potato starch was added to distilled water and cream of tartar (potassium hydrogen tartrate), a sweet taste developed over several months and this was more accentuated if vinegar (ethanoic acid) had also been added [2]. However, Fulhame in 1794 described the underlying fundamental concepts of catalysis, when he discovered that, although water was required for the oxidation of carbon monoxide, the water itself was not consumed by the chemical reaction [1,2]. Similarly, in 1812, Gottlieb Kirchoff, a Russian chemist, found that acids assisted starch hydrolysis without being used up in the process themselves [3]. In 1817, Sir Humphrey Davy noted that an explosion could result at lower than combustion temperatures if oxygen was combined with flammable gases and this mixture passed over platinum [4]. In 1818, Thendard demonstrated that whilst hydrogen peroxide decomposes in aqueous solution, it can be stabilised by the addition of acid. In 1820, Edmund Davy investigated the part played by noble metals in alcohol oxidation which was observed to occur quickly over platinum exposed to air [5]. Two years later in 1822, Dobereiner, corroborated Edmund Davy's findings by recording the combustion of oxygen and hydrogen over platinum at room temperature. Subsequently, Dulong and Thenard discovered that the reactivity of oxygen and hydrogen is dependent upon the nature of the additional substance employed when the tests are performed using substances other than platinum [1,3]. In 1825, Henry reported that some substances (such as hydrogen sulphide) have the ability to inhibit hydrogen combustion; also noting that catalysts derived from platinum are not effective for oxidation of carbon monoxide [6]. Turner showed how platinum-based catalysis function in combining hydrogen and chlorine. This finding prompted Peregrine Phillips to develop the original commercial catalytic methodology: the oxidation of sulphur dioxide over platinum-based catalysts to produce sulphuric acid [7]. These crucial innovative benchmarks in the history of catalysis led to the era of catalysis and many further investigations and developments.

1.1.2. Catalysts defined

The expression 'catalysis' derives from the combination of the Greek words '*kata*' meaning 'down' and '*lyein*' meaning 'loosen.' J.J Berzelius applied the term 'catalysis' for the first time in 1836 when reporting enhancements in the chemical reactions he was studying [3]. Berzelius defined a catalyst as a substance which enhances the rate of a chemical reaction without being used up itself in the reaction [8]. Subsequently, more precise definitions have been put forward as a consequence of improved comprehension of the catalytic process; for example, G. C. Bond, defines a catalyst as "a substance that increases the rate at which a chemical system approaches equilibrium, without being consumed in the process" [9]. Significantly, however, a catalyst does not alter the thermodynamics of the reaction, or the equilibrium position, as the catalyst acts to promote both forward and reverse reactions, increasing the reaction rate constants (k_1 and k_2) [10], as outlined below:

$$A \underset{k_2}{\overset{k_1}{\rightleftharpoons}} B$$
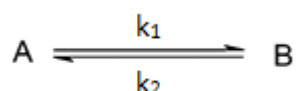
The rate constant (k) is given by the Arrhenius equation (Equation 1.1):

$$k = A \times \exp^{(-Ea/RT)} \quad \text{(Equation 1.1)}$$

where:

 A represents the molecular collision frequency,

E_a represents the activation energy (KJ mol^{-1}),

R represents the gas constant (8.314 JK^{-1} mol^{-1}) and

T represents the temperature in Kelvin (K)

The catalyst acts to lower the activation energy necessary for the reaction to occur, as depicted in Figure 1.1. Here, the catalyst is not used in the reaction; consequently, it is not identified in the final chemical equation, as it merely speeds up kinetically-favourable reactions. Hence, catalysts are not able to catalyse a reaction, which is thermodynamically untenable [9].
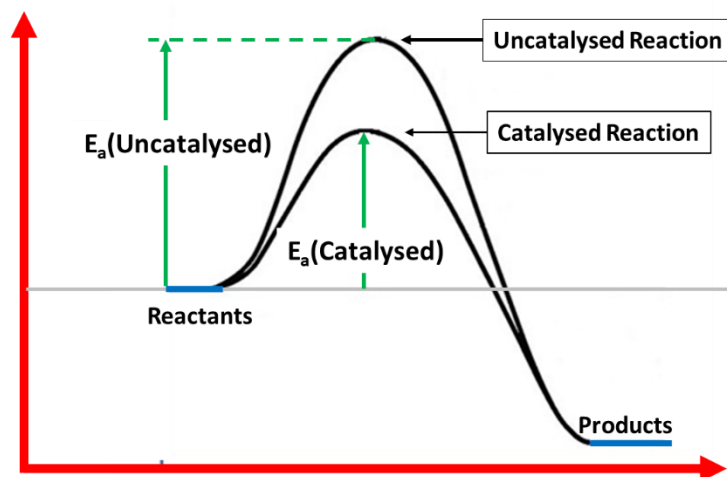
Figure 1.1 Diagram comparing the potential energy associated with un catalysed and catalysed reactions.

1.2. Types of catalysis

Generally, catalysis can be classified into three types: (i) bio-catalysis; (ii) homogeneous catalysis; and (iii) heterogeneous catalysis. These three types will be discussed in more detail in the subsequent Sections. Typically, bio-catalysts, are viewed as natural, sensitive and selective catalysts, involving rapid reactions, taking place under mild conditions. Homogeneous catalysts exert their action whilst in the same phase as the other reaction components, typically a liquid phase, whilst heterogeneous catalysts exert their action whilst in a different phase to other components of the reaction mixture.

1.2.1.   Bio-catalysis

Biocatalysts are typically enzymes, or naturally-occurring complex protein molecules, that catalyse reactions within living cells. All proteins are fundamentally composed of amino acids, linked together by peptide bonds, which determine an enzyme's structure. A cleft in the morphology of the protein molecule, surrounded by an array of amino acids, typically functions as the active site of an enzyme. Figure 1.2 shows the way in which an enzyme binds to its substrate in a reaction. Enzymes employ four different types of interaction to bind with their substrates: electrostatic interactions; hydrogen bonding; van der Waals interactions; and hydrophobic interactions [11,12].

Enzymes are highly efficient catalysts and, due to the specific morphology of their active site, they only catalyse specific reactions. Typically, an enzyme can complete around 1000 catalytic cycles per second. Therefore, biocatalysts have great commercial significance, particularly in the pharmaceutical and food industries., as they are utilised in the production of many drugs, food additives, flavourings and fragrances [12]. Enzymes offer additional benefits as they can be applied beyond the biological systems, to function as isolated compounds, capable of acting outside the living cell in both aqueous and organic solvents. However, during reactions care must be taken as enzymes are often heat sensitive. Heating can destroy an enzyme by denaturing the weak bonds, which maintain their functional shape – source of the enzyme's active site [12,13].
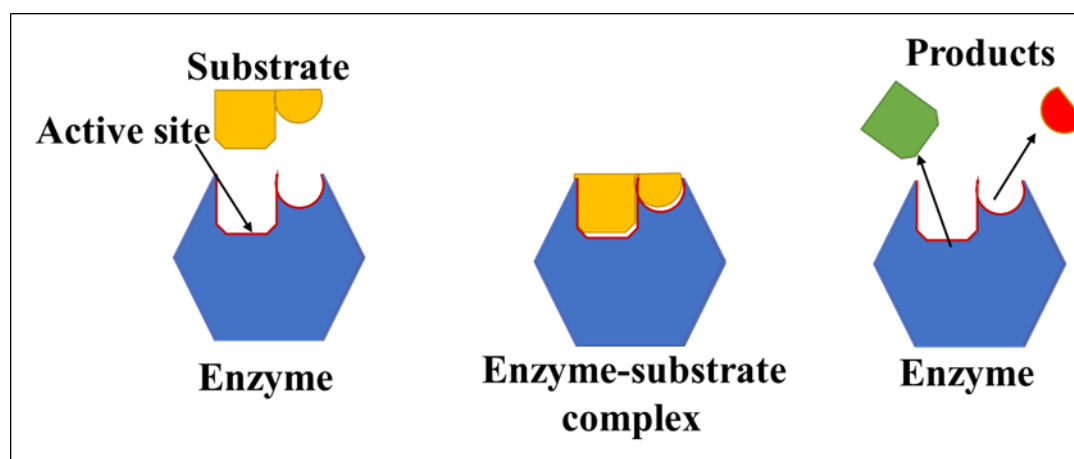
Figure 1.2 Depiction of enzyme substrate binding.

1.2.2. Homogeneous catalysis

In homogeneous catalysis, the catalyst and the reactant are present in the same phase, for example, in the gaseous phase for catalysis of ozone destruction by chlorine radicals [11]. The primary benefit of homogeneous catalysis is that all of the catalyst's active sites are available to the reactant, and therefore greater activity can be achieved. One drawback of homogeneous catalysis is associated with the potential difficulty and high cost of separating the catalysts from the reaction mixture; consequently, some homogeneous catalytic processes are not commercially feasible [14].

1.2.3. Heterogeneous catalysis

In heterogeneous catalysis, the catalyst exists in a phase different to the reaction mixture. The catalytic reaction occurs at the interface between the reaction mixture and the catalyst surface, on which the reactants are temporarily adsorbed. Transient bonds link the reactant molecules with the catalyst surface at the active site where the desired reaction takes place. The reaction product then desorbs from the catalyst surface due to the weakness of the transient bond linkages. Catalytic oxidation of carbon monoxide represents an example of heterogeneous catalysis, as depicted in Figure 1.3 [11]. Since catalyst metals (such as platinum and gold) are often expensive materials, it is commercially advantageous to employ the catalysts as nanometer-sized particles, with the nanometal being supported on the surface of an inert material or metal oxide (such as TiO_2), with the desired reaction occurring on the catalyst superficial surface. Therefore, the design of a highly active, selective and stable heterogeneous catalytic systems represents an important challenge associated with an area of intense academic research. Furthermore, heterogeneous catalysts have a wide commercial application in the production of inorganic chemicals, petrochemically-derived compounds and, also more recently for novel 'green' applications [15,16], such as fuel cells [17,18] and biotechnology [19–21]. Table 1.1 highlights some major industrial applications of heterogeneous catalytic processes [11,12,22].
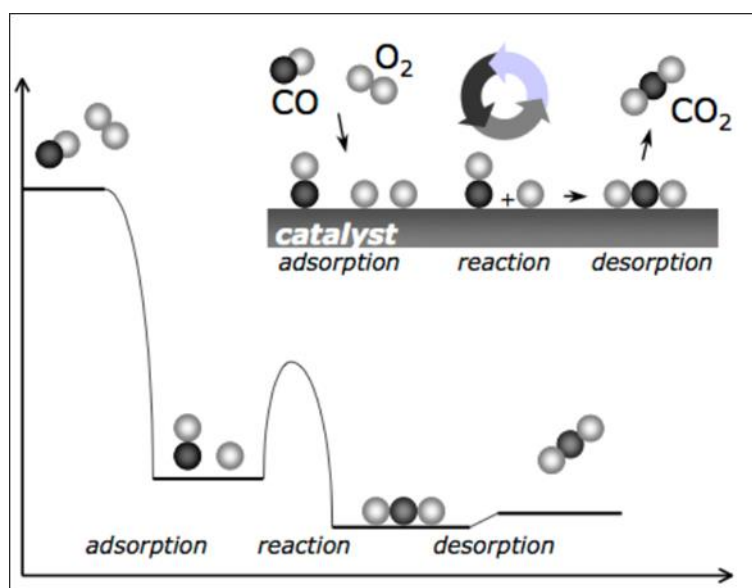
Figure 1.3 Reaction cycle and potential energy diagram for the catalytic oxidation of carbon monoxide (CO) by oxygen (O_2) [11].

Table 1.1 Largest processes based on heterogeneous catalysis.

Reaction	Catalyst
Catalytic cracking of crude oil	Zeolites
Hydrogenation of vegetable oils	Ni
Reduction of NO_x (in exhaust)	Rh, vanadium oxide
Manufacture of sulfuric acid	V_2O_5
Methanation	Ni
Oxidation of CO & hydrocarbons (car exhaust)	Pt, Pd
Acrylonitrile from propylene and ammonia	Bi–Mo, Fe–Sb (oxides)
Ammonia oxidation to NO and HNO_3	Pt–Rh
Ammonia synthesis	Fe
Water-gas shift reaction Fe (oxide)	Cu–ZnO
Ethylene epoxidation to ethylene oxide	Ag
Steam reforming of methane to CO & H_2	Ni
Hydrotreating of crude oil	Co–Mo, Ni–Mo, Ni–W (sulfidic form)
Vinyl chloride C_2H_3Cl)	Cu (as chloride)
Alkylation	H_2SO_4, HF, solid acids
Reforming of naphtha to gasoline	Pt, Pt–Re, Pt–Ir

1.3. Nanoparticle catalysts

1.3.1.   Monometallic nanoparticle catalysts

Monometallic nanoparticles (MNPs) are comprised of only a single metal species, which is responsible for the catalytic characteristics of the nanoparticle. MNPs come in a variety of forms depending on the properties - magnetic, metallic or transition metal nature, etc. – of the metal atom present. MNPs can be produced by a variety of methods, with the chemical production technique still the most important methodology.

Over the last few decades there has been an increased interest in the field of metallic nanoparticles because of their improved physico-chemical characteristics. Noble metal MNPs particularly represent an efficient catalyst for all redox reactions, which are employed within many manufacturing processes, such as the production of chemical and pharmaceuticals intermediates, as well as the transformation of waste by-products into usable compounds. MNPs utilised in these processes include Pt, Pd, Ag or Au.

For a long time, bulk gold (Au) for use in catalysis was found inert, or at least very inactive compared to other metals until it was used in nano form. In 1973, Bond *et al.,* reported that supported nanoparticles of Au based catalysts were actually helpful in the hydrogenation of olefins [23].   Over ten years later, in the mid-1980's, Haruta *et al.,* and Hutchings all simultaneously discovered the excellent catalytic activity demonstrated by Au when dispersed

as small nanoparticles [24,25]. These reactions were the breakthrough for Au catalysis, paving the way for the study of Au in many other catalytic applications over the last 30 years, as well as the developments in catalyst design to optimize performance. Au catalysts now have shown catalytic activity in a range of applications, including: chemical industrial processes [26]; environmental control for fuel cells [27]; CO oxidation at low temperatures [28]; in fuel cells and development of cleaner car exhaust fumes [29,30]. Major applications of the use of gold as a catalyst can be found in the generation of hydrogen peroxide; oxidation of alcohols; oxidation of hydrocarbons; hydrogenation of alkynes [26] and hydrogenation of 4-NP [31].

In addition to Au nano-particle, several chemical reactions are also executed using Pd as the active catalysis phase. Pd catalysts are formulated on unsupported Pd nanoparticles, which are protected by dendrites or polymer stabilizers. However, to improve its stability and resistance to morphological changes, Pd nanoparticles are often immobilized onto a support material.

For the past 40 years, palladium catalysts have played a significant role in organic transformation reactions and are acknowledged for their use in the generation of carbon-carbon bonds: for example, the Suzuki reaction, involves coupling aryl boronic acids to aryl halides. Another well-known industrial reaction catalyzed by Pd based catalysts is the Heck reaction, which involves the coupling of aryl halides to alkenes [32]. Furthermore, Pd nanoparticles also play an active role in hydrogenation reactions, such as hydrogenation of nitrophenol to aminophenol [33].

Silver (Ag) is another metal, which is one of the most intensively investigated nanoparticles because it represents a material with key technical applications [34]. Silver displays unique characteristic normally attributed to noble metals, with high conductivity, chemical stability and activity and other characteristics that can be controlled by the nanoparticles' size, size distribution and their shape, with an acceptable production cost. Therefore, there is currently much interest in developing a novel process to produce tailored supported nanoparticles. Ag nanoparticles are subject of intensive study with respect to the industrial production of both ethylene and propylene oxide, both of which are synthesized by direct epoxidation of their corresponding alkene, using molecular oxygen over supported Ag catalysts. Furthermore, silver nanoparticles have been widely applied for employment in a variety of redox processes involving functional groupings, e.g. the reduction of nitroaromatics [35–37] and carbonyl compounds [38].

1.3.2.   Bimetallic nanoparticle catalysts

Bimetallic nanoparticles (NPs) usually contain two metals within one catalyst system. Bimetallic NPs are often applied in catalysis to increase the catalytic efficiency of bimetallic catalyst systems to meet the global demand on noble metals [39–41] and to enhance the characteristics of metal NPs catalyst [29,40,42,43]. Bimetallic catalysts using common metals such as; Au, Pd, Ag or Pt and a 3d transition metals such as Fe, Co, Ni or Cu [44,45] are widely used for different catalytic applications. Combining Au and Pd, or Au and Pt, is frequently undertaken to ensure highly active NPs catalysts result. Interestingly, catalyst comprises of two metals would lead to a synergistic effect between the metals which generates a more highly efficient and selective catalyst than their monometallic analogous. The enhanced efficiency of bimetallic NPs is frequently correlated with the electronic interactions which take place between the two metals at the metal/metal interfaces. One metal will attract electrons from the active species, thereby altering its d-electron density and promoting efficient catalysis. Altering the characteristics of the electron orbitals will also change the interatomic distances between the metal atoms [39], which is important in promoting catalytic efficiency, leading to improved catalysis compared to that achievable with MNPs.

Bimetallic catalysts have been intensively investigated and results demonstrated its unique catalytic activity for a wide range of reactions including; hydrogenation of 4-chlorophenol [46], H_2O_2 generation [39], the Suzuki coupling reaction, alcoholic oxidation to aldehydes [47], CO oxidation[47] and the reduction of nitro-organics [44]. Such unique activity is not limited only to the number of metals in the system (i.e. mono- or bimetallic system), however, there are several factors which play important roles to improve the bimetallic system. Particle size, morphology, composition, surface area and porosity etc., are also found to be important parameters influencing catalytic properties of bimetallic catalysts in a variety of reactions [46]. Figure 1.4 illustrates a summary of the properties that could potentially influence the catalytic properties of bimetallic catalysts.

According to the literature, three common morphologies of bimetallic NPs include; random alloy; cluster in cluster, and core-shell (see Figure 1.5). Random alloy NPs comprise two metals which are randomly dispersed throughout the NPs. The cluster in cluster NPs comprise clusters of each metal dispersed throughout the NPs. Core-shell NPs comprise a core of one metal species with a surrounding shell of the second metal [48].
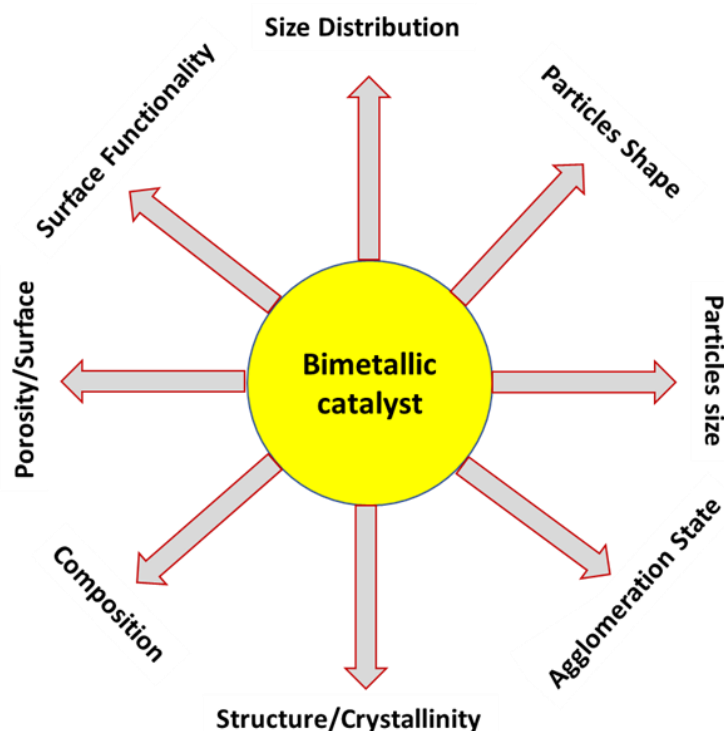
Figure 1.4 Factors affecting the catalytic features of bimetallic catalysts for different catalytic applications.

Random Alloy   Cluster in Cluster   Core-Shell
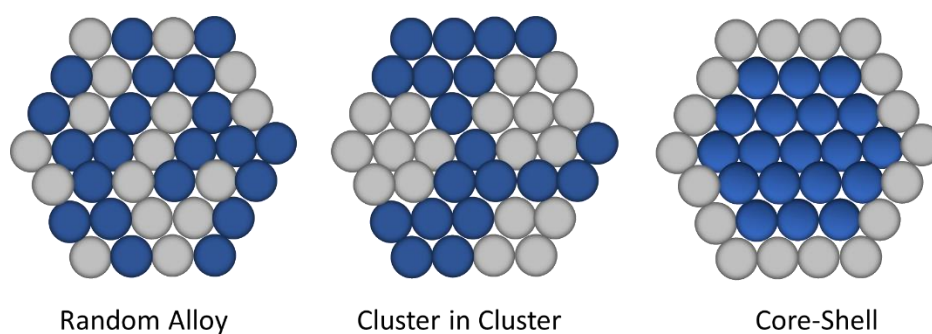
Figure 1.5 Common bimetallic NPs morphologies.

In recent years, growing attention has been paid to bimetallic catalysts (e.g. AuPd NPs). For instance, Hutchings *et al.,* [39] showed the significant influence of the presence of bimetallic

AuPd catalyst supported on alumina for the formation of hydrogen peroxide. They demonstrated that a supported AuPd catalyst generates significantly more hydrogen peroxide compared to its monometallic system which attributed to a synergistic effect between Au and Pd. In addition, Bawaked *et al.,* [46] investigated the solvent-free oxidation of crotyl alcohol utilizing AuPd in a variety of ratios, between Au and Pd, on a graphite support. They found that Au alone had low activity, however, the crotyl alcohol activity was significantly obtained using the bimetallic catalyst. Enache *et al.,* [46] also studied the impact of bimetallic AuPd on

a TiO$_2$ support generated from the impregnation method, finding that this catalyst appears to have greater activity than both Au/TiO$_2$ and Pd/TiO$_2$ catalysts. Furthermore, Albonetti, S. *et al.,* [50] produced bimetallic catalysts, AuCu and AuPd, in order to catalyse the reduction of 4-NP in the presence of sodium borohydride. They reported that the activity of the bimetallic AuPd catalyst was higher than that achieved by the bimetallic AuCu catalyst when operating under identical conditions. The synergistic effect was observed to be extremely robust with the AuPd catalyst which demonstrated a 93% higher activity relative to a gold monometallic catalyst; whilst the AuCu bimetallic catalyst activity only increased by 10%. This highlights that the nature of the second metal plays a significant role on enhancement the catalytic efficiencies in bimetallic catalysis. Prati *et al.,* discovered that AuPd NPs had around 4.5 times greater activity, in the selective oxidation of glycerol to glyceric acid, than monometallic analogous [51]. This led them to conclude that the increased activity and stability is a consequence of the altered morphology of the catalyst comprised of two metals.

1.4. Preparation of supported metal nanoparticle catalysts

Metal nanoparticles can be prepared *via* a variety of preparation techniques. Conventional approaches typically employed are founded on impregnation and precipitation methodologies, but the use of colloidal methods, particularly sol-immobilization method is increasingly gaining attention because of the capability of this method to fine tune catalyst characteristics. The following Sections will focus on the different preparation methods of supported nanoparticles and their individual benefits and constraints.

1.4.1. Impregnation

Nanoparticles of varying dimensions are frequently produced *via* the impregnation method. This technique requires 'wetting' of the solid support using a solution comprising the required quantity of metal precursor (generally a metal salt). When the required metal is dissolved in a volume of solvent equivalent to that of the total pore volume of the support (i.e. the incipient wetness point), a thick paste-like substance is generated, with this technique being referred to as 'incipient wetness impregnation'. The solvent is subsequently removed by evaporation, leaving an impregnated material, which can either be obtained in an oxidised state, or if required, can be subsequently reduced. Regulation of metal nanoparticle's morphology using this approach remains tricky. The particle size of the resultant metal nanoparticles depends upon three primary factors: the metal loading; the support's surface area; and the annealing atmosphere (post-treatment conditions). A low metal loading combined with a high surface

area support promotes the generation of smaller particles with greater dispersion [52]. Intense thermal treatments may be required to eliminated undesirable chlorine residues, and this can subsequently result in a high degree of particle agglomeration, especially with respect to higher metal loading catalysts [53]. A schematic representation of this preparation is presented in Figure 1.6.
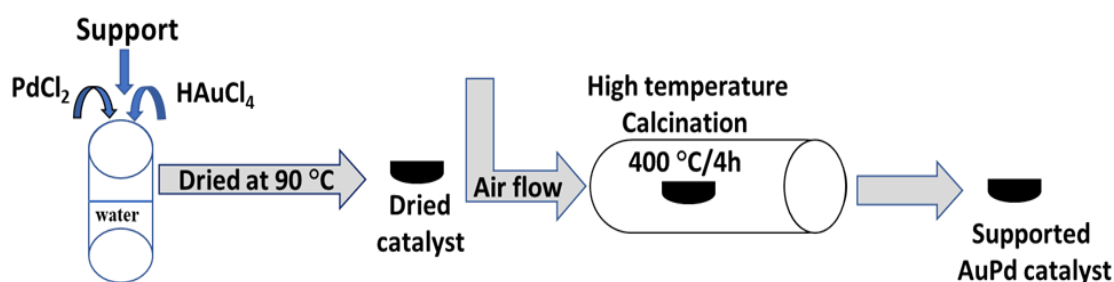
Figure 1.6 Schematic representation of the impregnation method for preparing AuPd supported nanoparticles.

1.4.2. Co-precipitation

The most popular technique to produce mixed-oxide catalysts is co-precipitation. It requires the concomitant precipitation of the metal and support material by addition of an aqueous alkali (such as NaOH, Na_2CO_3 or K_2CO_3). Typically, this approach enables a robust interaction between the metal and the supporting medium. A similar, but alternative technique, deposition-precipitation, requires the addition of the metal precursor to an aqueous suspension of the support medium prior to precipitating out the hydroxide by increasing the pH [54]. The surface of the support particles plays the part of a nucleating agent, which increases bonding of the active precursor to the support. The resulting hydroxide species can then be calcined and reduced to produce the required final compound [55]. A schematic representation of this preparation is presented in Figure 1.7.
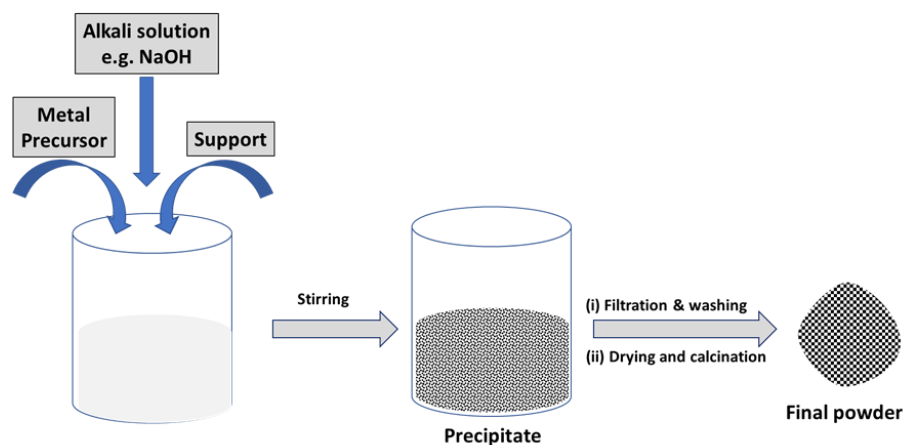
Figure 1.7 Schematic representation of the co-precipitation method for preparing metal supported nanoparticles.

1.4.3. Sol-immobilisation

A colloid can be described as a mixture in which one substance is divided into minute insoluble particles and is dispersed throughout a second substance. Essentially, the metal precursor, commonly a salt, is reduced to zero valent metal in the presence of a stabilising agent. There are two types of methods by which stabilising agents act to protect the metal from agglomeration: electrostatic repulsion or steric inhibition (see Figure 1.8). In some cases, molecules can function as both electrostatic and steric protectors. There are many different molecules that can act as stabilising agents, including donor ligands, polymers and surfactants. The sol-immobilization approach is in general deposing colloidal metal to a solid support material, by lowering the pH to below the support's isoelectronic point (i.e. point of zero charge e.g. around pH = 6 for TiO_2). This permits the charge interactions to take place between the metal and the support surfaces. Crucially, the characteristics of the preformed metal nanoparticles can be refined before they are immobilized onto the surface material, with a variety of potential reaction conditions: metal concentration; stabilized ligand : metal molar or weight ratio; type of reducing agent and concentration; choice of solvent; temperature; batch versus continuous flow system; etc. [56].
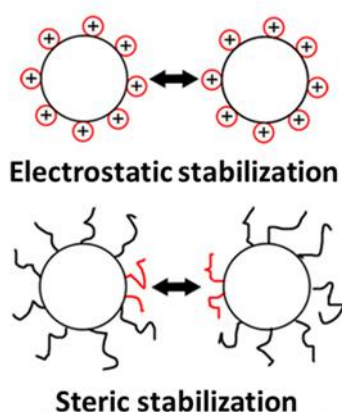
Figure 1.8 Schematic representation of steric and electrostatic stabilization.

polyvinyl alcohol (PVA) is a high molecular weight, long chain polymer which offers steric protection to the colloidal metal. As it is extremely water soluble (solubility ≈ 80 g/L), it can be employed as a protecting agent in environmentally-friendly 'green' preparation rather than using organic solvents. PVA was initially employed in this manner in 1996 by DiScipio [57] and it has been further developed over the last two decades by Dimitratos and Prati, [58,59] with successful application in the preparation of different supported metal nanoparticles [60,61]. The action of the stabilising agent during the synthesis procedures has been the subject of much research, which it has been shown that, at least for some liquid phase interactions, the existence of polymers on the surface of the metal particles does not impede the interaction, instead functioning to prevent metal nanoparticle conglomeration. Polymers are particularly useful, as they not only offer the capability to produce bespoke characteristics for nanometal particles, but they additionally promote the long-term stability of the nanoparticles whilst catalytic reactions are taking place [62].
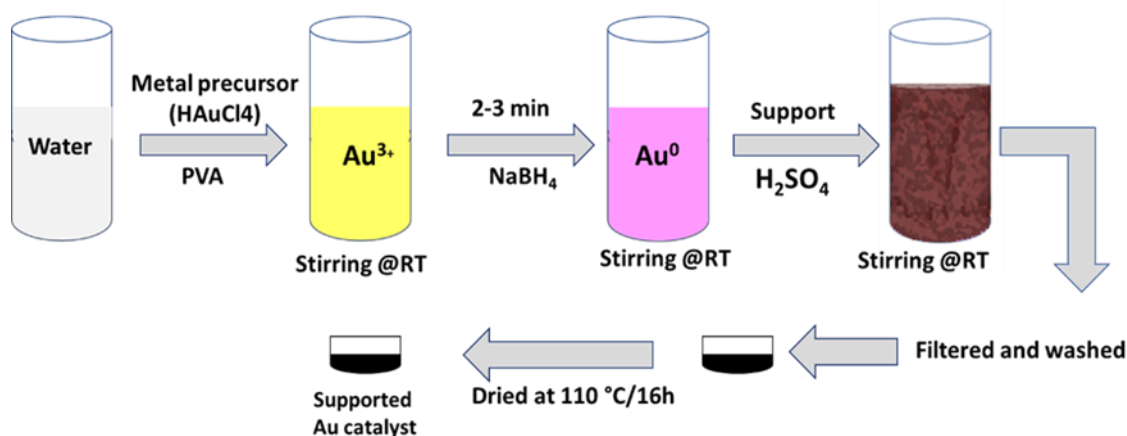
Figure 1.9 Schematic representations of sol-immobilisation method of preparing supported gold nanoparticles.

Polymers can be employed to encourage selective binding to crystal facets, to generate nanoparticles in accordance to specific shape or surface site requirements [63,64]. A range of reducing agents such as hydrogen, alcohols and hydrazine or boron hydride can be used, the choice of which can influence the metal properties [61]. A schematic representation of this preparation is presented in Figure 1.9.

1.5. Conventional catalyst support

The main purpose of utilising a catalytically active component in conjunction with an inert support medium is to facilitate dispersal of an expensive catalyst ingredient, such as a precious metal precursor (which typically only constitutes a very small fraction of the mixture), so that optimum effective distribution and use of the metal can be achieved by the provision of a larger active surface area, relative to a system involving only a bulk metal (e.g. a palladium black) [65]. In addition, this approach facilitates stabilisation of the active component and offers protection against particle growth [66]. Figure 1.10 shows how just the growth of small particles alone can result in a reduced active surface area, but using the active component applied on a support is able to stabilise the active surface area.

It is acknowledged that the characteristics of the support, such as reactivity, available surface area and pore size distribution, etc. impacts the final metal particle size, charge and morphology, generating specific active sites over the metal-support boundary [67]. Eventually, this can lead to variations in the catalytic characteristics of the metal nanoparticle generated.
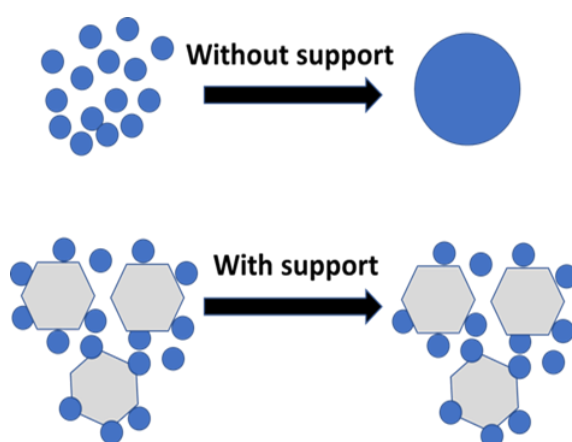
Figure 1.10 Rapid growth of active particles with no support (top) and supported thermostable active material (bottom).

Consequently, significant research effort to identify the most suitable support medium is needed to develop innovative catalysts.

1.6. Characteristics of support material

A catalyst support material are typically solids possessing a high surface area [68]. Table 1.2 lists requisite physicochemical parameters for a substance to be considered for use as a support material.

Table 1.2 Physical and chemical properties of support materials [65].

Chemical properties	Physical properties
Stable under reaction and regeneration conditions	Optimised bulk density
High specific activity/selectivity	High active surface area
Unreactive to unwanted reactions	Mechanical strength
Protects the catalyst from sintering	Optimises catalyst porosity
Minimises catalytic poisoning	Optimises metal crystal and particle size

A variety of catalyst supports exist, the most popular being alumina, silica, titania, magnesia, cupric oxide, nickel oxide, zeolites, silica-alumina and a range of carbon materials, such as charcoal and activated carbon [65]. Table 1.3 outlines and compares the key characteristics of some examples of typical catalyst supports. Support materials can be synthesized in a range of morphologies[65], including spheres, granules, extrudates, cylinders and powders; the final choice of which to use being dependent on the type of the reaction and the type of reactor to be utilized [69].

Table 1.3 Characteristics of typical catalyst supports [69].

Support	Properties	Applications
Carbon	surface area up to 1000 m^2g^{-1} unstable in oxide environment	hydrogenation
Zeolites	Highly defined pore system shape selective	bifunctional catalysts
Silica alumina	surface area up to 800 $m^2.g^{-1}$ medium strong acid sites	dehydrogenation; bifunctional catalysts
Al_2O_3	surface area up to 400 $m^2.g^{-1}$ thermally stable	catalyst for three-way converters; steam reforming
TiO_2	surface area up to 150 $m^2.g^{-1}$ limited thermal stability	selective catalytic reduction
MgO	surface area up to 200 $m^2.g^{-1}$	steam reforming

1.7. Significance of the support in heterogeneous catalysis

The identification of a suitable medium to provide physical support for metal catalysts is currently an important area of research interest. The underlying concept is that, to ensure optimal performance and minimal cost, the primary catalyst – active metal phase – should be dispersed thinly over an appropriate support to provide stability of the metal nanoparticles [70,71]. Furthermore, with porous characteristics, support materials offer a high dispersion of nanoparticle catalyst and simplify electron transfer, both of which contribute to better catalytic activities[72,72–74]. Nevertheless, the heterogeneous catalyst support may sometimes exert a structural effect, brought about by textural and active phase-linked effect [74]. Therefore, choice of support must retain its specific characteristics(such as surface area, porosity, dispersion, activity, and selectivity, etc.) [72,75]. The pores size and morphology of the selected support materials are crucial in enhancing the performance and stability of any heterogeneous catalyst [76,77]. According to the literature, the support of the heterogeneous catalyst can be active carbon [78], carbon nanofibers [79], zeolites [80], alumina [81] and metal oxides such as TiO_2 [82]. TiO_2 is a recognized heterogeneous catalyst support that is broadly utilized in fuel processing due to its tunable porous surface and distribution high thermal stability, and mechanical strength [72,83]. Titanium dioxide (TiO_2), also called titania, is a popular support choice for metal nanoparticles in heterogeneous catalysis due to its robust interaction with metal nanoparticles, excellent chemical and thermal stability, good mechanical strength and non-toxic, non-corrosive characteristics amongst all relative to other metal oxide support options. TiO_2 supported metal catalysts are popular because of the high activity exhibited by TiO_2 nanoparticles for a variety of redox reactions at low temperatures and pressures [84–90]. TiO_2 can exist in one of three crystalline forms: anatase; rutile and brookite. Brookite exists in an orthorhombic structure, and is rarely employed, being of no use for most applications. The rutile variety offers the greatest thermal stability of all the three phases: at temperatures greater than 600 °C, crystalline anatase and brookite undergo a phase transition, transforming into the rutile phase [91,92]. Most studies concentrated on producing titania in a variety of sizes and forms, e.g. thin films, powder, crystals, etc. [72]. TiO_2 manufacturing techniques typically require high temperatures to crystallize the amorphous material as one of the three TiO_2 phases, which leads to the production of larger particles and generally nonporous materials [93,94].

The TiO_2 powder (Degussa, P25) is well known commercial material which is containing anatase and rutile phases in the ratio of about 3:1 [95]. According to the literature, the morphology study for Degussa, P25 by Transmission electron microscopy (TEM) showed that the anatase and rutile particles separately form their agglomerates with average crystallize size of 85 and 25 nm, respectively [96]. Degussa, P25 is widely used in many applications such as solar energy storage, as catalyst in synthesis of organic compounds [95] and degradation of organic contamination in gaseous phase and aqueous system. Furthermore, it is one of the best TiO_2 photocatalysts and used frequently as a standard material in photocatalysis [96].

1.8. Reduction of 4-nitrophenol using supported nanoparticles

Nitrophenol can exist as one of three isomers (2-, 3- and 4-nitrophenol). 4-nitrophenol (4-NP) is also known as p-nitrophenol (p-NP), as the nitro- group is attached to the aromatic ring directly opposite to the hydroxyl group of the phenol molecule (i.e. in a para position). 4-NP is found in industrial wastewater from dyes, pesticides and explosives and it represents both a human health and environmental hazard as a consequence of its high solubility and toxicity [33]. Exposure to 4-NP can cause damage to blood cells and the central nervous system. As a result, it has been included on the list of priority pollutants by the EPA since 1976 [97]. In recent years, increasing attention has been paid to 4-NP, due to increasing concerns about its toxicity potential and negative impacts on the environment. Loos *et al.,* analysed 35 selected polar organic pollutants found in 122 water samples from 27 European rivers and found that 4-NP was one of the most ubiquitous river contaminants, detected in 97% of the samples, with a maximum concentration of 3471 μgL^{-1} (see Figure 1.11) [98]. Wennrich *et al.,* studied 11 nitrophenols in groundwater samples obtained from the vicinity of a former ammunitions factory in Germany. 4-NP was shown to be the second most concentrated nitrophenol, detected at a level of 88 μgL^{-1} [99]. The acceptable threshold concentration for 4-NP in surface water, near industrial and urban areas, was set at 100 μgL^{-1} in the Environmental Quality Standards Directive produced by the European Commission in 2006 [100]. These investigations highlight the requirement for the large-scale assessment of the environmental risks and relevant remediation approaches, particularly with respect to agricultural and industrial effluents. Therefore, there is a need to remove such chemicals from the industrial waste in order to keep environment safe. There are several well-known methods for removal of 4-NP include adsorption [101], photo-degradation [102] and electrochemical remediation [103]. However, these methods involve significant costs or extensive treatment times, making their application

unfeasible. One alternative approach is to facilitate the hydrogenation of 4-nitrophenol to produce 4-aminophenol using a stable heterogeneous catalyst.

The organic compound, 4-aminophenol (4-AP) is the product resulting from reduction of 4-NP, which has many useful applications. Typically, it is utilised as an intermediate product in the pharmaceutical industry in the production of analgesic and antipyretic drugs, such as paracetamol [104]. It also has application as a dye for wood staining treatments and in fur and feather colourings. The traditional method to produce 4-AP is through the iron-acid reduction of 4-NP or nitrobenzene. However, these approaches also result in the production of large quantities of Fe-FeO sludge (1.2 kg/kg product) [105] giving rise to significant disposal problems and environmental issues. An alternative approach could be to catalyse the hydrogenation of nitrobenzene *via* noble metal catalysis and concentrated sulphuric acid, albeit generating side products such as aniline and smaller amounts of other impurities [106]. In summary, the direct hydrogenation of 4-NP to 4-AP using a stable heterogeneous catalyst in the present of reducing reagent may offer a beneficial approach to remediate a variety of waste pollutants and could also result in the production of valuable chemical by-products (see Figure 1.12).
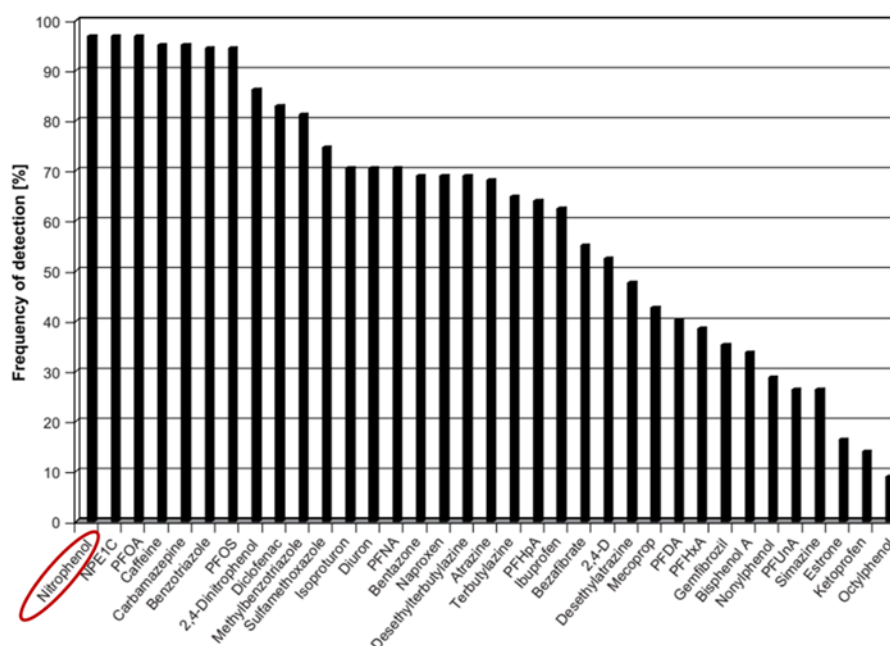
Figure 1.11 Frequency of appearance of the contaminants in the samples of European Rivers [98].

The free or immobilized nano-sized metal particles are used extensively in the reduction of 4-NP and common transition metals that are used are Ag, Pt, Pd, Ni, Rh, Au in the forms of

nanostructures [44,105,107]. This reduction reaction can be done by using sodium borohydride as the chosen reducing reagent at room temperature and therefore at mild reaction conditions.

Sodium borohydride ($NaBH_4$) is one of the most effective reducing agents for a variety of esters, ketones and acid halides [108,109]. However, because of kinetic impedance deriving from the potential difference between electron donor and acceptor molecules, sodium borohydride possesses a poor reductive capability with respect to nitro-compounds [110].
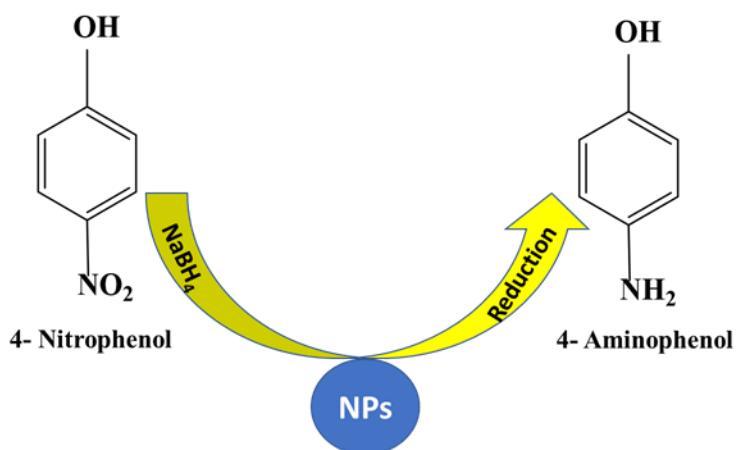
Figure 1.12 Direct reduction of 4-nitrophenol to 4-aminophenol by $NaBH_4$ over nanoparticles (NPs).

A comparison of the redox potentials of 4-NP and $NaBH_4$ indicates that whilst a redox reaction is theoretically thermodynamically feasible, it is kinetically restricted [111], which led Suzuki *et al.,* (1969) to develop the popular methodology for the reduction of 4-NP *via* application of an innovative $NaBH_4$ transition metal salt system [112]. This concept shows how the application of a transition metal to the solution can promote the reductive capabilities of $NaBH_4$ by facilitating electron transfer from the $NaBH_4$ to the 4-NP molecules. In 2002, Pal *et al.,* and Esumi *et al.,* firstly employed the reduction reaction in the evaluation of the catalytic activity of nano-sized metal particles. Since the potential of nano-sized metal particles lays between the potentials of BH_4^- ions and the nitroaromatics and serves as an electron relay, 4-Nitrophenol can be effectively reduced into 4-aminophenol. They also drew attention to the importance of size properties of metal catalysts and choice of reducing agent for the kinetics of reaction. In the course of these studies it is proved that the reaction did not proceed by other mild reducing agents such as hydrazine, molecular hydrogen and ascorbate anion even in the presence of nano-sized (reduced) metal particles as it proceeds in the case of $NaBH_4$ assisted reaction [113,114]. Later, the reduction of 4-NP by $NaBH_4$ in the presence of a metal catalyst has become one of the model reactions for evaluating the catalytic efficacy of noble metallic

nanoparticles since it is easy to monitor the reaction kinetics, and there are no by-products [31,33,44,115]. The reduction reaction is shown in Scheme 1.1.

This reduction reaction can be accomplished by using $NaBH_4$ as the reducing reagent at room temperature (a common choice as a consequence of to its robust reducing capabilities); however, other reducing agents, such as molecular H_2 [106] , silyl hydrides [116] , hydrazine hydrate [117] and formic acid [118] can also be employed. The application of reducing agents such as $NaBH_4$, formic acid and hydrazine hydrate as a hydrogen source for the 4-NP reduction is discussed in Chapter 5.
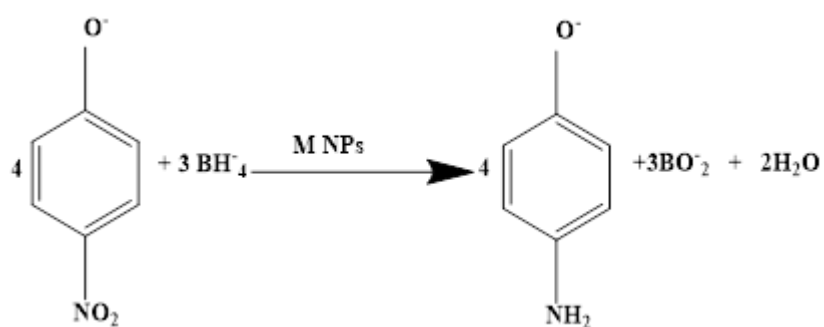
Scheme 1.1 Reduction of 4-NP using $NaBH_4$ [104].

1.9. Thesis structure

This thesis contains six Chapters in total. Chapter 1 gives a brief introduction of catalysis history and its types then focus on supported metal nanoparticles as powerful heterogeneous catalysis for several reactions with more attention on nitrophenol reduction reaction. Objectives of the present thesis are also highlighted.

In Chapter 2, catalysts preparation, experimental procedures, reaction setup, characterization techniques are explained in detail with the theory behind each characterisation techniques used in this work.

In Chapter 3, the preparation of Au/Pd nanoparticles catalysts supported on titanium dioxide (TiO$_2$) as monometallic and bimetallic using a sol-immobilization approach is reported. Deep characterization methods are also used in order to understand the physical and chemical properties for prepared catalysts. The catalytical performance of obtained catalysts are also evaluated toward the reduction of 4-NP with NaBH$_4$ as model reaction. The effect of the reactions conditions (e.g. 4-nitrophenol, NaBH$_4$, catalyst concentration, stirring rate and Au/Pd molar ratio) are also optimized.

In Chapter 4, Mono- and bimetallic catalyst (Au:Pd, 1:1 molar ratio) supported on nickel and copper oxides are synthesised. A comprehensive study of the influence of the nature of support toward 4-nitrphenol reduction has been conducted. In addition, induction time with copper oxide support is investigated.

In Chapter 5, a comparison study on the catalytic activities between AuPd and AgPd nanoparticles supported on TiO$_2$ were investigated toward 4-NP reduction reaction using three different reducing agents. The generality of the catalysts was also explored using different substrates. Chapter 6 summarizes and concludes the overall results and offers recommendations for future work.

1.10. Thesis objectives

As we described early, the preparation method of nanoparticles can affect their shape and morphology as well as altering their physical and chemical properties. Tuning these parameters is crucial for any given catalytic model. Among these methods, sol-immobilization method is considered to offer very narrow particle size distribution with small mean particle sizes. In addition, the method enhances the confinement, distribution and stability of the supported nanoparticles (mono and bimetallic supported nanoparticles). Moreover, it is quite easy, cheap and safe route comparing to other method of preparation.

Therefore, the main objectives of this study are to:

1. Prepare supported mono- and bimetallic AuPd and AgPd alloyed nanoparticles *via* a sol-immobilization method.
2. Characterize the prepared catalysts using the state-of-the-art techniques such as; UV-Vis spectroscopy, MP-AES, BET, XRD, TEM, HAADF-STEM and XPS.
3. Check the performance of AuPd and AgPd supported alloyed nanoparticles for the reduction of 4-nitrophenol, in aqueous phase, as a model reaction.
4. Study the effect of reaction parameters on the catalytic activity.
5. Study the effect of the bimetallic ratio on the AuPd and AgPd supported nanoparticles through sol-immobilization method on the reduction of 4-nitrophenol.
6. Explore the effect of support and induction time on the reduction of 4-nitrophenol.
7. Explore the effect of using different reducing agents for the catalyst's activity towards the reduction of 4-nitrophenol.

1.11. References

[1]   B. Lindström and L. J. Pettersson, Cattech, 2003, 7, 130–138.

[2]   J. W. Mellor, J. Phys. Chem., 1902, 7, 557–567.

[3]   J. Wisniak, Educ. quim., 2010, 21, 60–69.

[4]   H. Davy, Philos Trans R Soc L., 1817, 107, 77–85.

[5]   E. Davy, Philos. Trans. R. Soc. London, 1820, 110, 108–125.

[6]   W. Henry, Philos. Mag. Ser. 1, 1825, 65, 269–283.

[7]   L. Lloyd, Handbook of Industrial Catalysts, 2011.

[8]   B. JJ, Edinburgh New Philos. J., 1836, 21, 223 –228.

[9]   G. C. Bond, Heterogeneous catalysis : principles and applications, Clarendon, Oxford, 2nd edn., 1987.

[10]   M. Bowker, The basis and applications of heterogeneous catalysis, Oxford University Press, 1998.

[11]   I. Chorkendorff, J. W. Niemantsverdriet, Concepts of Modern Catalysis and Kinetics, John Wiley & Sons, 2003, 696 pp.

[12]   G. Rothenberg, Catalysis : concepts and green applications, Wiley-VCH, Weinheim ; Chichester, 2008.

[13]   Michael Bowker, The Basis and Applications of Heterogeneous Catalysis, Oxford University Press, New York, 1998.

[14]   D. J. Cole-hamilton, Science, 2003, 299 , 1702–1706.

[15]   S. Chassaing, V. Bénéteau and P. Pale, Curr. Opin. Green Sustain. Chem., 2018, 10, 35–39.

[16]   S. P. Gabriele Centi, Catal. Today, 2003, 77, 287–297.

[17]   F. Sanchez, D. Motta, A. Roldan, C. Hammond, A. Villa and N. Dimitratos, Top. Catal., 2018, 61, 1–13.

[18]   K. Wei, X. Wang, R. A. Budiman, J. Kang, B. Lin, F. Zhou and Y. Ling, J. Mater. Sci., 2018, 53, 1–19.

[19]   G. W. Huber, J. W. Shabaker and J. a Dumesic, Science, 2003, 300, 2075–2078.

[20]   Varadarajan and D. J. Miller, Biotechnol. Prog, 1999.

[21]   A. L. de Lima, C. M. Ronconi and C. J. A. Mota, Catal. Sci. Technol., 2016, 6, 2877–2891.

[22]   B. Cornils, W.A. Herrmann, Editors, Aqueous-Phase Organometallic Catalysis, 2nd Ed: Aqueous Phase Organometallic Catalysis, Wiley-VCH Verlag GmbH & Co. KGaA, 2004.

[23]   G. C. Bond, P. A. Sermon, G. Webb, D. A. Buchanan and P. B. Wells, J. Chem. Soc. Chem. Commun., 1973, 444–445.

[24]   G. J. Hutchings, J. Catal., 1985, 96, 292–295.

[25]   M. Haruta, T. Kobayashi, H. Sano and N. Yamada, Chem. Lett., 1987, 16, 405–408.

[26]   C. W. Corti, R. J. Holliday and D. T. Thompson, Gold Bull., 2002, 35, 111–117.

[27]   R. C. Zhang, D. Sun, R. Zhang, W. F. Lin, M. Macias-Montero, J. Patel, S. Askari, C. McDonald, D. Mariotti and P. Maguire, Sci. Rep., 2017, 7, 1–9.

[28]   M. Compagnoni, S. A. Kondrat, C. E. Chan-Thaw, D. J. Morgan, D. Wang, L. Prati, A. Villa, N. Dimitratos and I. Rossetti, ChemCatChem, 2016, 8, 2136–2145.

[29]   G. J. Hutchings, Dalt. Trans., 2008, 9226, 5523–9936.

[30]   G. J. Hutchings, Catal. Today, 2005, 100, 55–61.

[31]   T. Ma, W. Yang, S. Liu, H. Zhang and F. Liang, Catalysts, 2017, 7, 38–48.

[32]   L. Yin and J. Liebscher, Chem. Rev., 2007, 107, 133–173.

[33]   S. Rogers, R. Catlow, D. Gianolio, P. Wells and N. Dimitratos, Faraday Discuss., 2018, 208, 443-454.

[34]   A. Frattini, N. Pellegri, D. Nicastro and O. De Sanctis, Mater. Chem. Phys., 2005, 94, 148–152.

[35]   Y. Xia, Z. Gao, X. Liao, S. Yan, J. Han, X. Wang, C. Pan, Y. Zhang and W. Zhai, CrystEngComm, 2018, 20, 2135–2143.

[36]   A. Khorshidi and B. Ghorbannezhad, RSC Adv., 2017, 7, 29938–29943.

[37]   V. Asharani, D. Thirumalai and A Sivakumar, IOP Conf. Series: Mater. Sci. Eng., 2017, 263, 022010–022017.

[38]   T. Mitsudome, M. Matoba, T. Mizugaki, K. Jitsukawa and K. Kaneda, Chem. - A Eur. J., 2013, 19, 5255–5258.

[39]   Z. Jin, H. Xiao, W. Zhou, D. Zhang and X. Peng, R. Soc. Open Sci., 2017, 4, 171414–171429.

[40]   R. Zhang, B. Zhao, L. Ling, A. Wang, C. K. Russell, B. Wang and M. Fan, ChemCatChem, 2018, 1–10.

[41]   Y. Jin, C. Ma, M. Shi, Y. Chu, Y. Xu, T. Huang, Q. Huang and Y. Miao, Int. J. Electrochem. Sci., 2012, 7, 3399–3408.

[42]   H. Liu and Q. Yang, J. Mater. Chem., 2011, 21, 11961–11967.

[43]   S. D. Oh, M. R. Kim, S. H. Choi, J. H. Chun, K. P. Lee, A. Gopalan, C. G. Hwang, K. Sang-Ho and O. J. Hoon, J. Ind. Eng. Chem., 2008, 14, 687–692.

[44]   N. Arora, A. Mehta, A. Mishra and S. Basu, Appl. Clay Sci., 2018, 151, 1–9.

[45]   D. Motta, F. J. S. Trujillo, N. Dimitratos, A. Villa and L. Prati, Catal. Today, 2018, 308, 50–57.

[46]   X. Fang and D. Fang, RSC Adv., 2017, 7, 40437–40443.

[47]   C. Jia, W. Zhong, M. Deng, J. Jiang, C. Jia, W. Zhong, M. Deng and J. Jiang, The Journal of Chemical Physics, 2018, 148, 124701–124701.

[48]   H. L. Jiang, T. Akita, T. Ishida, M. Haruta and Q. Xu, J. Am. Chem. Soc., 2011, 133, 1304–1306.

[49]   A. Alshammari, V. Kalevaru, and A. Martin, Catalysts, 2016, 6, 97–121.

[50]   M. Blosi, S. Ortelli, A. L. Costa, M. Dondi, A. Lolli, S. Andreoli, P. Benito and S. Albonetti, 2016, 1–25.

[51]   G. L. Brett, Q. He, C. Hammond, P. J. Miedziak, N. Dimitratos, M. Sankar, A. A. Herzing, M. Conte, J. A. Lopez-Sanchez, C. J. Kiely, D. W. Knight, S. H. Taylor and G. J. Hutchings, Angew. Chemie - Int. Ed., 2011, 50, 10136–10139.

[52]   L. Delannoy, N. El Hassan, A. Musi, N. N. Le To, J.-M. Krafft and C. Louis, J. Phys. Chem. B, 2006, 110, 22471–22478.

[53]   M. Campanati, G. Fornasari and A. Vaccari, Catal. Today, 2003, 77, 299–314.

[54]   R. Zanella, S. Giorgio, C. R. Henry and C. Louis, J. Phys. Chem. B, 2002, 106, 7634–7642.

[55]   M. Comotti, W. C. Li, B. Spliethoff and F. Schüth, J. Am. Chem. Soc., 2006, 128, 917–924.

[56]   N. Dimitratos, A. Villa, L. Prati, C. Hammond, C. E. Chan-Thaw, J. Cookson and P. T. Bishop, Appl. Catal. A Gen., 2016, 514, 267–275.

[57]   R. G. Discipio, Book title "Preparation of colloidal gold particles 1996, 170, 168–170.

[58]   L. Prati and G. Martra, Gold Bull., 1999, 32, 96–101.

[59]   N. Dimitratos, F. Porta and L. Prati, Appl. Catal. A Gen., 2005, 291, 210–214.

[60]   E. J. Kim, J. H. Yeum and J. H. Choi, J. Mater. Sci. Technol., 2014, 30, 107–111.

[61]   C.-J. Jia and F. Schüth, Phys. Chem. Chem. Phys., 2011, 13, 2457–2487.

[62]   J. Shan and H. Tenhu, Chem. Commun., 2007, 4580–4598.

[63]   Q. F. Zhou, J. C. Bao and Z. Xu, J. Mater. Chem., 2002, 12, 384–387.

[64]   Y. Xiong, I. Washio, J. Chen, H. Cai, Z. Y. Li and Y. Xia, Langmuir, 2006, 22, 8563–8570.

[65]   and F. K. E.M. Holt, G.J. Kelly, in Reactor Design for Chemical Engineers, ed. J. M. W. and M. B. King, 1999, pp. 276–300.

[66]   E. Marceau, X. Carrier, M. Che, O. Clause, in Handbook of Heterogeneous Catalysis Edited by J. W. G. Ertl, H. Knozinger, F. Schuth, 2008, pp. 467–484.

[67]   Z. Qu, W. Huang, S. Zhou, H. Zheng, X. Liu, M. Cheng and X. Bao, J. Catal., 2005, 234, 33–36.

[68]   G. J. Hutchings, J. Mater. Chem., 2009, 19, 1222–1235.

[69]   O. Deutschmann, H. Knözinger, K. Kochloefl and T. Turek, Heterogeneous Catalysis and Solid Catalysts, 2009.

[70]   B. Uysal and B. S. Oksal, Res. Chem. Intermed., 2015, 41, 3893–3911.

[71]   N. Shibasaki-Kitakawa, H. Honda, H. Kuribayashi, T. Toda, T. Fukumura and T. Yonemoto, Bioresour. Technol., 2007, 98, 416–421.

[72]   S. Bagheri, N. Muhd Julkapli and S. Bee Abd Hamid, ScientificWorldJournal, 2014, 2014, 727496–727517.

[73]   J. M. Planeix, N. Coustel, B. Coq, V. Brotons, P. S. Kumbhar, R. Dutartre, P. Geneste, P. Bernier and P. M. Ajayan, J. Power Sources, 1994, 116, 7935–7936.

[74]   P. D. Kent, J. E. Mondloch and R. G. Finke, J. Am. Chem. Soc., 2014, 136, 1930–1941.

[75]   E. Guibal, Prog. Polym. Sci., 2005, 30, 71–109.

[76]   N. Masoud, B. Donoeva and P. E. de Jongh, Appl. Catal. A Gen., 2018, 561, 150–157.

[77]   S. De, S. Dutta and B. Saha, Catal. Sci. Technol., 2016, 6, 7364–7385.

[78]   F. Sanchez, D. Motta, A. Roldan, C. Hammond, A. Villa and N. Dimitratos, Top. Catal., 2018, 61, 254–266.

[79]   D. Motta, F. J. S. Trujillo, N. Dimitratos, A. Villa and L. Prati, Catal. Today, 2018, 308, 50–57.

[80]   C. Hammond, N. Dimitratos, J. A. Lopez-Sanchez, R. L. Jenkins, G. Whiting, S. A. Kondrat, M. H. Ab Rahim, M. M. Forde, A. Thetford, H. Hagen, E. E. Stangland, J. M. Moulijn, S. H. Taylor, D. J. Willock and G. J. Hutchings, ACS Catal., 2013, 3, 1835–1844.

[81]   N. D. Subramanian, J. Callison, C. R. A. Catlow, P. P. Wells and N. Dimitratos, Int. J. Hydrogen Energy, 2016, 41, 18441–18450.

[82]   M. Khawaji and D. Chadwick, Catal. Sci. Technol., 2018, 8, 2529–2539.

[83]   Q. Zhang, J. B. Joo, Z. Lu, M. Dahl, D. Q. L. Oliveira, M. Ye and Y. Yin, Nano Res., 2011, 4, 103–114.

[84]   J. Yu, J. Low, W. Xiao, P. Zhou and M. Jaroniec, J. Am. Chem. Soc., 2014, 136, 8839–42.

[85]   T. Ochiai and A. Fujishima, J. Photochem. Photobiol. C Photochem. Rev., 2012, 13, 247–262.

[86]   L. Ma, I. Jia, X. Guo and L. Xiang, Chinese J. Catal., 2014, 35, 108–119.

[87]   S. Wei, X. P. Fu, W. W. Wang, Z. Jin, Q. S. Song and C. J. Jia, J. Phys. Chem. C, 2018, 122, 4928–4936.

[88]   G. Wu, G. L. Brett, E. Cao, A. Constantinou, P. Ellis, S. Kuhn, G. J. Hutchings, D. Bethell and A. Gavriilidis, Catal. Sci. Technol., 2016, 6, 4749–4758.

[89]   M. Muuronen, S. M. Parker, E. Berardo, A. Le, M. A. Zwijnenburg and F. Furche, Chem. Sci., 2017, 8, 2179–2183.

[90]   M. Zhang, Q. Pei, W. Chen, L. Liu, T. He and P. Chen, RSC Adv., 2017, 7, 4306–4311.

[91]   A. Di Paola, M. Bellardita and L. Palmisano, Brookite, the Least Known TiO_2 Photocatalyst, 2013, vol. 3.

[92]   J. Xu, K. Li, W. Shi, R. Li and T. Peng, J. Power Sources, 2014, 260, 233–242.

[93]   T. Fröschl, U. Hörmann, P. Kubiak, G. Kučerová, M. Pfanzelt, C. K. Weiss, R. J. Behm, N. Hüsing, U. Kaiser, K. Landfesterd and M. Wohlfahrt-Mehrensc, Chem. Soc. Rev., 2012, 41, 5313–5360.

[94]   D. Ramimoghadam, S. Bagheri and S. B. Abd Hamid, BioMed Res. Int., 2014, 2014, 1–7.

[95]   B. Sun and P. G. Smirniotis, Catal. Today, 2003, 88, 49–59.

[96]   T. Ohno, K. Sarukawa, K. Tokieda and M. Matsumura, J. Catal., 2001, 203, 82–86.

[97]   Agency, U.E.P., Code of Federal Regulations, Washington, DC., 1987.

[98]   R. Loos, B. M. Gawlik, G. Locoro, E. Rimaviciute, S. Contini and G. Bidoglio, Environ. Pollut., 2009, 157, 561–568.

[99]   L. Wennrich, J. Efer and W. Engewald, Chromatographia, 1995, 41, 361–366.

[100]   World Health Organization, Concise International Chemical Assessment Document 20: Mononitrophenols, Geneva, 2000.

[101]   Z. Wu, X. Yuan, H. Zhong, H. Wang, G. Zeng, X. Chen, H. Wang, L. Zhang and J. Shao, Sci. Rep., 2016, 6, 1–13.

[102]   P. Xiong, Y. Fu, L. Wang and X. Wang, Chem. Eng. J., 2012, 195–196, 149–157.

[103]   P. Cañizares, C. Sáez, J. Lobato and M. A. Rodrigo, Ind. Eng. Chem. Res., 2004, 43, 1944–1951.

[104]   J. Noh and R. Meijboom, Appl. Nanotechnol. Water Res., 2014, 333–406.

[105]   H. Lu, H. Yin, Y. Liu, T. Jiang and L. Yu, Catal. Commun., 2008, 10, 313–316.

[106]   C. V Rode, M. J. Vaidya, R. Jaganathan and R. V Chaudhari, Chem. Eng. Sci., 2001, 56, 1299–1304.

[107]   S. M. El-Sheikh, A. A. Ismail and J. F. Al-Sharab, New J. Chem., 2013, 37, 2399–2407.

[108]   H. Bertschy, H. K. Chenault and G. . Whitesides, Enzym. Catal. Org. Synth. A Compr. Handb., 1995, 22, 6761–6764.

[109]   A. Saeed and Z. Ashraf, J. Chem. Sci., 2006, 118, 419–423.

[110]   O. A. Zelekew and D.-H. Kuo, RSC Adv., 2017, 7, 4353–4362.

[111]   B. Li, Y. Hao, X. Shao, H. Tang, T. Wang, J. Zhu and S. Yan, J. Catal., 2015, 329, 368–378.

[112]   T. Satoh, S. Suzuki, Y. Suzuki, Y. Miyaji and Z. Imai, Tetrahedron Lett., 1969, 10, 4555–4558.

[113]   K. Esumi, K. Miyamoto and T. Yoshimura, J. Colloid Interface Sci., 2002, 254, 402–405.

[114]   N. Pradhan, A. Pal and T. Pal, Colloids Surfaces A Physicochem. Eng. Asp., 2002, 196, 247–257.

[115]   S. M. Sadeghzadeh, R. Zhiani and S. Emrani, New J. Chem., 2018, 42, 988–994.

[116]   K. Junge, B. Wendt, N. Shaikh and M. Beller, Chem. Commun., 2010, 46, 1769–1771.

[117]   B. H. and S.-H. Y. Yong-Ming Lu, Hai-Zhou Zhu, Wei-Gu Li, J. Mater. Chem. A, 2013, 3783–3788.

[118]   R. Javaid, S. I. Kawasaki, A. Suzuki and T. M. Suzuki, Beilstein J. Org. Chem., 2013, 9, 1156–1163.

Chapter 2

Materials and methods

2.1. Introduction

Experimental techniques are very important tools to well understand the properties of supported metal nanoparticles as potential catalysts. For instance, many characterisation techniques have been used in catalysis area aiming to study the reaction mechanism and to analyse the catalyst chemical and physical properties [1]. Herein, we describe in detail the materials, the preparation method used throughout the whole thesis, characterization methods for the materials as well as a full description for the catalytic reactor and testing procedures used to evaluate the performance of the catalysts towards different reactions.

2.2. List of chemicals

In Table 2.1 below, materials were used in this study are summarized as follows:

Table 2.1 List of chemicals and reagents.

Substance	Supplier	Purity
4-Nitrophenol, $O_2NC_6H_4OH$	Sigma Aldrich	99.99%
3-Nitrophenol, $O_2NC_6H_4OH$	Sigma Aldrich	$\geq 99\%$
2-Nitrophenol, $O_2NC_6H_4OH$	Sigma Aldrich	$\geq 99\%$
4-Nitroaniline, $O_2NC_6H_4NH_2$	Sigma Aldrich	$\geq 99\%$
Nitrobenzene, $C_6H_5NO_2$	Sigma Aldrich	$\geq 99\%$
$HAuCl_4.3H_2O$	Alfa Aesar	99.99%
K_2PdCl_4	Sigma Aldrich	99%
$AgNO_3$	Sigma Aldrich	99%
Poly vinyl alcohol (PVA), (MW=10,000)	Sigma Aldrich	99%
$NaBH_4$	Sigma Aldrich	$\geq 98\%$
NaOH	Fisher	99%
Sulphuric acid, H_2SO_4	Fisher	95%
Formic acid, HCOOH	Sigma Aldrich	95%
Nitric acid, HNO_3	Fisher	70%
Hydrazine hydrate($NH_2NH_2 \cdot xH_2O$)	Sigma Aldrich	60% in H_2O
Urea, NH_2CONH_2	Sigma Aldrich	98%
TiO_2 (P25)*	Degussa	>99.5%
Nickel(II) oxide (NiO)	Sigma Aldrich	99.99%
Copper(II) oxide (CuO)	Sigma Aldrich	99.99%

* *TiO_2 (P25): rutile:anatase ratio = 15:85, as calculated from XRD diffraction patter of TiO_2 (P25).*

Materials were used as received from the supplier without any further purification. Deionised water was used as solvent for the reaction and catalysts' preparation.

2.3. Catalyst preparation

2.3.1.   The sol-immobilisation method

The method employed for metal nanoparticle generation is based on colloidal routes, in which zero-valent metal is stabilised in solution by the presence of a protecting agent. The subsequent metal nanoparticles are anchored on to a support material to yield the final catalyst, the overall process known as the sol-immobilisation method [2]. The use of polyvinyl alcohol (PVA) as stabilising agent has demonstrated that metal nanoparticles can be prepared with a narrow particle distribution, with the average metal particle size <10 nm, dependent on the stabilising/metal ratio [3–7]. The structure of PVA is illustrated in Figure 2.1, with the 200-230 repeating units for the PVA used in this study (molecular weight = 9-10000 g mol^{-1}). The large polymer structure work to stabilise metal nanoparticles through steric, rather than electrostatic interactions [8].
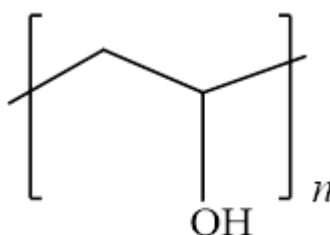
Figure 2.1 The monomer unit in the polymer, polyvinyl alcohol (PVA), where n is the number of repeating units.

2.3.2.   The sol-immobilisation synthesis procedure

Supported mono and bimetallic nanoparticles were prepared at room temperature using standard sol-immobilization method [9,10]. For instance, to prepare AuPd bimetallic catalyst with 1:1 molar ratio of the metals in 1 wt.% of support, an aqueous solution of K_2PdCl_4 (0.64 ml of 5.5 mg/ml) and $HAuCl_4.3H_2O$ (0.53 ml of 12.25 mg/ml) were added to 400 mL of H_2O and thus should give Au:Pd solution with 1:1 molar ratio. The required amount of Polyvinyl alcohol (PVA) 1 wt.% solution (100 mg of PVA MW = 9-10000 g/mole dissolved in 10 mL water) was added to the aqueous solutions of K_2PdCl_4 and $HAuCl_4.3H_2O$. The PVA/metals weight ratio is 0.65 for mono and 1.2 for bimetallic catalyst. The mixture was stirred for two minutes at room temperature. Then, a freshly prepared solution of $NaBH_4$ (0.1 M of $NaBH_4$ / metals (mol/mol) = 5) was then added to form a dark-brown sol. After 30 min of sol generation, the colloid was supported by adding 0.99 g of the support. The suspension was acidified to pH 2, through the drop-wise addition of concentrated H_2SO_4, which was added under vigorous stirring. For the

catalysts prepared in this thesis, the required amount of support was calculated to have a final metal loading of 1 wt. %. The slurry was then stirred for 1 h, then the catalyst was recovered by filtration, washed several times with deionized water to remove any soluble impurities (i.e. Na^+, Cl^-) and/or any excess of PVA and finally dried at 110 °C for 16 h. Similarly, monometallic (Au, Pd and Ag) and bimetallic (AuPd and AgPd) supported nanoparticles were prepared by the same method . For bimetallic systems, the targeted stoichiometric molar ratios between the two metals were as the follow; 0.13:0.87, 0.25:0.75, 0.5:0.5, 0.75:0.25 and 0.87:0.13). The general procedure of metal nanoparticle synthesis by sol-immobilisation method using the $NaBH_4$/PVA is shown in Figure 2.2.
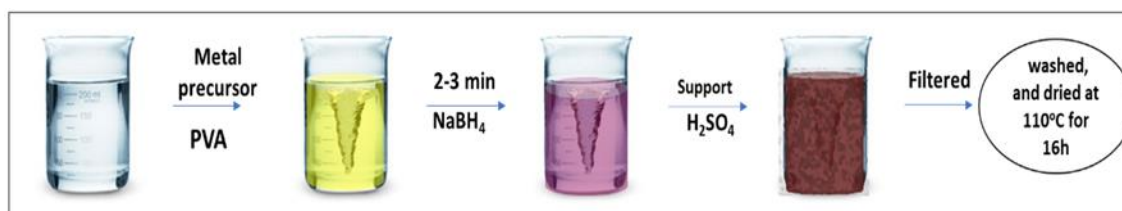
Figure 2.2 Sol-immobilisation method used for the preparation of supported metal nanoparticles.

2.3.3. Synthesis of nanosized nickel (II) oxide (NiO)

A synthesized Nickel(II) oxide (NiO) was prepared by Dr. Alberto Villa at the University of Milan according to Villa *et al.,* methodology [11]. In a typical preparation, appropriate molar quantities of $Ni(NO_3)_2 \cdot 6H_2O$ (5 x 10^{-4} M) and urea (urea/Ni molar ratio = 10) were added to 200 ml of water under magnetic stirring for 6 hrs at 80 °C. Consequently, $Ni(OH)_2$ was separated from the solution, filtered and washed by deionised water several times. The powder was dried at 60 °C for 12h and then calcined at 300 °C for 3h under static air. The powder obtained was labelled as NiO_s and stored in the desiccator to protect it from moisture. For comparison purposes commercial NiO material (as a bench mark support) was modified with urea using the procedure described previously [11]. Typically, 5 g of commercial NiO powder (NiO_c) was added into urea aqueous solutions (200 mL, 2.5 M). Subsequently, the suspension was heated up to 80 °C and stirred for 6 h. After cooling down to room temperature, the solid (green powders) were recovered by filtration and washed several times with deionized water. The recovered solid sample was dried at 60 °C for 12 h then used as it .

2.4. Catalyst testing

Catalytic performance of the synthesized catalysts was carried out in the liquid-phase reduction of 4-NP using three different reducing reagents, namely $NaBH_4$, Formic acid and hydrous hydrazine. The reactions were performed under mild reaction conditions using water as the desired solvent at 30 °C and atmospheric pressure in the presence of catalyst, with an excess of reducing reagent. The experiments were carried out using two types of reactors and it will be described in the next Section.

2.4.1. Off-line batch reactor

Reduction of 4-nitrophenol (4-NP) with different reducing agents was performed in a stirred glass reactor round-bottom flask (100 ml) and placed in an oil bath with a magnetic stirrer (Figure 2.3). In a typical reaction, the requisite amount of catalyst was suspended in 45 ml of aqueous solution of 4-NP (1.35×10^{-4} M). The reaction mixture was stirred at 1000 rpm for 20 minutes at 30 °C followed by the addition of 5 ml of the appropriate amount of the desired reducing agent to start the reaction. The specific conditions for each experiment are as follows: sodium borohydride (3.9×10^{-2} M, $NaBH_4$/4-NP molar ratio = 30), formic acid (0.06 M, formic acid/4-NP molar ratio = 45) and hydrazine (0.05 M, hydrazine /4-NP molar ratio = 40, and in all cases a 4-NP /metal molar ratio of 13 was used. At the specific sampling time, syringe filters (0.45 µm pore size) and a syringe (1mL) were used to transfer 1 ml of the reaction solution to the UV cuvette and then UV-Vis spectra were collected periodically to monitor the progress of the reaction.
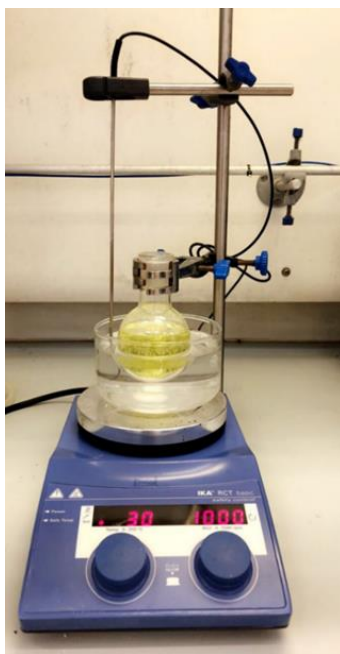
Figure 2.3 Schematic diagram of off-line batch reactor (glass reactor).

2.4.2.   On-line batch reactor

In addition to the off-line analysis, the reduction of 4-NP with $NaBH_4$ was also conducted on-line (monitoring continuously UV spectra as described below) in a quartz cuvette with an optical path length of 1cm due to the high conversion rate of 4-nitorphenol, which sometimes reach 100% conversion within one minute. Moreover, on-line batch reactor has been used to determine the initial concentration of 4-NP(C_0) in all experiments using the standard conditions. Typically, the requisite amount of catalyst was added directly into the cuvette, which contains fresh solution of 4-NP (2.7 mL, 1.35×10^{-4} M). The cuvette was subsequently placed into a Qpod 2e ABSKIT temperature controller (Avantes), which provides magnetic stirring and temperature controller by a Peltier system, both remotely controlled by a computer (Figure 2.4). When the desired temperature was reached, the fresh $NaBH_4$ solution (0.3 mL, 3.9×10^{-2} M) was added to give a total volume of 3 ml to initiate the reaction. The reduction process of 4-NP was subsequently monitored by measuring the UV-Vis absorption spectra of the reaction solution every 5 seconds until full conversion was achieved.

Figure 2.4 photograph of the AvaSoft UV-Vis Spectrometry setup (On-line batch reactor) for monitoring the reduction of 4-nitrophenol. (Cardiff Catalysis Institute).

2.4.3. Analysis of reaction

The progress of the reduction of 4-NP is easily monitored using UV-Vis spectroscopy because 4-NP ion shows a distinct absorption peak around 400 nm [12–14]. In the UV-Vis spectrum the absorption maxima corresponding to the 4-NP appears at 317 nm [15,16]. The presence of sodium borohydride leads to a shift in the absorption band of the 4-nitrophenol to 400 nm, indicating the presence of the nitrophenolate anion, which changes the color of the solution from pale yellow to dark yellow [15,17,18], an example for 4-nitrophenolate ion shown in Figure 2.5. Similar behavior was noticed when hydrous hydrazine was used as reducing agent , instead of $NaBH_4$ [19]. However, in the case of using formic acid (acidic conditions), the nitrophenolate ions peak wasn't observed because the formic acid acidifies the reaction medium, which decrease the rate of 4-nitrophenol ionization to 4-nitrophenolate ion, hence, no shift in the 4-NP absorbance band was observed [20].
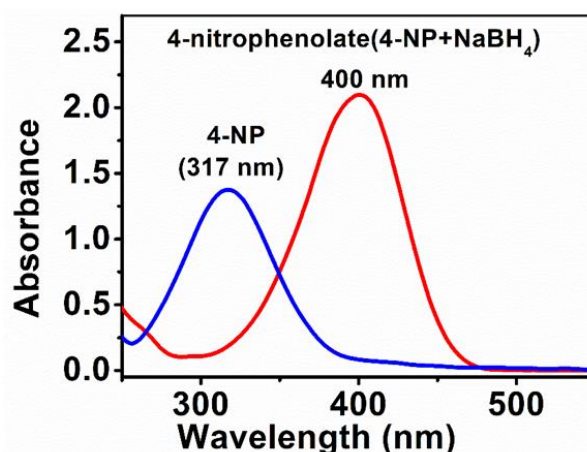
Figure 2.5 Example of UV–vis spectra of aqueous 4-NP solution (blue line) and aqueous 4-NP solution (4- nitrophenolate) in the presence of $NaBH_4$ (red line).

In this study, the concentration of 4-NP has been determined using the calibrations curve by observing the decay of 4-nitrophenol ion (4- nitrophenolate) absorbance in the basic and 4-NP absorbance in the acidic conditions at 400 nm and 317 nm respectively. Calibrations were performed in order to calculate a molar extinction coefficient of the 4-nitrophenolate ions, according to the Beer-Lambert law. An absorbance versus concentration plot gives a straight line, in which the molar extinction coefficient can be directly obtained from the gradient. The concentration absorption calibration plot for aqueous 4-NP in the presence of $NaBH_4$ is shown in Figure 2.6. The extinction coefficient was determined by first preparing a fresh solution of 4-NP with a concentration of 9.3×10^{-3} M, which was subsequently diluted to make solutions with

final concentrations between 1.67×10^{-4} M and 6×10^{-6} M. A 0.05 M solution of NaBH$_4$ was prepared in a 25 mL volumetric flask. 0.3 mL of this solution was added to the 1 cm^2 cuvette. A fresh NaBH$_4$ solution was prepared prior to each reaction due to its rapid decomposition. An extinction coefficient of 4-NP was found to be18620 M^{-1} cm^{-1}, which is in good agreement with values that reported in the literature (18,000–19,000) [21,22]. In the same way, the extinction coefficient was determined for 4-NP in the presence of hydrazine and formic acid 17630 and 9784 M^{-1} cm^{-1}, respectively.
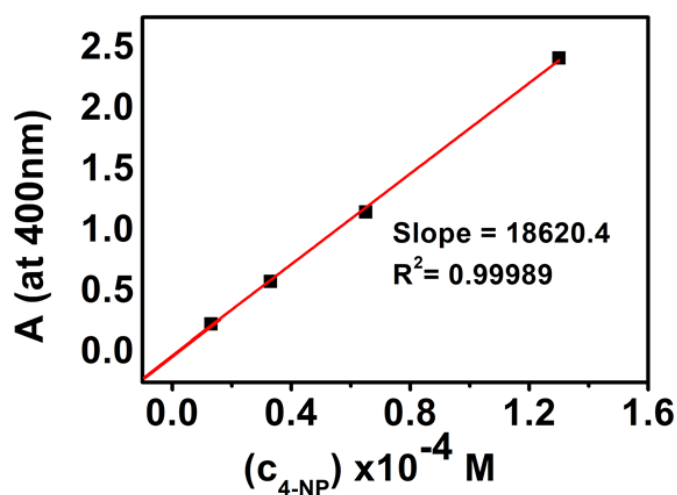
Figure 2.6 Calibration plot of absorbance against concentration for 4-nitophenol. The calibration line was determined by fitting the data to the Beer-Lambert law (Eq 2.1).

2.5. Reusability tests

The reusability of the catalysts was studied by carrying out the reaction in round bottom flask, using 45 mL of 4-NP solution (1.35×10^{-4} M) and 5 mL of aqueous NaBH$_4$ (0.039 M) as the reducing agent. Subsequently, required amount of the catalyst was added to initial the reaction, which was allowed to proceed for specific time. After this time the catalyst was separated from the solution, washed with 20 mL of deionised water before being reused. The UV-Vis spectra at 0 s was recorded using on-line batch reactor procedure by using 0.3 mL and 2.7 mL of the same solutions of NaBH$_4$ and 4-NP respectively without the presence of the catalyst.

2.6. Instrumentation

2.6.1. UV-Vis spectroscopy

Background

This method refers to absorption or reflectance spectroscopy in the 200-800 nm region of the electromagnetic spectrum. Molecules containing π-electrons or non-bonding electrons undergo electronic transitions upon exposure to UV-Vis light, promoting an electron from ground to excited state. One of the most widely used methods for characterizing the optical and electronic structure of metal nanoparticles is through UV-Vis spectroscopy. For metals that possess a plasmon-resonance band, such is the case with Au, Ag and Cu, it can be an indicative tool towards the metal particle size based on the intensity and position of the band during the sol formation [23,24]. The plasmon resonance arises due to free conduction electrons oscillating because of induced electromagnetic radiation interaction [25]. The SPR band appears in the range400-600 nm, depending on the metal, with increasing particle size causing a red shift, and increased particle distribution causing band broadening. Not only particle size affects the plasmon resonance, as other factors including solvent and surface functionalization can contribute to the exact frequency and intensity of the band. Whether the metal possesses a plasmon resonance band or not, such is the case with palladium, the technique is useful to follow the reduction process from a metal salt, to metal nanoparticle during the sol-immobilization process. The quantitative determination of highly conjugated organic compounds can be performed using UV-Vis spectroscopy. The Beer-Lambert law states that the absorbance of a solution is directly proportional to the concentration of the absorbing species in the solution and the path length, according to equation 2.1.

$$A = \varepsilon l c \qquad\qquad (\textit{Eq 2.1})$$

Where A is the absorbance, ε is the molar extinction coefficient with units of $M^{-1}cm^{-1}$, L is the path length of the cuvette in cm and c is the concentration of a given solution expressed in M. The molar extinction coefficient can be calculated by maintaining the same path length whilst varying the concentration of analyte to establish a calibration curve. A plot of absorbance against concentration will yield a slope equal to the ε.

Instrumentation setup

All absorbance UV-Vis spectra were recorded using *in-situ* AvaSoft UV-Vis Spectrometry and a Q-blue wireless temperature controller. Figure 2.7 shows the diagram and photograph of the UV-Vis instrument that used for monitoring the reduction of 4-NP. The Qpod 2e was connected by a fibre-optic cable (Cable with 200 μm Fibre) to an Avantes system of Ava-light-DH-S-BAL Deuterium-Halogen light sources, which have standard wide-range bands of deep UV deuterium lamp (215–500 nm), and halogen lamp (500–2500 nm). The Ava-Spec Avantes Fibre Optic spectrometer system (Avantes ULS2048-USB2-UA-50) was used as the detector in the range 200 –800 nm.
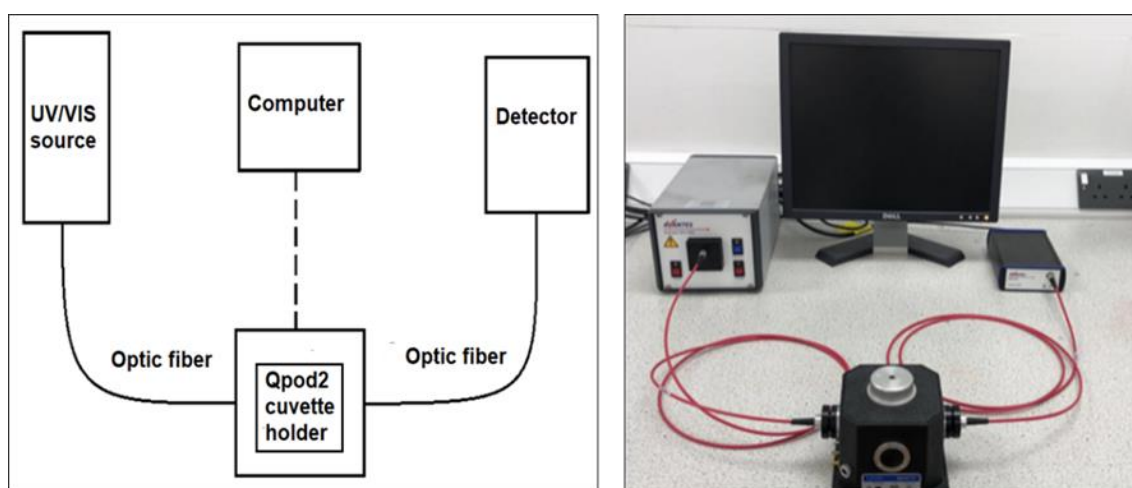
Figure 2.7 Scheme and picture of photograph of AvaSoft UV-Vis Spectrometry setup for monitoring the reduction of 4-nitrophenol to 4-aminophenol.

All measurements were performed in a single quartz cuvette with a 1 cm^2 path length. For each series of measurements, the absorption of distilled water is measured as the reference baseline and subtracted from each measurement. Measurements were taken in the range of 200 nm - 800 nm at room temperature. All the obtained UV-Vis spectra were manually normalised in the Origin Pro software, so that the absorbance at 600 nm was equal to zero, as illustrated in Figure 2.8. This translation process was necessary due to the variations in the UV-Vis baseline.
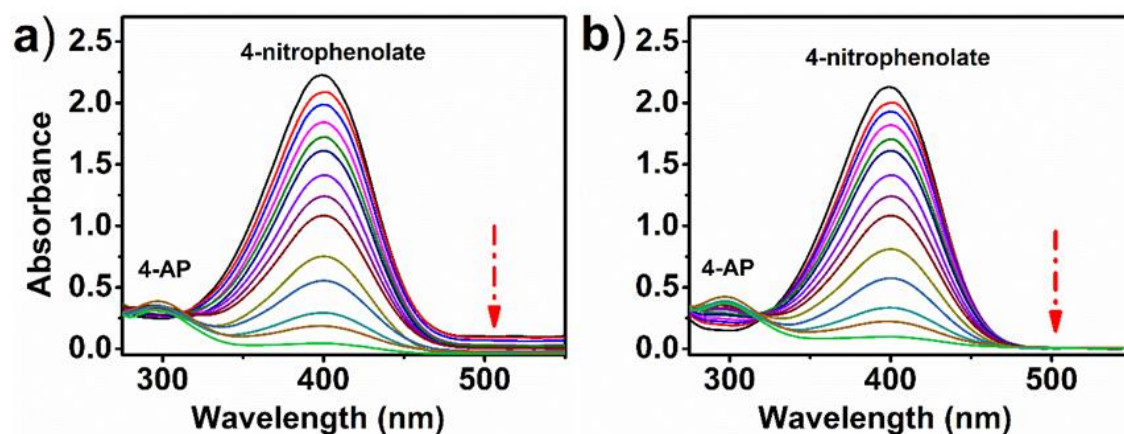
Figure 2.8 UV-Vis spectra collected during the catalytic reduction of 4-NP using Au/TiO$_2$ catalyst; A) before baseline correction and B) after baseline correction.

2.7. Catalyst characterisation

2.7.1. X-Ray powder diffraction (XRD)

Background

X-ray diffraction (XRD) is commonly used for phase identification, as well as providing information of the crystallite size, shape and atomic spacing in the material [25]. The prepared catalysts are powders, consisting of small crystallites with random orientations[26]. Statistically, one or more crystals will be in the correct orientation so that the Bragg's law (Equation 2.2) can be satisfied [25]. As the powder contains of small particles randomly orientated all diffraction angles will be represented.

$$n\lambda = 2d\ sin\theta \qquad (Equation\ 2.2)$$

where:

n	The order of the reflection (an integer number,).
λ	The incident X-ray wavelength.
d	Spacings between atomic layers in the powdered sample.
θ	The diffraction angle.

The X-ray diffraction equipment consists of: an X-ray source, a sample holder and a detector (Figure 2.9).

The Scherrer equation (equation 2.3) can be used to estimate an average crystallite size from powder XRD) [27]. As the particle size increases, the diffraction lines narrow, and vice versa. By fitting a Gaussian peak to the diffraction line, the full width half maximum(FWHM) can be obtained and applied to calculate the crystallite size [27].
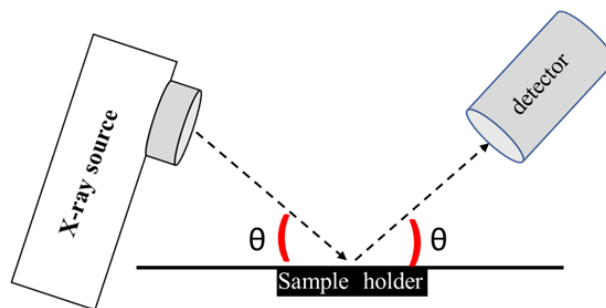
Figure 2.9 Schematic diagram of typical XRD.(θ: diffraction angle).

$$\text{Crystallite size} = \frac{K * \lambda}{FWHM * \cos\theta} \qquad (\textbf{\textit{Equation 2.3}})$$

where

K   the Scherrer constant = 0.89.

λ   the wavelength of X-ray (nm).

FWHM   the full peak width at half maximum.

θ   the angle of diffraction.

Experimental procedure

For each sample, the catalysts were placed in a sample holder, and the powder X-ray diffraction (XRD) patterns were recorded with PANalytical X-PertPro X-Ray diffractometer with a Cu $K_{\alpha 1}$ X-ray source run at 40 kV and 40 mA fitted with an X'Celerator detector. The powdered sample was placed in an aluminium holder and flattened until smooth. Scans 2θ were recorded between $= 5 - 80°$ at a step size of 0.017°.

2.7.2. X-Ray photoelectron spectra (XPS)

Background

X-Ray photoelectron spectroscopy (XPS) developed by K. Siegbahn and his group in 1960 for who awarded in 1981 the noble prize for his extensive work in developing XPS [28]. XPS is one of the most important and useful surface analysis technique in the characterisation of heterogeneous catalysts [29]. It is mostly used for studying the
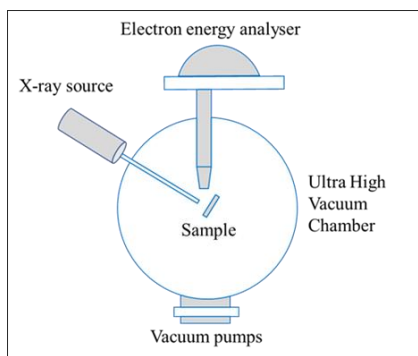
Figure 2.10 Schematic diagram of typical XPS.

oxidation state of elements and the surface composition of supported metal catalysts. Figure 2.10 is a schematic diagram of a typical XPS instrument, which consists of an x-ray source, a high vacuum chamber that holds the sample and an electron energy analyzer. Typically, the sample surface is irradiated with X-Rays, and based on the photoelectric effect, the sample surface emits photo electrons which are measured [28]. When atom absorbs a photon of energy (hv), a core or valence electron with binding energy(E_b) is ejected with kinetic energy, (E_k) which can be related by equation 2.4:

$$E_k = hv - E_b - \Phi \qquad \textit{(Equation 2.4)}$$

where;

E_k the kinetic energy of the photoelectron

h Planck's constant

v the frequency of the exciting radiation

E_b the binding energy of the photoelectron with respect to the Fermi level of the sample.

Φ the work function of the spectrometer

XPS spectrum is typically a plot of bonding energy of electron versus the intensity of photoelectrons. A set of binding energies is characteristic of an element, and XPS can be useful to analyse the formation of samples, considering the peak areas and cross sections for photoemission. Binding energy contains chemical information on oxidation state, because the energy levels of core electrons depend slightly on the chemical state of the atom [28]. The height of each peak of an XPS spectra is generally directly proportional to the abundance of photon-emitting atoms near to the sample surface, whilst the exact bonding energy associated with particular peaks is dependent upon chemical oxidation state, as well as the local environments surrounding the emitting atoms [30]. Consequently, the abundance of any element can be ascertained from XPS peak intensity,

whilst data relating to oxidation state, surface coverage can be determined from bonding energy.

Experimental

All XPS analysis was carried out using a Kratos Axis Ultra DLD spectrometer equipped with an Al K$_\alpha$ X-ray 300 W source and according to the following method. A monochromatic Al Kα X-ray source operating at120 W. Data was collected with pass energies of 160 eV for survey spectra, and 40 eV for the high-resolution scans. The system was operated in the Hybrid mode, using a combination of magnetic immersion and electrostatic lenses and acquired over an area approximately 300 x 700 μm^2. A magnetically confined charge compensation system was used to minimize charging of the sample surface, and all spectra were taken with a 90 ° take off angle. A base pressure of ~ 1x10^{-9} Torr was maintained during collection of the spectra. Binding energies were calibrated using the C1s binding energy of carbon taken as 284.7 eV. Peaks were fitted as Gaussian Lorentzian curves GL(30) using CasaXPS software.

2.7.3.   Electron microscopy

Electron microscopy is very powerful technique for studying the size, shape, morphology, and structure of nanoparticles. Electron microscopy covers a range of techniques including transmission electron microscopy (TEM) and scanning electron microscopy (SEM). Electrons in this technique have characteristic wavelength below 1 Å, electron microscopes can obtain atomic details. Whilst the resolution of conventional optical microscopes is limited to 100 nm.

Scanning electron microscopy (SEM)

Scanning electron microscopy (SEM) is one of the main techniques that used for catalysts characterisation. Zworykin *et al.,* was the first one that he described the modern SEM [31]. A schematic diagram of the SEM is shown in Figure 2.11. In this technique, electrons are used instead of light to generate images. Consequently, SEM can produce high quality images with comprehensive detail on macroscopic catalytic structure due to the tremendous sample focal depth achievable, particularly when compared with optical microscopy. Furthermore, chemical composition of the catalyst can be analysed when this powerful technique is combined with energy-dispersive X-ray spectroscopy (EDX or XEDS) [31,32].
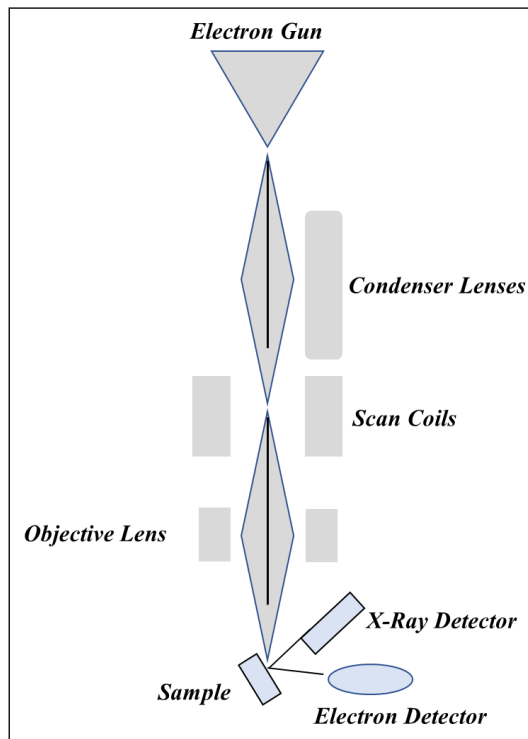
Figure 2.11 Schematic diagram of scanning electron microscope (SEM)

A Scanning Electron Microscope functions by generating a beam of electrons from an electron gun situated at the top of the microscope. This electron beam takes a vertical path down the microscope, which is maintained under vacuum conditions. This electron beam passes across electromagnetic fields and lenses, which further focus the beam onto the sample. When the primary electron beam encounters the sample (see Figure 2.12), the sample surface gives off three kinds of electronic emissions: i) backscattered electrons; ii) secondary electrons; and iii) Auger electrons. The first two of these are utilised by the SEM, whilst the third is important in Auger scanning microscopy. Atomic de-excitation also results in the emission of photons with spectral range varying from x-ray to the visible region [33]. Secondary electrons constitute lower energy electrons which are detected *via* attraction toward a phosphor screen where their light intensity is quantified *via* a photomultiplier. During the electron beam focusing process, some electrons will hit atomic nuclei and rebound; these are termed 'backscattered electrons', and these provide details on sample surface morphology and the mean atomic number of the scanned sample area. The sample surfaces directly opposite the detector appear brighter than those oriented at an angle, and this effect generates image contrast. Since secondary electrons derive from the sample surface, whereas the backscattered electrons derive from the bulk, SEM can therefore provide a '3D' representation of the sample under investigation. One key supplementary analytical tool frequently used in conjunction with SEM is energy
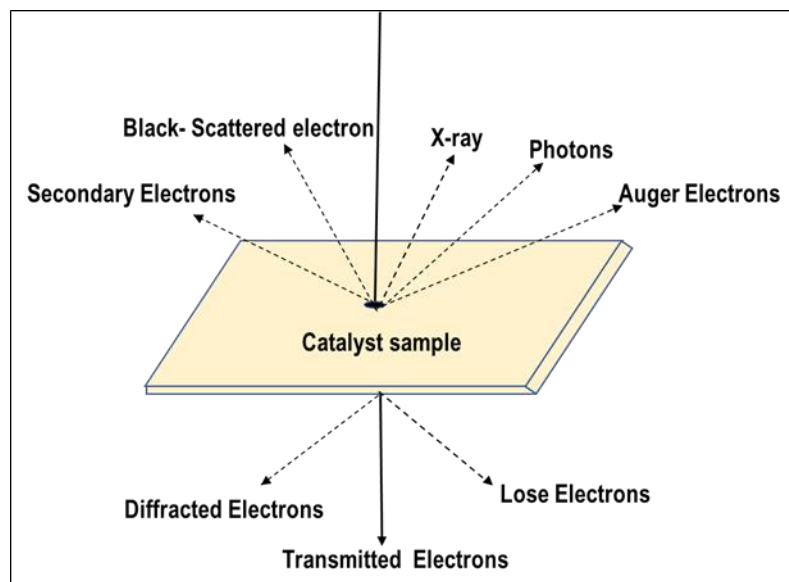
Figure 2.12 Interactions between electrons and the sample in SEM.

dispersive X-ray emission (EDX Combination of these two techniques permits elemental analysis of samples to be conducted. The EDX technique facilitates elemental analysis by collection of X-rays emitted from the sample when the beam interaction with sample's atoms. X-rays with characteristic energy are emitted by each element present in the sample. These signals are represented as peak on the resulting spectra, and the intensity of the peak associated to the quantity of that element present within the sample.

Transmission electron microscopy (TEM)

In addition to the SEM, the transmission electron microscopy (TEM) is another form of electron microscopy used for material characterization [34]. It is useful for determining the particle size, composition, distribution and shape of the materials amongst other properties [35]. An illustration of a TEM is shown in Figure 2.13. The operation of the TEM involves the use of a filament (or electron gun) emitting electrons from the top of a vacuumed column (~ 10-5 mbar), where they are focused on to the specimen by a series of electromagnetic lenses (condenser lenses). The energy of the electron beam is typically 200 keV, and the vacuum enables the beam to travel without interference from air molecules [31]. Depending on the thickness and atomic number of the elements in the specimen of interest, there will be a different level of interaction, with some of the electrons either being absorbed or scattered. After sample interaction, projection lenses spread the beam on to a fluorescent screen. The specimen can be viewed on this screen and is used to manually align and focus the instrument. The microscope is also fitted with a charged coupled device (CCD) camera in order convert the electron intensity into a digital image. Generally, the samples were viewed in bright field imaging mode, in which

the specimen appears darker, dependent on the sample thickness and atomic number of the elements in the specimen, and regions with no sample will appear bright. A second operational mode is dark field imaging, in which the scattered electron beam after interaction with the sample is detected and processed to an image in which the sample appears bright, on a dark background.
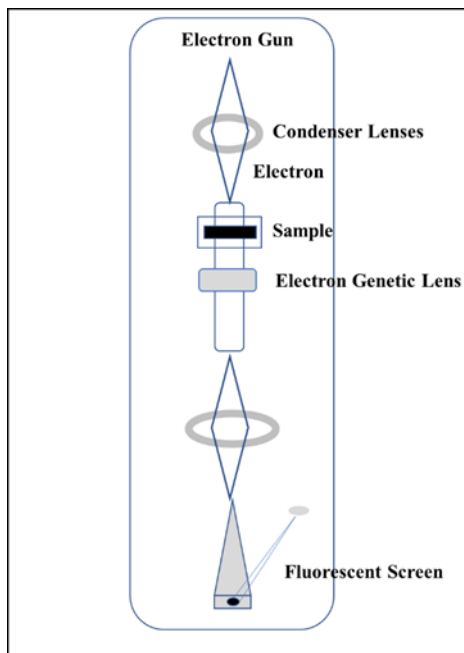
Figure 2.13 Schematic diagram of transmission scanning microscope (TEM).

Scanning TEM High Angle Annular Dark Field (STEM HAADF) Microscopy.

For high resolution analysis of small metal clusters, samples were analysed in the Nanoscale Physics Research Laboratory at the University of Swansea using STEM HAADF microscopy. In scanning TEM, the electron beam is focused into a narrow spot, which is subsequently scanned over the sample in a raster. This mode can be coupled with a high angle detector to form atomic resolution images. The detector operates by detecting the electrons that are scattered at high angles, rather than the Bragg scattered electrons (Figure 2.14). The atomic number of the scattering atoms (Z number) is more influential to the image created, with heavier atoms scattering more electrons, resulting in brighter regions amongst a dark background [36]. The samples for HAADF were examined using STEM (JEOL 2100 F) in high -Angle annular dark -field (HAADF).
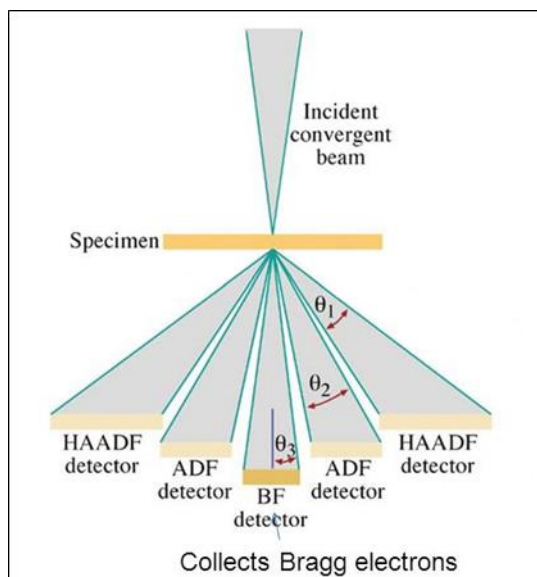
Figure 2.14 Illustration of the types of modes available depending on the extent of electron scattering from the sample [15].

Experimental (SEM, TEM HAADF)

Samples for examination by TEM were prepared by dispersing the catalyst powder in high purity ethanol using ultra-sonication. 50 µL of the suspension was dropped unto a holey carbon film supported by a 300-mesh copper TEM grid followed by the evaporation of the solvent. The samples for TEM were then examined using a JEOL JEM 2100 TEM operating at 200 kV. Particle size distributions were calculated using a post processing programme, ImageJ. For each image the scale bar was used as a reference to transform the scale in to image pixels per nm. Using the line tool, the diameter of each particle was manually picked, and the resulting metal particle size displayed in an output file (origin). The procedure was repeated across (250-300) particles before the average diameter was calculated from the output file. SEM-EDX was carried out using Hitachi TM3030PLUS equipped with a Quantax70 energy-dispersive X-ray spectroscope (EDX). The powder samples were placed on the carbon tape which was attached to the sample holder.

2.7.4. Surface area measurements (BET)

Background

The BET surface area measurement was developed by Brunauer, Emmett, and Teller in 1938 [37]. It is often used for the determination of the surface area, pore volume and pore size of materials [38]. Surface area plays a major role in the reactivity of catalysts due to the fact that the catalyst that has greater surface area provides better access to the reacting

species, and hence, are more active [37]. The total surface area of a solid is based on the volume of gas that is adsorbed on this surface at a given temperature and pressure [39]. Normally, nitrogen gas (N_2) is used in BET measurements as the adsorptive gas at a cryogenic temperature (77 K). After the N_2 gas is exposed to solid in vacuum Part of the gas will adsorb unto the surface of the solid whilst part remain unadsorbed [40]. BET equation (Equation 2.5) is as follow:

$$\frac{P}{[V(P_\circ - P)]} = \left(\frac{1}{VmC}\right) + \left(\frac{C-1}{VmC}\right)\left(\frac{P}{P_\circ}\right) \qquad \textbf{\textit{(Equation 2.5)}}$$

where;

V	Volume of adsorbed gas at pressure P.
V_m	Volume of the monolayer of adsorbed gas.
P	Equilibrium gas pressure
P_0	The saturation pressure of the adsorbate
C	BET constant.

C and V_m values can be determined by plotting $P/V(P_0-P)$ against P/P_0 and this should yield straight line. Once C and V_m are calculated [41], the surface area can be determined from the following equation (Equation 2. 6).

$$SA\left(\frac{m^2}{g}\right) = \frac{V_m \times N_A \times \sigma}{M \times V_0} \qquad \textbf{\textit{(Eq 2. 6)}}$$

where;

SA	surface area.
N_A	Avogadro number (6.023×10^{23}).
V_0	Molar volume of gas.
M	Mass of the sample.
σ	Molecular area of N_2 (0.162 nm^2 at 77 K).

Experimental

The samples were prepared for surface area measurements (BET) by outgassing at 120°C for 3 hours and then connecting to a Quantachrome Autosorb Analyser automatic multi point surface area analyser. During the analysis, the samples were immersed in liquid N_2. The surface area of the samples was measured using the BET method based on the adsorption isotherm in the partial pressure (P/P_o) range (0.05-0.35).

2.7.5. Thermogravimetric analysis (TGA)

Background

Thermogravimetric analysis (TGA) is a thermo-analytical technique used for recording small and precise changes in weight with temperature or time due to dehydration or decomposition [42]. The measurement is carried out in an atmosphere of H_2, N_2, He, air, or other gases depending on the application of interest, and the weight of the sample is constantly recorded as a function of the temperature. Change in the weight of sample is a result of the formation of various chemical and/or physical events [43]. TGA equipment comprises of basically, an automatic re equilibrating balance, which allows for the continuous monitoring of the changes in sample weight, a furnace that allows for controlled the heating of the sample and a gas flow circuit to control the sample environment (Figure 2.15). In some applications, TGA can be coupled with IR spectroscopy or mass spectrometry to identify and quantify desorption products   Quartz, ceramic and platinum materials are common sample holders used for TGA analysis.
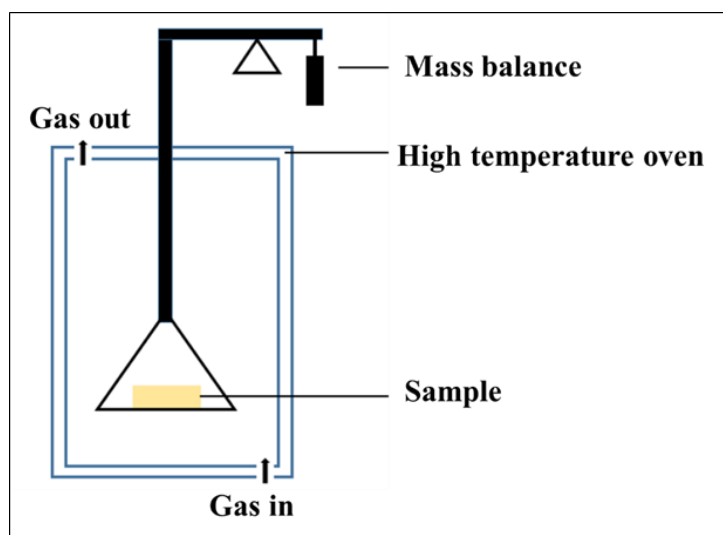
Figure 2.15 Schematic diagram of the TGA experimental set up.

Experimental

TGA analysis was carried out on a Perkin Elmer TGA 4000/ Pyris 6 with Auto sampler. For each analysis, 40 mg of a powdered sample of catalyst is placed into an aluminum oxide pot. The analysis was performed in N_2 gas atmosphere introduced at a rate of 50 ml/min and the heating range was from room temperature to 900°C at a constant rate of 5°C/min.

2.7.6. Microwave Plasma Atomic Emission Spectroscopy (MP-AES)

Background

MP-AES is an analytical technique for elemental analysis [44]. In this work, a nitrogen plasma is generated by microwave energy, which is subsequently heated to around 5000 K *via* a quartz torch to excite and vaporize the atoms in a liquid sample. An aerosol is created from liquid or acid digested solid samples which is sprayed inside the torch, and thus led to the atomization and electron excitation of sample. This leads to the electrons in the sample to an excited state from a ground state. After the atoms relax into lower quantised energy levels, a specific quantum of energy is released as photons, which have a wavelength characteristic of each element. The photons are detected using a charge coupled device (CCD). Each wavelength is analysed sequentially. This method enables multiple wavelengths related to the same element to be quantified, which reduces the interference from other elements that have similar emission wavelengths [45]. The diagram in Figure 2.16 shows the basic principles of MP-AES.
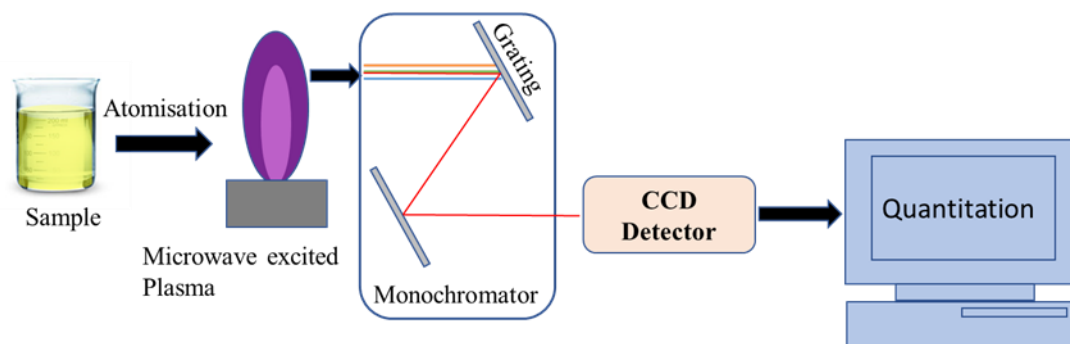
Figure 2.16 Schematic illustration of the basic principles of microwave plasma atomic emission spectroscopy.

Experimental

Agilent 4100 MP-was used to determine the actual metal loadings and leaching for all the catalysts used in this work. About 20 mg of each sample was placed into a 50 ml volumetric flask and then filled with 6 mL freshly prepared aqua-regia. The sample was left overnight to allow for complete digestion of the samples. The digested sample was then diluted with deionised water up to a total volume of 50 ml. The obtained solution was filtered with a 0.45µm PTFE syringe filter prior to analysis. For each element analysed, calibrations of multiple wavelengths were used.

2.7.7.   Gas chromatography-Mass spectrometry (GC-MS)

Background

Gas Chromatography–Mass Spectrometry (GC-MS) is one of the most extensively used for chemical analysis. It is an essential analysis technique in catalysis for the separation, identification and quantification of reaction products [46]. Nowadays, GC-MS can be used in various applications such as identification of unknown samples, fire and explosives investigation, drug detection and environmental analysis [47–50]. The GC-MS is composed of two major building blocks: the gas chromatograph and the mass spectrometer. The basic components of a GC consist of an injecting port, a column as stationary phase within an oven and a detector as shown in Figure 2.17. The Gas Chromatography (GC) works on the principle that on injection, a sample is heated into the gas phase and mixed with an inert carrier gas (commonly Ar, He or N_2) followed by transportation through the column. A capillary column is generally made of fused silica with a polymer coating called the stationary phase. Separation of products is facilitated by the length of columns which for capillary columns can be up to 100 m. A wide range of stationary phases are also available for the separation of many complex mixtures. These columns can range in polarity, length and also analysis temperature.

Capillary columns are widely used for the analysis of complex mixtures; however, they are insufficient for large volumes. Here, a small volume should be injected compared to when using a packed column, or the use of a split injector. The basic set up of a split/spless injector comprises of a rubber septum through which the syringe is inserted. The sample is injected into a heated glass liner where it is vaporised and mixed with a carrier gas. In a split less injector set up using small volumes, the sample is carried through the liner and passes on to the column. For use of a split injector, the sample is split *via* variation of the ratio between the flow rates of the carrier gas and that which exits the split vent. Therefore, only a portion of the injected sample passes through the column.

Various detectors are available for use in gas chromatography, each with different benefits and detection limits. Typical detectors include flame ionisation (FID), thermal conductivity (TCD) and mass spectrometry (MS). The FID detector is very sensitive to hydrocarbons [52], whilst the TCD detector is less sensitive, however, it is appropriate for all compounds, so, it is commonly used for gas analysis [53]. GC-FID could be used for both qualitative and quantitative analysis, however GC-MS should be used when mixture composition is unknown and/or individual components are not available.

MS is used to identify compounds quickly and accurately at a molecular level after separation from complex mixtures of chemicals [54]. It has three main compartments that are operated under a high vacuum: ion source, mass analyser and detector. In GC-MS, (Figure 2.17) effluent from the GC column is usually ionised using an electron impact technique in which high-energy electrons excite neutral analyte molecules causing the loss of electrons and fragmentation. The charged particles are then delivered into the mass-analysers where they are separated by their mass-to-charge (m/z) ratio by either magnetic or electrical fields. The mass spectrum is generated as a plot of ion abundance as a function of m/z. The presence of fragments with certain m/z and their abundance are characteristic for each compound and are used for their identification. A ÒlibraryÓ of known mass spectra, covering several thousand compounds, is stored on a computer database.
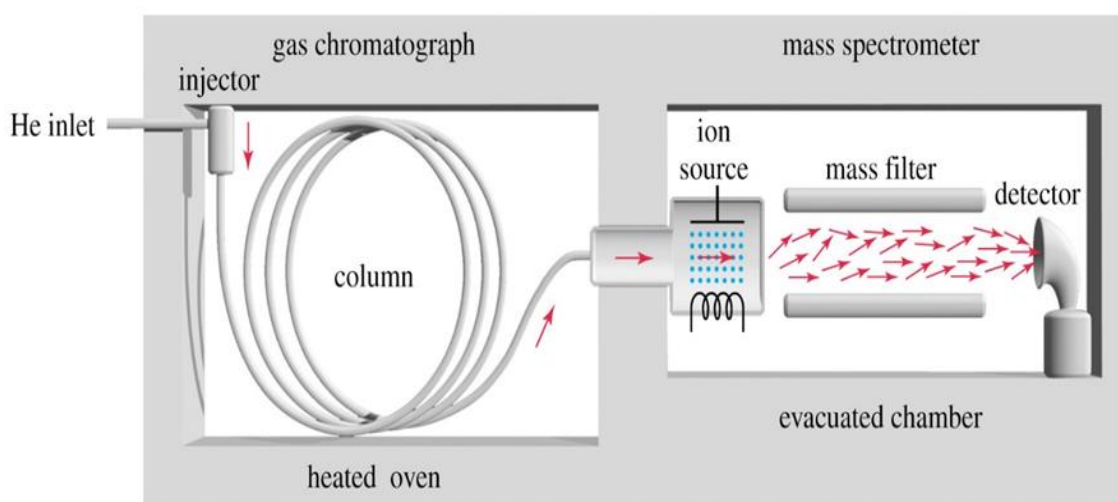
Figure 2.17 Schematic diagram of gas chromatography - mass spectrometry [51].

Experimental

The Gas chromatography-Mass spectrometry was employed in this work for the identification and confirmation of reaction product(s). After the reaction, 200 μL of reaction mixture was diluted with methanol (1 mL) prior to the GC-MS analysis. The analysis was carried out on a Waters GCT Premier orthogonal acceleration time-of-flight mass spectrometer coupled to an Agilent 6890 gas chromatogram fitted with an Agilent DB 35 column (30 m, 0.25 mm i.d.,0.25 μm film of 35%-cyano –methylpolysiloxane) (see Figure. 2.18).

Figure 2.18 Photograph of gas chromatography- mass spectrometry (Cardiff Catalysis Institute).

2.7.8.   High performance liquid chromatography (HPLC)

Background

Another complimentary technique to the gas chromatography is the High-Performance Liquid Chromatography (HPLC). Both the GC and the HPLC techniques share similar operating principles except for the mobile phases used in the techniques. The liquid mobile phase is used to transport the analytes in the HPLC whereas, gases are utilised as the carrier phase in the GC. For the HPLC analysis the analytes should be soluble in the mobile phase, and the HPLC is highly convenient to analyse sample that are heat sensitive and/or non-volatile. The analytes are injected into the liquid phase carrier, and separation is achieved based on the selective retention/ interaction of the components of the analytes with a solid stationary column material. Detection of analytes in HPLC can be carried out with different detectors, hence, the HPLC technique can be assembled with more than one. The most common liquid chromatography detectors are the UV-Vis and RID, which detects organic compounds.

Experimental

The conversion of formic acid was determined by using HPLC model Agilent 1220 Infinity LC using a column (reversed phase) MetaCarb 87H 250 x 4.6 mm, Agilent, at 60 °C and a flow rate of 0.4 mL min^{-1}. An actual photograph of the system is displayed in Figure 2.19. The instrument is equipped with a Variable Wavelength (VW) detector pre-set at 210 nm. The eluent was an aqueous solution of phosphoric acid (0.1 wt. %). Succinic acid was used as external standard for the quantification of the concentration formic acid remaining in reagent solution. Seven formic acid solutions were made in order

to perform the calibration and the response factor of the HPLC calibration for formic acid is 1.5286 (see Figure 2.20).

Figure 2.19 HPLC Agilent 1220 Infinity LC.
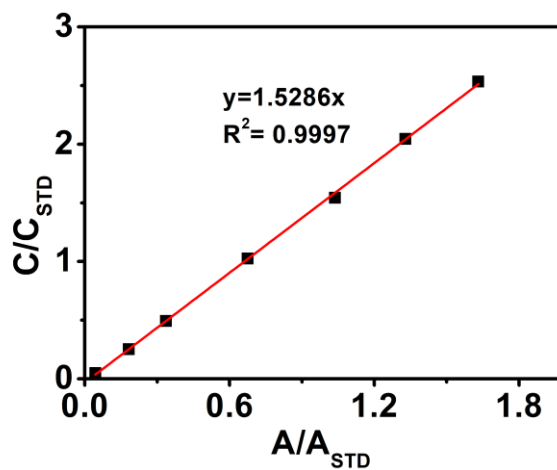
Figure 2.20 Calibration curve and response factor of the HPLC calibration for formic acid.

2.9. References

[1]   A. Brückner, Catal. Rev., 2003, 45, 97–150.

[2]   A. Villa, D. Wang, G. M. Veith, F. Vindigni and L. Prati, Catal. Sci. Technol., 2013, 3, 3036–3041.

[3]   E. K. Gibson, A. M. Beale, C. R. A. Catlow, A. Chutia, D. Gianolio, A. Gould, A. Kroner, K. M. H. Mohammed, M. Perdjon, S. M. Rogers and P. P. Wells, Chem. Mater., 2015, 27, 3714–3720.

[4]   H. Shi, N. Xu, D. Zhao and B. Q. Xu, Catal. Commun., 2008, 9, 1949–1954.

[5]   S. Rogers, R. Catlow, D. Gianolio, P. Wells and N. Dimitratos, Faraday Discuss., 2018, 208, 443–454.

[6]   S. M. Rogers, C. R. A. Catlow, C. E. Chan-Thaw, A. Chutia, N. Jian, R. E. Palmer, M. Perdjon, A. Thetford, N. Dimitratos, A. Villa and P. P. Wells, ACS Catal., 2017, 7, 2266–2274.

[7]   L. Abis, S. J. Freakley, G. Dodekatos, D. J. Morgan, M. Sankar, N. Dimitratos, Q. He, C. J. Kiely and G. J. Hutchings, ChemCatChem, 2017, 9, 2914–2918.

[8]   A. Kraynov and T. Müller, Appl. Ion. Liq. Sci. Technol., 2011, 1–27.

[9]   T. Loewenstein, A. Hastall, M. Mingebach, Y. Zimmermann, A. Neudeck and D. Schlettwein, Phys. Chem. Chem. Phys., 2008, 10, 1844–1847.

[10]   N. Dimitratos, C. Messi, F. Porta, L. Prati and A. Villa, J. Mol. Catal. A Chem., 2006, 256, 21–28.

[11]   A. Villa, C. E. Chan-Thaw, G. M. Veith, K. L. More, D. Ferri and L. Prati, ChemCatChem, 2011, 3, 1612–1618.

[12]   A. A. Ismail, A. Hakki and D. W. Bahnemann, J. Mol. Catal. A Chem., 2012, 358, 145–151.

[13]   S. Fountoulaki, V. Daikopoulou, P. L. Gkizis, I. Tamiolakis, G. S. Armatas and I. N. Lykakis, ACS Catal., 2014, 4, 3504–3511.

[14]   C. Lin, K. Tao, D. Hua, Z. Ma and S. Zhou, Molecules, 2013, 18, 12609–12620.

[15]   H. Liu and Q. Yang, J. Mater. Chem., 2011, 21, 11961–11967.

[16]   A. Goyal, S. Kapoor, P. Samuel, V. Kumar and S. Singhal, RSC Adv., 2015, 5, 51347–51363.

[17]   R. Majumdar, B. G. Bag and P. Ghosh, Appl. Nanosci., 2016, 6, 521–528.

[18]   J. Sun, Y. Fu, G. He, X. Sun and X. Wang, Catal. Sci. Technol., 2014, 4, 1742–1748.

[19]   D. Bhattacharjee, K. Mandal and S. Dasgupta, RSC Adv., 2016, 6, 64364–64373.

[20]   R. Javaid, S. I. Kawasaki, A. Suzuki and T. M. Suzuki, Beilstein J. Org. Chem., 2013, 9, 1156–1163.

[21]   G. N. Bowers Jr., R. B. McComb, R. G. Christensen and R. Schaffer, Clin. Chem., 1980, 26, 724–729.

[22]   A. Rehor, N. E. Botterhuis, J. A. Hubbell, N. A. J. M. Sommerdijk and N. Tirelli, J. Mater. Chem., 2005, 15, 4006–4009.

[23]   L. Prati, A. Villa, C. E. Chan-Thaw, R. Arrigo, D. Wang and D. S. Su, Faraday

Discuss., 2011, 152, 353–365.

[24]   R. . Sheldon, I. W. C. . Arends and A. Dijksman, Catal. Today, 2000, 57, 157–166.

[25]   R. Sharma, D. Bisen, U. Shukla and B. Sharma, Recent Res. Sci. Technol. 2012, 4, 77–79.

[26]   F. A. Settle, Handbook of Instrumental Techniques for Analytical Chemistry, Prentice Hall PTR, Upper Saddle River, NJ, Har/Cdr., 1997.

[27]   J. W. & S. Harold P. Klug and Leroy E. Alexander, Ben Post, 1975, 4, A18–A18.

[28]   I. Chorkendorff, J.W. Niemantsverdriet, Concepts of Modern Catalysis and Kinetics, John Wiley & Sons, 2003.

[29]   O. Sublemontier, C. Nicolas, D. Aureau, M. Patanen, H. Kintz, X. Liu, M.-A. Gaveau, J.-L. Le Garrec, E. Robert, F.-A. Barreda, A. Etcheberry, C. Reynaud, J. B. Mitchell and C. Miron, J. Phys. Chem. Lett., 2014, 5, 3399–3403.

[30]   J.F.Watts and J.Wolstenholm, An introduction to Surface Analysis by XPS and AES, John Wiley & Sons Ltd, Chichester, UK, 2003.

[31]   J. Kuo, Electron microscopy : methods and protocols., Humana Press Inc., 2nd edn., 2007.

[32]   W. Krakow, F. A. Ponce and D. J. Smith, High Resolution Microscopy of Materials, ambridge University Pres, 1989.

[33]   J. . Imelik, B., Vedrine, Catalyst characterization : physical techniques for solid materials, New York : Plenum Press, 1994.

[34]   S. Neogy, R. T. Savalia, R. Tewari, D. Srivastava and G. K. Dey, 2006, 44, 119–124.

[35]   A. Villa, N. Dimitratos, C. E. Chan-Thaw, C. Hammond, G. M. Veith, D. Wang, M. Manzoli, L. Prati and G. J. Hutchings, Chem. Soc. Rev., 2016, 45, 4953–4994.

[36]   J. W. Niemantsverdriet, Spectroscopy in catalysis : an introduction, Weinheim ; Chichester : Wiley-VCH, 2nd edn., 2000.

[37]   S. Brunauer, P. H. Emmett and E. Teller, J. Am. Chem. Soc., 1938, 60, 309–319.

[38]   P. Schneider, Appl. Catal. A, Gen., 1995, 129, 157–165.

[39]   M. Thommes, K. Kaneko, A. V. Neimark, J. P. Olivier, F. Rodriguez-Reinoso, J. Rouquerol and K. S. W. Sing, Pure Appl. Chem., 2015, 87, 1051–1069.

[40]   J. R. and Francoise Rouquerol and K. Sing, Adsorption by Powders and Porous Solids: Principles, Methodology and Applications, London, 1999.

[41]   F. Rouquerol, J. Rouquerol and K. Sing, Adsorption by Powders and Porous Solids, Academic Press, San Diego, 1999.

[42]   J. P. Coats, A. W, Redfern, Anal. , 88, 906–924.

[43]   T. C. Daniels, " Thermal Analysis, Kogan Page Ltd, London, 1973.

[44]   S. V Smirnova, T. O. Samarina, D. V Ilin, I. V Pletnev, T. O. Samarina, D. V Ilin and I. V Pletnev, Anal. Chem., 2018, 90, 6323–6331.

[45]   Agilent Technologies, Microwave Plasma Atomic Emission Spectroscopy (MP-AES), Application eHandbook, 2016.

[46]   V. R. Choudhary and L. K. Doraiswamy, Ind. Eng. Chem. Prod. Res. Dev., 1971, 10, 218–237.

[47]   K. F. Sichilongo, V. C. Obuseng and H. Okatch, Chromatographia, 2012, 75, 1017–1037.

[48]   I. C. Santos and K. A. Schug, J. Sep. Sci., 2017, 40, 138–151.

[49]   H. P. Burchfield and E. E. Storrs, 1962, 84, 4172–4173.

[50]   D. F. Gurka, S. Pyle and R. Titus, Anal. Chem., 1997, 69, 2411–2417.

[51]   CRASTO A 2014 Gas Chromatography - Mass Spectrometry (GC-MS), Orgspectroscopyint.blogspot.co.uk.

[52]   L. Patterson, J. Chromatogr. Sci., 1986, 24, 466–472.

[53]   J. R. Martínez and E. Stashenko, Adv. Gas Chromatogr. 2014.

[54]   Elena Stashenko and Jairo Rene Martínez, Gas Chromatography-Mass Spectrometry, Advances in Gas Chromatography, InTech, 2014.

Chapter 3

Investigation of catalytic performance of AuPd/TiO$_2$ catalysts during 4-nitrophenol reduction by NaBH$_4$

3.1. Introduction

The reduction of 4-nitrophenol (4-NP) is an industrially useful reaction since 4-NP is considered as one of most toxic and water pollutants [1–5]. 4-nitrophenol derived from many processes in industries such as agro chemistry, pigments and pharmaceutical factories [6–9]. Due to their high toxicity, more attention has been given to develop new methods to remove this compound from the environment such as direct conversion of 4-NP by using reductant in the presence of metal nanoparticles (NPs) to produced 4-aminophenol (4-AP) [10]. On the other side, 4-aminophenol has less toxicity and useful in many industries such as in drugs (analgesic and antipyretics), corrosion inhibitors [8,11]. Recently, metallic nanoparticles have received much attention in the field of catalysis because of their unique properties such as sizes and shapes. To evaluate and derive a definite conclusion about the efficacy of various catalysts with different shapes, sizes, and even porosities, a model reaction is necessary [12]. This reaction must be trustworthy, convincing, should proceed without side reactions in the presence of catalyst and should not continue in the absence of a catalyst. Also, it should be easy to monitor using fast and a simple experimental set up. As such, the reduction of 4-nitrophenol using sodium borohydride (NaBH$_4$) is considered as a model reaction for catalytic study because of the following reasons; i) the reduction of 4-NP can be easily monitored using UV-Vis spectroscopy by observing the decrease in absorption of the 4-nitrophenolate anion at 400 nm [13], leading directly to the rate constant; ii) the product of the reaction is only 4-aminophenol and no by-products are formed [12,14]; iii) this reaction can be catalysed by any immobilized or free NPs in aqueous solution under mild conditions [13,15]; iv) although this reaction thermodynamically favourable at ambient condition, it is not kinetically so since the reduction potential of 4-nitrophenol to 4-aminophenol is (E°=0.76 V), while that of borate-borohydride (H$_3$BO$_3$/BH$_4^-$) is (E°= -1.33 V) [12,16]. Because of the kinetic barrier, the reduction reaction does not take place in the absence of metal nanocatalysts, even in 48 h [17]. However, the reaction proceeds easily in the presence of catalysts [21–23].This reaction has great attention over the last years. In 2001, Pal and co works [11] reported for the first time this reaction as model reaction using Cu, Ag, and Au NPs. Therefore, 4-NP reduction is very important and valuable in green chemistry and from an industrial and academic point of view. Since then, interest in this reaction has grown significantly among researchers. The most popular metal nanoparticles for this reaction were Au, followed by Ag and Pd [21].

Gold nanoparticles - both free and immobilized- have been investigated under mild conditions, as catalyst for the reduction of 4-NP by several authors [1–5]. In many cases, the catalytic activity in this reaction increases as the particle size decreases. Ismail *et al.,* [22] performed a systematic investigation of the effect of Au particle size and its surface area on the hydrogenation of 4-NP by using Au/TiO$_2$. They observed that the catalytic activity was increased by 6-fold when the Au particle size was decreased from 350 to 25 nm, attributed to the higher metal surface area for the smaller Au NPs. Aromal and co-workers have observed a complete reduction of 4-NP after 30 minutes in the presence of 20 nm Au NPs, while the reaction was accomplished within only 15 minutes under action of 15 nm size Au NPs [23]. Later, Li *et al.,* [24] prepared Au/TiO$_2$ with different Au nominal loadings (2, 5, and 10 wt.%) by sol-gel method for the reduction of 4-nitrophenol. They found that Au particles size in the range of 20–60 nm and they linked the catalytic activity to the total surface area of Au nanoparticles in Au/TiO$_2$ samples. As the Au loading amount increases, the number of Au particles on the TiO$_2$ support increases initially and thus the total surface area increases. Moreover, they found that the Au particle sizes grow larger, as the Au loading increases, resulting in decreased in the catalytic activity of Au/TiO$_2$.

In most studies, Au particles size was larger than 10 nm, therefore, there is a need to study the effect of Au particles size that is less than 10 nm on the reduction of 4-nitrophenol. Generally, for reduction reactions, supported bimetallic catalysts are known to be superior catalysts with excellent catalytic activities, compared to their monometallic analogues, due to the synergistic effect between the two metals [15]. AuNPs is often combined with other metals to prepare high performance bimetallic catalysts, which results in a change in their interfaces' electronic structure [25]. Because of their relatively low cost and high-end performance, a number of research projects have centered on the application of bimetallic structures of AgAu, CuAu, PtAu, FeAu and PdAu for 4-NP reduction [26–30]. Examples of such bimetallic structures capable of excellent catalytic activity, reusability and stability include the AgAu core-shell NPs, AgAu NPs alloy and alloy-graphene hybrids [31–33]. However, and despite the excellent catalytic activities reported for the above stated bimetallic nanoparticles, Pd based catalysts have undoubtedly exhibited the best overall performance for hydrogenation reaction of 4-NP [34]. Furthermore, many studies showed that Pd-based bimetallic NPs are more effective and exhibit higher catalytic performance than Pt based Au bimetallic NPs [35–39]. Alloying Au with either Pd results in a stronger binding energy and yields a correspondingly faster reaction rate

constant than alloying Au with Pt as shown in the work reported by Henkelman *et al.,* [35]. Very few studies report on the heterogeneous catalytic reduction of 4-NP using AuPd bimetallic systems [40–42]. Meijboom and co works [43] successfully demonstrated the synthesis of bimetallic gold and palladium nanoparticles using the dendrimer-templating method. They showed that the bimetallic catalysts are very active and stable for a long period of time more than monometallic catalysts. However, they did not study the effect of Au/Pd ratio on catalytic activity and the reusability of their catalysts. Further to this study, an investigation into the synergistic effect between Au and Pd, on the catalyst's efficiency for 4-NP reduction was reported by Lang *et al.,* [44]. They demonstrated that a novel hollow Cu$_2$O@CuO/(AuPd) heterostructure can be obtained by the galvanic replacement reaction of Cu$_2$O cubes (acting as a sacrificial template) with bimetallic precursors in an EtOH solution at room temperature. The Cu$_2$O on the surface of the nanocube is oxidized into CuO, forming a hollow Cu$_2$O–CuO core–shell structure. In addition, Pd^{II} and Au^{III} are reduced to Pd^0 and Au^0, resulting in the formation of AuPd alloy NPs that get deposited on the hollow Cu$_2$O–CuO core–shell structure. Their method does not require any additional reducing agents, and thus simplifies the reaction system. The resulting hollow Cu$_2$O@CuO-supported AuPd alloy NPs show higher catalytic activity in the reduction of 4-NP than those of Cu$_2$O, CuO, CuO–Cu$_2$O/Au and CuO–Cu$_2$O/Pd nanomaterials. Recently, Albonetti and co-workers [42] synthesis mono and bimetallic colloids (Pd/Au) by microwave heating using glucose as reducer and Polyvinylpyrrolidone (PVP) as the chelating agent. The mean metal particle size for both supported mono and bimetallic nanoparticles were in the range 3-4 nm. The synergistic positive effect of the bimetallic phase was assessed for Pd/Au alloy NPs in the reduction of 4-NP and AuPd catalyst with composition (1:1 atomic ratio) show the maximum performance.

Determine the optimum window between the AuPd molar ratio for efficient and effective activity in reduction of 4-NP is desired and it was investigated in several studies. The influence of the bimetallic Au/Pd atomic ratio on the catalytic reduction of 4-NP has gained great attention and characteristic by a volcano shape. The volcano-shaped curve is recognized as one of the few universal phenomena in heterogeneous catalysis[45]. While the volcano behaviour is discussed in a physical chemistry textbook because of its fundamental significance in chemical kinetics, it offers an important guideline in practice when developing new catalysts or when improving their performance [46]. The usual explanation given to these reactions is the apparent validity of Sabatier's principle [47],

59

which says that a chemical species reaches an optimum stability at its maximum reactivity. Therefore, the species should not be too stable nor too unstable to attain the maximum. It is also a sign that the catalysts' surface consists of different kinds of sites and therefore the adsorbates are progressively led to occupy thermodynamically less favourable sites as the coverage increases. An optimal catalyst will balance these two regimes such that the barriers are low enough to be overcome and that the adsorbed molecules may diffuse and desorb from the surface [45]. Chen *et al.,* [45] studied the catalytic activity of different atomic ratio of Au and Pd bimetallic NPs for the reduction of 4-NP by synthesize AuPd NPs supported on graphene nanosheets (GNs). They reported that the activity of bimetallic AuPd/GNs catalyst was higher than monometallic Au/GNs and Pd/GNs catalysts by a factor 8 and 5 respectively attributed to the synergistic effect of Au and Pd species. Moreover, among all these catalysts, AuPd with molar ratio (1:1) express the highest activity. Similar ratio for AuPd was reported for the same reaction by Fang and co works [41] who synthesized AuPd bimetallic nanoparticles deposited on an ultrathin graphitic carbon nitride nanosheets. However, recent work has done by Srisombat *et al.,* [46] reported different ratio for AuPd bimetallic where the highest catalytic activity of bimetallic was obtained with the ratio 1:4. They concluded that the catalytic activity strongly depends on AuPd particle size more than the chemical constituents.

It has been known that the shape and size of mono and bimetallic nanoparticles are strictly dependent on the preparation methods and conditions and affect the physicochemical properties of the final nanomaterial. Metal nanoparticles have been synthesized by several methods so far, to the best of our knowledge, only few studies have been reported using of sol-immobilisation method for this reaction and focusing on preformed bimetallic nanoparticles, although its advantages over other preparation methods (see Chapter 1). Sol-immobilisation method using PVA and NaBH$_4$ as stabilising and reducing agents, respectively, is an effective method to prepare small metal nanoparticles with a narrow particle distribution, compared to conventional techniques such as wet impregnation and deposition-precipitation. Rogers *et al.,* [13] prepared monometallic 1%Pd/TiO$_2$ by sol-immobilisation method using PVA and NaBH$_4$ for the hydrogenation of 4-NP to 4-AP and they reported high activity compared to the other catalysts prepared by different methods. For example, the turnover frequencies (TOFs) for 1%Pd/TiO$_2$ in their work was 247 hr^{-1}, while Sun *et al.,* [47] reported TOF of 70 hr^{-1} for a 5 wt. % Pd/C,

indicating lower activity than the 1% Pd/TiO$_2$ catalyst preparing by sol-immobilisation method.

This work describes the design and pre-formed colloidal AuPd nano-particles with a narrow metal particle size distribution *via* a sol-immobilisation method. These pre-formed nanoparticles were immobilised on TiO$_2$ (P25) to prepare AuPd/TiO$_2$ with different AuPd atomic ratio. This work will therefore focus on evaluation of the catalytic performance using supported bimetallic AuPd nanoparticles and by varying in a systematic way Au/Pd molar ratios. Sodium borohydride has been used as reducing agent under mild reaction conditions. In this study, the experimental parameters (e.g. 4-nitrophenol, NaBH$_4$ and catalyst concentration, stirring rate and Au/Pd molar ratio) have been optimized to achieve the best catalyst performance.

3.2. Experimental

3.2.1. Catalyst preparation

The sol-immobilisation method described in detail in Chapter 2 (Section 2.3.2), was used to prepare monometallic Au/TiO$_2$, Pd/TiO$_2$ and bimetallic Au$_x$Pd$_{1-x}$/TiO$_2$ catalysts with different nominal molar ratios denoted as Au$_x$Pd$_{1-x}$/TiO$_2$(where x = 0.87, 0.75, 0.5, 0.25, and 0.13.) The total theoretical metal loadings on the TiO$_2$ support for both the monometallic Au, Pd and bimetallic AuPd in this Chapter were chosen to be 1 wt. %. Table 3.1 presents all the prepared catalysts and an abbreviated notation used for all through this Chapter.

Table 3.1 Details of the monometallic Au/TiO$_2$, Pd/TiO$_2$ and Au$_x$Pd$_{1-x}$/TiO$_2$.

Sample notation	%Au (mol/mol)	%Pd (mol/mol)
Au/TiO$_2$	100	-
Au$_{0.13}$Pd$_{0.87}$/TiO$_2$	13	87
Au$_{0.25}$Pd$_{0.75}$/TiO$_2$	25	75
Au$_{0.5}$Pd$_{0.5}$/TiO$_2$	50	50
Au$_{0.75}$Pd$_{0.25}$/TiO$_2$	75	25
Au$_{0.87}$Pd$_{0.13}$/TiO$_2$	87	13
Pd/TiO$_2$	-	100

3.2.2. Catalyst characterisation

The catalysts were characterised using powder X-ray diffraction (XRD) for phase identification, crystallinity and crystallite size, X-ray photoelectron spectroscopy (XPS) for the identification of metal oxidation state, surface ratio of Au/Pd, transmission electron microscopy (TEM) for particle size and size distribution, Surface area measurements (BET) and scanning electron microscope (SEM) equipped with (EDX) for morphology and determination of elemental composition. Microwave Plasma Atomic Emission Spectroscopy (MP-AES) for bulk determination of total metal loading and also for determination of leaching after the reaction performed. UV-Vis Spectroscopy used to assess the reduction of metal precursors and formation of colloidal metal nanoparticles (presence and absence of plasmon peak of Au). The experimental procedures for all of these techniques is described in Chapter 2.

3.2.3. Catalytic reactions

The catalytic performance of the synthesized catalysts was evaluated in the reduction of 4-NP by NaBH$_4$ as a model reaction. The reaction was carried out under mild conditions using water as the desired solvent, temperatures of 30°C and atmospheric pressure under constant stirring (1000 rpm). To maintain a pseudo-first order reaction kinetics, a large excess of NaBH$_4$ over 4-NP was used (optimized molar ratio of NaBH$_4$/4-NP = 30). A typical reaction procedure is the following, 5ml of NaBH$_4$ (0.03 M) is added to a batch reactor that contains catalyst and the aqueous solution of 4-NP (45 ml, 1.35×10^{-4} M, 4-NP/metal molar ratio = 13). The total volume of the reaction mixture was 50 ml. At different time interval (min), aliquot from the reaction mixture was then withdrawn using 1 ml syringe equipped with a filter (0.45 µm pore size) and transferred into the UV cuvette for a UV-Vis measurement. Subsequently, the UV-Vis spectra (in the range of 200 – 800 nm) were recorded and the concentration of 4-NP traced from the decay of the absorption band centred at 400 nm. Based on the calibration curve of standard solution of 4-NP, which previously described in Chapter 2, the molar extinction coefficient was estimated for 4-NP to be 18620 M^{-1} cm^{-1}. Finally, the concentration of 4-NP, as a function of time during the catalytic reaction, was calculated using the Beer's Lambert's law equation as discussed in Chapters 2.

3.3. Results and discussion

3.3.1. UV-Vis spectroscopy

The UV-Vis spectroscopy was used during the formation of Au and Pd colloids to monitor the extent of reduction of the respective metal salt precursors. In particular, UV-Vis spectroscopy was used to evaluate the Au surface plasmon resonance (SPR) band, which is not observed for Pd nanoparticles (Pd NPs). Figure 3.1(a) shows the UV-Vis spectrum of the HAuCl$_4$ precursor, with a peak at 222 nm, indicative of the ligand to metal charge transfer in [AuCl$_4$]$^-$ [48]. After reducing the Au salt precursor by NaBH$_4$ as a strong
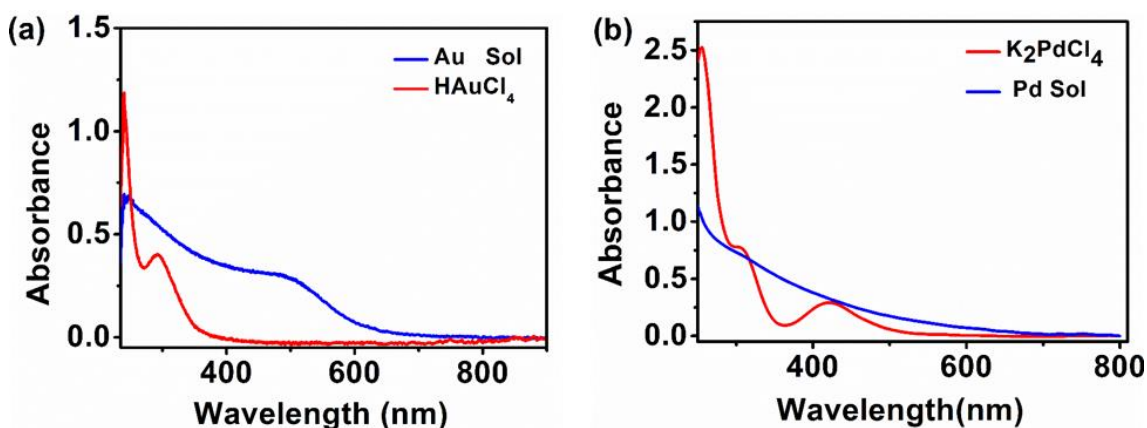
Figure 3.1 UV-Vis spectra of (a) HAuCl$_4$ precursor before chemical reduction and the Au sol generated after chemical reduction of the salt by NaBH$_4$ in the presence of PVA. (b) K$_2$PdCl$_4$ precursor before chemical reduction and Pd sol generated after chemical reduction of the salt by NaBH$_4$ in the presence of PVA.

reducing agent, and stirring for 30 minutes, the 222 nm band disappears, and a new broad band appears at ~ 500-510 nm. The presence of the SPR band indicates that Au nanoparticles have been formed and the Au particle size is small. This result is in agreement with reported data which suggested that the surface plasmon band position, bandwidth and intensity of Au NPs are affected by its size and shape, small Au particles have broader spectra than larger particles [49,50]. In contrast to gold, palladium metallic sol displays no surface plasmon band (Figure 3.1b) [51]. The Pd NPs were formed after 30 minutes of stirring with PVA and NaBH$_4$ and it was confirmed by the disappearance of the Pd salt precursor peak after reduction (λ max =210 and 425 nm) as has previously been reported [52,53].

The next step was to synthesise AuPd nanoparticles by varying the AuPd molar ratio using NaBH$_4$ in the presence of PVA. The obtained UV-Vis spectra of bimetallic colloids

prepared with different Au/Pd molar ratios are illustrated in Figure 3.2. The UV-Vis spectra of the AuPd sols indicates the disappearance of the gold surface plasmon band as
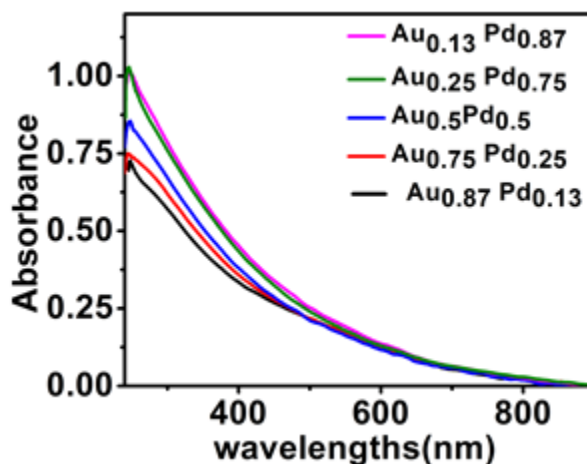
Figure 3.2 UV-Vis spectra of the AuPd sols prepared with different Au/Pd molar ratios, generated after chemical reduction of the HAuCl$_4$ and K$_2$PdCl$_4$ salts by NaBH$_4$ in the presence of PVA.

previously reported for this system by several studies [42,52,54]. This is a phenomenon commonly found in the formation of sols of bimetallic nanoparticles where one of the component metals lacks a surface plasmon band. Deki and co works [55] synthesised nano-sized AuPd bimetallic with various compositions dispersed on a polymer thin film matrix and they concluded that the progressive decrease of the Au plasmon band in the UV-Vis spectra observed by increasing the Pd content was the result of changes in the band structure of the Au particles due to alloying with Pd. These results suggest the formation of bi-metallic nanoalloys, which is in agreement with reported data by Hutchings et [53].

3.3.2. MP-AES analysis

MP-AES Analysis was used to determine the actual Au, Pd and AuPd metal loading immobilised onto TiO$_2$, following a theoretical (nominal) metal loading of 1 wt. % in all cases. The actual loading of Au and Pd in all the catalysts as obtained from the MP-AES analysis is illustrated in Table 3.2. The data of MP-AES confirm that the metal loading of all the samples is close to the expected nominal value. In addition, these results imply that the AuPd ratio can be easily tuned by adjusting the ratio of precursors during preparation.

Table 3.2 MP-AES data for Pd/TiO$_2$, Au/TiO$_2$ and Au$_x$Pd$_{1-x}$/TiO$_2$ catalysts.

Catalyst	Metal loading wt. %	Au/Pd ratio (mol/mol)
Au/TiO$_2$	0.99	100:0
Au$_{0.13}$Pd$_{0.87}$/TiO$_2$	0.96	11:89
Au$_{0.25}$Pd$_{0.75}$/TiO$_2$	0.97	27:73
Au$_{0.5}$Pd$_{0.5}$/TiO$_2$	0.95	51:49
Au$_{0.75}$Pd$_{0.25}$/TiO$_2$	0.98	76:24
Au$_{0.87}$Pd$_{0.13}$/TiO$_2$	0.97	84:16
Pd/TiO$_2$	0.94	0:100

(i) Each result is average of three readings. (ii) %RSD for all results is ± 0.8.

3.3.3. SEM-EDX analysis

SEM-EDX was used to characterize the surface morphologies, dispersion, homogeneity and the elemental composition of all prepared catalysts. Representative examples of SEM images of Au/TiO$_2$, Pd/TiO$_2$ and Au$_{0.5}$Pd$_{0.5}$/TiO$_2$ catalysts are shown in inset of Figure 3.3. The support was the dominant in all images and shows an irregular shape. Au or Pd NPs were not observed which could be due to the lower resolution of SEM and the fact that these metals are expected to be less than 10 nm as a result of using the sol-immobilization method [56]. However, the presence of Au and Pd NPs were detected by Energy dispersive X-ray spectroscopy (EDX). EDX analyses were also conducted to determine elemental composition and confirm the presence of Au and Pd NPs on the support surface for all prepared catalysts (see Figure 3.3 as a representative of the EDX measurements). The corresponding EDX data are shown in Table 3.3. The results show that Au and Pd NPs were successfully loaded onto TiO$_2$ support with uniform distribution and the ratio between Au and Pd NPs is in good agreement with MP AES results.

Table 3.3 EDX data for Au/TiO$_2$, Pd/TiO$_2$ and Au$_{0.5}$Pd$_{0.5}$/TiO$_2$.

Catalyst	Metal loading wt. %	Au/Pd ratio (mol/mol)
Au/TiO$_2$	0.96	100:0
Au$_{0.13}$Pd$_{0.87}$/TiO$_2$	0.98	09:91
Au$_{0.25}$Pd$_{0.75}$/TiO$_2$	0.99	20:80
Au$_{0.5}$Pd$_{0.5}$/TiO$_2$	0.98	52:48
Au$_{0.75}$Pd$_{0.25}$/TiO$_2$	0.98	74:26
Au$_{0.87}$Pd$_{0.13}$/TiO$_2$	0.97	86:14
Pd/TiO$_2$	0.98	0:100
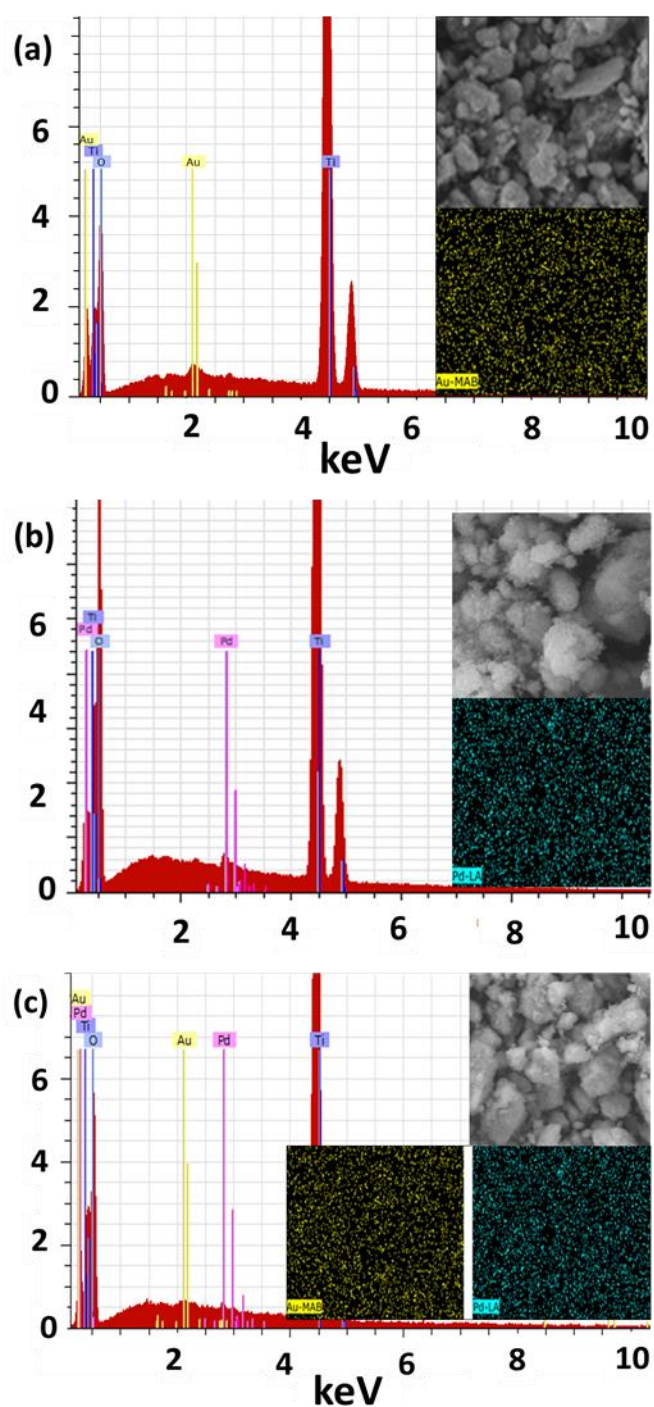
Figure 3.3 EDX patterns with corresponding SEM images (inset) of (a) Au/TiO$_2$, (b) Pd/TiO$_2$ and (c) Au$_{0.5}$Pd$_{0.5}$/TiO$_2$ samples as representative examples.

3.3.4. XRD analysis

Powder XRD was conducted for the bare support TiO$_2$ (P25), Au/TiO$_2$, Pd/TiO$_2$ and a range of bimetallic catalysts Au$_x$Pd$_{1-x}$/TiO$_2$ to determine the crystallinities and phase

purities. The XRD patterns for bare support TiO$_2$, Au/TiO$_2$, Pd/TiO$_2$ and Au$_x$Pd$_{1-x}$/TiO$_2$ are illustrated in Figure 3.4. The assignments of diffraction peaks for metallic Au would be expected at 2θ = 38.°, 44.°, 64° and 77°   were   (111), (200), (220) and (311) planes, respectively, agreement with (JCPDS No. 04-0784) [57]. Also, diffraction peaks of metallic Pd are expected to be θ=40.4°, 46.9°and 68.6°, which corresponding to the Pd (111), (200) and (220) phases, respectively, (JCPDS No. 01-087-0645) [58]. The main diffraction peaks of metallic Au and metallic Pd are expected would be expected at 2θ that indicated by the solid and dashed lines vertical lines in Figure 3.4. It can be seen from Figure 3.4 that the Au or Pd diffraction peaks were not detected because of the smaller crystallite size that is lower than detectability limit of XRD (<5 nm), which is in agreement with TEM results, where the particle sizes of these metals are in the range of 1- 4 nm. Such observation is also in good agreement with previous results [13,28]. Moreover, the high metal dispersion on the TiO$_2$ support could also contribute to this observation which is consistent with the data obtained by SEM-EDX.

On the other hand, the support used in present work is commercial TiO$_2$ (P25) consisting of mixed anatase 85 % and rutile 15%. The diffraction peaks corresponding to the TiO$_2$ were clearly detected at 27.5°, 36.2°, 54.5° and 69.2° for the rutile phase (JCPDS No. 21-1276) [59], whereas diffraction peaks corresponding to anatase phase TiO$_2$ could be observed as characteristic peaks at 2θ=25.3°, 48.0°, 53.8°, and 62.6° (JCPDS No. 21-1272) [60]. Clearly, from Figure 3.4 that all the catalysts show the same powder XRD pattern consistent with that of the TiO$_2$ support, which implies that no new phase was formed during the catalyst preparation step. This suggests that the nanoparticles were adsorbed onto the TiO$_2$ surface and were not integrated into the TiO$_2$ lattice.
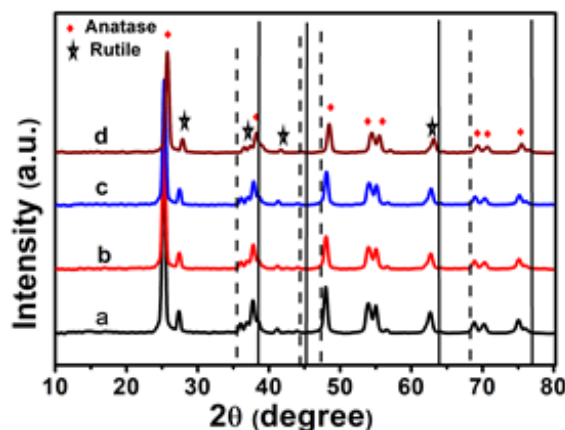
Figure 3.4 XRD patterns for; a) bare TiO$_2$, b) Au/TiO$_2$, c) Pd/TiO$_2$ and d) Au$_x$Pd$_{1-x}$/TiO$_2$ The position where diffraction peaks due to Pd (dashed lines) and Au (solid lines) are marked on the diffractogram.

3.3.5. Surface area measurement (S$_{BET}$)

The total surface area can often play an important role in determining the catalytic performance of a catalyst [58]. In this study, the surface areas of the synthesized catalysts were measured in order to know the effect of total surface area on catalytic reaction. The BET surface Area and pore volume for the bare support TiO$_2$ and of the final catalyst presented in Table 3.4. The calculated and measured surface area values show that no substantial difference in surface area and porosity due to metal deposition. These data are similar to the work that has been reported by Cattaneo *et al.,* [28] who synthesized mono and bimetallic AuPd supported on TiO$_2$ with same metal loading (1%) *via* sol-immobilisation method. Therefore, in this work, the surface area and porosity of catalysts were not considered as an important factor to distinguish between their catalytic activities toward 4-NP reduction reaction.

Table 3.4 BET analysis of bare TiO$_2$, Au/TiO$_2$, Pd/TiO$_2$ and Au$_x$Pd$_{1-x}$/TiO$_2$.

Catalyst	S$_{BET}$ (m²/g)	Pore volume (cm^{3}g^{-1})
TiO$_2$	60 (± 2)	0.36
Au/TiO$_2$	58.7 ±3)	0.33
Pd/TiO$_2$	55 ±1)	0.34
Au$_x$Pd$_{1-x}$/TiO$_2$	(56-58) ±4)	0.32-0.35

3.3.6. XPS analysis

It is well reported in literature that in addition to particles size, the oxidation state and surface composition of the supported AuPd metal are also could affect the catalytic performance [61,62]. Therefore, XPS analyses have been carried out for the synthesized catalysts to study the oxidation stat, surface composition and indicating alloy formation, the obtained spectra were shown in Figures (3.5, 3.6 and 3.7). The XPS profiles of TiO$_2$ is illustrated in Figure 3.5, and it can be showed that the Ti 2p$_{3/2}$ and Ti 2p$_{1/2}$ spin-orbital splitting photoelectrons for all samples can be seen at binding energies of 458.54 eV and 464.23, respectively. It is evident from Figure 3.5 that the Ti 2p (3/2) spectra show that the deposition of the NPs does not alter the oxidation states of Ti, which remained to be Ti^{4+} in all cases. These data are in accordance with data obtained by Yang *et al.,* [63].
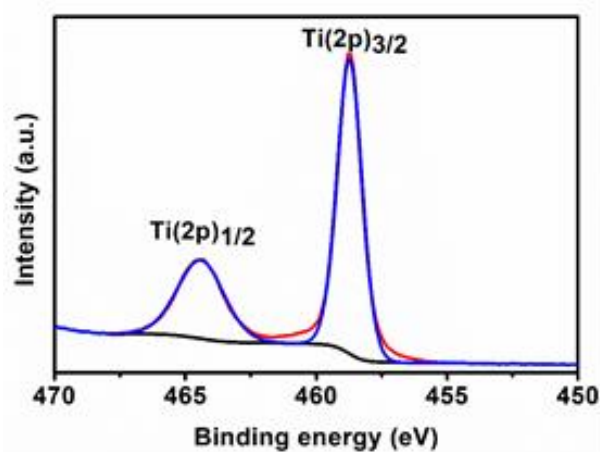
Figure 3.5 XPS core level spectra of Ti(2p) for TiO$_2$.

The XPS data for Au4f spectra of all supported mono and bimetallic catalysts shown in Figure 3.6. For the whole series of samples, Au4f NPs (Au^0) can be identified by two XPS peaks, which are assigned to Au 4f$_{7/2}$ and Au 4f$_{5/2,}$ [64]. The binding energy for Au 4f$_{7/2}$ peak in all catalyst was between 83.5- 83.1 eV, confirming that Au is in the metallic state [28,65]. This is consistent with the literature that, sol-immobilisation method creates mono and bimetallic particles where it consists AuPd alloy with both Pd and Au in metallic state [66,67]. This could be due to the fact that the presence of the ligand - polyvinyl alcohol (PVA)- which may cover the active metal as protecting agent and therefore possibly stabilize the accessibility of the metal.

For the monometallic Au/TiO$_2$ sample, the binding energy of Au 4f$_{5/2}$ was 83.5 eV, which is lower than that of bulk gold (84.0 eV) [28]. This slight decrease in binding energy of Au 4f$_{7/2}$ can be attributed to particle size effects and charging of Au particles (the presence of Au with a partially negative charge, Au$^{\delta-}$). The decrease in the Au 4f$_{7/2}$ binding energy was observed in number of studies [68–71] at a wide range from −0.2 to −1.2 eV. Radnik et $al.,$ [71] considered the reduced coordination number of Au atoms as the main reason of the negative binding energy shift and related it to the degree of rounding of Au nanoparticles which is dependent on the particle–support interaction. In addition, the authors did not exclude the process of electron transfer from the support to the Au particle as a possible contribution to the decrease of the Au 4f$_{7/2}$ binding energy. Arrii et $al.,$ [72] have further developed the idea that particle–support interactions play a crucial role. They suggested that the shift of the Au 4f$_{7/2}$ peak towards lower binding energy can be better explained by an initial state effect associated with electron transfer from Ti^{3+} surface defect states to Au clusters.
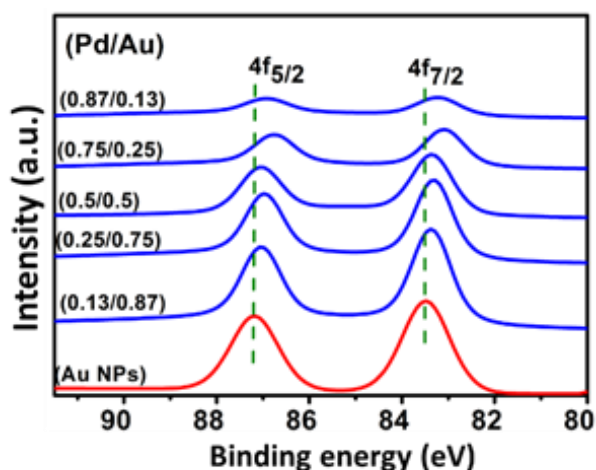
Figure 3.6 XPS core level spectra of Au(4f) for Au/TiO$_2$ and the series of Au$_x$Pd$_{1-x}$/TiO$_2$ catalysts; nominal Pd/Au ratios are as indicated.

Similar to the monometallic, the binding energies of Au(4f) in the all bimetallic Au$_x$Pd$_{1-x}$/TiO$_2$ catalysts show a negative shift to lower energy than the expected bulk value of Au^0 (84.0 eV) as expected when forming the alloy [28]. The corresponding Au XPS binding energies and their chemical shifts showed in Table 3.5 for the various concentrations studied. As shown in Figure 3.6 and Table 3.5, upon addition of Pd, the Au 4f peaks are further shifted negatively and this shift increases with increasing Pd/Au ratio. Therefore, the Au$_{0.87}$Pd$_{0.13}$/TiO$_2$ catalyst has a lower concentration of Pd which exhibited binding energy at 83.37eV with shifting 0.63 eV than bulk Au 4f. Whereas, the most pronounced shift by 0.9 eV was occurring in the bimetallic catalyst with higher amount of Pd which is Au$_{0.13}$Pd$_{0.87}$/TiO$_2$. Regarding previous studies [52,56,57], binding energy of both Pd and Au tends to decrease when forming the alloy. Furthermore, particle size can have an effect as well on the binding energy of metals [58].

Table 3.5 The binding energies (BE) and their chemical shifts of Au(4f$_{7/2}$) and Pd(3d$_{5/2}$) for all synthesized catalysts.

Catalyst	Au4f$_{7/2}$		Pd3d$_{5/2}$	
	B$_E$	Shift in B$_E$ (eV)	B$_E$	Shift in B$_E$ (eV)
Au/TiO$_2$	83.5	0.5	-	-
Au$_{0.87}$Pd$_{0.13}$/TiO$_2$	83.37	0.63	334.56	0.84
Au$_{0.75}$Pd$_{0.25}$/TiO$_2$	83.35	0.65	334.64	0.76
Au$_{0.5}$Pd$_{0.5}$/TiO$_2$	83.31	0.69	334.69	0.71
Au$_{0.25}$Pd$_{0.75}$/TiO$_2$	83.22	0.78	334.77	0.63
Au$_{0.13}$Pd$_{0.87}$/TiO$_2$	83.1	0.9	334.89	0.51
Pd/TiO$_2$	-	-	334.99	0.41

(i) B$_E$ of bulk Au 4f$_{7/2}$ peak= 48 eV and (ii) B$_E$ of bulk Pd3d$_{5/2}$ peak= 335.4 eV

On the other hand, the Pd(3d) XPS spectra of the all catalyst can be identified by two peaks assigned to Pd 3d$_{5/2}$, and Pd 3d$_{3/2}$ [73]. The oxidation state of Pd 3d was found on the surface of all bimetallic catalysts in the metallic state (Pd^0), while monometallic Pd/TiO$_2$ catalyst displayed a mixture of Pd^0 (334.99 eV) and Pd^{II} (337 eV), and the ratio (Pd^{II}/Pd^0) was 20 % (see Figure 3.7). These data were similar to the recent study by Rogers *et al.,* [13], who synthesized Pd/TiO$_2$ *via* sol-immobilisation method and found that the catalyst sample contained two types of Pd (i.e. Pd^{II} and Pd^0). The XPS data for Pd3d spectra of supported mono and bimetallic catalysts with different Pd/Au ratios are shown in the Figure 3.8. These results show that the binding energy of Pd3d$_{5/2}$ peak for mono-and Bi-metallic catalysts at about (334.99 -334.56 eV) which are lower than that of bulk Pd at about 335.4 eV(see Table 3.5) [74]. Furthermore, the binding energies of metal Pd had a negative shift with the increase of Au loading amount in the AuPd alloy, resulted in enhanced electronegativity of the nanoparticles, reflecting electron transfer between Pd and Au [73].The binding energy for Au$_{0.13}$Pd$_{0.87}$/TiO$_2$, which has 13% of Au, at 334.89 eV, was shifted by(-0.51 eV), while after increased the amount of Au to 87% in the Au$_{0.87}$Pd$_{0.13}$ /TiO$_2$ catalyst, a further negatively shifted in the binding energy was observed by (-0.84 eV) and the peak was at 334.56 eV. Moreover, it has been clearly shown that upon addition and promotion of Au, the original Pd feature is gradually weakened, and a new Pd feature at lower binding energy emerges and grows up, these date in agreement with Wang *et al.,* [54].
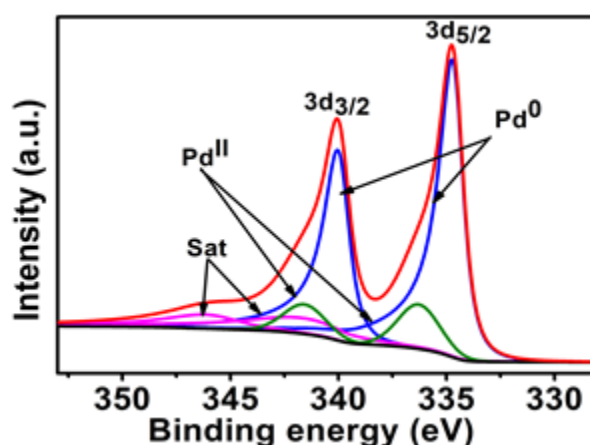
Figure 3.7 XPS core level spectra of Pd(3d) for Pd/TiO$_2$ catalyst.

This observation negative shift in binding energies for Au(4f) and Pd(3d) in the bimetallic AuPd has been studied and some authors have related this negative shift to the change in electronic structure as a function of cluster size [68,72]. Other authors attributed it to (i)

electron transfer from the support to the nanoparticles [54], or (ii) charge transfer from Pd to Au, increasing the *s*-state occupancy for Au and indicating alloy formation [75], this could be a result of strong interaction between Au and Pd as observed in PdAu alloys [54,76]. Very recent study by Chen *et al.,* [73] have proved the previous mechanism for electron transfer between Pd and Au that suggested by Lee *et al.,* [48] and Yi *et al.,* [73]. They studied the properties of Pd-Au bimetallic catalysts and found negative shifts of binding energies in the bimetallic Pd-Au particles and proposed a charge compensation model that Pd loses *sp*-electrons and gains *d* -electrons while Au gains *sp*-electrons and loses *d*-electrons.
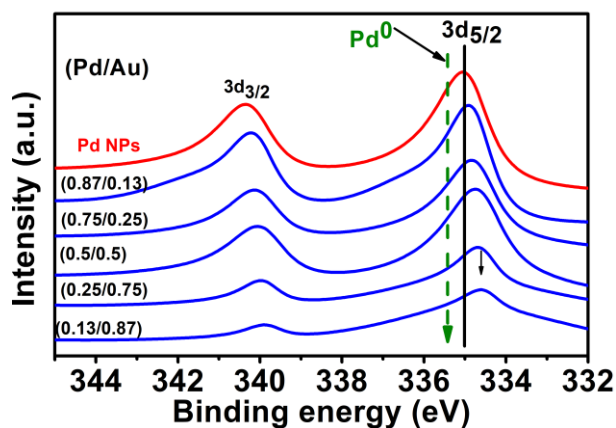
Figure 3.8 XPS core level spectra of Pd(3d) for Pd/TiO$_2$ and the series of Au$_x$Pd$_{1-x}$/TiO$_2$ catalysts; nominal Pd/Au ratios are as indicated.

3.3.7. TEM analysis

 It has been reported that the catalytical activity of supported metal NPs (e.g. Pd, Au, Ag etc.) are directly linked to their particle size [22], shape[77], morphology[78], and composition[79]. Therefore, transmission electron microscopy (TEM) analysis is very essential to discover these features.

The TEM images show good distribution of the Au and Pd particles immobilized on the TiO$_2$ support with no obvious sign of aggregation of the Au and Pd nanoparticles and relative good dispersion. Moreover, the shape of the particles is almost spherical for all catalysts. As shown in the inset of Figure 3.9 (a &b), monometallic Au/TiO$_2$ and Pd/TiO$_2$ resulted in a narrow particle size distribution in the range from 1 to 6 nm with an mean particle size of 2.60 and 2.62 nm, respectively. The mean particle size of all the supported bimetallic Au$_x$Pd$_{1-x}$ nanoparticles were between 2.07 ($\pm$0.61) – 3.20 $\pm$ 1.10 nm. The TEM for Au$_{0.5}$Pd$_{0.5}$/TiO$_2$ catalyst show a uniformly distributed on the support with a narrow

size particle distribution from 2 to 4 nm with a smaller mean particle size of ~2 nm. The TEM for Au$_{0.5}$Pd$_{0.5}$/TiO$_2$ catalyst show spherical AuPd NPs with narrow size distribution uniformly distributed in high dispersion on the TiO$_2$ and exhibit a smaller mean particle size of ~2 nm. These results in good agreement with recent study by Cattaneo *et al.,* [28] who synthesized Au$_{0.5}$Pd$_{0.5}$/TiO$_2$ with small mean particle size (2.1 nm) by using sol-immobilisation method. The mean particle size of all catalysts is summarised in Table 3.6. As we can observe from this table that the mole ratio of (1:1) is the optimum of obtaining small metal particle size.

Table 3.6 Mean values (nm) obtained by TEM of the supported monometallic and bimetallic catalysts.

sample	Mean particle size (nm)	Std-dev
Au/TiO$_2$	2.60	0.88
Pd/TiO$_2$	2.62	0.92
Au$_{0.87}$Pd$_{0.13}$/TiO$_2$	2.57	0.71
Au$_{0.75}$Pd$_{0.25}$/TiO$_2$	3.20	1.10
Au$_{0.5}$Pd$_{0.5}$/TiO$_2$	2.07	0.61
Au$_{0.25}$Pd$_{0.75}$/TiO$_2$	2.85	0.72
Au$_{0.13}$Pd$_{0.87}$/TiO$_2$	2.64	0.82
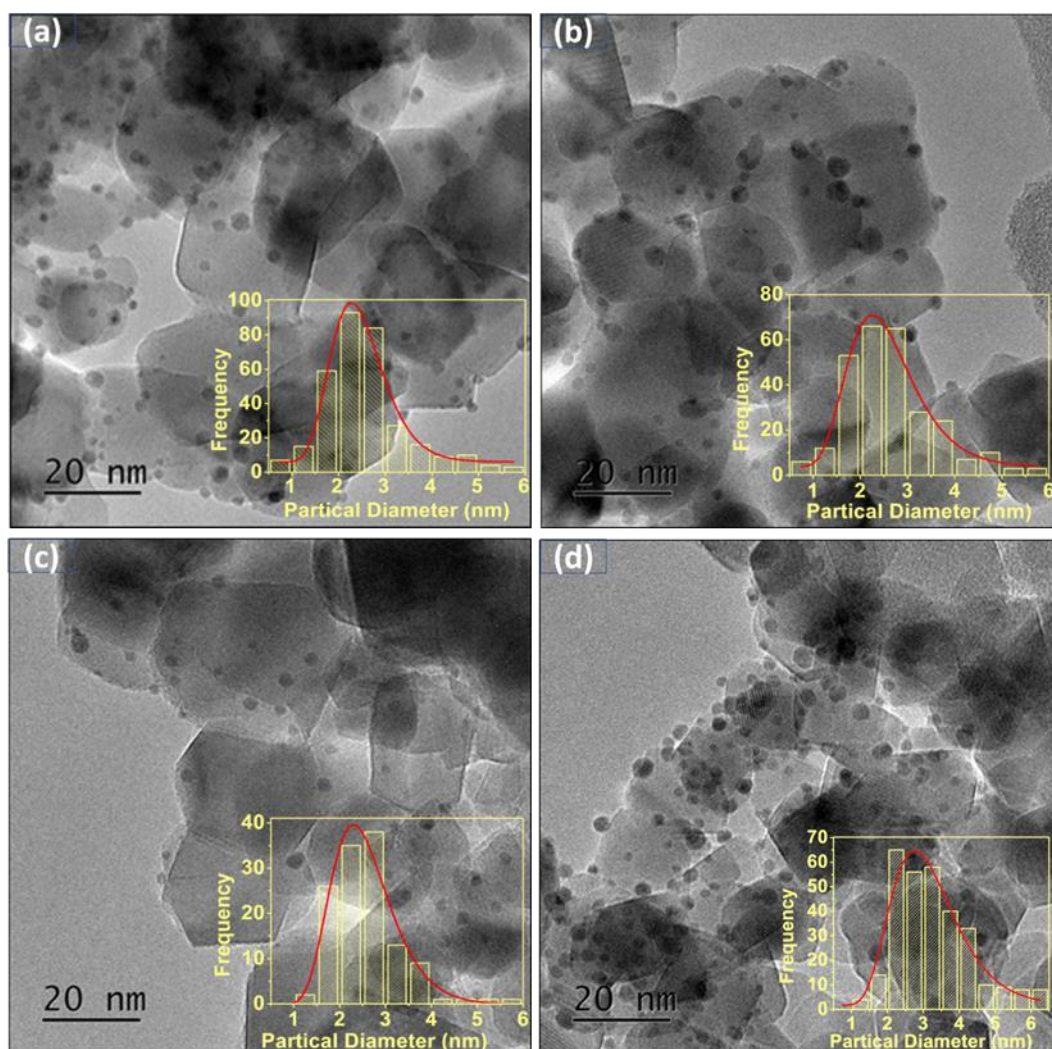
Figure 3.9 TEM images and metal particle distribution (inset) of different bimetallic compositions a) Au/TiO$_2$ b) Pd/TiO$_2$ c) Au$_{0.87}$Pd$_{0.13}$/TiO$_2$ d) Au$_{0.75}$Pd$_{0.25}$/TiO$_2$ e) Au$_{0.5}$Pd$_{0.5}$/TiO$_2$ f) Au$_{0.25}$Pd$_{0.75}$/TiO$_2$ and g) Au$_{0.13}$Pd$_{0.87}$/TiO$_2$.
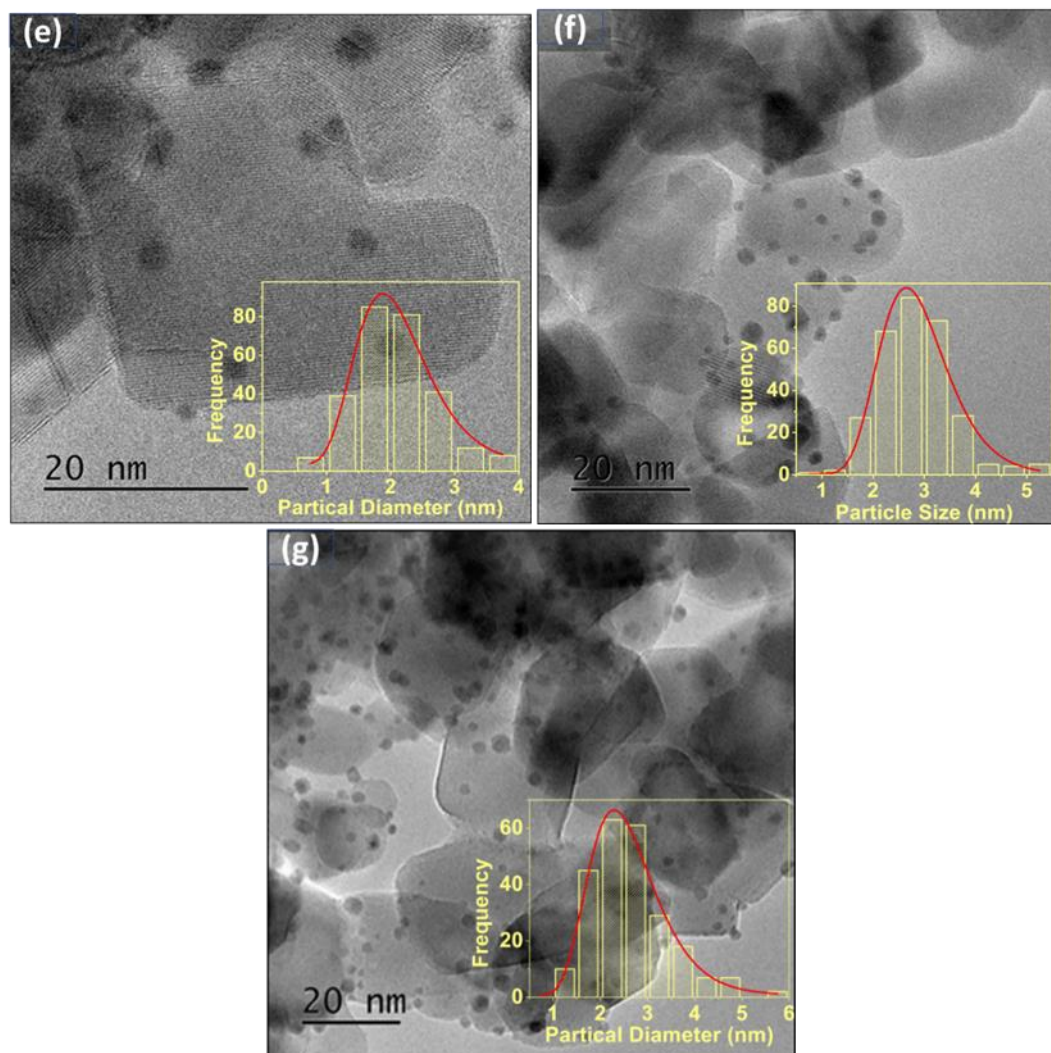
Figure 3.9 (***continued***) TEM images and metal particle distribution (inset) of different bimetallic compositions a) Au/TiO$_2$ b) Pd/TiO$_2$ c) Au$_{0.87}$Pd$_{0.13}$/TiO$_2$ d) Au$_{0.75}$Pd$_{0.25}$/TiO$_2$ e) Au$_{0.5}$Pd$_{0.5}$/TiO$_2$ f) Au$_{0.25}$Pd$_{0.75}$/TiO$_2$ and g) Au$_{0.13}$Pd$_{0.87}$/TiO$_2$.

3.4. Reduction of 4-nitrophenol by NaBH$_4$

The reduction of 4-Nitrophneol was conducted under very mild conditions at 30 °C and atmospheric pressure using an excess of freshly prepared NaBH$_4$ (NaBH$_4$/4-NP = 30 molar ratio) as a reducing agent under alkaline conditions. Upon addition of NaBH$_4$ to the system, 4-NP is converted to 4-nitrophenolate anion. The 4-NP peak moves from λ 317 nm to λ400 nm and the colour of solution changes from light yellow to dark yellow, indicating the presence of the 4-nitrophenolate anion (Figure 3.10) [80]. This peak remains unaltered over time, which suggests that the reduction does not proceed in the absence of a catalyst, as reported by several authors [83–85]. It could be explained by that the kinetic barrier between nitrophenolate anions and borohydride ions is too high for any reaction to occur between them in the absence of a catalyst, as discuses early. Hence, this reaction has been chosen to evaluate the catalytic activity of the prepared NPs [12,80].
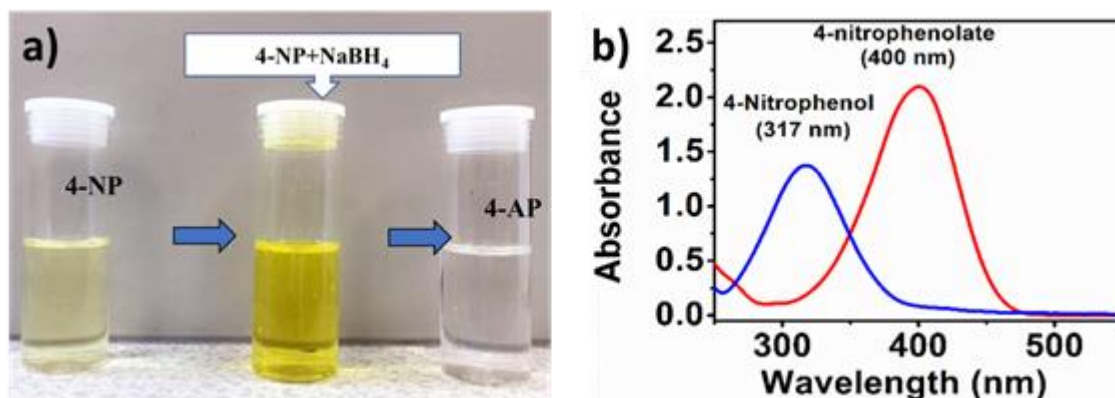
Figure 3.10 a) Image for colour change during catalytic reduction of 4-NP to 4-aminophenol by NaBH$_4$. b) An example of UV–Vis spectra of aqueous 4-NP solution (blue line) and aqueous 4-NP solution (4-nitrophenol ion) in the presence of sodium borohydride (red line)

A significant reduction of the peak at λ 400 nm is observed after addition of catalyst, along with the development of a peak at λ 300 nm (Figure 3.11a) and color change to be colourless, indicating the formation of 4-aminophenol (Figure 3.10a). In order to maintain the *pseudo* first-order condition, the concentration of NaBH$_4$ is much higher than 4-NP,

so it essentially remains constant during the reaction and also to prevent aerial oxidation of 4-AP [84]. The total reduction reaction is summarized in Equation 3.1 [21].
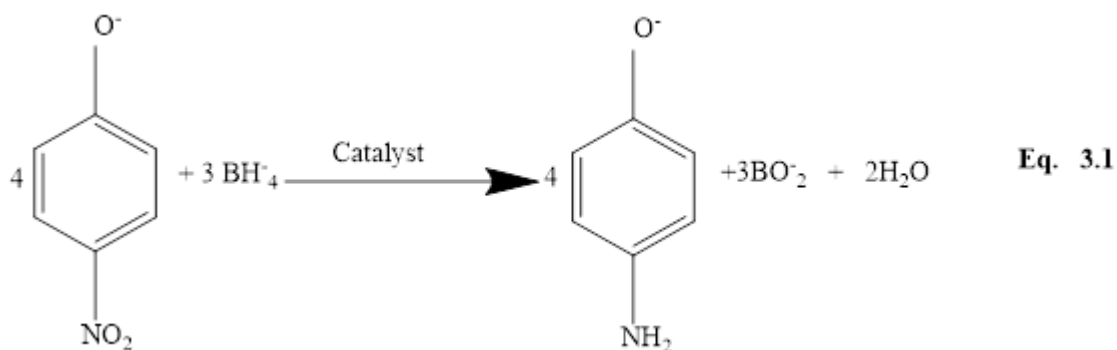
The reaction can be split into two parts: the hydrogen radical production from borohydrite by electron transfer (Equation. 3.2) and the addition of protons to 4-NP while removing oxygen (Equation. 3.3). These reactions can proceed almost independently.

$$BH_4^- \ + \ 2H_2O \longrightarrow BO_2^- \ + \ 4H_2 \qquad \qquad \text{Eq. 3.2}$$
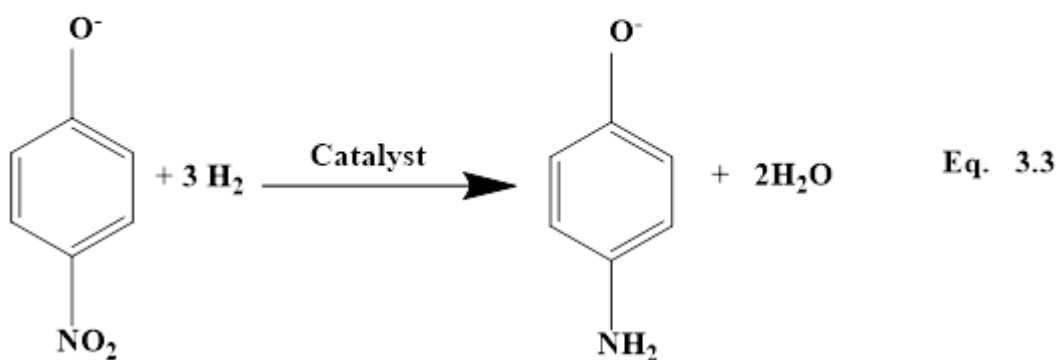
The reaction rate depends on 4-NP and NaBH$_4$ concentration. In order to ensure *pseudo-first-order* reaction conditions, excess NaBH$_4$ was used in the reaction therefore the reduction rate is independent of borohydride concentration [83]. So, in this case, *pseudo-first-order* kinetic with regard to the 4-nitrophenolate concentration could be applied to evaluate the catalytic rate [82,83]. Therefore, the kinetic equation of the reduction could be shown as

$$\ln[C_t] = \ln[C_0] - Kt \qquad \qquad \text{Eq. 3.4.}$$

Where K$_{app}$ is the apparent rate constant, C$_t$ is the 4-NP concentration at time **t** during the reaction, and C$_0$ is the initial 4-NP concentration.

According to the Equation 13.4 and from the graph in Figure 3.11 b, K_{app} which is the apparent rate constant that dependent on the concentrations of 4-NP only and not on the concentration of applied catalyst or NaBH$_4$ can be determined by the slope. Figure 3.11b displays a short time frame (the induction time (t_0) with no change in absorption).
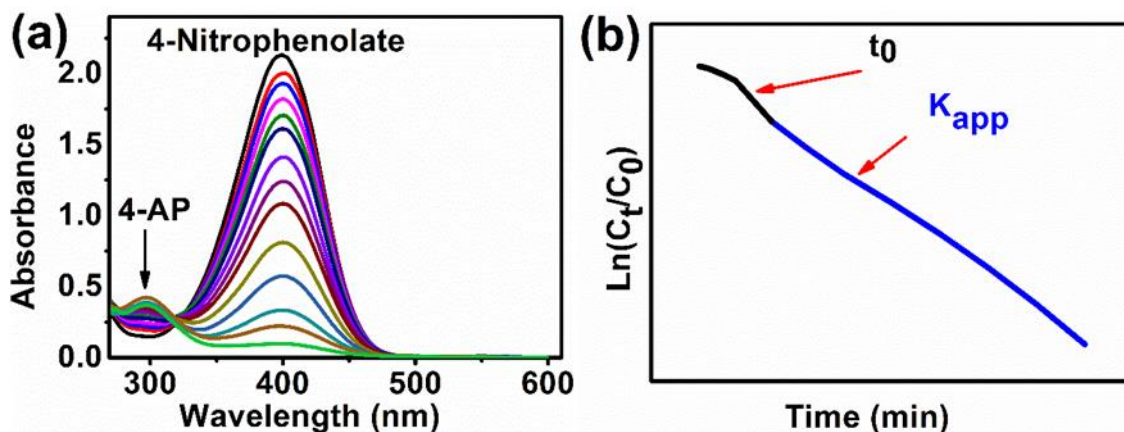
Figure 3.11 (a) UV-Vis spectra collected during the catalytic reduction of 4-NP with NaBH$_4$ using Au/TiO$_2$ catalyst in the range of 250 to 600 nm, where the 4-nitrophenolate absorbance peak at 400 nm decrease with time and (b) example for the first order kinetic graph

Several reports confirmed that 4-aminophenol (4-AP) was the sole product of reduction of 4-NP and no side reaction occurred [85–87]. Figure 3.11a show that aminophenol (4-AP) exhibits a weak absorption peak at around 300 nm and several isosbestic points indicate that there are no side reactions takes place and that only one product is formed. To further confirm this observation, the reaction media after 100 % conversion has been analysed by gas chromatography equipped with mass spectroscopy (GC-MS) and the results confirmed that the 4-aminophenol was the sole product of the reaction (see appendix Figure A1).

3.4.1.   Optimization of the reaction conditions

The reaction parameters such as stirring rate and the catalyst concentration on the catalytic activity have been optimized to determine the optimum conditions to carry out the reaction under kinetic regime control (diffusion and mass transfer regime). Moreover, the influence of 4-NP and NaBH$_4$ concentration have been investigated to maintain the pseudo first-order condition and to understand the mechanism of the catalytic reduction of 4-NP with NaBH$_4$.

3.4.1.1.   Effect of 4-nitrophenol and NaBH$_4$ concentration

To understand the mechanism of the catalytic reduction of 4-NP with NaBH$_4$ and to maintain the pseudo first-order condition, the influence of two reactants concentration (i.e. 4-NP of NaBH$_4$) on the 4-NP reduction was investigated in depth by varying the concentration of either 4-NP or NaBH$_4$, while keeping all other conditions constant. Figure 3.12 shows the range of concentrations used, with (a) showing the 4-NP concentrations and (b) showing variations in sodium borohydride concentration.
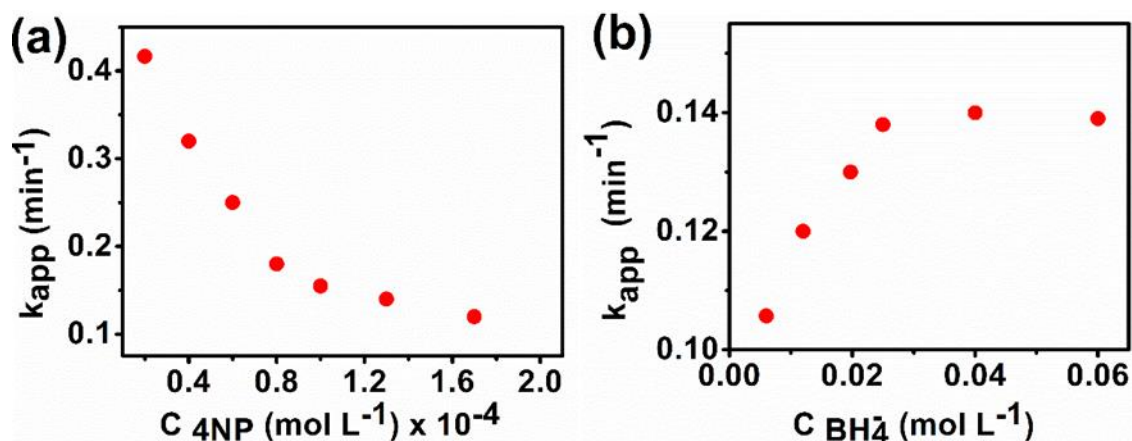
Figure 3.12 Apparent rate constant K$_{app}$ versus the concentration of; (a) 4-NP and (b) NaBH$_4$. Reaction conditions: 9.2 mg of Au/TiO$_2$, 30 ºC, 1000 rpm. The concentration of 4-NP varies between [(0.2 – 1.7) ×10^{-4} M] with a constant concentration of NaBH$_4$ [0.04 M].

First, a wide 4-NP concentration regime (0.2 – 1.7 × 10^{-4} M) was tested with NaBH$_4$ at constant concentration. Second, a range of NaBH$_4$ concentration (0.006– 0.06 M) with constant 4-NP concentrations was examined. The concentration of the catalyst is kept constant on the all experiments. The trends of the graphs obtained are similar to those reported by several authors [21,87,88]. Study of the dependence of the apparent rate constant on the 4-NP and sodium borohydride concentrations in Figure 3.12 makes it clear

that the rate constant decreases as 4-NP concentration increases and attains its highest level when borohydride concentration increases to a certain limit. Moreover, Figure 3.12 shows a definite non-linear dependence for variations in both concentrations – at high concentrations.

These observations firmly support the heterogeneous surface catalytic reaction for 4-NP reduction. The high concentration of 4-NP results is nearly full surface coverage. This slows down both the reaction with borohydride ions and the injection of electrons onto the metal surface. The nonlinear relation of K_{app} to the borohydride concentration, as well as the saturation at high concentrations, directly indicate that the reactants are competing for the reactive sites on the metal surface and the reaction follow closely the Langmuir–Hinshelwood mechanism in agreement with several publications [12,21,89,90]. This means that there should be an optimal concentration where the reaction rate is at a maximum.

3.4.1.2. Effect of stirring speed

Generally, mass-transfer limitations play an important role for a valid [92] determination of the reaction rate of liquid-phase catalytic hydrogenation reactions [91]. Therefore, the effect of stirring speed on the reduction of 4-NP over Au/TiO$_2$ was investigated to study the effect of mass-transfer limitations on the reaction rate, the obtained data is shown in Figure 3.13. From the Figure 3.13, it can be seen that below stirring speed of 1000 rpm the reaction is under the influence of diffusion limitation, however, beyond 1000 rpm the reaction process is outside the influence of diffusion and control by the rate of the
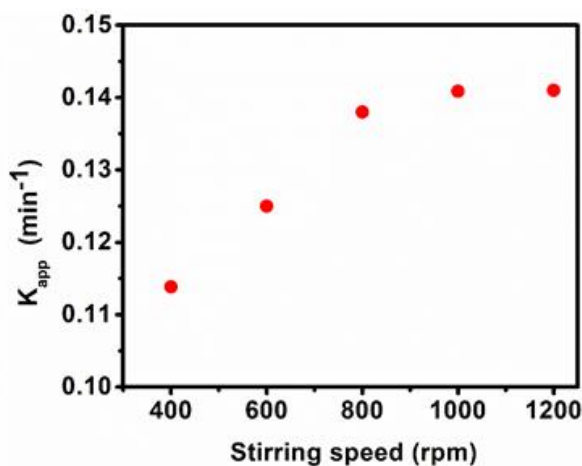
Figure 3.13 Effect of stirring speed on the reduction of 4-NP over Au/TiO$_2$. Reaction conditions: 4-NP/metal molar ratio = 13, NaBH$_4$/4-NP molar ratio = 30, T = 30 ℃, stirring speed = (400 - 1200) rpm.

reaction. This implies that the reaction rate must be investigated at a speed of at least 1000 rpm.   Therefore, it can be assumed that under these conditions external mass transfer is not limiting the reaction rate. Therefore, a stirring speed of 1000 rpm has been selected for subsequent studies.

3.4.1.3. Effect of catalyst amount

The catalyst amount can kinetically and mechanistically be affected the reduction of 4-nitrophenol. In the case of heterogeneous catalysis, the reaction rate generally increases linearly with the amount of catalyst [58,60, 61, 70, 87]. However, such study is useful to avoid the effect of mass transfer limitations. The influence of catalyst amount on the catalytic reduction rate of 4-NP by NaBH$_4$ was studied by different amounts of Au/TiO$_2$ (2-10 mg). Figure 3.14 displays the effect of catalyst amount on the catalytic activity of 4-NP reduction. The rate constant obtained from the slope of the kinetic curves has been related to catalyst dose, while keeping other parameters such as the initial concentrations of 4-NP and borohydride constant. It is evident from Figure 3.14 that the apparent rate constant is found to be increased from 0.03 to 0.14 min^{-1} with increase in catalyst amount from 2 to 10 mg and showed a linear relationship as reported by several authors [21,87,88]. A linear dependency of this sort may show an absence of external mass transfer that there are no limitations on bulk diffusion. Therefore, in the present study a higher substrate to metal ratio was used for all experiments (4-NP/metal molar ratio = 13).
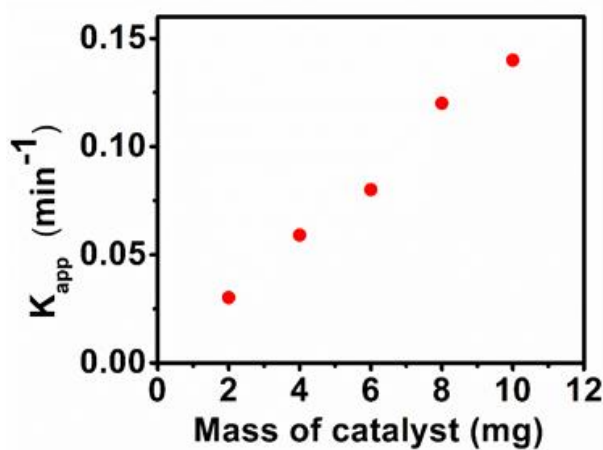
Figure 3.14 Effect of catalyst mass on the reduction of 4-NP using Au/TiO$_2$. Reaction conditions: [2-10 mg] of Au/TiO$_2$, 4-NP [1.35×10^{-4} M], 5 ml NaBH$_4$ [0.04 M], T=30 ºC, stirring rate =1000 rpm.

3.4.2. Catalytic activity of monometallic Au/TiO$_2$ and Pd/TiO$_2$

After establishing the reaction conditions (4-NP and NaBH$_4$ concentration, stirring speed and the catalyst concentration) and adjust them to the optimum values, a screening of the monometallic catalysts Au/TiO$_2$ and Pd/TiO$_2$ and bimetallic catalysts Au$_x$Pd$_{1-x}$/TiO$_2$ with different Au and Pd molar ratio was performed. The catalytic activity of the Au/TiO$_2$ was studied for 4-NP reduction by using NaBH$_4$ as reducing agent. Figure 3.15 illustrates the 4-NP conversion and Ln[4-NP] as a function of time in the presence of Au/TiO$_2$. The absorbance slope derived from Figure 3.15 shows an apparent rate constant (K$_{app}$) of 0.14 min^{-1}.
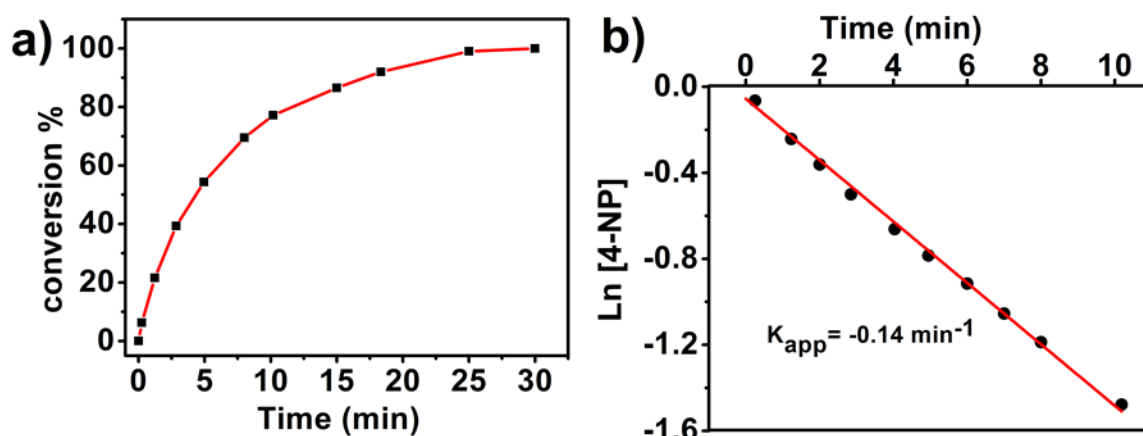
Figure 3.15 a) Reduction of 4-NP conversion over Au/TiO$_2$. b) ln[4-NP] as a function of time. Reaction conditions: 4-NP/metal molar ratio = 13, NaBH$_4$ /4-NP molar ratio = 30, T=30 °C, stirring rate = 1000 rpm.

To investigate the contribution of the reaction conditions and the catalyst support, two blank reactions were performed – one involving no solid catalyst and the other with only the TiO$_2$ (P25) support material. The results of both blank experiments show that the 4-NP is inert to NaBH$_4$ in both reactions even after a period of 24 h.

Very little details exist in the literature on the use of Au supported on TiO$_2$ for catalysing 4-NP, which could be due to the difficulty of monitoring the catalytic reaction with UV-Vis spectroscopy in the presence of TiO$_2$ because the absorbance of TiO$_2$ is in the same region of the substrate leading to a lot of scattering in the UV spectra. That means non-stirring conditions is required which are difficult to apply as it affects the homogeneity of the catalysts in the reaction media and thus affect the total rate of the reaction. Moreover, the reactants will suffer from mass transfer limitation as they need to diffuse to the catalyst surface to start the reaction. Accordingly, in this work, the activity of Au/TiO$_2$ was

investigated with high substrate/metal ratio under high stirring, 1000 rpm, by running the reaction on batch reactor and then the catalyst was isolated by using a 0.45 µm syringe filter before doing the measurement of the UV. Figure 3.16 show the UV-Vis spectra for the reduction of 4-NP before and after isolated TiO$_2$ from the reaction solution.
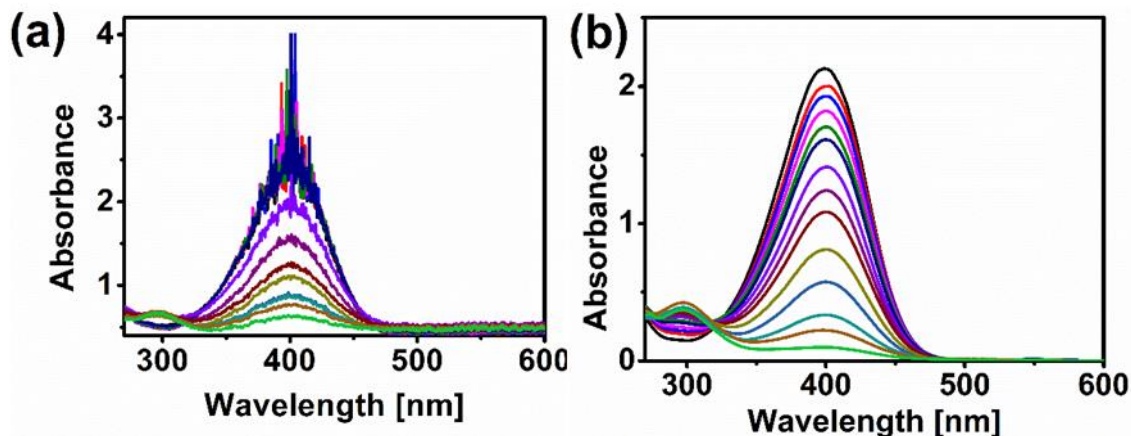
Figure 3.16 UV-Vis absorption spectra of the reduction of 4-NP by Au/TiO$_2$ (a) without filtration of the reaction sample (b) after filtration of the reaction sample.

Similar to the Au NPs, a monometallic Pd/TiO$_2$ catalyst was also used to catalyse the reduction of 4-NP under similar reaction conditions for comparative purposes. The reaction rate with Pd/TiO$_2$ as the catalyst is compared with the monometallic Au/TiO$_2$ catalyst in Table 3.7.

Table 3.7 Summary of apparent rate constants of Pd/TiO$_2$ and Au/TiO$_2$ catalysts on the reduction 4-NP by NaBH$_4$.

Catalyst	K_{app} (min^{-1})
Au/TiO$_2$	0.14
Pd/TiO$_2$	0.2

As expected, the results in the table 3.7 indicate clearly that the catalytic activity of Pd/TiO$_2$ catalyst on the reduction of 4-NP is higher than Au/TiO$_2$ catalyst, similar to what is obtained elsewhere [34]. Indeed, it proposed that, during the hydrogenation of nitroaromatic compounds, the Pd clusters adsorb BH_4^-/H$_2$ dissociative with a much lower activation barrier than Au.

3.4.3.   Catalytic activity of Au$_x$Pd$_{1-x}$/TiO$_2$

Recently, it was found that addition of palladium to gold enhance the activity and selectivity in several reactions [28,45] Generally, bi-metallic catalysts are found to be more active than their mono-metallic counterparts therefore there is growing interest in studying and understanding this subject [15,28] The enhanced activity can be related to many factors such as the electronic effect of bi-metallic systems which results in an increase in the binding of adsorbate molecules to the metal surface. Another factor is the geometric effect where atomic arrangement on the support can enhance the activity. Therefore, the presence of Au and Pd on the surface at different compositions influence reaction rates and kinetic pathways.   In order to study this, a bimetallic catalyst AuPd/TiO$_2$ was prepared using sol-immobilization method with co-reduction of Au and Pd on the surface at (1:1) molar ratio. The activity of the bi-metallic catalyst was compared to the monometallic catalysts and the results are summarized in Table 3.8.

Table 3.8 A summary of K$_{app}$ of monometallic Au/TiO$_2$ and Pd/TiO$_2$ catalysts and bimetallic Au$_{0.5}$Pd$_{0.5}$/TiO$_2$ catalysts on the reduction of 4-NP by NaBH$_4$.

Catalyst	K$_{app}$ (min^{-1})
Au/TiO$_2$	0.14
Pd/TiO$_2$	0.2
Au$_{0.5}$Pd$_{0.5}$ /TiO$_2$	0.38

The results given in Table 3.8 clearly showed that Au$_{0.5}$Pd$_{0.5}$/TiO$_2$ has superior activity with K$_{app}$ =0.38 min^{-1} compared to Au//TiO$_2$ (K$_{app}$ =0.14 min^{-1}) and adding Pd to Au enhanced the activity of the catalyst. Nanosized Pd catalysts have been shown by studies to facilitate a new reaction pathway for the reduction of nitroaromatic compounds in which Pd enhances the relay of hydrogen and which would not be available if Pd were absent. There is a synergy between neighbouring Au and Pd sites in the bimetallic catalysts that makes such new pathway possible. Pd can adsorb BH$^-_4$/H$_2$ dissociative with a much lower activation barrier than Au. Thus, activated H atoms can migrate to Au or mixed AuPd sites located in the neighbourhood. The acceleration of hydrogen involving reactions because metallic Pd acts as a "hydrogen relay system" is well established [42,92]. This reaction adds protons to 4-NP while at the same time removing its oxygen. This equation explains how hydrogen radicals are produced from NaBH$_4$ in presence of Pd nanoparticles:

$$BH_4^- + 2H_2O \rightarrow BO_2^-{}_+ 4H_2 \qquad (Eq\ 1.2)$$
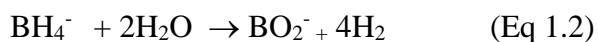
Splitting the overall reaction into hydrogen production (Equation 1.2) and hydrogen consumption shows the great advantage derived from having a material that, by absorbing hydrogen, ensures the almost independent execution of these reactions. Its ability to store hydrogen allows Pd to facilitate intermediate storage of hydrogen radicals capable of reacting with 4-NP; at the same time, the nitro group is also activated by the catalyst. There is no requirement for adsorption of BH_4^- and 4-NP to be either close to each or at the same time. The bimetallic AuPd NPs catalysts are hydrogen relay systems as well as electron relay systems. The metal to metal interfaces greatly improves rates of electron transfer by Au NPs, while the Pd does the same for hydrogen. This combination of metal to metal interfaces and Pd are what explains the catalytic ability possessed by bimetallic AuPd catalysts, which can make possible new reaction pathways that would not otherwise be available.

In the introduction of this Chapter, we explained how different optimum Au/Pd ratios were observed in 4-NP reduction reaction with different supports and reaction conditions. They linked the high catalytic activities of these optimum Au/Pd ratio to several factors on top of these were Au and Pd particles size and the number of AuPd interfaces within the surfaces and if they present as alloys or individuals [46,67,93]. Taking in mind, we are aiming to investigate the optimum Au/Pd molar ratio and understand the factors that influence its activity by using sophisticated characterization techniques such as MP-AES, TEM, XPS, XRD, SEM-EDX, BET surface area and HAADF -STEM. A series of AuPd/TiO$_2$ catalysts were synthesized with different molar ratio *via* sol-immobilization technique and co-reduction of Au and Pd using NaBH$_4$ as strong reducing agent. The molar ratio of Au:Pd was varied (i.e. 0.13:0.87, 0.25:0.75, 0.5:0.5, 0.75:0.25 and 0.87:0.13), to find the optimum ratio that give the highest catalytic activity. To ensure direct catalyst-catalyst comparison, the molar ratio of the NPs to substrate was fixed in all the reactions (4-NP/metal molar ratio =13). This allows us to use apparent rate constant (K$_{app}$) for direct comparison between the catalysts without considering the amount of catalysts used in the reaction. The values of apparent rate constant for the reaction over Au$_x$Pd$_{1-x}$/TiO$_2$ catalysts with different molar ratio along with monometallic catalysts for comparison purpose are listed in Table 3.9.

Table 3.9 summarize of K$_{app}$ of monometallic Au/TiO$_2$ and Pd/TiO$_2$ catalysts and bimetallic Au$_x$Pd$_{1-x}$/TiO$_2$ catalysts on the reduction of 4-NP by NaBH$_4$.

Catalyst	K$_{app}$ (min^{-1})
Au/TiO$_2$	0.14
Pd/TiO$_2$	0.2
Au$_{0.13}$Pd$_{0.87}$/TiO$_2$	0.24
Au$_{0.25}$Pd$_{0.75}$/TiO$_2$	0.25
Au$_{0.5}$Pd$_{0.5}$/TiO$_2$	0.38
Au$_{0.75}$Pd$_{0.25}$/TiO$_2$	0.29
Au$_{0.87}$Pd$_{0.13}$/TiO$_2$	0.22

The results in Table 3.9 obviously prove that the activity of all ratio of AuPd bimetallic for 4-NP reduction higher than monometallic catalysts. Furthermore, the catalyst activity increases significantly from 0.14 for Au/TiO$_2$ to 0.22 min^{-1} in the Au$_{0.87}$Pd$_{0.13}$/TiO$_2$ catalyst only when add small quantities of palladium to gold. Among of these ratios, the catalyst of poor palladium (i.e. Au$_{0.87}$Pd$_{0.13}$/TiO$_{2)}$ showed lower activity with K$_{app}$ of 0.22 min^{-1}. However, further addition of palladium along with gold showed a significant increase in the K$_{app}$ till the molar ratio (1:1), where the activity reached a maximum with K$_{app}$ of 0.38 min^{-1}, beyond which it then progressively decreases as the palladium content was increased. This can be shown in Figure 3.17 which shows how the molar ratio between Pd and Au affects the apparent rate constant and showed that the highest activity was achieved at (1:1) Pd:Au molar ratio.
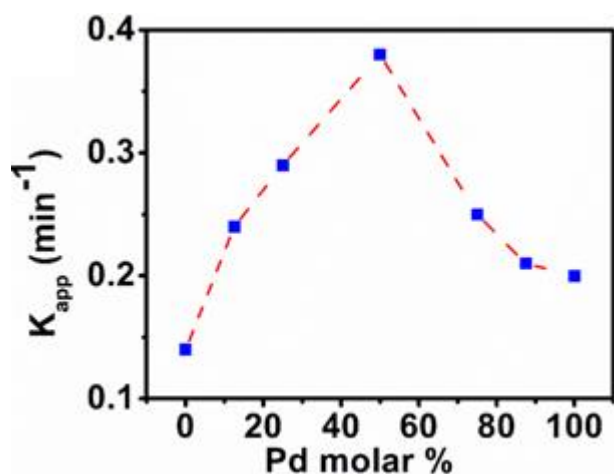
Figure 3.17 Apparent rate constant K$_{app}$ versus Pd molar ratio of the series of Au$_x$Pd$_{1-x}$/TiO$_2$. Reaction conditions: 4-NP/metal molar ratio = 13, NaBH$_4$ /4-NP molar ratio = 30, T = 30 ºC and stirring rate = 1000 rpm.

Studying influence of Au/Pd molar ratio displayed "volcano behaviour" with (1:1) Au:Pd molar ratio catalyst resulting as the most active catalyst toward 4-NP reduction with K$_{app}$ of 0.38 min^{-1}. The steep rise in catalytic activity is expected when the Pd is combined

with Au which explains the left half of the volcano however this was not the case when the Pd molar ratio is more than gold (right half of the volcano). The greater catalytic activity of Au$_{0.5}$Pd$_{0.5}$/TiO$_2$ catalyst can be linked to several factors such as AuPd NPs size, synergistic effect and/or it could be related to the structure of alloys that can be formed at this composition. According to the TEM results, AuPd NPs prepared with molar ratio of (1:1) produced the smallest particles (~2 nm) with exhibiting the narrowest size particle distribution from 2 to 4 nm compared with other metal ratios. However, statistically, the difference in particle size between bi-metallic catalysts is not that significant to allow us to draw a conclusion (the mean particle size was between $2.07 \pm 0.61 - 3.20 \pm 1.10$ nm. Another factor that can help us to understand the difference in activity is the quantity of metal to metal interfaces in AuPd system at different molar ratio. XPS data showed that the level of interaction between both metals increases with increasing Pd molar ratio but it doesn't explain the low activity of Au$_{0.13}$Pd$_{0.87}$ /TiO$_2$ which has the highest Pd molar ratio of all catalysts. Therefore, a characterization by HAADF-STEM and EDX maps were conducted to investigate the geometry-activity relationship of AuPd nanoparticles on the surface of Au$_{0.13}$Pd$_{0.87}$/TiO$_2$, Au$_{0.5}$Pd$_{0.5}$ /TiO$_2$ and   Au$_{0.87}$Pd$_{0.13}$ /TiO$_2$. Figure 3.18 shows the representative HAADF-STEM images and corresponding EDX mappings of Au$_{0.13}$Pd$_{0.87}$ /TiO$_2$, Au$_{0.5}$Pd$_{0.5}$ /TiO$_2$ and   Au$_{0.87}$Pd$_{0.13}$ /TiO$_2$ nanoparticles. The results of HAADF-STEM and EDX maps indicate the presence of single Au and Pd NPs along with random AuPd alloys on the surface of all bimetallic catalysts. Moreover, the results show that Au$_{0.5}$Pd$_{0.5}$ /TiO$_2$ catalyst has rich population of AuPd alloy with ratio around 52% while in the case of Au$_{0.13}$Pd$_{0.87}$ /TiO$_2$ and Au$_{0.87}$Pd$_{0.13}$/TiO$_2$ catalysts were 25% 10%, respectively, which could explain the highest activity of this catalyst over other catalysts. Interface sites between Au NPs and Pd NPs were observed and distributed homogeneously of the catalyst surface. These sites are very important for the activity of bimetallic catalysts as described in literature.
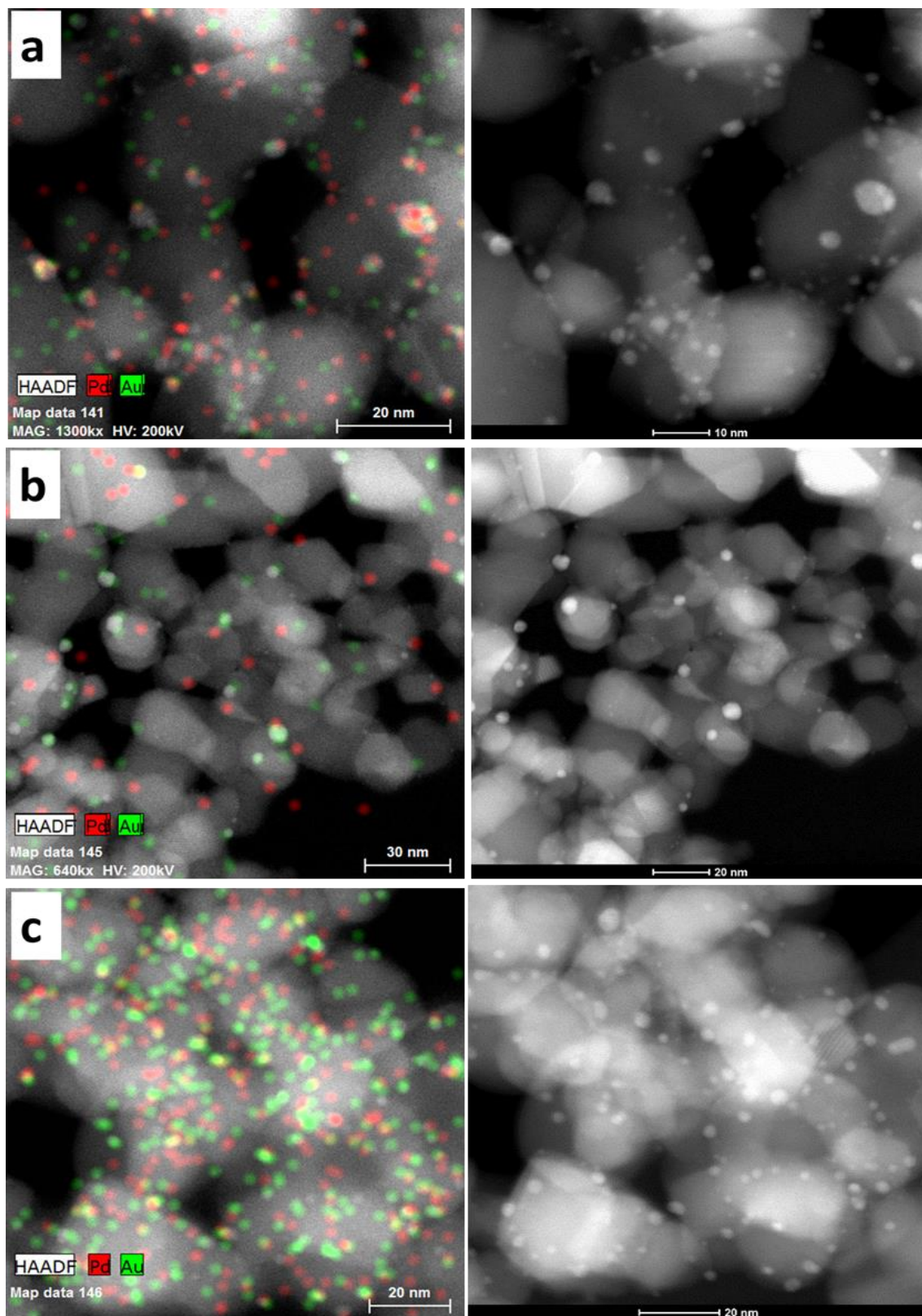
Figure 3.18 Representative HAADF-STEM images and corresponding EDX mappings of a) Au$_{0.13}$Pd$_{0.87}$/TiO$_2$, b) Au$_{0.87}$Pd$_{0.13}$/TiO$_2$ and c) Au$_{0.5}$Pd$_{0.5}$/TiO$_2$ catalysts.

3.5. Catalyst reusability

The reusability and stability are very important aspect of catalysts when considering its use in industry with good efficiency. Therefore, the reusability and stability of our catalyst was investigated in the reduction of 4-NP and used catalyst has been characterized by arrange of characterization techniques. To assess the reusability of Au$_{0.5}$Pd$_{0.5}$/TiO$_2$, the reduction of 4-NP reaction has been carried out for four times under standard conditions (i.e. T= 30 °C, stirring rate =1000 rpm) by performing the reaction in a 100 mL round bottom flask, using 45 mL of 4-NP solution (1.35×10^{-4} M). An excess NaBH$_4$ (5 ml, 3.6×10^{-2} M) and a larger amount of the catalyst in the initial experiments were added to initiate the reaction(4-NP /Metal molar ratio = 5). After 1 min, the reaction was stopped, and a sample was collected and analysed using a UV-Vis spectrophotometer. After completion of the reaction, the catalyst was separated from the solution. Before reuse the catalyst was washed with 10 mL of deionised water for 3 times. The UV-Vis spectra at 0 s was recorded using 2.7 mL and 0.3 mL of the same solutions of 4-NP and NaBH$_4$ respectively, without the presence of catalyst. The reaction was subsequently repeated for 4 times. Figure 3.19. illustrates the catalyst reusability for the Au$_{0.5}$Pd$_{0.5}$/TiO$_2$ catalyst. It is clear from this figure that the catalyst showed good stability after 4 runs, however, a slightly losing in the activity was observed and the conversion decreased from 80% to 75% at the fourth test.
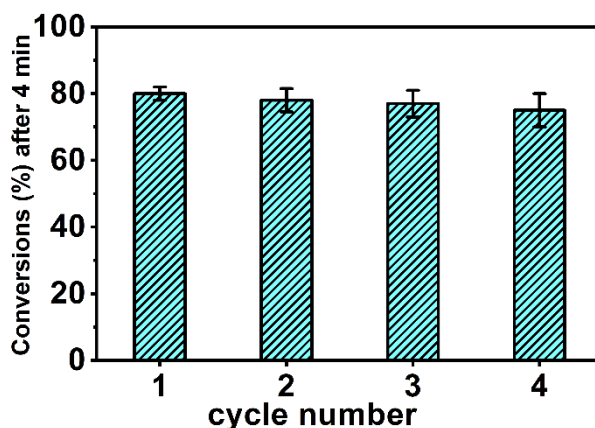
Figure 3.19 Reusability of the catalyst Au$_{0.5}$Pd$_{0.5}$/TiO$_2$ for the reduction of 4-NP using NaBH$_4$. Reaction conditions: 4-NP /metal molar ratio = 5, NaBH$_4$/4-NP molar ratio = 30, T = 30 ºC and stirring rate = 1000 rpm.

In addition, the leaching of active components into the reaction medium was investigated as follows: the reduction reaction was conducted for 1 min over Au$_{0.5}$Pd$_{0.5}$/TiO$_2$ at the normal reaction conditions. The catalyst was subsequently removed, and the liquid aliquot

was returned to the reactor. The reaction was run for an additional 10 min and no further reaction took place after removing the catalyst indicating that the reaction is catalysed by heterogeneous catalyst rather than homogenous. Furthermore, the leaching of Au and Pd nanoparticles in the reaction medium has been also examined using MP-AES, and no Au or Pd NPs was detected in the reaction medium after the reaction above the detection limit of MP-AES which is 1 to 2 ppb.

Additionally, TEM and XPS analysis were used to characterise used catalyst in order to investigate the particle size, agglomeration and also to analyse chemical composition and oxidation state of Au and Pd NPs. The TEM images of the used catalyst (Figure 3.20) show clearly that the AuPd nanoparticles still remain highly dispersed even after 4 cycles without agglomeration. However, the mean particle size for Au$_{0.5}$Pd$_{0.5}$/TiO$_2$ used catalyst indicate that there is a very small increase in mean particle size from 2.07 ± 0.61 to 2.2 ± 0.73 nm. Nevertheless, the average of AuPd particles diameter is still very small. Regarding XPS analyses for used catalyst, both metals (i.e. Au & Pd) are in metallic state and no significant changes in metal composition between the used and fresh catalysts (Table 3.10).
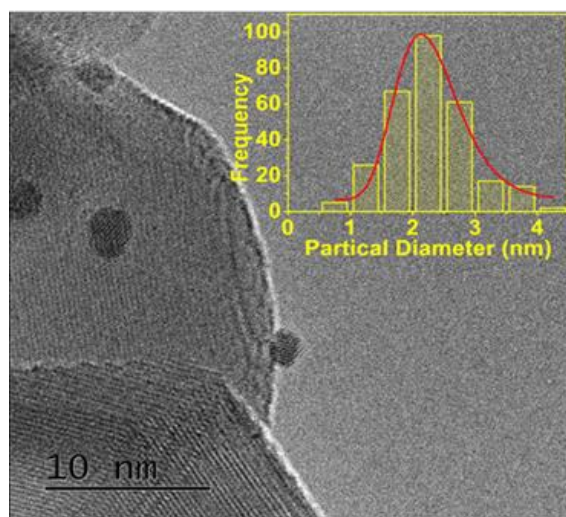
Figure 3.20 TEM image and particle size distribution(inset) of Au$_{0.5}$Pd$_{0.5}$/TiO$_2$ used catalyst.

Table 3.10 XPS quantification analysis on fresh and used Au$_{0.5}$Pd$_{0.5}$/TiO$_2$ catalyst.

Catalyst	Au:Pd ratio(mol/mol)
Au$_{0.5}$Pd$_{0.5}$/TiO$_2$ (fresh)	46: 54
Au$_{0.5}$Pd$_{0.5}$/TiO$_2$ (used)	53:47

3.6. Conclusions

Mono- and bimetallic Au and Pd nanoparticles supported on TiO$_2$ have been successfully synthesized using sol-immobilization method. For unsupported Au and Pd NPs, UV-Vis spectroscopy data confirmed the formation of mono and bimetallic nanoparticles. MP-AES results assessed the real metal loading of supported mono- and bimetallic catalysts (i.e. Au, Pd, and AuPd alloy NPs) and were ranged between 0.94 and 0.98 wt%, which is comparable to the nominal value (1 wt.%). The BET measurements of prepared catalysts showed no significant difference in surface area and porosity. No peaks related to Au and Pd NPs were detected by XRD due to their small particles size and high dispersion on the TiO$_2$. This observation is in line with TEM results where the mean particle size of all the supported mono and bimetallic Au$_x$Pd$_{1-x}$ nanoparticles were found to between (2.07±0.4) – (3.20±1.10) nm. Interestingly, the smallest AuPd NPs were found in the catalyst Au$_{0.5}$Pd$_{0.5}$/TiO$_2$ with exhibiting the narrowest particle size distribution. In addition, identification of AuPd Alloy NPs was determined using HAADF-EDX confirming that (1:1) ratio have the highest quantity of alloy particles. The catalytic activity of the synthesized catalysts was evaluated toward 4-NP reduction by NaBH$_4$ as model reaction. The reaction parameters have been optimized under kinetic regime control and found to be: 4-NP/metal molar ratio of 13, NaBH$_4$/4-NP molar ratio of 30, and 1000 rpm. At optimum parameters, the Pd/TiO$_2$ was found to be more active than the Au/TiO$_2$. Nevertheless, bimetallic catalysts Au$_x$Pd$_{1-x}$/TiO$_2$ show higher activity compared with their monometallic counterparts. These results suggest that a small amount of Pd added to Au is necessary to observe a synergistic catalytic effect when compared with the monometallic counterparts. All bimetallic catalysts were found to be catalytically active and the highest activity was obtained with the bimetallic catalyst with a (1:1) ratio of gold and palladium nanoparticles which might be due to the presence of small particle size, the synergetic effect between the Au and Pd NPs as well as alloying system. Finally, the best catalyst (Au$_{0.5}$Pd$_{0.5}$/TiO$_2$) was reused for four times with constant catalytical performance.

3.7. References

[1]   W. Shen, Y. Qu, X. Pei, S. Li, S. You, J. Wang, Z. Zhang and J. Zhou, J. Hazard. Mater., 2017, 321, 299–306.

[2]   M. Farrag and S. Ibrahim, J. Nano. Adv. Mat., 2017, 65, 57–65.

[3]   T. Ma, W. Yang, S. Liu, H. Zhang and F. Liang, Catalysts, 2017, 7, 38–48.

[4]   X. Zhao, Z. Li, Y. Deng, Z. Zhao, X. Li and Y. Xia, Materials (Basel)., 2017, 10, 557–568.

[5]   S. M. Ansar and C. L. Kitchens, ACS Catal., 2016, 6, 5553–5560.

[6]   A. Boehncke, G. Koennecker, I. Mangelsdorf and A. Wibbertmann, IPCS Concise Int. Chem. Assess. Doc., 1999, 1–37

[7]   B. Zhang, Y. Yuan, K. Philippot and N. Yan, Catal. Sci. Technol., 2015, 5, 1683–1692.

[8]   S. K. Ghosh, M. Mandal, S. Kundu, S. Nath and T. Pal, Appl. Catal. A Gen., 2004, 268, 61–66.

[9]   H. L. Jiang, T. Akita, T. Ishida, M. Haruta and Q. Xu, J. Am. Chem. Soc., 2011, 133, 1304–1306.

[10]   O. A. O'Connor and L. Y. Young, Environ. Toxicol. Chem., 1989, 8, 853–862.

[11]   N. Pradhan, A. Pal and T. Pal, Colloids Surfaces A, 2002, 196, 247–257.

[12]   T. Aditya, A. Pal and T. Pal, Chem. Commun., 2015, 51, 9410–9431.

[13]   S. Rogers, R. Catlow, D. Gianolio, P. Wells and N. Dimitratos, Faraday Discuss., 2018,208, 443-454.

[14]   C. Wang, F. Yang, W. Yang, L. Ren, Y. Zhang, X. Jia, L. Zhang and Y. Li, RSC Adv., 2015, 5, 27526–27532.

[15]   T. Ma, F. Liang, R. Chen, S. Liu and H. Zhang, Nanomaterials, 2017, 7, 239–348.

[16]   H. P. Karki, D. P. Ojha, M. K. Joshi and H. J. Kim, Appl. Surf. Sci., 2018, 435, 599–608.

[17]   S. Saha, A. Pal, S. Kundu, S. Basu and T. Pal, Langmuir, 2010, 26, 2885–2893.

[18]   C. Lin, K. Tao, D. Hua, Z. Ma and S. Zhou, Molecules, 2013, 18, 12609–12620.

[19]   M. Panchal, A. Kongor, V. Mehta, M. Vora, K. Bhatt and V. Jain, J. Saudi Chem. Soc., 2018, 22, 558-568

[20]   S. Panigrahi, S. Basu, S. Praharaj, S. Pande, S. Jana, A. Pal, S. K. Ghosh and T. Pal, J. Phys. Chem. C, 2007, 111, 4596–4605.

[21]   J. Noh and R. Meijboom, Appl. Nanotechnol. Water Res., 2014, 333–406.

[22]   A. A. Ismail, A. Hakki and D. W. Bahnemann, J. Mol. Catal. A Chem., 2012, 358, 145–151.

[23]   S. Aswathy Aromal, K. V. Dinesh Babu and D. Philip, Spectrochim. Acta - Part A Mol. Biomol. Spectrosc., 2012, 96, 1025–1030.

[24]   B. Li, Y. Hao, X. Shao, H. Tang, T. Wang, J. Zhu and S. Yan, J. Catal., 2015, 329, 368–378.

[25]   J. Schwank, Gold Bull., 1985, 18, 2–10.

[26]   V. K. Gupta, N. Atar, M. L. Yola, Z. Üstündağ and L. Uzun, Water Res., 2014, 48, 210–217.

[27]   Z. Zhang, J. Zhang, G. Liu, M. Xue, Z. Wang, X. Bu, Q. Wu and X. Zhao, Korean J. Chem. Eng., 2017, 34, 2471–2479.

[28]   S. Cattaneo, S. J. Freakley, D. J. Morgan, M. Sankar, N. Dimitratos and G. J. Hutchings, Catal. Sci. Technol., 2018, 1677–1685.

[29]   R. Cai, P. R. Ellis, J. Yin, J. Liu, C. M. Brown, R. Griffin, G. Chang, D. Yang, J. Ren, K. Cooke, P. T. Bishop, W. Theis and R. E. Palmer, Small, 2018, 1703734, 1–10.

[30]   N. Arora, A. Mehta, A. Mishra and S. Basu, Appl. Clay Sci., 2018, 151, 1–9.

[31]   Y. Du, N. Cao, L. Yang, W. Luo and G. Cheng, New J. Chem., 2013, 37, 3035–3042.

[32]   T. Wu, J. Ma, X. Wang, Y. Liu, H. Xu, J. Gao, W. Wang, Y. Liu and J. Yan, Nanotechnology, 2013, 24 (12), 125301–125310.

[33]   S. Zhang, Y. Shao, H. G. Liao, J. Liu, I. A. Aksay, G. Yin and Y. Lin, Chem. Mater., 2011, 23, 1079–1081.

[34]   W. Yao, F.-L. Li, H.-X. Li and J.-P. Lang, J. Mater. Chem. A, 2015, 3, 4578–4585.

[35]   Z. D. Pozun, S. E. Rodenbusch, E. Keller, K. Tran, W. Tang, K. J. Stevenson and G. Henkelman, J. Phys. Chem. C, 2013, 117, 7598–7604.

[36]   E. Cao, G. Brett, P. J. Miedziak, J. M. Douthwaite, S. Barrass, P. F. McMillan, G. J. Hutchings and A. Gavriilidis, Catal. Today, 2017, 283, 195–201.

[37]   H.-L. Jiang and Q. Xu, J. Mater. Chem., 2011, 21, 13705–13725.

[38]   S. A. Lewis, J. P. Wilburn, M. S. Wellons, D. E. Cliffel and C. M. Lukehart, Phys. Status Solidi Appl. Mater. Sci., 2015, 212, 2903–2909.

[39]   H. M. Song, D. H. Anjum, R. Sougrat, M. N. Hedhili and N. M. Khashab, J. Mater. Chem., 2012, 22, 25003–25010.

[40]   J. H. Carter, S. Althahban, E. Nowicka, S. J. Freakley, D. J. Morgan, P. M. Shah, S. Golunski, C. J. Kiely and G. J. Hutchings, ACS Catal., 2016, 6, 6623–6633.

[41]   W. Fang, Y. Deng, L. Tang, G. Zeng, Y. Zhou and X. Xie, J. Colloid Interface Sci., 2017, 490, 834–843.

[42]   M. Blosi, S. Ortelli, A. Costa, M. Dondi, A. Lolli, S. Andreoli, P. Benito and S. Albonetti, Materials (Basel)., 2016, 9, 550–575.

[43]   N. Bingwa, R. Patala, J. H. Noh, M. J. Ndolomingo, S. Tetyana, S. Bewana and R. Meijboom, Langmuir, 2017, 33, 7086–7095.

[44]   W. Yao, F.-L. Li, H. Li and J. Lang, J. Mater. Chem. A, 2015, 3, 4578–4585.

[45]   X. Chen, Z. Cai, X. Chen and M. Oyama, J. Mater. Chem. A, 2014, 2, 5668–5674.

[46]   L. Srisombat, J. Nonkumwong, K. Suwannarat, B. Kuntalue and S. Ananta, Colloids Surfaces A Physicochem. Eng. Asp., 2017, 512, 17–25.

[47]   J. Sun, Y. Fu, G. He, X. Sun and X. Wang, Catal. Sci. Technol., 2014, 4, 1742–1748.

[48] C. L. Bianchi, P. Canton, N. Dimitratos, F. Porta and L. Prati, Catal. Today, 2005, 102, 203–212.

[49] W. Haiss, N. T. K. Thanh, J. Aveyard and D. G. Fernig, Anal. Chem., 2007, 79, 4215–4221.

[50] S. M. Rogers, C. R. A. Catlow, C. E. Chan-Thaw, D. Gianolio, E. K. Gibson, A. L. Gould, N. Jian, A. J. Logsdail, R. E. Palmer, L. Prati, N. Dimitratos, A. Villa and P. P. Wells, ACS Catal., 2015, 5, 4377–4384.

[51] Jiang, L.; Xu, Q. The Journal of Physical Chemistry A, 2005, 109 (6), 1026–1032.

[52] G. J. Lopez-Sanchez, J A. Dimitratos, N. Miedziak, P. Ntainjua, E. Edwards, J K. Morgan, D. Carley, A. F.Tiruvalam, R. Kiely, C J. Hutchings, Phys. Chem. Chem. Phys., 2008, 10, 1921–1930.

[53] J. Feng, C. Ma, P. J. Miedziak, J. K. Edwards, G. L. Brett, D. Li, Y. Du, D. J. Morgan and G. J. Hutchings, Dalt. Trans., 2013, 42, 14498–14508.

[54] J. Chang, C. Liu, J. Liu, Y. Zhou, X. Gao and S. Wang, Nano-Micro Lett., 2015, 7, 307–315.

[55] S. Deki, K. Akamatsu, Y. Hatakenaka, M. Mizuhata and A. Kajinami, Nanostructured Mater., 1999, 11, 59–65.

[56] A. Villa, D. Wang, G. M. Veith, F. Vindigni and L. Prati, Catal. Sci. Technol., 2013, 3, 3036–3041.

[57] S. Wang, M. Zhang and W. Zhang, ACS Catal., 2011, 1, 207–211.

[58] H. Khojasteh, M. Salavati-Niasari, A. Abbasi, F. Azizi and M. Enhessari, J. Mater. Sci. Mater. Electron., 2016, 27, 1261–1269.

[59] R. Su, R. Tiruvalam, Q. He, N. Dimitratos, L. Kesavan, C. Hammond, J. A. Lopez-Sanchez, R. Bechstein, C. J. Kiely, G. J. Hutchings and F. Besenbacher, ACS Nano, 2012, 6, 6284–6292.

[60] R. Liang, RSC Adv., 2014, 4, 36959–36966.

[61] G. J. Hutchings, Catal. Today, 2005, 100, 55–61.

[62] C. Samanta, Appl. Catal. A Gen., 2008, 350, 133–149.

[63] S. F. Kou, W. Ye, X. Guo, X. F. Xu, H. Y. Sun and J. Yang, RSC Adv., 2016, 6, 39144–39149.

[64] P. N. Amaniampong, K. Li, X. Jia, B. Wang, A. Borgna and Y. Yang, ChemCatChem, 2014, 6, 2105–2114.

[65] C. Jia, P. Yang, J. Li, B. Huang and K. Matras-Postolek, ChemCatChem, 2016, 8, 839–847.

[66] N. Dimitratos, J. A. Lopez-Sanchez, J. M. Anthonykutty, G. Brett, A. F. Carley, R. C. Tiruvalam, A. A. Herzing, C. J. Kiely, D. W. Knight and G. J. Hutchings, Phys. Chem. Chem. Phys., 2009, 11, 4952–4961.

[67] J. Pritchard, L. Kesavan, M. Piccinini, Q. He, R. Tiruvalam, N. Dimitratos, J. A. Lopez-Sanchez, A. F. Carley, J. K. Edwards, C. J. Kiely and G. J. Hutchings, Langmuir, 2010, 26, 16568–16577.

[68] P. Konova, A. Naydenov, C. Venkov, D. Mehandjiev, D. Andreeva and T. Tabakova, J. Mol. Catal. A Chem., 2004, 213, 235–240.

[69] F. W. Chang, H. Y. Yu, L. S. Roselin, H. C. Yang and T. C. Ou, Appl. Catal. A Gen., 2006, 302, 157–167.

[70] J. H. Yang, J. D. Henao, M. C. Raphulu, Y. Wang, T. Caputo, A. J. Groszek, M. C. Kung, M. S. Scurrell, J. T. Miller and H. H. Kung, J. Phys. Chem. B, 2005, 109, 10319–10326.

[71] J. Radnik, C. Mohr and P. Claus, Phys. Chem. Chem. Phys., 2003, 5, 172–177.

[72] S. Arrii, F. Morfin, A. J. Renouprez and J. L. Rousset, J. Am. Chem. Soc., 2004, 126, 1199–1205.

[73] E. Desimoni and B. Brunetti, Chemosensors, 2015, 3, 70–117.

[74] M. Brun, A. Berthet and J. . Bertolini, J. Electron Spectros. Relat. Phenomena, 1999, 104, 55–60.

[75] R. Liu, Y. Yu, K. Yoshida, G. Li, H. Jiang, M. Zhang, F. Zhao, S. ichiro Fujita and M. Arai, J. Catal., 2010, 269, 191–200.

[76] P. A. P. Nascente, S. G. C. Castro de, R. Landers and G. G. Kleiman, Phys. Rev. B, 1990, 43, 4659–4666.

[77] A. G. M. da Silva, T. S. Rodrigues, L. S. K. Taguchi, H. V. Fajardo, R. Balzer, L. F. D. Probst and P. H. C. Camargo, J. Mater. Sci., 2015, 51, 603–614.

[78] J. Huang, S. Vongehr, S. Tang, H. Lu and X. Meng, J. Phys. Chem. C, 2010, 114, 15005–15010.

[79] Q. Zhang, J. Y. Lee, J. Yang, C. Boothroyd and J. Zhang, Nanotechnology, 2007, 18(24), 245605–245613.

[80] M. Li and G. Chen, Nanoscale, 2013, 5, 11919–11927.

[81] M. Bordbar, RSC Adv., 2017, 7, 180–189.

[82] Y. Mei, G. Sharma, Y. Lu, M. Ballauff, M. Drechsler, T. Irrgang and R. Kempe, Langmuir, 2005, 21, 12229–12234.

[83] Y. Mei, Y. Lu, F. Polzer, M. Ballauff and M. Drechsler, Chem. Mater., 2007, 19, 1062–1069.

[84] K. Hayakawa, T. Yoshimura and K. Esumi, Langmuir, 2003, 19, 5517–5521.

[85] R. Rajesh and R. Venkatesan, Journal Mol. Catal. A, Chem., 2012, 359, 88–96.

[86] B. Liu, Q. Wang, S. Yu, P. Jing, L. Liu, G. Xu and J. Zhang, Nanoscale, 2014, 6, 11887–11897.

[87] A. Fedorczyk, J. Ratajczak, O. Kuzmych and M. Skompska, J. Solid State Electrochem., 2015, 19, 2849–2858.

[88] S. Wunder, F. Polzer, Y. Lu, Y. Mei and M. Ballauff, J. Phys. Chem. 2010, 114, 8814–8820.

[89] F. Muench, M. Rauber, C. Stegmann, S. Lauterbach, U. Kunz, H. J. Kleebe, Catalysts 2017, 7, 38-47.

[90] P. Zhao, X. Feng, D. Huang, G. Yang and D. Astruc, Coord. Chem. Rev., 2015, 287, 114–136.

[91] M. Goepel, H. Kabir, C. Küster, E. Saraçi, P. Zeigermann, R. Valiullin, C. Chmelik, D. Enke, J. Kärger and R. Gläser, Catal. Sci. Technol., 2015, 5, 3137–

3146.

[92]   K. Kusada, H. Kobayashi, R. Ikeda, Y. Kubota, M. Takata, S. Toh, T. Yamamoto, S. Matsumura, N. Sumi, K. Sato, K. Nagaoka and H. Kitagawa, J. Am. Chem. Soc., 2014, 136, 1864–1871.

[93]   R. Liu, H. M. Chen, L. P. Fang, C. Xu, Z. He, Y. Lai, H. Zhao, D. Bekana and J. F. Liu, Environ. Sci. Technol., 2018, 52, 4244–4255.

Chapter 4

Catalytic activity of supported AuPd nanoparticles for the reduction of 4-nitrophenol by NaBH$_4$: Effect of support

4.1. Introduction

One important factor defining a catalyst is its ability to operate a given reaction, without itself altering its chemical/electronic structure, which may lead to catalyst's deactivation. Immobilisation of metal active components onto a support has the advantages to enhance catalyst's durability and stability under operating conditions. Moreover, it provides a strong metal-support interaction (SMSI) which minimize metal leaching and the extended growth of dispersed active sites [1]. In addition, supports are used to reduce the mobility of the metal nanoparticles and thus diminishing their tendency to agglomerate during the reaction. another role of the support that has been addressed in some cases is the possibility that the support acts actively in the reaction mechanism by redox cycling of the support metal ions [2]. Supports such as MnO_2 and CeO_2 and others that have a metal with two stable redox states, such as Fe_2O_3, could be representative examples. In this case the cooperation of the support with gold catalysis would arise from stabilization of positive gold species and by intervening in the reaction mechanism. SMSI between gold nanoparticles and the support in the catalytic cycle has been claimed frequently to rationalize the variations of catalytic activity of gold nanoparticles on different supports. For instance, for CO oxidation it has been reported that amorphous silica is an inadequate support for gold nanoparticles making them less active catalyst compared to other metal oxides.

In general, the high thermal and chemical stabilities, as well as high surface areas that porous metal oxides have, making them suitable candidates for many applications [3]. In addition, metal oxides are abundant, easy to prepare, inexpensive and could be used as acid-base or redox active sites to catalyse different types of reactions [19]. The most frequently used porous support for noble metal nanoparticles is mesoporous SiO_2 [6]. In addition, other oxides, such as TiO_2, Al_2O_3, ZnO, MgO, Co_3O_4, and mesoporous zeolite materials have been reported as supports for noble metal nanoparticles [7–10]. CuO and NiO, as active oxides, were used as active components for the hydrogenation of 4-nitrophenol using $NaBH_4$ and showed remarkable performance [11]. The activity of CuO and NiO in such reactions are assigned to the facile switch of Cu^{II}/Cu or Ni^{II}/Ni couples making them could catalysts in redox reactions [11]. Similarly, they were used as supports for monometallic nanoparticles [12,13]. However, to best our knowledge, there are no reports of bimetallic (AuPd) nanoparticles supported onto CuO and NiO for the reduction of 4-nitrophenol to 4-aminophenol. In addition, such bimetallic system, as found

previously in Chapter 3, showed a remarkable activity towards the reduction of 4-NP with the aid of NaBH$_4$, as a reducing agent. We believe that such activity could be enhanced by providing strong-metal support interactions between Au and/or Pd and the given support in addition to the synergistic effect between both metals (Au and Pd) . Therefore, we report here a comparison of AuPd bimetallic supported nanoparticles using, not only different types of support, but also using same support with different morphology.

4.2. Experimental

4.2.1. Catalyst preparation

In this Chapter, monometallic Au and Pd, and bimetallic (AuPd) supported on copper and nickel-based oxides were prepared using sol-immobilisation method as described in Chapter 2 (Section 2.3.2). All theoretical loadings of monometallic (Au & Pd) and bimetallic (AuPd) in this Chapter are 1 wt.%. For bimetallic system, the molar ratio of Au/Pd was kept constant at value of 1 (as it was found in Chapter 3 to be the optimal molar ratio between Au and Pd for the aqueous reduction of nitrophenol by NaBH$_4$ (reducing agent). All catalysts in this Chapter are prepared using PVA (stabilising agent), except for the commercial nickel oxide (NiO), as previous studies showed no deposition of targeted nanoparticles when PVA was used as a stabiliser.

The treated nickel oxide (NiO$_s$) was prepared by treating the commercial NiO$_c$ using urea aqueous solution, similar to the preparation method reported elsewhere [14]. Typically, experimental detail for this treatment is described in Chapter 2 (Section 2.3.3). All supports and catalysts with their metal loadings and sample notation, that will be discussed in the Chapter, are summarized and presented in Table 4.1.

Table 4.1 Supports, metal loading and the sample notation for all catalysts.

Support	Metal	Metal loading (wt%)		Sample notation
		theoretical	exp.[a]	
NiO$_c$ (commercial)	Au	1	0.96	Au/NiO$_c$
	Pd	1	0.93	Pd/NiO$_c$
	AuPd*	1	0.95	AuPd/NiO$_c$
NiO$_s$ (Synthesized)	Au	1	0.99	Au/NiO$_s$
	Pd	1	0.97	Pd/NiO$_s$
	AuPd*	1	0.98	AuPd/NiO$_s$
CuO	Au	1	0.98	Au/CuO
	Pd	1	0.99	Pd/CuO
	AuPd*	1	0.97	AuPd/CuO

(i) [a] Results (exp. wt.%) are obtained from the MP-AES analysis.
(ii) * All bimetallic AuPd catalysts have Au/Pd molar ratio = 1.
(iii) Each result is average of three readings.
(iv) %RSD for all results is ± 0.8.

4.2.2. Catalyst characterisation

Due to the heterogeneity of the catalyst's matrices, a complementary of different techniques have been employed to unravel their chemical and electronic structures such as; powder X-ray diffraction (XRD), X-ray photoelectron spectroscopy (XPS), transmission electron microscopy (TEM), Surface area measurements (BET), Thermogravimetric analysis (TGA) and Microwave Plasma Atomic Emission Spectroscopy (MP-AES). For experimental details for each technique, please see Chapter 2.

4.2.3. Catalytic reactions

The catalytic performance and efficiency optimization of the synthesized catalysts was carried out in the reduction of 4-nitrophenol using NaBH$_4$ as the reducing agent. The reaction was performed under the typical reaction conditions in Chapter 3 (previously optimised and showed that reaction is taken place in chemical kinetic regime). Typically, the reaction was performed in 100 ml round bottom flask at temperature of 30 °C and stirring rate of 1000 rpm. The amount of catalyst was suspended in 45 ml of aqueous solution of 4-NP(4-NP/metal molar ratio = 13). To start the reaction, 5 ml of NaBH$_4$ (NaBH$_4$/4-NP molar ratio = 30) was added to the reaction mixture. The total volume of the reaction mixture was 50 ml. At different time interval (min), aliquot from the

reaction mixture was then withdrawn using 1 ml syringe equipped with a filter (0.45 µm pore size) and transferred into the UV cuvette for a UV-Vis measurement. Subsequently, the UV-Vis spectra (in the range of 200 – 800 nm) were recorded and the concentration of 4-NP traced from the decay of the absorption band centred at 400 nm. Based on the calibration curve of standard solution of 4-NP, which previously described in Chapter 2, the molar extinction coefficient was estimated for 4-NP to be 18620 M^{-1} cm^{-1}. Finally, the concentration of 4-NP, as a function of time during the catalytic reaction, was calculated using the Beer's Lambert's law equation as discussed in Chapters 2 and 3.

4.3. Results and discussions

4.3.1. XRD patterns

4.3.1.1. NiO based materials

X-ray diffraction (XRD) analysis is conducted here to elucidate the stabilized phases of bare NiO supports (as synthesised & commercial) as well as phases of supported Au and Pd components of the prepared catalysts. Figure 4.1 shows the XRD of the commercial (NiO_c, left) and as-synthesised (NiO_s, right) based materials, as indicated. Generally, the intensity of XRD diffraction patterns observed for NiO_s materials are lower than those observed for NiO_c. This suggests that NiO_s having lower particle size (5.4 nm) than NiO_c (43 nm) as calculated by Scherrer equation at $2\theta = 43.2°$ (as shown in Table 4.2). For both NiO_c and NiO_s supports, there are diffraction peaks attributable to NiO with face-centered cubic phase at 37.4°, 43.2°, 62.6° and 75.5° of 2θ, which can be assigned to (111), (200), (220) and (311) planes, respectively. The results suggest the successful preparation of NiO pure bulk phase which are in agreements with the reported literature and match well with the standard XRD pattern for NiO bulk phase (JCPDS No. 04-0835)[15].

The XRD diffraction peaks, if there is any, for metallic Au phase would be expected to appear at 38.3°, 44.3°, 64.7° and 76.8° of 2θ, which are correspond to the Au (111), (200), (220) and (311) planes, respectively, see vertical solid lines in Figure 4.1 (JCPDS No. 04-0784) [16]. Also, the diffraction peaks of metallic Pd phase, if there is any, are expected to emerge at 40.4°, 46.9° and 68.6° of 2θ, which corresponding to the Pd (111), (200) and (220) phases, respectively, see vertical dashed lines in Figure 4.1 (JCPDS No. 01-087-0645) [17]. Investigation in Figure 4.1, we can observe that there is no any diffraction peak for both metallic Au or Pd phases. Thus, the XRD results suggest the confinement
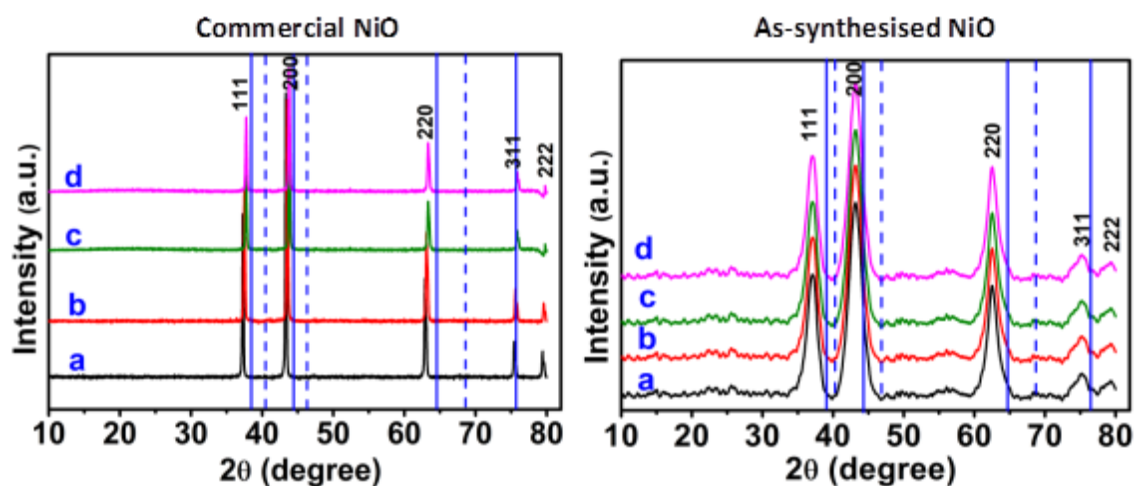
Figure 4.1 XRD patterns of a) bare NiO, b) Au/NiO, c) Pd/NiO and d) AuPd/NiO catalysts for commercial and as-synthesised NiO supports, as indicated.

and distribution of Au and Pd phases, in all catalysts, in a nanosized form which could not be detected using XRD analysis and will be confirmed and discussed later using TEM results. Such observation is also in agreement with reported data [18,19].

Table 4.2 The crystallite size of bare NiO supports calculated by Scherrer's equation.

Support	Crystallite size [nm]
NiO_c	43
NiO_s	5

4.3.1.2. CuO based materials

The crystal structures of bare CuO and supported metal nanoparticles of Au and Pd (i.e. Au/CuO, Pd/CuO and AuPd/CuO) were investigated by XRD and results are shown in Figure 4.2. The diffraction peaks at 2θ of 32.4°, 35.5°, 38.8°, 48.7°, 53.1°, 58.3, ,61.5°, 66.2°,68.1°,72.6°, and 75.2° can be contributed to the reflections of CuO (110), (-111), (200), (-202), (020), (202), (-113), (-311), (220), (311) and (-222), respectively . All the diffraction peaks are matched well with CuO bulk phase (JCPDS No. 48-1548) [8]. No diffraction peaks could be detected for other forms of copper oxides (such as; $Cu(OH)_2$ and Cu_2O) suggesting the high purity and crystallinity of stabilized CuO phase with crystallite size of ~ 14 nm, as estimated Scherrer's equation.

As described previously, the position of diffraction peaks for metallic Au phase should appear at 2θ = 38.3°, 44.3°, 64.7° and 76.8° (solid lines in Figure 4.2), while for metallic Pd phase should appear at 2θ = 40.4°, 46.9° and 68.6° (dashed lines in Figure 4.2). However, the XRD diffraction patterns of Au/CuO, Pd/CuO and AuPd/CuO catalysts are very similar to that observed for bare CuO support and there is no any reflections for

neither metallic Au nor Pd phases, which suggests their distribution and confinement as very small nanoparticles and the incorporation of these metals didn't alter the structure of CuO support or affect its crystallinity.
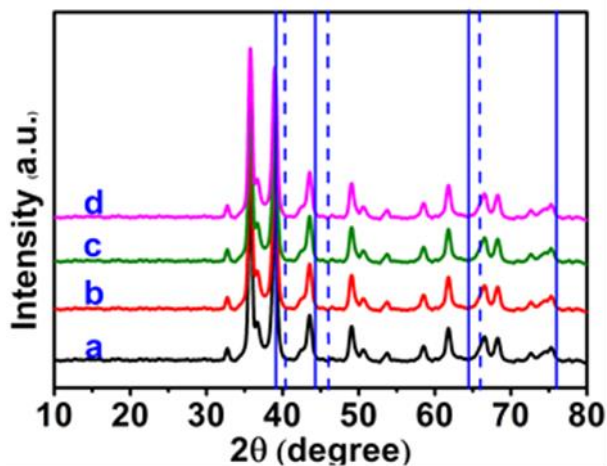
Figure 4.2 XRD patterns for a) bare CuO, b) Au/CuO, c) Pd/CuO and d) AuPd/CuO catalysts.

4.3.2. XPS analysis

Further to elucidating the elements speciation, analysis of surface and chemical composition was probed using XPS technique.

4.3.2.1. NiO based materials

Ni(2p) core level spectra

The XPS core level spectra of Ni(2p) region for synthesised and commercial NiO supports are shown in Figure 4.3. XPS data for both supports revealed the presence of Ni^{2+}-O species at 853.96 eV, with a second peak centred at 855.4 eV, which could be assigned
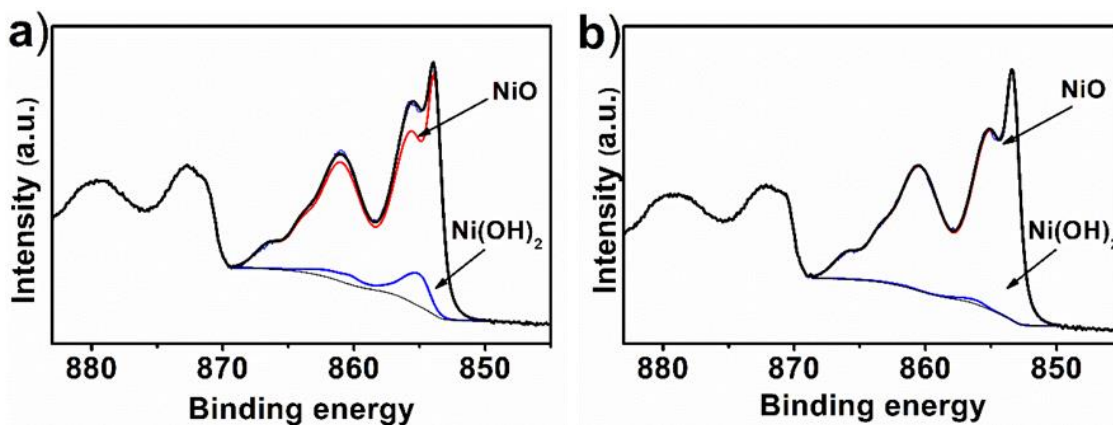
Figure 4.3 Ni(2p) region XPS core level spectra of bare a) NiO_s and b) NiO_c supports.

to the presence of Ni^{2+}-OH species [20,21]. In addition, no peak was detected at binding energy of 852.6 eV suggesting the absence of metallic nickel (Ni^0) phase at the surface for all catalysts. The analysis reveals that the surface of the NiO_s support is composed of significantly higher amount of $Ni(OH)_2$ compared to the NiO_c support. The ratio between the $Ni(OH)_2$ and NiO in both supports was calculated using XPS software and the data are summarised in Table 4.3.

Table 4.3 The ratio between $Ni(OH)_2$ and NiO species in the NiO_c and NiO_s

Catalyst	NiO %	$Ni(OH)_2$ %
NiO_c	99.8	0.2
NiO_s	92	8

Au(4f) core level spectra

The XPS core level spectra of Au(4*f)* for monometallic Au catalysts (Au/NiO$_{(s,c)}$) show that Au4f$_{7/2}$ peak in the range of 84.1–83.9 eV. This suggests the predominant of metallic Au nanoparticles in these catalysts[14]., as shown in Figure 4.4. The Au4f spectrum of
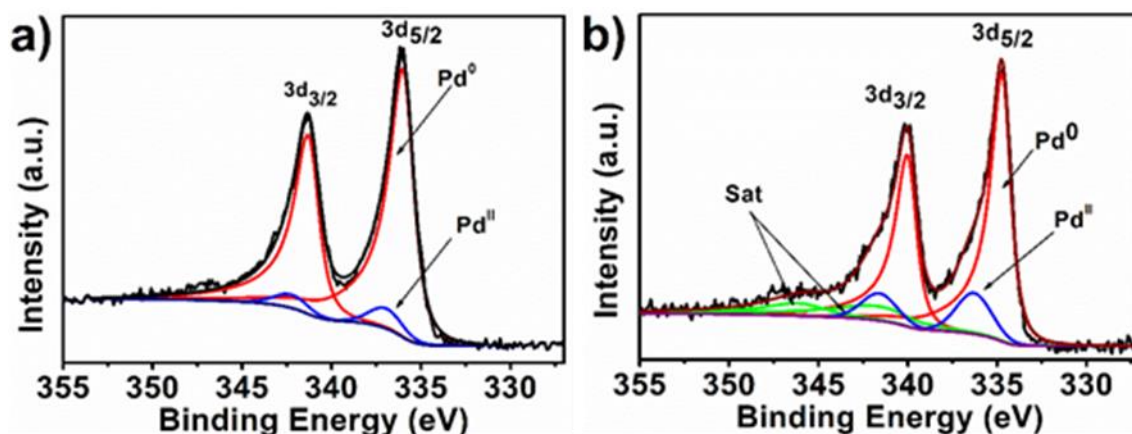
Figure 4.5 Pd(3d) core level spectra for; a) Pd/NiO$_c$ and b) Pd/NiO$_s$ catalysts.
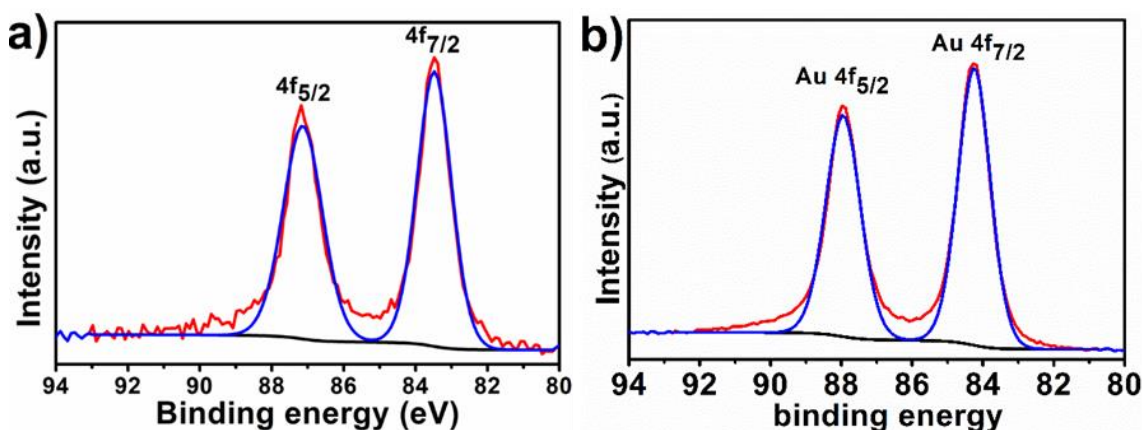
Figure 4.4 Au(4f) core level spectra for; a) Au/NiO$_c$ and b) Au/NiO$_s$ catalysts.

Au/NiO$_{(s,c)}$ catalysts could be deconvoluted into two peaks centred at 83.7 eV and 86.4 eV, which are assigned to Au4f$_{7/2}$ and Au4f$_{5/2}$, respectively [14].

Pd(3d) core level spectra

For the monometallic Pd/NiO$_{(s,c)}$ catalysts, the XPS core level spectra of Pd(3d) suggest the confinement of Pd nanoparticles, on the catalyst's surface, in a metallic (Pd^0) and oxidic (Pd^{II}) states along with Ni^{2+}-O species as shown in Figure 4.5. As seen in spectrum of Pd/NiO$_{(s,c)}$, the XPS spectra of Pd (3d) of Pd/NiO$_{(s,c)}$ can be fitted into four peaks located at 335.2, 336.99, 340.46 eV and 342.29 eV. The two peaks located at 335.2 and 340.46 eV are assigned to the main peaks of Pd 3d$_{5/2}$ and Pd 3d$_{3/2}$ doublet of metallic Pd [3], while the other two peaks maximized at 336.99 and 342.29 eV correspond to Pd^{II} as PdO [4,5].

Similarly, bimetallic AuPd/NiO$_c$ catalysts were examined by XPS and the results shown in Figure 4.6. XPS Data indicate that both Au and Pd nanoparticles in all bimetallic catalysts supported on NiO are in the metallic state (Au^0) and (Pd^0). The presence of Au in metallic state in the bimetallic samples was confirmed by two peaks centred at binding energies of 83.7 eV and 86.4 eV, which corresponding to Au 4f$_{7/2}$ and Au 4f$_{5/2}$, respectively, while the presence of Pd metal was confirmed by two peaks centred at binding energies 335.2 eV and 340.46 eV, which are assigned to Pd^0 3d$_{5/2}$, and Pd^0 3d$_{3/2}$ respectively.
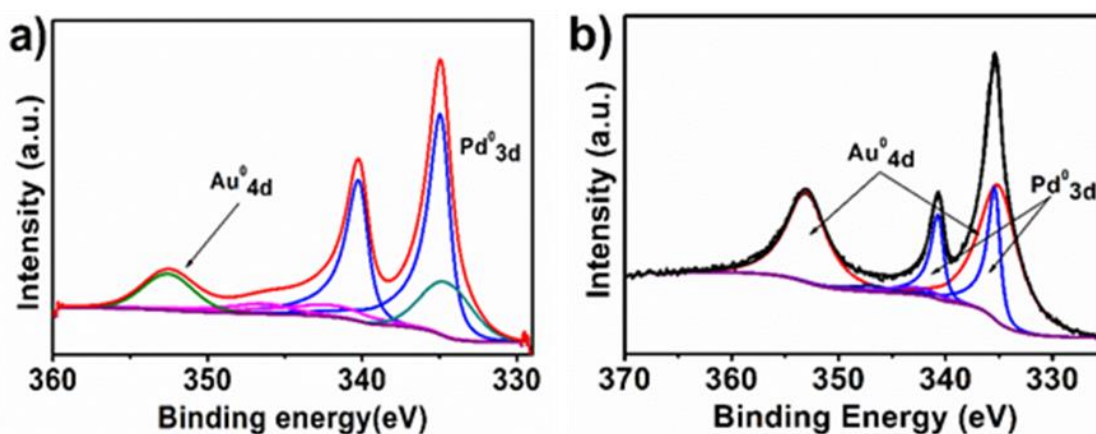
Figure 4.6 Au(4f) core level spectra for; (a) AuPd/NiO$_c$ and (b) AuPd/NiO$_s$ catalysts.

4.3.2.2. CuO based materials

Further to elucidate the role of CuO as a catalyst support, XPS is conducted here, in this Section, to understand the surface chemical composition and oxidation state of Cu species at the metal-support interface. Figure 4.7 presents the Cu(2p) XPS core level spectrum of

bare CuO support. The Cu(2p$_{3/2}$) and Cu(2p$_{1/2}$) peaks centered at 934.2 and 954.1 eV (with theoretical splitting value of 19.9 eV), respectively, confirms the stabilization of copper in the(+2) chemical state in the form of CuO and/or Cu(OH)$_2$. However, XRD data confirmed the absence of Cu(OH)$_2$. The shake-up satellite peaks of the Cu(2p$_{3/2}$) and Cu(2p$_{1/2}$) at 942.4 and 962.6 eV, respectively confirmed the presence of Cu^{II} as CuO on the surface. The peak deconvolution also showed that neither Cu^{I} nor Cu^{0} exist on the surface of the samples due to the absence of their characteristic peak at binding energy of 933 eV [22,23].
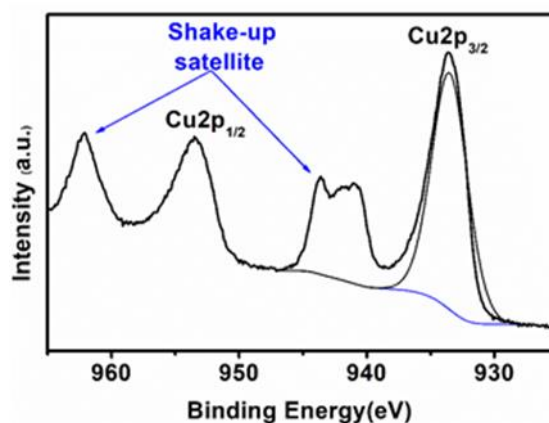
Figure 4.7 Cu(2p) core level spectra of bare CuO support.

Figure 4.8(a) presents the XPS of Au/CuO catalyst. The spectrum can be identified by the two peaks characteristic for Au(4f) transition which centred at binding energies of 84.1eV and 87.8 eV and could be assigned to Au 4f$_{7/2}$ and Au 4f$_{5/2,}$ respectively [24]. The results suggest the confinement of Au nanoparticles in metallic state only in this catalyst. In addition, and to gain a complete picture of the element speciation from Pd side, the Pd(3d) core level spectra of Pd/CuO catalyst have been recorded and presented in Figure 4.8(b).
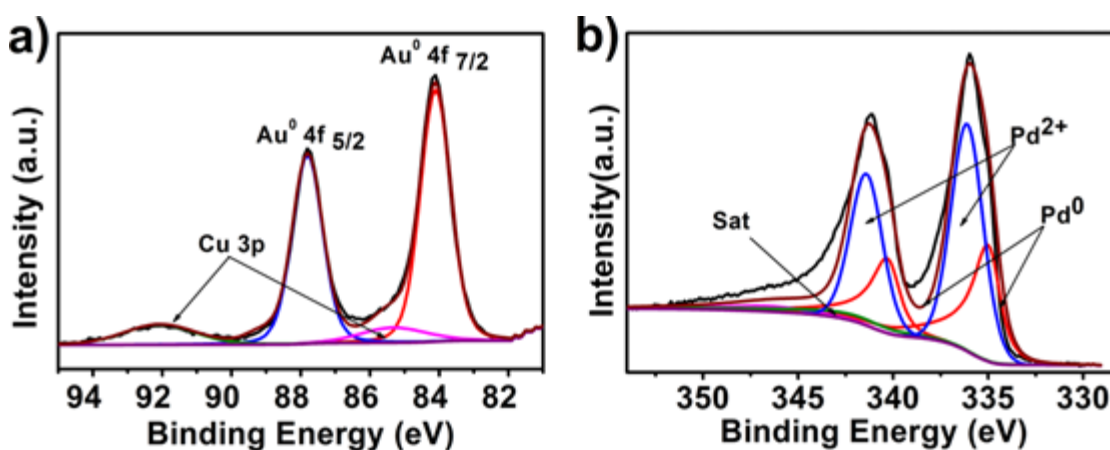
Figure 4.8 Au(4f) core level spectra for; a) Au/CuO and b) Pd/CuO catalysts.

The results show that Pd is stabilized into two forms; metallic (as Pd^0) and oxidic (as Pd^{II}) forms. The Pd^0 state is confirmed by two peaks centred at 335 and 340.26 eV, while Pd^{II} state is indicated by the presence of two peaks at 336.1 and 341.41 eV, respectively, which are corresponding to $3d_{5/2}$, and $3d_{3/2}$ doublet transitions, respectively [25].

For bimetallic AuPd/CuO catalyst, the Au(4f) core level spectra is very similar to the spectra obtained for monometallic Au/CuO catalyst with only metallic Au as a predominant phase (see Figure 4.9) [25]. In contrast, the spectra obtained for Pd(3d) transitions in bimetallic AuPd/CuO catalyst is very interesting. Although, both metallic and oxidic forms of Pd are co-exist, which is similar to monometallic, the ratio between these two forms are very different. We can observe clearly from these results that metallic form of Pd is increased in the bimetallic catalyst compared to monometallic analogous (Pd^0/Pd^{II} ratio is 0.75 for monometallic vs 2.9 for bimetallic). This suggests that the synergism between Au and Pd in bimetallic catalysts stabilizes the metallic form of Pd phase.
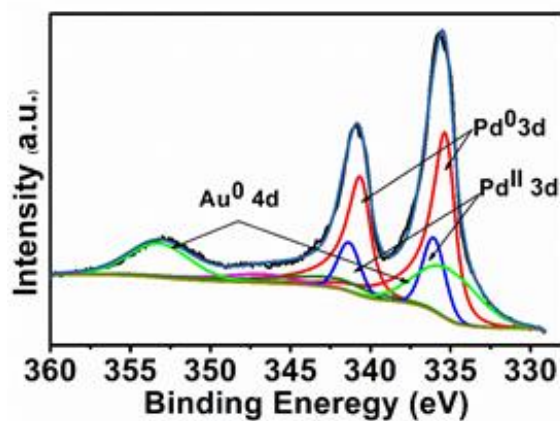
Figure 4.9 Au(4f) core level spectra for AuPd/CuO catalyst.

4.3.3.   Morphology and particle size analysis by TEM

TEM is a powerful technique to capture information about the size and distribution of supported nanoparticles and it has been used extensively to study similar systems [26]. Similarly, TEM was performed here for all supported (mono- and bimetallic of Au and Pd) nanoparticles in order to investigate their internal morphologies and also to estimate the distribution of their sizes within the catalysts' matrices.

4.3.3.1.   NiO based materials.

Figure 4.10 (a, b and c) shows the TEM micrographs obtained for Au/NiO_c, Pd/NiO_c and $AuPd/NiO_c$ catalysts, respectively, while Figure 4.10 (d, e and f) illustrates the micrographs obtained for Au/NiO_s, Pd/NiO_s and $AuPd/NiO_s$ catalysts, respectively. The mean particle sizes are summarized and presented in Table 4.4. In generally, all supported nanoparticles are well confined and distributed onto both supports (NiO_c and NiO_s) without any obvious agglomerations (see Figure 4.10). However, comparisons of the particle size distributions for monometallic Au and Pd catalysts show that materials supported on NiO_s tend to have a narrow particle size distribution and lower mean particle size than those supported on NiO_c. Also, the TEM results show that the mean particle size of monometallic catalysts prepared with PVA (i.e. Au/NiO_s, and Pd/ NiO_s), are smaller (~ 4.4 nm) than those (i.e. Au/NiO_c, and Pd/ NiO_c) prepared in the absence of PVA (7.2 nm). Interestingly, the results did not show any significant variation in the mean particle size for the bimetallic AuPd supported systems for both supports ($NiO_{(s,c)}$ prepared in presence or absence of PVA, compared to monometallic Au and Pd systems. Our results are in good agreement with the recent findings by Graham et. *al* [27] who synthesised Au and AuPd catalysts by the same method (sol-immobilization) in the presence and absence of stabilizing agent.

Table 4.4 Mean values of particle size obtained by TEM analysis of Au, Pd and AuPd nanoparticles supported on both NiO_c and NiO_s oxides

Support	Metal	Mean (nm)	Std-dev
	Au	7.2	3.7
NiO_c	Pd	7.2	3.3
	AuPd	4.6	1.1
	Au	4.2	1.2
NiO_s	Pd	4.5	1.3
	AuPd	4.0	1.3
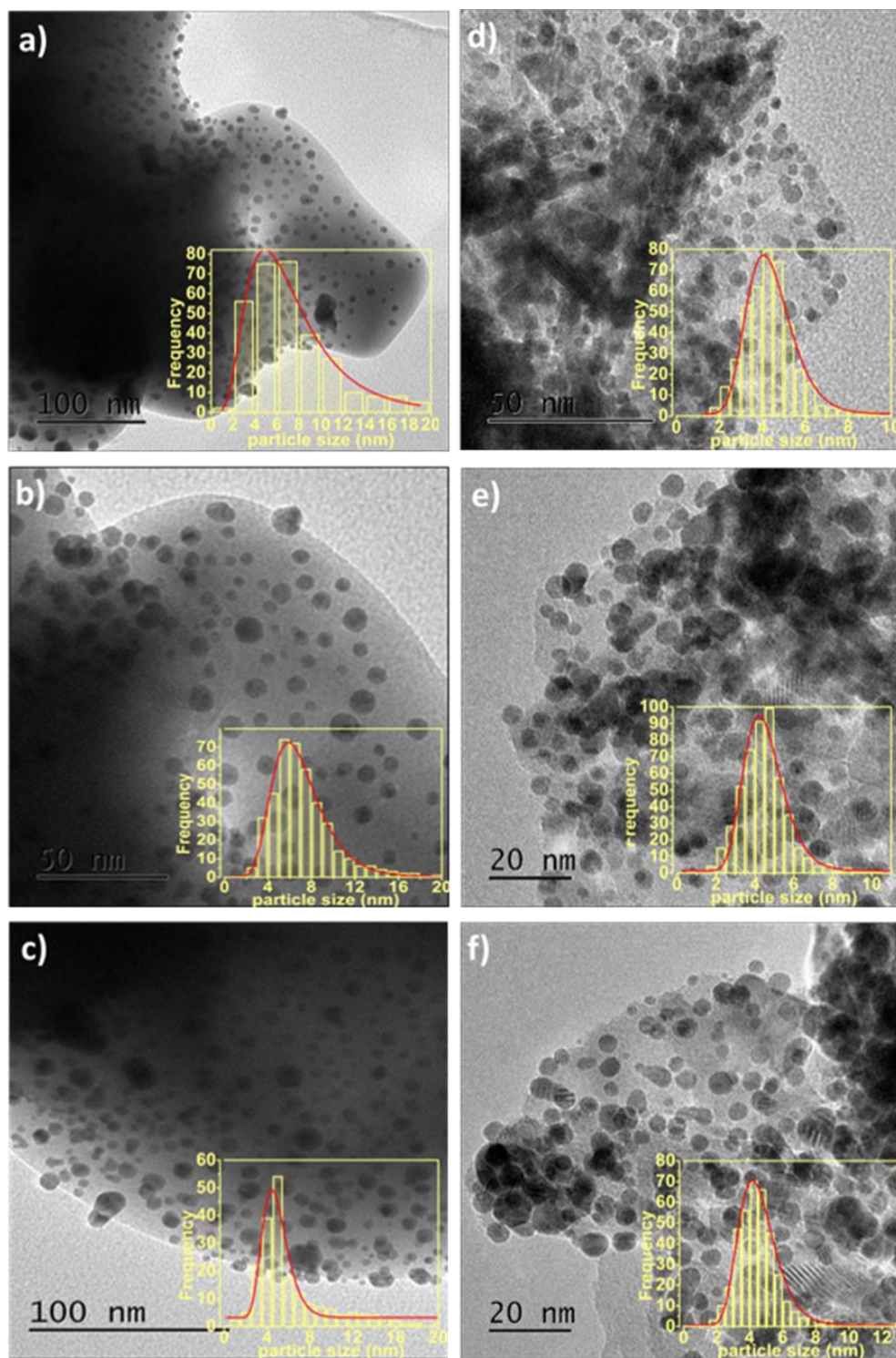
Figure 4.10 TEM images and their corresponding particle size distributions (insets) for (a) Au/NiO$_s$, (b) Pd/NiO$_c$, (c) AuPd/NiO$_c$, (d) Au/NiO$_s$, (e) Pd/NiO$_s$ and (f) AuPd/NiO$_s$ catalysts.

4.3.3.2. CuO based materials.

TEM analyses also were used for CuO based catalysts to look at the distribution of the supported nanoparticles and to gain their mean particle sizes. The obtained images are presented in Figure 4.11. The values of the mean particle sizes are summarized in Table 4.5. The obtained TEM images clearly show that supported nanoparticles are highly dispersed onto CuO surface with sphere-like morphology and their mean particle size values have an average of ~ 4 (±1) nm., see Figure 4.11(d) and Table 4.5 over all catalysts. Regarding to the morphology of CuO itself, the obtained TEM images clearly identify several predominant shapes of the support such as; spherical, flower and nanorods-like particles, as shown in Figure 4.11 (a, b and c), respectively. These morphologies have been previously reported for CuO based materials [28–33]. As shown in the Figure 4.11, Au and Pd nanoparticles in Au/CuO, Pd/CuO and AuPd/CuO catalysts are distributed homogeneously on the surface of the CuO. No obvious agglomeration was observed in all the samples and the average diameter was found to be ~ 4.1 (±1.2) nm as given in Table 4.5
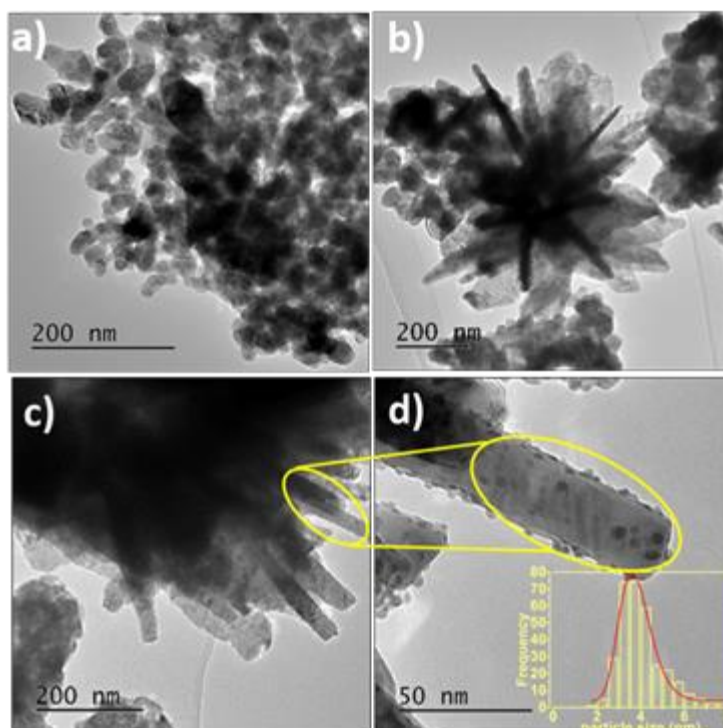
Figure 4.11 TEM images of CuO based materials having (a) spherical-like, (b) flower-like and (c) nanorods-like, morphologies, and (d) Au/CuO catalyst having nanorod-like morphology with corresponding particle size distributions (inset), as a representative example.

Table 4.5 Mean values of particle size obtained by TEM analysis of Au/CuO, Pd/CuO and AuPd/CuO catalysts.

Catalyst	Mean (nm)	Std-dev
Au/CuO	4.0	1.1
Pd/CuO	4.4	1.3
AuPd/CuO	3.8	1.2

4.3.4. Specific surface area (S_{BET})

The specific surface areas (S_{BET}) and textural properties of the materials under investigation were assessed using N_2 physical adsorption/desorption analysis at 77 K. As a result, the values of S_{BET} were estimated and the obtained results are summarized in Table 4.6. The S_{BET} values of NiO_c and NiO_s supports are 52 ($\pm$3) and 188 ($\pm$5) $m^2 g^{-1}$, respectively. It's worth to mention here that there are good correlations between crystallite size obtained from XRD data and S_{BET} values. Smaller crystallite size obtained for NiO_s (5 nm vs 43 nm for NiO_c) have bigger S_{BET} value (188 $m^2 g^{-1}$, vs 52 $m^2 g^{-1}$ for NiO_c). The S_{BET} of CuO support is determined also by applying BET equation and have a value of 9 ($\pm$1) $m^2 g^{-1}$. Moreover, there is no significant difference in the surface area on $NiO_{(c,s)}$ and CuO after the immobilization of Au, Pd and AuPd on the support due to low loading of these metals (1%).

Table 4.6 S_{BET} values of catalysts' supports obtained by N_2 physisorption at 77 K.

Support	S_{BET} ($m^2 g^{-1}$)
NiO_c	52 ($\pm$3)
NiO_s	188 ($\pm$5)
CuO	9 ($\pm$1)

4.4. Effect of support on the reduction of 4-nitrophenol by NaBH₄

It is well known that the interaction between the active nanoparticles and support has a positive impact of the activity for any given reaction. So far, and to get insight onto the reduction of 4-nitrophenol by NaBH$_4$, we aimed in this Section to study the incorporation of catalyst's support such as NiO (commercial), synthesised NiO (NiO$_s$) and CuO (commercial) into the activity of AuPd nanoparticles for the reduction of 4-nitrophenol by NaBH$_4$.

4.4.1. Activity of NiO$_c$ (commercial) based catalysts.

NiO, as a catalyst's support, has been reported extensively for reduction of 4-NP [34–36]. Based on the reaction optimisation, which previously described in Chapter 3 (reaction conditions: 4-NP/metal molar ratio = 13, 4-NP [1.35×10^{-4} M], NaBH$_4$/4-NP molar ratio = 30, T = 30 °C, stirring rate = 100 rpm), here we aimed to screen the activity of NiO$_c$, Au/NiO$_c$, Pd/NiO$_c$ and AuPd/NiO$_c$ catalysts for the reduction of 4-NP under kinetic regime and mild reaction conditions. Figure 4.12 (a and b) shows the conversion % of 4-NP and the corresponding Pseudo-first-order kinetic model, respectively, as a function of time, over Au/NiO$_c$, Pd/NiO$_c$ and AuPd/NiO$_c$ catalysts. The apparent rate constant (K$_{app}$) of NiO$_c$, Au/NiO$_c$, Pd/NiO$_c$ and AuPd/NiO$_c$ catalysts are summarized in Table 4.7.
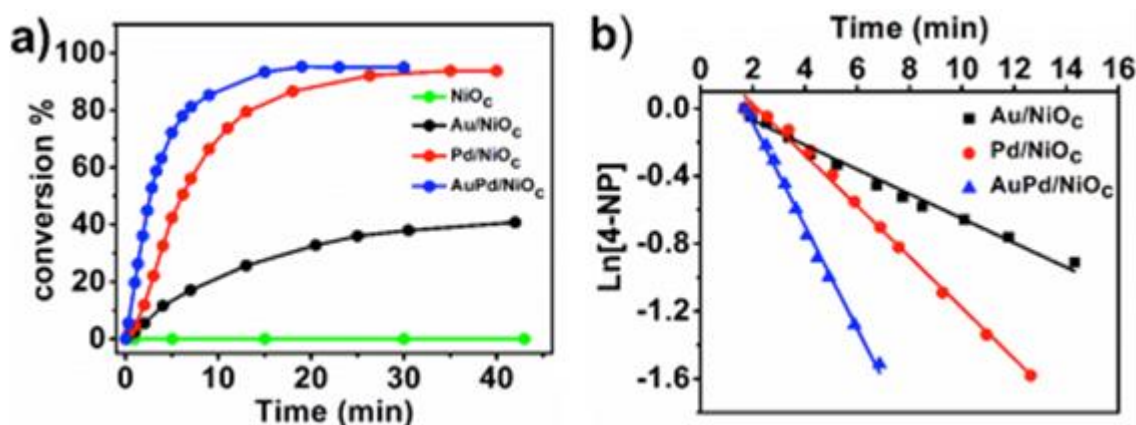
Figure 4.12 a) Conversion (%) and b) ln[4-NP], as a function of time, for the reduction of 4-NP over Au/NiO$_c$, Pd/NiO$_c$ and AuPd/NiO$_c$ catalysts, as indicated. Conversion (%) of NiO$_c$ support is also presented for comparisons. Reaction conditions: 4-NP/metal molar ratio =13, [4-NP] = 1.35×10^{-4} M, NaBH$_4$/4-NP molar ratio = 30, T = 30 °C and stirring rate = 1000 rpm.

Table 4.7 Catalytic activity of bare NiO_c and Au/NiO_c, Pd/NiO_c and $AuPd/NiO_c$ catalysts towards the reduction 4-NP by $NaBH_4$.

Catalyst	K_{app} (min^{-1})
NiO_c	0
Au/NiO_c	0.08
Pd/NiO_c	0.13
$AuPd/NiO_c$	0.25

It can be seen in Figure 4.12 and Table 4.7 that the bare NiO_c support was not active in the reduction of 4-NP. Regarding the activity of mono- and bi-metallic catalysts, $AuPd/NiO_c$ catalyst gave the highest activity suggesting that there might be a synergistic effect between Au and Pd metals, as observed and explained previously in Chapter 3. Moreover, the results clearly show a trend in activity and it was found in the following order; $AuPd/NiO_c$ > Pd/NiO_c > Au/NiO_c. The apparent rate constant of reduction of 4-nitrophenol by $AuPd/NiO_c$ (K_{app} = 0.25 min^{-1}) catalyst has increased by 2 fold than Pd/NiO_c (K_{app} = 0.13 min^{-1}) and 3 times faster than Au/NiO_c (K_{app} = 0.08 min^{-1}) as shown in Table 4.7. The high activity observed for $AuPd/NiO_c$ catalyst, compared to monometallic analogous, could be attributed to the formation of AuPd alloy nanoparticles and hence there might be a synergistic effect between Au and Pd as evidenced from XPS analysis, which is previously described in Chapter 3. The close vicinity between AuPd in the alloying system would increase the probability of interaction of the adsorbed reactant molecules and hence lead to an increase of the reaction rate.

4.4.2. Activity of NiO_s (synthesised) based catalysts.

In order to study the effect of support and to get better understanding on the catalytic activity and to compare this with commercial NiO material, NiO nanoparticles have been prepared and used as a catalysts' support for mono- and bi-metallic Au and Pd nanoparticles. For comparison purposes, the activity testing was performed also under the same conditions used for NiO_c based materials. The catalytic activity of NiO_s, Au/NiO_s, Pd/NiO_s and $AuPd/NiO_s$ catalysts are presented in Figure 4.13 and the obtained results for apparent rate constants (K_{app}) are summarized and cited in Table 4.8.

The observed apparent rate constants were calculated to represent the catalytic efficiency of the as synthesised materials. It is obvious from our results that the bare NiO_s is active in the reduction of 4-NP (K_{app} = 0.01 min^{-1}), while the bare NiO_c is inactive (K_{app} = 0.0 min^{-1}), see Tables 4.7 and 4.8. This remarkable activity observed for bare NiO_s support could be attributed to several factors such as surface area, particle size, crystallinity and/or

surface chemical composition in respect to bare NiO_c support. According to N_2 physisorption and XRD analyses, bare NiO_s support have higher S_{BET} values [S_{BET} = 188 (± 5) vs 52 (± 3) m^2g^{-1}] and lower crystal size [5 vs 43 nm] and poor crystallinity [amorphous vs crystalline] than those obtained for bare NiO_c support.

Regrading to the activity of Au/NiO_s, Pd/NiO_s and $AuPd/NiO_s$ catalysts, bimetallic $AuPd/NiO_s$ catalyst showed the highest performance amongst monometallic analogous due to the synergistic effect of AuPd alloy. Moreover, the results clearly show a trend in activity and it was found in the following order; $AuPd/NiO_s > Pd/NiO_s > Au/NiO_s$. This activity trends are expected and very similar to the trends observed for NiO_c based catalysts.

The activity of monometallic Au/NiO_s and Pd/NiO_s catalysts is increased by a factor of ~ 3.5 when compared to Au/NiO_c and Pd/NiO_c analogous. For bimetallic $AuPd/NiO_s$ system, the activity is also enhanced by a factor of ~ 3 in respect to $AuPd/NiO_c$ catalyst. These results are expected due to the differences in physical and chemical properties of bare NiO_s and NiO_c supports. We should also keep in our mind that all NiO_s based catalysts were prepared with PVA and have smaller mean particle sizes (mean average = 4) than those supported on NiO_c oxide (mean average = 6.6 nm), as estimated form the TEM results. This could be considered as another factor for the high activity observed for NiO_s based catalysts.
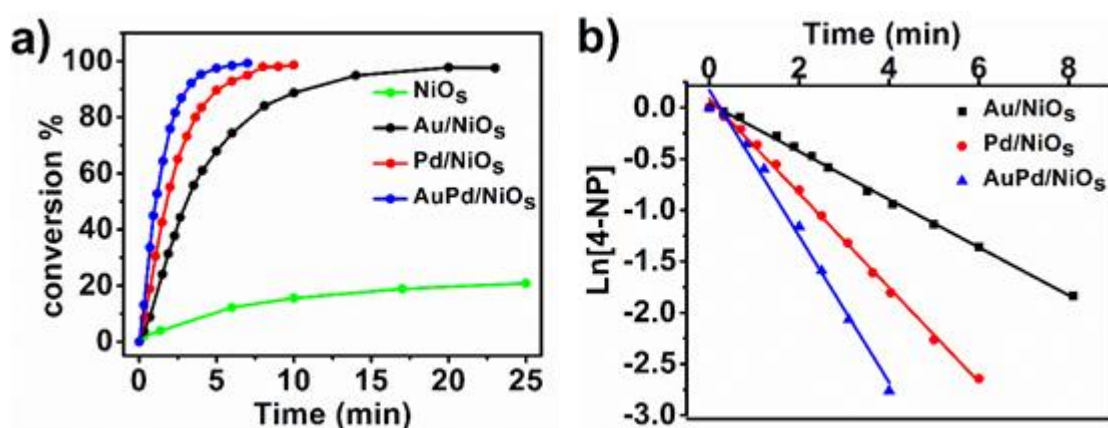
Figure 4.13 a) Conversion (%) and b) ln[4-NP], as a function of time, for the reduction of 4-NP over Au/NiO_s, Pd/NiO_s and $AuPd/NiO_s$ catalysts, as indicated. Conversion (%) of NiO_s support is also presented for comparisons. Reaction conditions: 4-NP/metal molar ratio =13, [4-NP] = 1.35×10^{-4} M, $NaBH_4$/4-NP molar ratio = 30, T = 30 ºC and stirring rate = 1000 rpm.

Table 4.8 Catalytic activity of NiO_s, Au/NiO_s, Pd/NiO_s and $AuPd/NiO_s$ in the reduction of 4-nitrophenol by $NaBH_4$.

Catalyst	K_{app} (min^{-1})
NiO_s	0.01
Au/NiO_s	0.28
Pd/NiO_s	0.46
$AuPd/NiO_s$	0.78

4.4.3. Modification of NiO_c (commercial) with urea

To get into insight the observed trend in catalytic activity and the role of NiO_s as a catalyst's support, commercial NiO material (NiO_c) has been modified using urea and under the same conditions that were used to synthesis NiO_s, herein after denoted as NiO_c-urea. Then the activity of all supports (NiO_c, NiO_c-urea and NiO_s) was screened in the reduction of 4-NP by $NaBH_4$. Figure 4.14 (a, b and c) shows the conversion % of 4-NP as a function of time over bare NiOc, NiO_c-urea and NiO_s supports, respectively. Clearly, the results show that NiO_s exhibits the highest activity (21% conversion at 30 min) compared with non-active NiO_c material. Interestingly, none-active NiO_c sample exhibited some activity in the reaction after the treatment with urea (10% conversion at 30 min). However, it is still lower than the activity of NiO_s materials by a factor of ~2, (21% vs 10% conversion at 30 min).

In order to understand the role of urea and how it enhance the activity of commercial NiO_c sample, and of course this might give us an understanding why NiO_s exhibits the highest activity, we have done a number of complementary techniques such as ; TGA, XRD and XPS analyses.
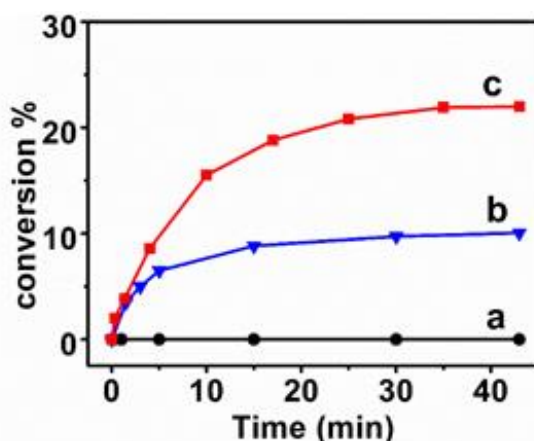
Figure 4.14 Conversion (%) of 4-NP reduced by $NaBH_4$ over (a) NiO_c, (b) NiO_c-urea and (c) NiO_s as a function of time. Reaction conditions: [4-NP] = 1.35×10^{-4} M, support weight = 10 mg, $NaBH_4$/4-NP molar ratio = 30, T = 30 ºC and stirring rate = 1000 rpm.

The effect of urea on the formation of NiO phase was studied by González-Calbet *et al.,* [37]. According to their findings, urea (in this work) could be used to hamper the transformation of $Ni(OH)_2$ to NiO. Our XPS results showed that NiO_s (which was synthesized with urea) have a significant amount of $Ni(OH)_2$ after calcination for 3 h at 300 °C. However, this is not the case when NiO_c was treated with urea. The hypothesis here is that urea was hydrolysed at 120 °C *via* a hydrothermal treatment and decomposed into NH_3 and CO_2. Then, NH_3 can be hydrolysed with water to release hydroxyl anions which finally can react with Ni^{2+} ions to form $Ni(OH)_2$ precursor [36], as shown in reactions (1 - 3).

$CO(NH_2)_2$ → NH_3 + HNCO   Reaction 1

$HNCO + H_2O$ → $NH_3 + CO_2$ Reaction 2

$NH_3 + H_2O$ → $NH_4^+ OH^-$ Reaction 3

Figure 4.15(a, b and c) shows the XRD patterns obtained for NiO_c, NiO_c-urea and NiO_s, respectively. The results show that the crystallinity of NiO_c sample was decreased after the treatment with urea as the intensity of diffraction peaks was decreased after the treatment. The observed decrease in crystallinity also lead to a decrease in the crustal size. This was also confirmed by calculating the particle crystal sizes using Scherrer's equation and the obtained results are presented in Table 4.9. As can be seen that after the treatment with urea, the crystal size of NiO_c decreased from 43 to 36 nm. So far, this decrease in the particle crystallite size of NiO_c-urea sample could be the reason for its observed activity [38].
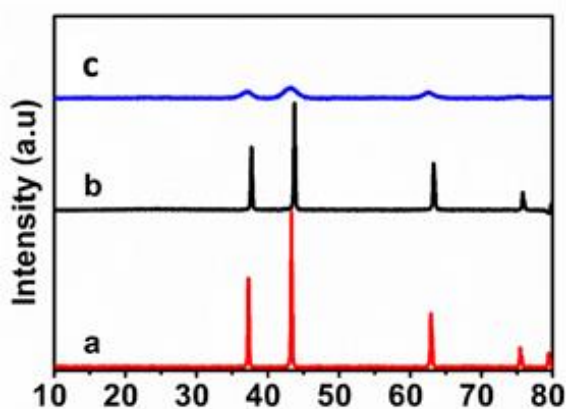
Figure 4.15 XRD patterns of a) fresh NiO_c, b) NiO_c after treated by urea and c)NiO_s

Table 4.9 Average crystallite size calculated by Scherrer equation for NiO_c-urea, NiO_c and NiO_s.

Support	Crystallite size [nm]
NiO_c-urea	36
NiO_c	43
NiO_s	5

To further go insight the role of NiO support in the reduction of 4-NP, surface chemical composition of bare NiO support was conducted using XPS analysis, see Figure 4.16. As a result, the percentage of $Ni(OH)_2$ species over NiO_c sample (before and after treatment with urea) was calculated and the extracted parameters are presented in Table 4.10. The XPS results, which previously discussed in Section 4.5.2, showed that both bare NiO_s and NiO_c supports have fraction of $Ni(OH)_2$ species with a percentage of 8 and 0.2%, respectively. Upon treatment of NiO_c with urea, the fraction of $Ni(OH)_2$ species was further increased to 1.3%. So far, the enhancement in activity for NiO_c-urea could be correlated to the fraction of surface OH group.
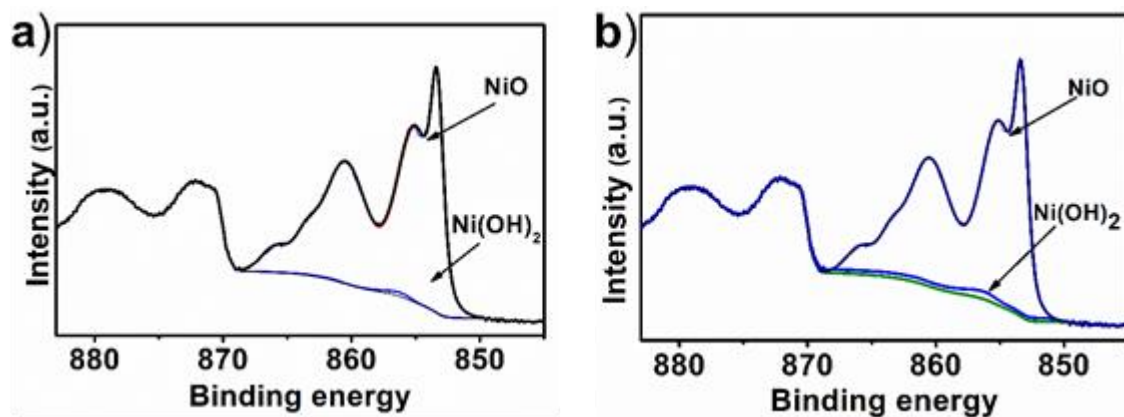
Figure 4.16 XPS spectra of NiO_c support: (a) fresh and (b) treated with urea.

Table 4.10 The percentage (%) of NiO and $Ni(OH)_2$ species in NiO_s, NiO_c and NiO_c-urea estimated from XPS analysis.

Catalyst	NiO %	$Ni(OH)_2$ %
NiO_c	99.8	0.2
NiO_c-urea	98.7	1.3
NiO_s	92	8

The increase of surface OH group upon urea treatment is further evidenced by using TGA analysis, see Figure 4.17. The TGA analysis was conducted in a flow of N_2 gas (50 ml/min) upon heating to 800 ^{0}C (5°C/min). It is noticed that the weight of samples decreases slowly with increasing temperature. On heating upto 800 ^{0}C, the total weight loss (%) for NiO_c is only 0.19%, while for NiO_c-urea sample is 0.33% and occurs in two steps. This weight loss(%) could be attributed to the loss of hydroxyl groups from the support surface [39]. Upon heating to 150 $^{\circ}$C, both supports lose the same amount of weight due to the physical adsorbed water. The difference in the total loss is 0.1 wt.% between the two supports suggesting that only few fractions of NiO was hydrolysed to $Ni(OH)_2$ by urea. No residual urea was found on the surface of the treated support by elemental analysis for carbon, hydrogen and nitrogen which confirm that this loss is a result of OH groups only.
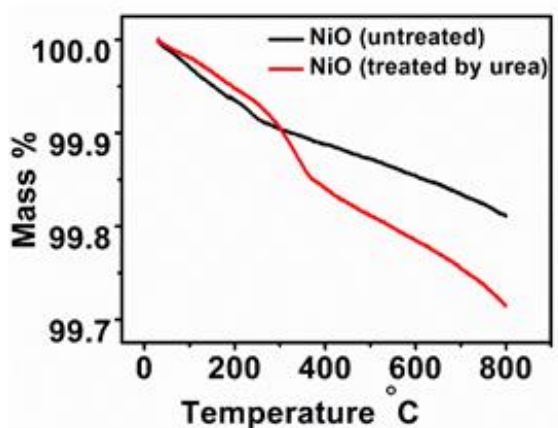
Figure 4.17 TGA analysis of NiO_c and NiO_c-urea samples.

The characterisation results confirmed that the presence of hydroxyl group on the surface of NiO are the main difference between the commercial and synthesised support. In our investigation we proved that the hydroxyl group on the surface of the support is a result of urea treatments. Wang *et al.,* showed that $Ni(OH)_2$ can catalyse the reduction of 4-nitrophenol, which explain the activity of NiO_s and NiO_c treated with urea. The role of $Ni(OH)_2$ in the reduction of 4-nitrophenol was investigated in several reports [40,41]. They reported that, $Ni(OH)_2$ can stabilise the intermediates and facilitate the adsorption of the reactants, which results in lowering the activation energy allowing the reaction to proceed as observed in this work**.**

4.4.4.   Activity of CuO based catalysts.

CuO has been reported as promising material for different catalytic applications including the reduction of 4-NP [3,26,42]. Moreover, the activity of CuO could be enhanced when prepared in nanoscale. Our previous results showed the crucial role of the support in our probe reaction model (reduction of 4-NP). So far, and in order to go insight the effect of support, all CuO based catalysts (i.e. CuO, Au/CuO, Pd/CuO and AuPd/CuO) are screened towards the reduction of 4-NP. In order to compare the role of CuO with NiO as a catalyst support, we have mimicked the reaction conditions as NiO based reactions. The activity results on CuO based catalysts are presented in Table 4.11. As can be seen, bare CuO support is active for the reduction of 4-NP. Moreover, the immobilization of mono- and bi-metallic Au and Pd nanoparticles onto CuO support lead to tremendous enhancement of the activity and hence for the apparent reaction rate. However, there was a trend in the activity as in the following order; AuPd/CuO > Pd/CuO > Au/CuO > CuO. This trend is very similar with the trends observed for NiO_c and NiO_s based catalysts. In general, the activity of CuO based catalysts, compared to the most active NiO_s based catalysts which discussed in Section 4.6.2, are more active for this reaction. Comparing the activity of bare supports (CuO and NiO_s), the activity of bare CuO can compete the activity of NiO_s (K_{app} = 0.3 vs 0.01 min^{-1}, respectively). Also, the conversion (%) of 4-NP over bare CuO support reached 100% after only 5 min, while bare NiO_s support showed only 10% at the same time. However, there was an induction time observed for bare CuO support and this will be discussed in detail later in the following Sections. For the supported catalysts, the apparent rate constants of Au/CuO, Pd/CuO and AuPd/CuO catalysts (K_{app} = 0.8, 1.4 and 1.8 min^{-1}, respectively) are higher than analogous catalysts supported on NiO_s material (see Table 4.8 in Section 4.6.2).

Table 4.11 Catalytic activity of bare CuO and Au/CuO, Pd/CuO and AuPd/CuO catalysts towards the reduction 4-NP by $NaBH_4$.

Catalyst	K_{app} (min^{-1})
CuO	0.3
Au/CuO	0.8
Pd/ CuO	1.4
AuPd/CuO	1.8

The apparent rate constants (K_{app}) of Au/CuO, Pd/CuO and AuPd/CuO catalysts were increased significantly compared to bare CuO support by a factor of 2.6, 4.6 and 6, respectively. The results suggest the promotion effect of Au and/or Pd components in improving the catalytic activity of CuO support in this reaction [26].

The apparent rate constants were used to compare our catalytic findings with the literature. For Au/CuO catalyst, Gholami *et al.,* [26] studied the reduction of 4-NP over Au/CuO catalyst. They found that the K_{app} value of Au/CuO catalyst is higher than K_{app} value of bare CuO support by a factor of 1.5, while our results showed increased by a factor of 2.6 under similar conditions of metal loadings. The difference in the activity could be correlated to different reasons; such as mean particle size and surface properties of the prepared catalysts. In their work the mean particle size is 8 nm, while our catalyst (Au/CuO) is only 4 nm as obtained by TEM analysis. Furthermore, the morphology of bare CuO support in their work possess irregular shape, while our bare CuO support has a predominant nanorods and flower-like shape as evidenced by TEM analysis and these results are further in agreement with the work done by Zou at *al* [29]. Similar reasons for the activity of Pd/CuO catalyst in the reduction of 4-NP were also reported by Nasrollahzadeh *et al.,* [3].

The K_{app} value of AuPd/CuO catalyst is higher than the K_{app} value reported by Long *et al.,* [43] under similar reaction conditions (even with higher metal loading than our work; 1.88 vs 1 wt.%) by a factor of 1.6. Our high activity could be attributed mainly to the small AuPd mean particle size (4 nm) than their work (15 nm). This result confirms the advantage of using sol-immobilization method for controlling smaller particle size. Additionally, the high performance of AuPd system, in respect to monometallic analogous, could be attributed to the strong interaction (synergism) between Au and Pd provided by this method of preparation. Furthermore, the strong metal-support interaction (between AuPd and CuO support) is another key factor for the activity. In summary, these factors, plus those mentioned above for the monometallic Au and Pd analogous, could be the reasons for observed activity.

4.5. Induction time

Induction time is simply described as the time expended to initiate the activity of a catalyst [16,44–49], which generally diminishes with the reuse of the catalyst. As we described above (Section 4.6.4) that bare CuO support together with Au/CuO, Pd/CuO and AuPd/CuO catalysts showed very promising activity towards the reduction of 4-NP. The rate of the reaction over these catalysts was very fast/quick and even the reaction starts and finish within ~ 2 min. From previous observation particularly for experiments conducted over bare CuO support that there was an induction time at the start of the reaction. In order to fully understand the origin of this induction time, firstly, we have conducted an *in-situ* experiment for bare CuO, Au/CuO, Pd/CuO and AuPd/CuO

catalysts. The conditions for this reaction are described in detail in Chapter 2 (Section 2.4.2) and mentioned in the caption of Figure 4.18 below. Typically; the requisite amount of catalyst was added directly into the cuvette, which contains fresh solution of 4-NP (2.7 mL, 1.35×10^{-4} M). The cuvette was subsequently placed into a cuvette holder, which

provides magnetic stirring and temperature controller, both remotely controlled by a computer. When the desired temperature was reached, the fresh $NaBH_4$ solution (0.3 mL, 3.9×10^{-2} M) was added to give a total volume of 3 ml to initiate the reaction. The reduction process of 4-NP was subsequently monitored by measuring the UV-Vis absorption spectra of the reaction solution every 5 seconds until full conversion was achieved.

The results of the *in-situ* experiments over bare CuO support as well as Au/CuO, Pd/CuO and AuPd/CuO catalysts are presented in Figure 4.18. The results show clearly that all catalysts have an induction time, which varies from sample to sample. The highest induction time was observed for bare CuO support (~1.5 min), followed by Au/CuO catalyst (~ 1 min). The other two catalysts (Pd/CuO and AuPd/CuO) showed very short induction time due to their highest activity towards the probe reaction.

According to the literature, induction time can be attributed to many reasons. Pradhan *et al.,* [50], who studied the activity of silver nanoparticles, observed an induction period which was attributed to the presence of an oxide layer on the surface of the silver nanoparticles, and they found that the induction period diminishes by conducting the reaction in a nitrogen atmosphere instead of air. Although, the oxide shell layer is widely
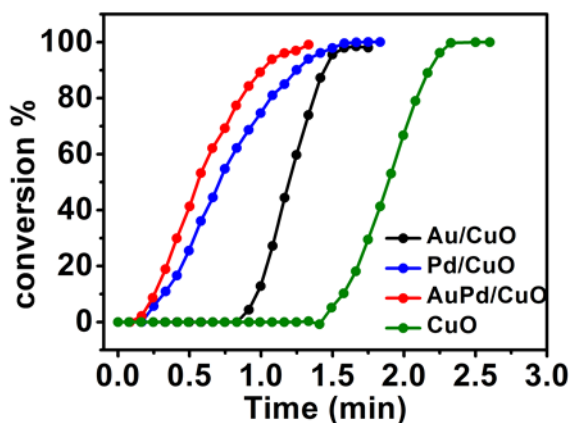
Figure 4.18 Conversion (%) as a function of time, *in situ*, during the reduction of 4-NP by $NaBH_4$ over bare CuO, Au/CuO, Pd/CuO and AuPd/CuO catalysts. Reaction conditions: 4-NP/metal molar ratio = 1/2 molar ratio, 2.7 ml of 4-NP [1.35×10^{-4} M], $NaBH_4$/4-NP molar ratio = 30, T = 30 ºC, 1200 rpm (reaction was carried out in a 1 cm cuvette).

cited as the source of the induction period for silver nanoparticles [51–53] this is not without dispute as others have noticed induction time for nanoparticles of non-oxidizable metals (e.g., Pt, Au)[54,55]. Hence, dissolved oxygen in the reaction solution has been proposed as another possible reason for the observed induction period [56–60]. It was explained that the dissolved oxygen will react at a faster rate with the $NaBH_4$ than nitrophenol. To avoid this, in many cases, nitrogen is purged before adding $NaBH_4$. The induction time is sometimes explained with the diffusion of the reactants – 4-nitrophenol [61–64] or borohydride [49]. Ballauff and co-workers proposed an alternate explanation that the reaction could only begin once the catalyst surface underwent a surface reconstruction brought on by the attachment of reactants to the surface [55]. A view also shared by Chen and co-workers for the catalytic reduction of resazurin by NH_2OH [65].

From the previous initial experiments, discussed above, we found that bare CuO support is exhibited the highest induction time. So far, and in order to fully understand the reason for this, we shall focus only on studying the effect of induction time, *in situ*, in detail over this support. According to literature described above, we believe that the major reasons which could be responsible for this induction time; (i) dissolved oxygen in the reaction media, (ii) surface oxidation state (i.e. reduction of the oxidic outer shell of CuO support, as we used strong reducing agent, $NaBH_4$).

To investigate the effect of dissolved oxygen of the reaction media, an in-situ experiment was performed. Prior to the addition of $NaBH_4$, the aqueous solution contains both the catalyst and the substrate was purged with N_2 for ~ 10 min, then the UV-Vis spectra were recorded simultaneously every ~ 5 seconds until full conversion (%) was achieved. The results of this experiment showed that the induction time was reduced by 12 %, which suggest that there is an effect from the dissolved oxygen present in the reaction media for the observed induction time phenomena [56–60]. However, these results indicated that the dissolved oxygen was not only the reason for induction time phenomena as we still observe an induction time.

So far, attention has been made to investigate the effect the second possible reason (reduction of the oxidic outer-shell of CuO support) on the induction time. As a result, we have conducted a distinct, in-situ, experiment (similar to that presented in Figure 4.18, without purging with N_2 gas) over bare CuO support previously treated by $NaBH_4$. The result of this experiment is illustrated in Figure 4.19. Interestingly, and as can be seen in

this Figure, that the induction time over bare CuO support treated is further decreased by 75% compared to the untreated CuO support.

To further get insight into the effect of $NaBH_4$ towards CuO support, XPS and XRD analyses were conducted on bare CuO support, before and after the treatment with $NaBH_4$, to discriminate their surface compositions, oxidation states and crystallite-phase change.
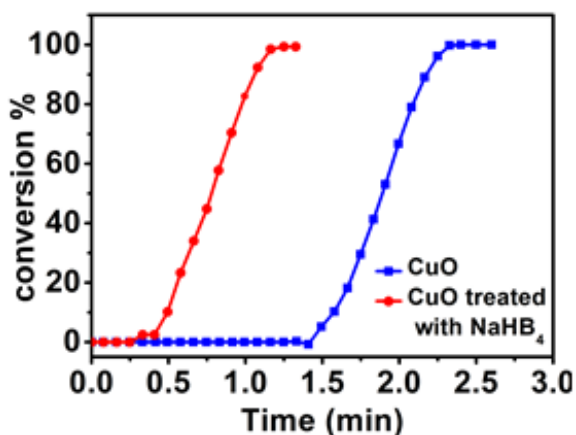
Figure 4.19 Conversion (%) as a function of time, *in situ*, during the reduction of 4-NP by $NaBH_4$ over bare CuO support (fresh and after treatment with $NaBH_4$). Reaction conditions: 2.7 ml of 4-NP [1.35×10^{-4} M], weight of CuO = 2 mg, $NaBH_4$/4-NP molar ratio = 30, T = 30 ºC and stirring rate = 1200 rpm.

We expect that $NaBH_4$ may reduce Cu^{II} in the CuO phase to lower oxidation state (i.e. Cu^I and/or Cu^0). So far, the XPS spectra obtained for bare CuO support, before and after the treatment, are presented in Figure 4.20 for comparisons. The XPS spectra of bare CuO support, as discussed before in Section 4.5.2.2, are characterized by $Cu(2p_{3/2})$ and $Cu(2p_{1/2})$ doublet centred at 934.2 and 954.1 eV, respectively, as well as, the two-shake-up satellite feature of $Cu(2p_{3/2})$ and $Cu(2p_{1/2})$ doublet centred at 942.4 and 962.6 eV, respectively. On the other hand, the XPS spectra of Cu^I and Cu^0 phases are characterized by $Cu(2p_{3/2})$ and $Cu(2p_{1/2})$ doublet peaks centred at 933 eV without any shake-up satellite features [22,23]. Based on the above statements, any decrease in the intensity of the two-shake-up satellite feature centred at 942.4 and 962.6 eV for the CuO phase could be used as an evidence for the reduction of CuO phase to lower oxidation states (Cu^I and/or Cu^0 phases). As can be seen from the obtained XPS spectra (see Figure 4.20), there is an

obvious decrease in the intensity of shake-up satellite peaks upon the treatment with NaBH₄. This suggest that fractions of CuO phase are reduced to Cu^I and/or Cu^0 phases.
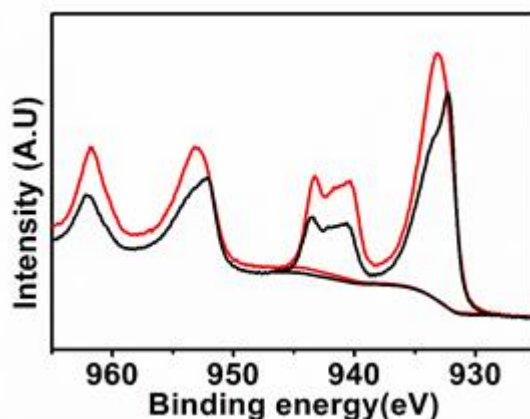
Figure 4.20 XPS spectra of the CuO(untreated) and CuO after treated by NaBH₄.

To further investigate the reduction of bare CuO support, when treated by NaBH₄, to lower oxidation states (Cu^I and/or Cu^0 phases), XRD analysis was performed on CuO material, before and after the treatment, and the obtained patterns are presented in Figure 4.21 for comparisons. The XRD diffraction peaks, if there is any, for Cu^I phase (as Cu_2O) would be expected to appear at $2\theta =$ 29.5°, 34.5°, 42.2°, 52.3°,61.5°, 67.9°,73.4, which are correspond to (110), (111), (200), (211), (220), (310) and (311) Cu_2O facets, respectively (JCPDS, 05–667) [66]. While the assignments of diffraction peaks for metallic Cu would be expected at $2\theta =$ 32.5, 43.64°, 50.80° and 74.42 °, which are correspond to (110), (111), (200), and (220) facets of metallic copper, respectively (JCPDS No. 04-0836). The expanded region in Figure 4.21 shows clearly new additional four peaks, in the treated CuO sample, at $2\theta =$ 236.38°, 42.28° 43.64º and 50.80º. These peaks are corresponded to the diffractions of Cu^I(111), Cu^I(200), Cu^0(111) and Cu^0 (200), respectively. These results suggest the presence of Cu^I and Cu^0 phases in treated-CuO sample and confirm the reduction of CuO phase when treated with NaBH₄, which in consistent with the XPS analysis explained above.

In conclusion, the reduction of 4-NP by NaBH₄ over all CuO based materials possess an induction time which was dramatically shortened over bare CuO support, pre-treated with NaBH₄. The results of XPS and XRD analyses on this material (bare CuO support, before and after the treatment with NaBH₄) confirm that fractions of bare CuO phase were reduced to Cu_2O and/or Cu^0 phases before the reduction of 4-NP by NaBH₄, and thus surface reconstructions upon the treatment with NaBH₄ might be the main reason for this induction time. Another factor which might be responsible for the induction time is the
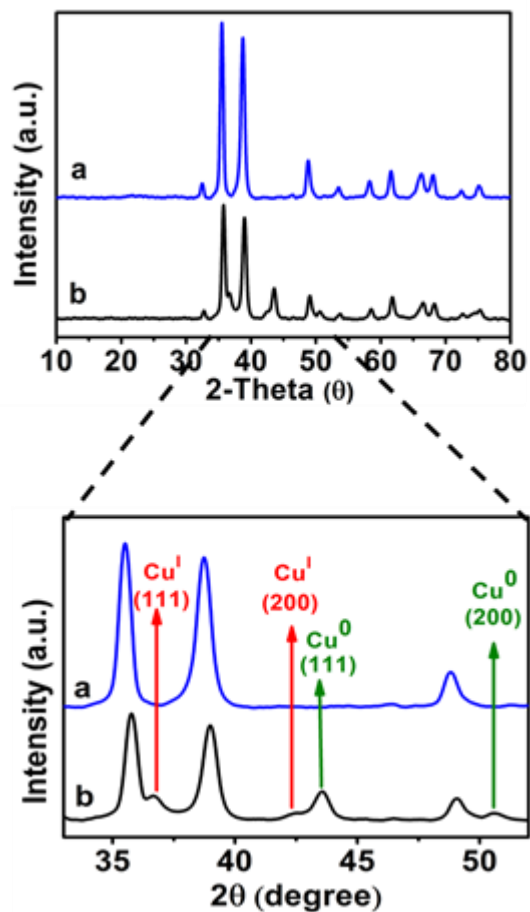
Figure 4.21 XRD patterns for bare CuO support: a) fresh and b) after treated with NaHB₄ (inset graph represents a zoom in area).

presence of dissolved oxygen in water. The oxygen will react at a faster rate with $NaBH_4$ than 4-NP [67]. This was confirmed by shortening the induction time when the reaction was purged with N_2 gas prior to the reaction.

4.6. Comparison of the catalytic activity of Au and Pd supported on various metal oxide supports for the reduction of 4-Nitrophenol by NaBH₄.

In the present Section, the catalytic activity of mono- and bimetallic Au and Pd nanoparticles supported on various types of metal oxide supports, namely NiO_s, CuO and TiO_2, were compared for the aqueous-phase reduction of 4-NP using $NaBH_4$, as a reducing agent. For the catalytic reduction of 4-nitrophenol, NiO_s, CuO and TiO_2 supported catalysts have limited studies despite the high chemical stability of these materials under the reaction conditions. The activity of the supports alone was investigated, and the results are presented in Figure 4.22. The results are clearly show that TiO_2, as a catalyst's support, is inactive in this reaction as reported in the literature [68,69] and this also was confirmed in Chapter 3. TiO_2 was found to cause retardation of hydrogen evolution from the aqueous-phase solution of sodium borohydride [11]. In contrast, bare CuO support starts to work after an induction time of ~ 4 min (investigated early in Section 4.7). Afterwards, it is showed the highest
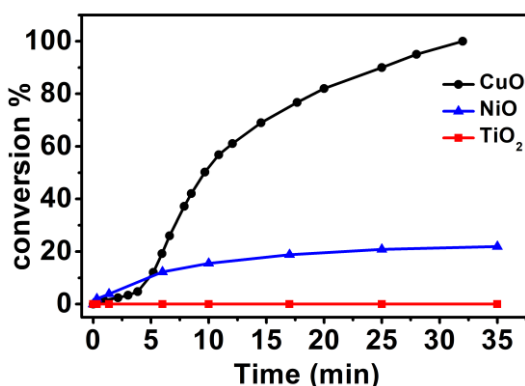
Figure 4.22 Conversion (%) as a function of time (min) for the reduction of 4-nitrophenol by $NaBH_4$ over bare CuO, NiO_s and TiO_2 supports. Reaction conditions: weight of support = 10 mg, [4-NP] = 1.35×10^{-4} M, $NaBH_4$/4-NP molar ratio = 30, T = 30 °C, and stirring rate = 1000 rpm.

activity with 100% conversion within 35 min. For bare NiO_s support, it shows a reasonable activity, but lower than bare CuO support. The catalytic activity of the supports follows the following order; CuO >> NiO_s > TiO_2 (not active). Similar order in the activity was reported by Gopal and Mandlimath [11]. The surface positive charge of CuO and NiO is claimed to facilitate the interaction between the metal oxide surface and the donor species of BH_4^- anion [11].

Figure 4.23(a, b and c) shows the conversion (%) of 4-NP reduction by $NaBH_4$ over Au, Pd and AuPd nanoparticles, respectively supported on CuO, NiO_s and TiO_2 oxides. Their corresponding apparent rate constant values are summarized in Table 4.12. The obtained results clearly demonstrate that the catalytic activities of the catalysts follow the same

125

order as bare supports and are in the following order; (Au/CuO >> Au/NiO$_s$ > Au/TiO$_2$), (Pd /CuO >> Pd/NiO$_s$ > Pd/TiO$_2$) and (AuPd/CuO>> AuPd/NiO$_s$ > AuPd/TiO$_2$).

Generally, the results showed that all mono- and bimetallic Au and Pd nanoparticles supported on CuO material have a superior activity than those supported on NiO$_s$ and TiO$_2$ oxides. In addition, the average mean particle size of the active supported metal components has insignificant effect on the catalyst's activity, otherwise, TiO$_2$ supported catalysts with the smallest particle size (~ 2 nm vs 4 nm for CuO and NiO$_s$ based catalysts) would have the highest activity amongst all catalysts. This finding is in agreement with the literature [70]. Also, the results of N$_2$ adsorption/desorption analysis suggests that there is no any correlation between the catalysts' activity and their corresponding specific surface area (S$_{BET}$). As can be seen that the most active catalysts (CuO based catalysts), have lower surface area by a factor of ~ 7 and ~ 21 than TiO$_2$ and NiO$_s$ based catalysts, respectively. This finding is in reported by Yin *et al.,* [11].

The highest activity observed for CuO based catalysts (Au/CuO, Pd,CuO and AuPd/CuO) could be correlated to the following factors; One of these factors is the strong metal-support interaction at the metal/metal oxide interfaces, which was evidenced by the XPS analysis of the Cu(2P). Taking AuPd/CuO catalyst as an example with the highest activity for the reduction of 4-NP, the binding energy of Cu(2p3/2) was shifted to higher value (933.8 eV) than bare CuO support (933.3 eV). Another factor which could be a reason for this remarkable activity might be is the presence of multiple phases of copper oxides such as CuO, Cu$_2$O and metallic Cu phase, as evidenced from the XPS and XRD analyses. Thus, this could facilitate the electronic transitions at the metal/metal oxide interfaces and eventually promote the catalytic reaction. Moreover, there is also another strong lateral interaction between Au and Pd. This factor is already evidenced by XPS analysis as there was an evidence for the formation of AuPd alloy.

Table 4.12 Apparent rate constant values during the reduction of 4-NP by NaBH$_4$ over supported mono- and bimetallic Au and Pd nanoparticles.

Catalyst	K$_{app}$ (min^{-1})
Au/TiO$_2$	0.14
Au/NiO$_s$	0.28
Au/CuO	0.8
Pd/TiO$_2$	0.2
Pd/NiO$_s$	0.46
Pd/CuO	1.5
AuPd/TiO$_2$	0.38
AuPd/NiO$_s$	0.78
AuPd/CuO	1.8
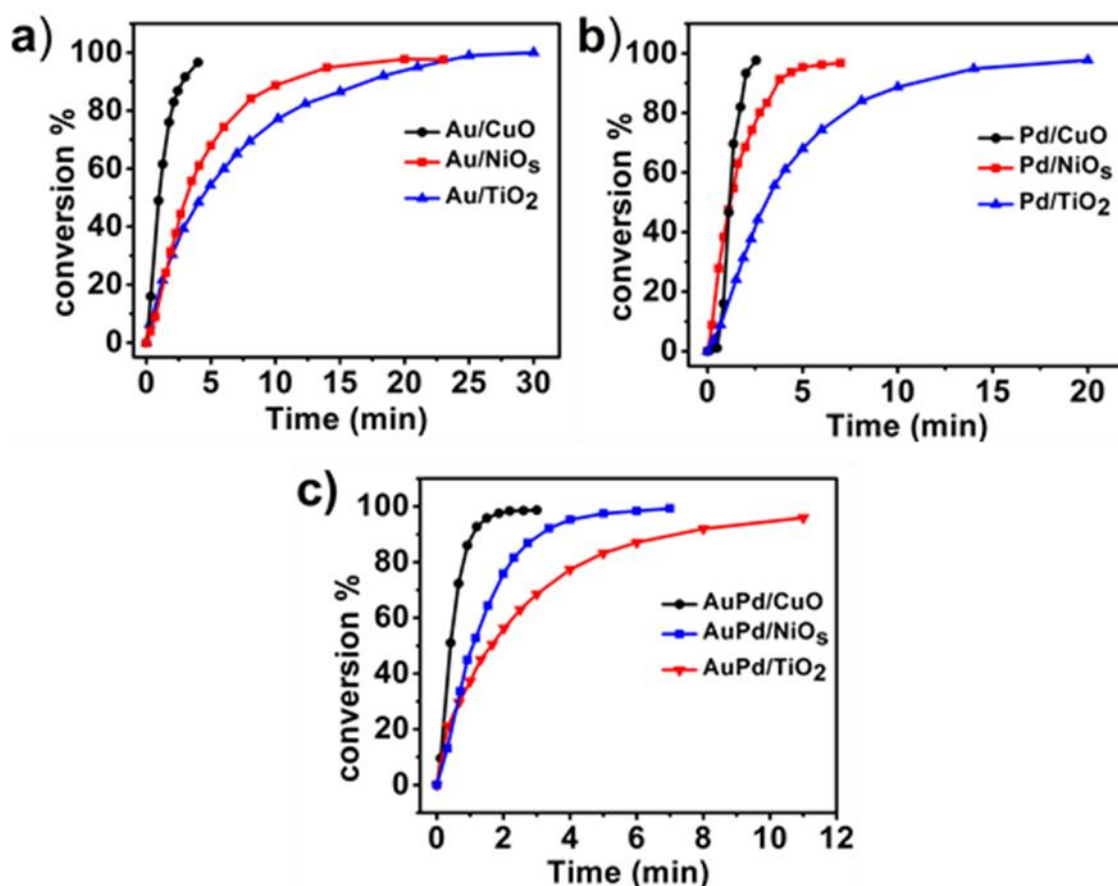
Figure 4.23 Conversion (%) as a function of time (min) for the reduction of 4-NP by NaBH$_4$ over a) Au, b) Pd and c) AuPd nanoparticles supported on CuO, NiO$_s$ and TiO$_2$ oxides. Reaction conditions: 4-NP/metal molar ratio = 13, [4-NP] = 1.35×10^{-4} M, NaBH$_4$/4-NP molar ratio = 30, T = 30 °C, and stirring rate = 1000 rpm.

4.7. Catalysts' reusability

The recovery and reusability of the given heterogeneous catalyst are very important and have advantages when used in large scale industry. To evaluate the reusability of the prepared catalysts, we have focus on testing the reusability of bimetallic (AuPd) supported nanoparticles on various metal oxides(i.e. AuPd/CuO, AuPd/NiO$_s$ and AuPd/NiO$_c$), which were exhibited the highest activity towards the reduction of 4-NP. The standard procedure for studying reusability described in detail in Chapter 2 (Section 2.5). Typically, the reusability study was conducted in 100 ml round bottom flask and under the following conditions; 4-NP/metal molar ratio = 13, NaBH$_4$/4-NP molar ratio = 30, T = 30 C and stirring rate = 1000 rpm. Each reaction was stopped after 1.5 min, then the sample collected for the UV-Vis measurement. The amount of catalyst was filtered off, washed several times by deionized water, dried at room temperature and finally recharged again for further cycles (four cycles in total). The obtained data for each cycle

are summarized in Table 4.13 and illustrated in Figure 4.24. Generally, and as can be seen from Table 4.13, all catalysts are catalytically active and stable over four runs. It's worth to mention here that NiO based catalysts showed slight decrease in their activity from run 1 to run 4 (from 64 – 57% and from 42 – 33% for $AuPd/NiO_s$ and $AuPd/NiO_c$ catalysts, respectively). In contrast, the conversion (%) over AuPd/CuO catalyst was increased after the first cycle (from 90 – 95.5%) and remained almost stable through run 4. The increase of AuPd/CuO catalyst's activity could be attributed to a fraction reduction of CuO support to lower phases (Cu_2O and/or Cu^0, evidenced by XPS and XRD). Also, it might be a reason

for enhancing the induction time.

Table 4.13 Reusability study of AuPd/CuO, $AuPd/NiO_s$ and $AuPd/NiO_c$ during the reduction of 4-NP by $NaBH_4$. Conversion (%) was taken at 1.5 min.

| Catalyst | Conversion (%) after 1.5 minutes | | |
	AuPd/CuO	$AuPd/NiO_s$	$AuPd/NiO_c$
Fresh	90	64	42
2nd cycle	95.5	61	38
3rd cycle	95.5	60	35
4th cycle	95	57	33

Reaction conditions: 4-NP/metal molar ratio = 13, [4-NP] = 1.35×10^{-4} M, $NaBH_4$/4-NP molar ratio = 30, T = 30 ºC and stirring rate = 1000 rpm.
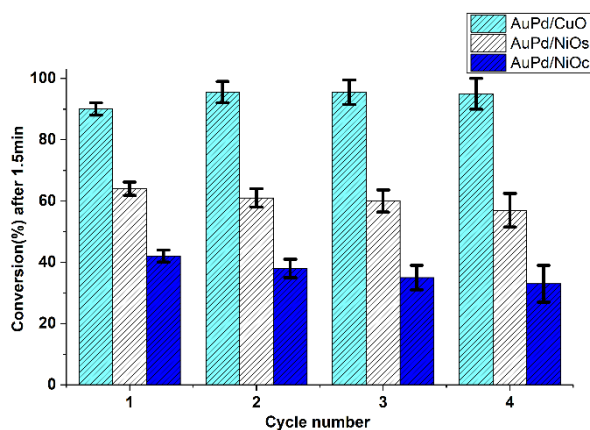
Figure 4.24 Reusability study for $AuPd/NiO_c$, $AuPd/NiO_s$, and AuPd/CuO during the reduction of 4-nitrophenol. Reaction conditions: 4-NP/metal molar ratio = 13 , [4-NP] = 1.35×10^{-4} M, $NaBH_4$/4-NP molar ratio = 30, T = 30 ºC, stirring rate = 1000 rpm and reaction time = 1.5 min.

To further go insight into the effect of particle size in catalyst's reusability, the internal morphology of the used catalysts (after four cycles) was probed by TEM analyses. The obtained TEM images are illustrated in Figure 4.25 and the mean particle size presented in Table 4.14. Clearly, the TEM images, after four cycles, show that all AuPd supported nanoparticles are still highly dispersed without any agglomeration. As can be seen from Table 4.14, the mean particle size of AuPd/NiO$_s$ catalyst was slightly increased from 4 – 4.5 nm, while increased from 4.6 - 5.4 nm and from 3.8 – 4 nm for AuPd/NiO$_s$ and AuPd/CuO catalysts, respectively. Although, the mean particles sizes were slightly increased over all used catalysts compared to the fresh catalysts, the differences between TEM particle sizes values for used and fresh catalyst are within the margins of errors.
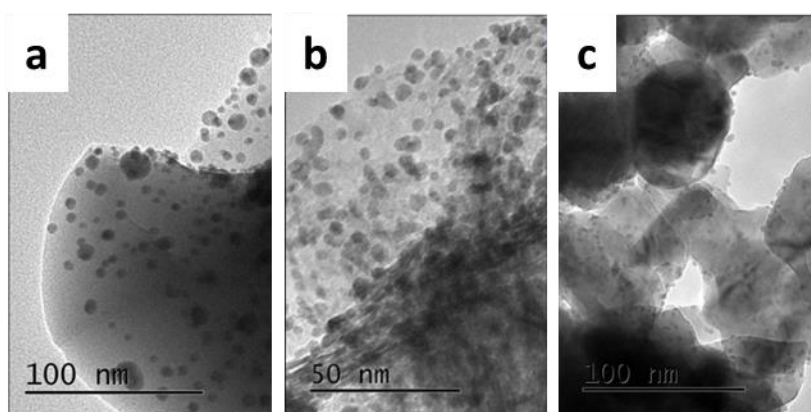
Figure 4.25 TEM images of used a) AuPd/NiO$_c$, b) AuPd/NiO$_s$ and c)AuPd/CuO catalysts (after three runs).

In addition, the catalysts' stability was further investigated by XPS and the obtained results are presented in Table 4.14. The results for used catalysts did not suggest any significant changes in metal composition after being used. The XPS data, for the used AuPd/CuO catalyst, show that Cu^{II} might be reduced to Cu^I or Cu^0 during the reaction by excess NaBH$_4$, which is consistent with our previous observation discussed before in Section 4.7. This might explain the increasing in the catalytic activity of AuPd/CuO catalyst after the first run. Figure 4.26 show a slight decrease in the intensity of the satellite shake-up peak centred at 942.4 eV, which attributed to Cu(2p$_{3/2}$), and was taken as an evidence for the reduction of Cu^{II} to Cu^I and/or Cu^0 at the metal/metal oxide interfaces, as discussed early in this Chapter (see Section 4.7).

Moreover, the leaching of the nanoparticles was checked by MP-AES and the results show that no evidence of Au or Pd leaching in the reaction medium after the reaction above the

detection limit of MP-AES which is 1 to 2 ppb. In summary, the overall loss in activity of AuPd/NiO$_s$ and AuPd/NiO$_c$ is probably due to the increase in mean particle.
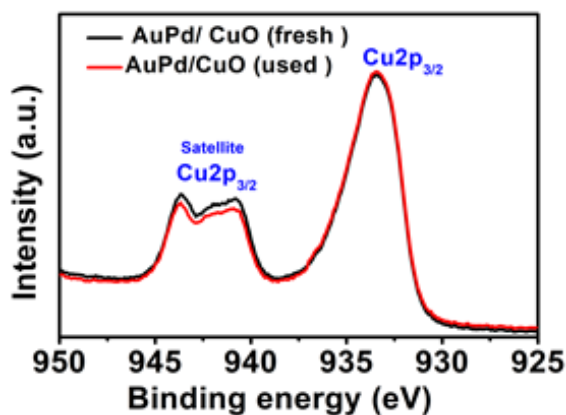
Figure 4.26 Cu(2p$_{3/2}$) core level spectra for AuPd/CuO catalyst (fresh and used), as indicated.

Table 4.14 XPS quantification analysis and means particle size on fresh and used catalysts.

Catalyst	Au/Pd ratio (mol/mol)[a]		Mean particle size(nm)[b]	
	Fresh	Used	Fresh	Used
AuPd/NiO$_c$	44:56	40:60	4.6 ±1.1	5.4 ±1.2
AuPd/NiO$_s$	49:51	45:55	4.0 ± 1.3	4.5 ±1.0
AuPd/CuO	46:54	42:58	3.8 ± 1.2	4.1 ±0.93

[a] Au/Pd molar ratios (mol/mol) are extracted from XPS analysis.
[b] Mean particle sizes (nm) are extracted from TEM analysis.

4.8. Conclusions

We found previously in Chapter 3 that sol-immobilization method can be used to prepare metal nanoparticles with tailored properties, which subsequently showed great performance in the reduction of 4-NP by $NaBH_4$ with the highest activity observed for AuPd (1:1) supported on TiO_2. In this Chapter we examined the effect of different support, mainly CuO and NiO based oxides, on the activity of mono- and bimetallic Au and Pd nanoparticles towards the reduction of 4-NP by $NaBH_4$.

The results revealed that all supported nanoparticles were successfully prepared *via* sol-immobilization approach and showed promising activity, stability and reusability, towards the reduction of 4-NP by $NaBH_4$ with the presence of an observable induction time.

To better understanding the structure-activity correlations, all catalysts as well as their corresponding supports were characterized, ex situ, using a number of complementary techniques including; TGA, XRD, TEM, N_2 physisorption, MP-AES and XPS analyses. The results showed that we have successfully prepared well dispersed supported nanoparticles with small mean particle size as evidenced by TEM and XRD analyses.

Generally, the results of the activity testing showed that bimetallic AuPd supported nanoparticles are more active than their monometallic analogous, with the highest activity observed for CuO support, and the activity was followed the following order; AuPd/CuO (K_{app} = 1.8 min^{-1}) > AuPd/NiO$_s$ (K_{app} = 0.78 min^{-1}) > AuPd/NiO$_c$ (K_{app} = 0.25 min^{-1}). The highest activity observed for AuPd/CuO catalyst was correlated, not only, to strong metal-support interactions, but also to metal-metal synergism between Au and Pd in the AuPd alloy. This was evidenced by XPS analysis. In addition, our results referred that the particle size of supported nanoparticles as well as the specific surface area of the prepared catalyst has been not significant factors in the catalysts' activity, as approved by TEM and BET surface area measurements.

Moreover, it is worth to mention that an initial screening for the activity of bare metal oxides supports (CuO and NiO) showed a remarkable activity of CuO compared to NiO material. This activity was attributed to the presence of Cu^0 and/or Cu^+ phases at metal/metal oxide interfaces, as evidenced by XPS and XRD.

The XRD results revealed that CuO, NiO$_c$ and NiO$_s$ supports are stabilised in nanosized crystal structure with sizes of 14, 43 and 5 nm, respectively. The absence of any

diffraction patterns for the supported nanoparticles (Au, Pd and/or AuPd) suggested that these nanoparticles are very small and out of the detection limit of the XRD instrument which agreed with TEM analysis.

4.9. References

[1]   H. Tang, J. Wei, F. Liu, B. Qiao, X. Pan, L. Li, J. Liu, J. Wang and T. Zhang, J. Am. Chem. Soc., 2016, 138, 56–59.

[2]   A. Corma and H. Garcia, Chem. Soc. Rev., 2008, 37, 2096–2126.

[3]   M. Nasrollahzadeh, S. M. Sajadi, A. Rostami-Vartooni and M. Bagherzadeh, J. Colloid Interface Sci., 2015, 448, 106–113.

[4]   X. Lu, Y. Yin, L. Zhang, L. Xi, S. Oswald, J. Deng and O. G. Schmidt, Nano Energy, 2016, 30, 69–76.

[5]   R. AlBilali and N. Dimitratos, Catal. Letters, 2017, 147, 2372–2384.

[6]   C. Wang, F. Yang, W. Yang, L. Ren, Y. Zhang, X. Jia, L. Zhang and Y. Li, RSC Adv., 2015, 5, 27526–27532.

[7]   C. Alegre, S. Siracusano, E. Modica, A. S. Aricò and V. Baglio, Mater. Renew. Sustain. Energy, 2018, 7, 1–10.

[8]   J. Noh and R. Meijboom, Appl. Nanotechnol. Water Res., 2014, 333–406.

[9]   G. J. H. S. Meenakshisundaram, E. Nowicka, P.J. Miedziak, G.L. Brett, R.L. Jenkins, N.Dimitratos, S.H. Taylor, D.W. Knight, D. Bethell, Faraday Discuss., 2009, 145, 341–356.

[10]   M. Haruta, T. Kobayashi, H. Sano and N. Yamada, Chem. Lett., 1987, 16, 405–408.

[11]   T. R. Mandlimath and B. Gopal, J. Mol. Catal. A Chem., 2011, 350, 9–15.

[12]   Z. Zhang, J. C. Jung and N. Yan, Nanoscale, 2016, 8, 19684–19695.

[13]   L. Pan, S. Ma, L. Li and Y. Chen, J. Sol-Gel Sci. Technol., 2014, 72, 161–170.

[14]   A. Villa, C. E. Chan-Thaw, G. M. Veith, K. L. More, D. Ferri and L. Prati, ChemCatChem, 2011, 3, 1612–1618.

[15]   L. A. García-Cerda, K. M. Bernal-Ramos, S. M. Montemayor, M. A. Quevedo-López, R. Betancourt-Galindo and D. Bueno-Báques, J. Nanomater. 2011, 162495-162501.

[16]   S. Wang, M. Zhang and W. Zhang, ACS Catal., 2011, 1, 207–211.

[17]   H. Khojasteh, M. Salavati-Niasari, A. Abbasi, F. Azizi and M. Enhessari, J. Mater. Sci. Mater. Electron., 2016, 27, 1261–1269.

[18]   S. Cattaneo, S. J. Freakley, D. J. Morgan, M. Sankar, N. Dimitratos and G. J. Hutchings, Catal. Sci. Technol., 2018, 1677–1685.

[19]   S. Rogers, R. Catlow, D. Gianolio, P. Wells and N. Dimitratos, Faraday Discuss., 2018,208, 443–454.

[20]   A. P. Grosvenor, M. C. Biesinger, R. S. C. Smart and N. S. McIntyre, Surf. Sci., 2006, 600, 1771–1779.

[21]   H. W. Nesbitt, D. Legrand and G. M. Bancroft, Phys. Chem. Miner., 2000, 27, 357–366.

[22]   D. A. Firmansyah, T. Kim, S. Kim, K. Sullivan, M. R. Zachariah and D. Lee, Langmuir, 2009, 25, 7063–7071.

[23]   D. Choi and D.-J. Jang, New J. Chem., 2017, 41, 2964–2972.

[24] D. R. Kumar, D. Manoj, J. Santhanalakshmi and J. J. Shim, Electrochim. Acta, 2015, 176, 514–522.

[25] M. H. Ab Rahim, R. D. Armstrong, C. Hammond, N. Dimitratos, S. J. Freakley, M. M. Forde, D. J. Morgan, G. Lalev, R. L. Jenkins, J. A. Lopez-Sanchez, S. H. Taylor and G. J. Hutchings, Catal. Sci. Technol., 2016, 6, 3410–3418.

[26] E. Akbarzadeh, M. Falamarzi and M. R. Gholami, Mater. Chem. Phys., 2017, 198, 374–379.

[27] L. Abis, S. J. Freakley, G. Dodekatos, D. J. Morgan, M. Sankar, N. Dimitratos, Q. He, C. J. Kiely and G. J. Hutchings, ChemCatChem, 2017, 9, 2914–2918.

[28] A. Kumar, A. K. Srivastava, P. Tiwari and R. V. Nandedkar, J. Phys. Condens. Matter, 2004, 16, 8531–8543.

[29] V. Rajendran and J. Gajendiran, Mater. Res. Bull., 2014, 56, 134–137.

[30] M. Yang, J. He, M. Hu, X. Hu, C. Yan and Z. Cheng, Sensors Actuators, B Chem., 2015, 213, 59–64.

[31] M. Vaseem, A. Umar, S. H. Kim and Y. B. Hahn, J. Phys. Chem. C, 2008, 112, 5729–5735.

[32] Y. Qin, F. Zhang, Y. Chen, Y. Zhou, J. Li, A. Zhu, Y. Luo, Y. Tian and J. Yang, J. Phys. Chem. C, 2012, 116, 11994–12000.

[33] P. Gao, Y. Chen, H. Lv, X. Li, Y. Wang and Q. Zhang, Int. J. Hydrogen Energy, 2009, 34, 3065–3069.

[34] T. L. Lai, K. F. Yong, J. W. Yu, J. H. Chen, Y. Y. Shu and C. Bin Wang, J. Hazard. Mater., 2011, 185, 366–372.

[35] O. A. Zelekew and D.-H. Kuo, RSC Adv., 2017, 7, 4353–4362.

[36] L. Pan, L. Shen, L. Li and Q. Zhu, J. Mater. Sci. Mater. Electron., 2016, 27, 3065–3070.

[37] A. Querejeta-Fernández, M. Parras, A. Varela, F. Del Monte, M. García-Hernández and J. M. González-Calbet, Chem. Mater., 2010, 22, 6529–6541.

[38] S. BR and J. XR, J. Theor. Comput. Sci., 2016, 3 (2), 1000149–1000158.

[39] T. N. Ramesh, J. Phys. Chem. B, 2009, 113, 13014–13021.

[40] D. Jia, H. Gao, W. Dong, S. Fan, R. Dang and G. Wang, ACS Appl. Mater. Interfaces, 2017, 9, 20476–20483.

[41] F. Bao, F. Tan, W. Wang, X. Qiao and J. Chen, RSC Adv., 2017, 7, 14283–14289.

[42] W. Che, Y. Ni, Y. Zhang and Y. Ma, J. Phys. Chem. Solids, 2014, 77, 1–7.

[43] W. Yao, F.-L. Li, H.-X. Li and J.-P. Lang, J. Mater. Chem. A, 2015, 3, 4578–4585.

[44] Y. Gao, X. Ding, Z. Zheng, X. Cheng and Y. Peng, Chem. Commun., 2007, 3720–3722.

[45] Y. Lu, Y. Mei, M. Ballauff and M. Drechsler, J. Phys. Chem. B, 2006, 110, 3930–3937.

[46] A. Murugadoss and A. Chattopadhyay, Nanotechnology, 2008, 19, 015603–015611.

[47] A. Murugadoss and A. Chattopadhyay, J. Phys. Chem. C, 2008, 112, 11265–11271.

[48]   Y. Mei, G. Sharma, Y. Lu, M. Ballauff, M. Drechsler, T. Irrgang and R. Kempe, Langmuir, 2005, 21, 12229–12234.

[49]   A. M. Signori, K. De O. Santos, R. Eising, B. L. Albuquerque, F. C. Giacomelli and J. B. Domingos, Langmuir, 2010, 26, 17772–17779.

[50]   N. Pradhan, A. Pal and T. Pal, Colloids Surfaces A, 2002, 196, 247–257.

[51]   T. Jana, Subhra; Pal, J. Nanosci. Nanotechnology, 2007, 7, 2151–2156.

[52]   S. Sarkar, A. K. Sinha, M. Pradhan, M. Basu, Y. Negishi and T. Pal, J. Phys. Chem. C, 2011, 115, 1659–1673.

[53]   K. D. Zhang, J.-T., Wei, G., Keller, T.F., Gallagher, H., Stoetzel, C., Mueller, F.A., Gottschaldt, M., Schubert, U.S., Jandt, Mater. Eng, 2010, 295, 1049–1057.

[54]   A. M. Kalekar, K. K. K. Sharma, A. Lehoux, F. Audonnet, H. Remita, A. Saha and G. K. Sharma, Langmuir, 2013, 29, 11431–11439.

[55]   S. Wunder, F. Polzer, Y. Lu, Y. Mei and M. Ballauff, J. Phys. Chem. 2010, 114, 8814–8820.

[56]   Y. Lu, Y. Mei, R. Walker, M. Ballauff, M. Drechsler, Polymer, 2006, 47, 4985–4995.

[57]   S. Panigrahi, S. Basu, S. Praharaj, S. Pande, S. Jana, A. Pal, S. K. Ghosh and T. Pal, J. Phys. Chem. C, 2007, 111, 4596–4605.

[58]   D. Wei, Y. Ye, X. Jia, C. Yuan and W. Qian, Carbohydr. Res., 2010, 345, 74–81.

[59]   J. Huang, S. Vongehr, S. Tang, H. Lu and X. Meng, J. Phys. Chem. C, 2010, 114, 15005–15010.

[60]   E. Menumerov, R. A. Hughes and S. Neretina, Nano Lett., 2016, 16, 7791–7797.

[61]   J. Han, J. Dai, L. Li, P. Fang and R. Guo, Langmuir, 2011, 27, 2181–2187.

[62]   K.-L. Wu, X.-W. Wei, X.-M. Zhou, D.-H. Wu, X.-W. Liu, Y. Ye and Q. Wang, J. Phys. Chem. C, 2011, 115, 16268–16274.

[63]   J. Zeng, Q. Zhang, J. Chen and Y. Xia, Nano Lett., 2010, 10, 30–35.

[64]   J. Han, L. Li and R. Guo, Macromolecules, 2010, 43, 10636–10644.

[65]   X. Zhou, W. Xu, G. Liu, D. Panda and P. Chen, J. Am. Chem. Soc., 2010, 132, 138–146.

[66]   X. Zhao, Y. Tan, F. Wu, H. Niu, Z. Tang, Y. Cai and J. P. Giesy, Sci. Total Environ., 2016, 571, 380–387.

[67]   A. A. Ismail, A. Hakki and D. W. Bahnemann, J. Mol. Catal. A Chem., 2012, 358, 145–151.

[68]   Z. Ma, L. Zhang, R. Chen, W. Xing and N. Xu, Chem. Eng. J., 2008, 138, 517–522.

[69]   S. M. Rogers, PhD thesis, "Design Metal Nanoparticles for Catalysis, 2017, pages 108–128.

[70]   C. Lin, K. Tao, D. Hua, Z. Ma and S. Zhou, Molecules, 2013, 18, 12609–12620.

Chapter 5

Investigation of the catalytic performance of bimetallic catalysts AuPd and AgPd supported on TiO$_2$: Effect of reducing agent

5.1. Introduction

Over the last decade, supported noble metal nanoparticles (NPs) such as Au, Ag, Pt and Pd, have attracted enormous interest in the field of heterogeneous catalysis because of their unique physical, chemical and catalytic properties compared to bulk counterparts [1–5]. Tailoring metal NPs is an important step in optimising their performance for a given process; the metal particle size, shape and structure are all crucial factors in dictating the overall catalytic performance. To investigate these parameters, the reduction of 4-nitrophenol(4-NP) by $NaBH_4$ has been widely used as model reaction, since it is easy to monitor with simple and fast analytical techniques, and there are no by-products[6].

Colloidal methods, particularly the sol-immobilisation method, have been successfully utilised to generate metal NPs with desirable characteristics, compared to conventional techniques such as wet impregnation and deposition–precipitation [7]. Typical steps in colloidal synthesis to control the particle properties (particle size and shape) include changing the type of stabilising and reducing agents, the concentrations of each component, and the metal concentration[8,9].

The sol-immobilisation method is a preparation technique with great ability to prepare supported metal nanoparticles with tailored properties. Generally, this preparation method affords small metal nanoparticles < 10 nm with a narrow particle size distribution [8,10].

Recently, many reports showed that Ag NPs can be used as an efficient catalyst to catalyse reduction reactions. He *et al.,* [11] synthesized Ag-deposited on silica-coated magnetic nanoparticles with average particle sizes of 15($\pm$5) nm for the catalytic reduction of 4-NP by $NaBH_4$ (as a reducing agent).

Bimetallic NPs, composed of two different metal elements, have received a great deal of attention, particularly in the field of catalysis, as they have often shown enhanced catalytic performance compared with their corresponding monometallic counterparts, due to alloy effects and/or synergistic effects [28–33]. Oh *et al.,* [19] reported synthesis of Pd based bimetallic catalysts such as Pd-Au, Pd-Pt, Pd-Cu, Pd-Ni and Pd-Ag combinations. They have compared the efficiency of these bimetallic systems towards 4-NP reduction and found Pd-Ag system have similar activity to Pd-Au bimetallic catalyst. They could not

correlate the obtained activity with the characterization results and there was no significant difference in size between both catalysts.

Recently, Noveron *et al.,* [20] studied the activity of Pt, Au, Ag and Pd nanoparticles towards the catalytic reduction of 4-NP with $NaBH_4$. They synthesised these nanoparticles (Pt, Au, Ag and Pd) with average core diameters of about 2, 8, 26 and 39 nm, respectively, by using sodium rhodizonate as a bifunctional reducing & stabilizing agent. The results indicated that the activity of Ag NPs exhibited significantly higher rates for the reduction of 4-NP with $NaBH_4$ as compared to Au, Pt and the Pd NPs by a factor of ~ 1.9, 2, and 13, respectively. In addition, a remarkable improvement for the reduction of 4-NP as the Au, Pd and Ag particle size decreased [21–23]. The effect of Pd particle size on the activity of 4-NP reduction has been investigated recently by Rogers *et al.,* in which a systematic variation in Pd particle size was achieved *via* modification of sol-immobilisation method by varying the temperature and solvent environments during the sol-immobilisation synthesis procedure [23].

In this Chapter, we are interested in studying how the presence of Au and Ag in the Pd bimetallic system influences the overall catalytic performance towards the reduction of 4-NP by $NaBH_4$. So far, pre-formed colloidal Ag, Pd and AgPd nanoparticles with a narrow particle size distribution were prepared *via* a sol-immobilisation method. These pre-formed nanoparticles were then immobilised onto TiO_2 and tested for the reduction of 4-nitrophenol to 4-aminophenol (4-AP) under mild reaction conditions. In addition, the effect of reducing agent, reaction rate & kinetics and catalyst performance has been studied in this Chapter by using different reducing agent (i.e. $NaBH_4$, hydrous hydrazine and formic acid as an alternative green reducing agent). The results from formic acid was compared to the results obtained from the two common reducing agents in the literature, sodium borohydride and hydrous hydrazine.

5.2. Experimental

5.2.1. Catalyst preparation

The sol-immobilisation method, as detailed in Chapter 2 (see Section 2.3.2), was used to prepare monometallic Ag/TiO_2, Pd/TiO_2 and bimetallic catalysts Ag_xPd_{1-x}/TiO_2 at different nominal molar ratio (x = 0.13, 0.25, 0.5, 0.75, 0.87). In this method the PVA and $NaBH_4$ were used as stabilising and reducing agents, respectively. All catalysts were dried at 110 ^{O}C for 16 h. All theoretical loadings for monometallic and bimetallic catalysts in

this Chapter were chosen to be 1 wt. % on to TiO_2 (nominal loading). An abbreviated notation for all performed catalysts that used through this Chapter are presented in Table 5.1.

Table 5.1 Details of the monometallic Ag/TiO_2, Pd/TiO_2 and Ag_xPd_{1-x}/TiO_2 catalysts prepared with different Ag:Pd molar ratios.

Sample notation	%Ag (mol/mol)	%Pd (mol/mol)
Ag/TiO_2	100	-
Pd/TiO_2	-	100
$Ag_{0.13}Pd_{0.87}/TiO_2$	13	87
$Ag_{0.25}Pd_{0.75}/TiO_2$	25	75
$Ag_{0.5}Pd_{0.5}/TiO_2$	50	50
$Ag_{0.75}Pd_{0.25}/TiO_2$	75	25
$Ag_{0.87}Pd_{0.13}/TiO_2$	87	13

5.2.2. Catalyst characterisation

To better understand the catalytic performance, a range of characterisation techniques were used in this study. The catalysts were characterised using powder X-ray diffraction (XRD) for phase identification, crystallinity and crystallite size, X-ray photoelectron spectroscopy (XPS) for the identification of metal oxidation state and surface ratio of Ag/Pd, transmission electron microscopy (TEM) for particle size and particle size distribution , high angle annular dark field (HAADF) to understanding the structure/morphology of nanocatalysts and Microwave Plasma Atomic Emission Spectroscopy (MP-AES) for bulk determination of total metal loading and determination of leaching after the reaction performed. In addition, UV-Vis Spectroscopy used to assess the reduction of metal precursors and formation of colloidal metal nanoparticles (presence and absence of plasmon peak of Ag). The experimental procedures for all of these techniques are described previously in Chapter 2 (Section 2.7).

5.3. Results and discussion

5.3.1. UV-Vis spectroscopy

The UV-Vis spectroscopy was used during the formation of Ag and AgPd colloids to evaluate the state of reduction of the metal salt precursors to confirm the formation of mono- and bimetallic nanoparticles. In particular, the UV-Vis spectroscopy was used to evaluate the Ag surface plasmon resonance (SPR) band in monometallic catalyst (i.e. Ag/TiO_2). Figure 5.1 shows the UV-Vis spectrum of the $AgNO_3$ precursor before

reduction, with a peak at ~ 300 nm which is in good agreement with reported value [6]. In addition, there is no surface plasmon resonance band observed in between 330–700 nm range for $AgNO_3$ indicated that there is no Ag NPs were formed before the addition of $NaBH_4$. However, after adding $NaBH_4$ and stirring for 30 minutes, the maximum absorbance band for Ag NPs detected at ~ 400 nm (Figure 5.1). This absorption band was an indication for Ag NPs formation with small particles size(<10 nm) [16], which is consistent with TEM results (1.7 nm, will be discuss later in Section 5.3.4). These results are in good agreement with previous reports [24,25].
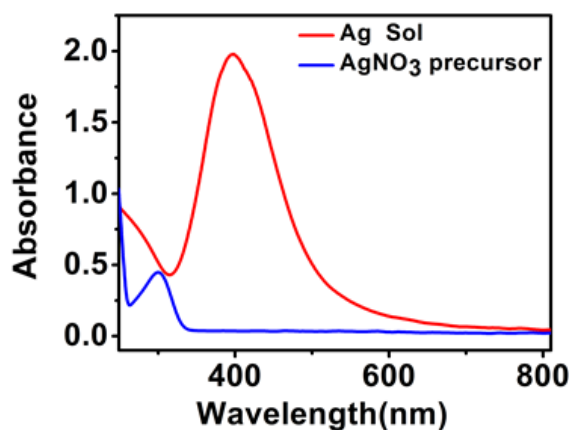
Figure 5.1 UV-Vis spectra of the $AgNO_3$ precursor before chemical reduction and the Ag sol generated after chemical reduction of the salt by $NaBH_4$ in the presence of PVA.

Generally, the SPR bands are influenced by the shape, morphology, size, dielectric environment and composition of the prepared nanoparticles [26,27]. Previous studies have shown that spherical Ag nanoparticles with diameter smaller than 100 nm show a plasmonic resonance in the UV-Vis spectra, centered between 400 and 470-500 nm depending on the size. Less than 10 nm nanoparticles in water resonate at about 400-410 nm and larger particles will show a red-shift [28]. In this work, the SPR band characteristics of Ag NPs was detected around ~400 nm (Figure 5.1), which strongly suggests that the Ag NPs were spherical and have smaller size less than 10 nm in agreement with TEM data as we will show later in Section 5.3.4.

The next step was to synthesise Pd-Ag nanoparticles by varying the Pd/Ag molar ratio using $NaBH_4$ in the presence of PVA. The obtained UV-Vis spectra of bimetallic colloids prepared with different Pd/Ag molar ratios are illustrated in Figure 5.2. According to the literature, no surface plasmon resonance band was observed for Pd nanoparticles [29],

unlike with Ag [16]. As seen from the UV-Vis spectra of AgPd sols, the surface plasmon resonance of Ag is not present, for the bimetallic colloidal nanoparticles with high concentration of Pd, namely $Ag_{0.25}Pd_{0.75}$ and $Ag_{0.13}Pd_{0.87}$, and the UV-Vis spectra is similar to that of Pd nanoparticle. This is a phenomenon commonly found in the formation of sols of bimetallic nanoparticles where one of the component metals lacks a surface plasmon band. This may be due to the fact that increasing the Pd content was the result of changes in the band structure of the Ag particles due to alloying with Pd, as reported in the literature by Deki et, al. [30]. However, with increasing the concentration of Ag in the composition of bimetallic, namely $Ag_{0.5}Pd_{0.5}$, $Ag_{0.75}Pd_{0.25}$ and $Ag_{0.87}Pd_{0.13}$, the SPR band for AgPd sols were observed at ~ 400 nm as abroad peaks depended on the concentration of Ag NPs in the solution. These results suggest that we have a mixture of AgPd alloys but also segregated Ag and Pd nanoparticles. At higher ratio of Pd we increase the AgPd alloy formation at lower no, which is in a good agreement with data reported in the literature [16].
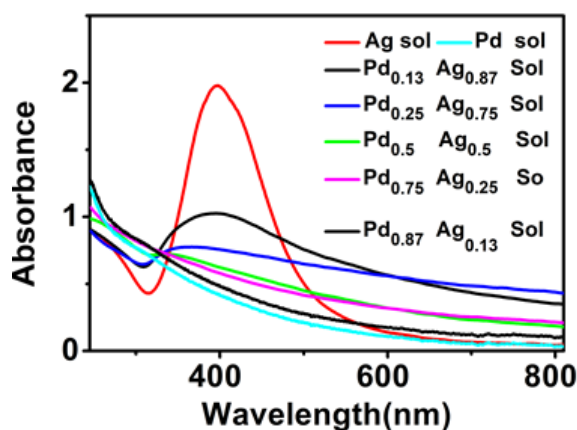
Figure 5.2 UV-Vis spectra of Ag, Pd sols and the Pd-Ag sols prepared with different Pd/Ag molar ratios, generated after chemical reduction of the Pd and Ag salts by $NaBH_4$ in the presence of PVA.

5.3.2. MP-AES analysis

MP-AES Analysis was used to determine the actual Ag, Pd and AgPd metal loading immobilised onto TiO_2, following a theoretical (nominal) metal loading of 1 wt. % in all cases. The actual loading of Ag and Pd in all the catalysts as obtained from the MP-AES analysis is presented in Table 5.2. The data confirm that the metal loading of all the samples is close to the expected nominal value. In addition, these results imply that the

Ag/Pd ratio can be easily tuned by adjusting the ratio of metal precursors during preparation.

Table 5.2 Results of MP-AES analysis for Pd/TiO_2, Ag/TiO_2 and Ag_xPd_{1-x}/TiO_2 catalysts.

Catalyst	Ag wt. %	Pd wt. %
Ag/TiO_2	0.98	-
Pd/TiO_2	-	0.94
$Ag_{0.13}Pd_{0.87}/TiO_2$	0.13	0.86
$Ag_{0.25}Pd_{0.75}/TiO_2$	0.23	0.75
$Ag_{0.5}Pd_{0.5}/TiO_2$	0.5	0.48
$Ag_{0.75}Pd_{0.25}/TiO_2$	0.74	0.24
$Ag_{0.87}Pd_{0.13}/TiO_2$	0.85	0.12

5.3.3. Powder X-Ray Diffraction (XRD)

XRD is an efficient tool to identify the crystal structure of supported nanoparticles, especially for bimetallic nanoparticles [31,32]. In order to study the crystal structure and crystal size of bare supports and/or gaining valuable information of the supported nanoparticles, XRD was conducted for bare TiO_2 (P25) support, monometallic (Ag/TiO_2) and a range of bimetallic catalysts Ag_xPd_{1-x}/TiO_2. The XRD patterns of bare support TiO_2 (P25), and all catalysts are presented in Figure 5.3. The diffraction peaks corresponding to TiO_2 (P25) , which is a mixture of anatase and rutile (85:15, respectively) were clearly detected at $2\theta = 27.5°$, $36.2°$, $54.5°$ and $69.2°$ for the rutile phase and these particular diffraction peaks were obtained by referring to the JCPDS file no. 21-1276 [33]. While the diffraction peaks corresponding to anatase phase TiO_2 could be observed as characteristic peaks at $2\theta = 25.3°$, $48.0°$, $53.8°$, and $62.6°$ (JCPDS No. 21-1272) [34].

The XRD diffraction peaks, if there is any, for metallic Ag phase in both mono- and bi-metallic catalysts would be expected to appear at $2\theta = 38.14°$, $44.46°$, $64.50°$ and $77.44°$, which are assigned to the Ag (111), (200), (220) and (311) planes, respectively, see vertical solid lines in Figure 5.3, (JCPDS, standard file no. 04-0783) [35]. Also, diffraction peaks of metallic Pd phase in mono- and bi-metallic catalysts, if there is any, are expected to be at $2\theta = 40.4°$, $46.9°$ and $68.6°$ (JCPDS file 01-087-0645), which corresponding to the Pd (111), (200) and (220) phases, respectively [36]. A PdO (Pd^{II}) diffraction peaks would be expected at $2\theta = 33.6°$, $33.9°$ and $54.8°$ (JCPDS file 00-006-0515) [36]. As can be seen from Figure 5.3, the absence of any diffraction peaks for

mon- and bimetallic Ag and Pd supported nanoparticles suggests the stabilization of these nanoparticles in very small sizes and hence out of the detection limits (<5 nm) of the XRD diffractometer. It was reported in the literature that prepared catalysts through sol-immobilisation method produced metal catalysts with mean metal particle size around 4 nm [10,23,36]. Such results are found to be in good agreement with our TEM results (see Section 5.3.4) where the mean metal particle sizes of the supported metal nanoparticles in all catalysts are less than 4 nm. Moreover, the high metal dispersion on TiO_2 support, which has been observed by TEM analysis, could also contribute to this observation [10].
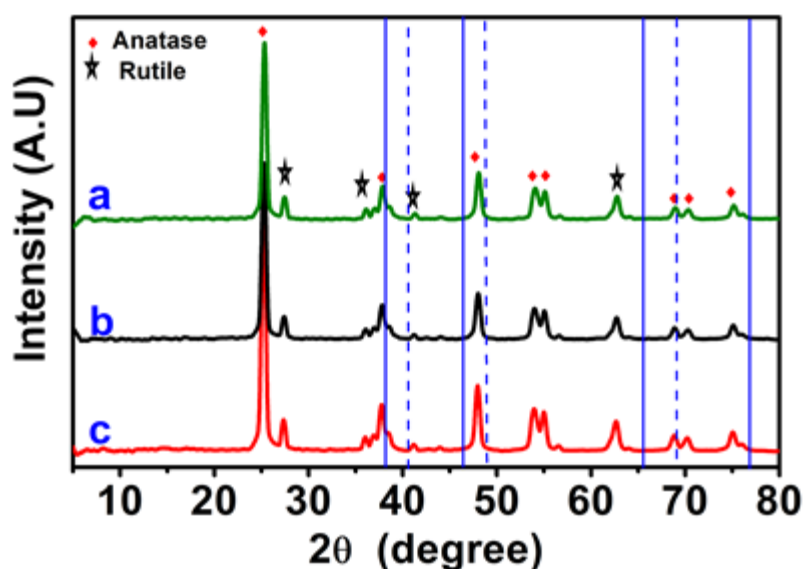
Figure 5.3 XRD diffraction patterns obtained for a) TiO_2 (P25), b) Ag/TiO_2 and c) $Ag_{0.5}Pd_{0.5}$/TiO_2. The positions of any Ag (solid lines), and Pd (dashed lines) nanoparticles that may exist in the catalysts.

5.3.4. Transmission electron microscopy (TEM) analysis

TEM was used to study the morphology of the supported metal nanoparticles and to obtain the mean metal particle size and particle size distribution of Ag/TiO_2, Pd/TiO_2 and Ag_xPd_{1-x}/TiO_2 catalysts. Figure 5.4 displays representative TEM images and particle size distribution of the as-synthesised catalysts. the TEM images clearly show good distribution of Ag and Pd nanoparticles on the surface of TiO_2 and there is no sign of aggregation/agglomeration of nanoparticles. The particle size data for all prepared catalysts are summarized in Table 5.3.

As can be seen from Table 5.3, the monometallic Ag/TiO_2 catalyst shows the smallest mean particle size (1.74 nm) with narrow particle size distribution, 1 – 4 nm, compared to the mean particle size of monometallic Pd/TiO_2 catalyst (2.62 nm) and all other bimetallic systems.

For the bimetallic AgPd supported nanoparticles, $Ag_{0.13}Pd_{0.87}/TiO_2$ catalyst has the smallest mean particle size (2.24 nm) with narrow particle size distribution, 1 – 5 nm, while $Ag_{0.87}Pd_{0.13}/TiO_2$ catalyst possesses the largest mean particle size (3.94 nm) with broad particle size distribution, 1 – 10 nm. Interestingly, the results clearly demonstrate that as silver loading increases from 13 to 87%, in this catalyst ($AgPd/TiO_2$), the resulting mean particle size increased from 2.24 to 3.94 nm. Similar trend was also reported by Sun [18]. In contrast to this observation, Yadong and co-workers saw that particles size were increased by increasing the Pd concentration in AgPd alloy. However, they used a different capping reagent (ODE) which can affect the binding in both metals and the strength of binding that will affect formation and growth [37]. It was claimed that the dependence of the size of the alloy nanoparticles on the composition to be related to the collision energy, sticking coefficient, rate of nucleation and growth between the constituent metals (Ag and Pd) [18].

Table 5.3 Mean value (nm) of particle sizes obtained by TEM analysis for mono- and bimetallic of Ag and Pd supported catalysts.

Catalysts	Mean particle size (nm)	Std-dev ($\pm$)
Ag/TiO_2	1.74	0.75
Pd/TiO_2	2.62	0.92
$Ag_{0.13}Pd_{0.87}/TiO_2$	2.24	0.58
$Ag_{0.25}Pd_{0.75}/TiO_2$	2.26	0.61
$Ag_{0.50}Pd_{0.50}/TiO_2$	2.77	0.76
$Ag_{0.75}Pd_{0.25}/TiO_2$	3.17	1.35
$Ag_{0.87}Pd_{0.13}/TiO_2$	3.94	1.78
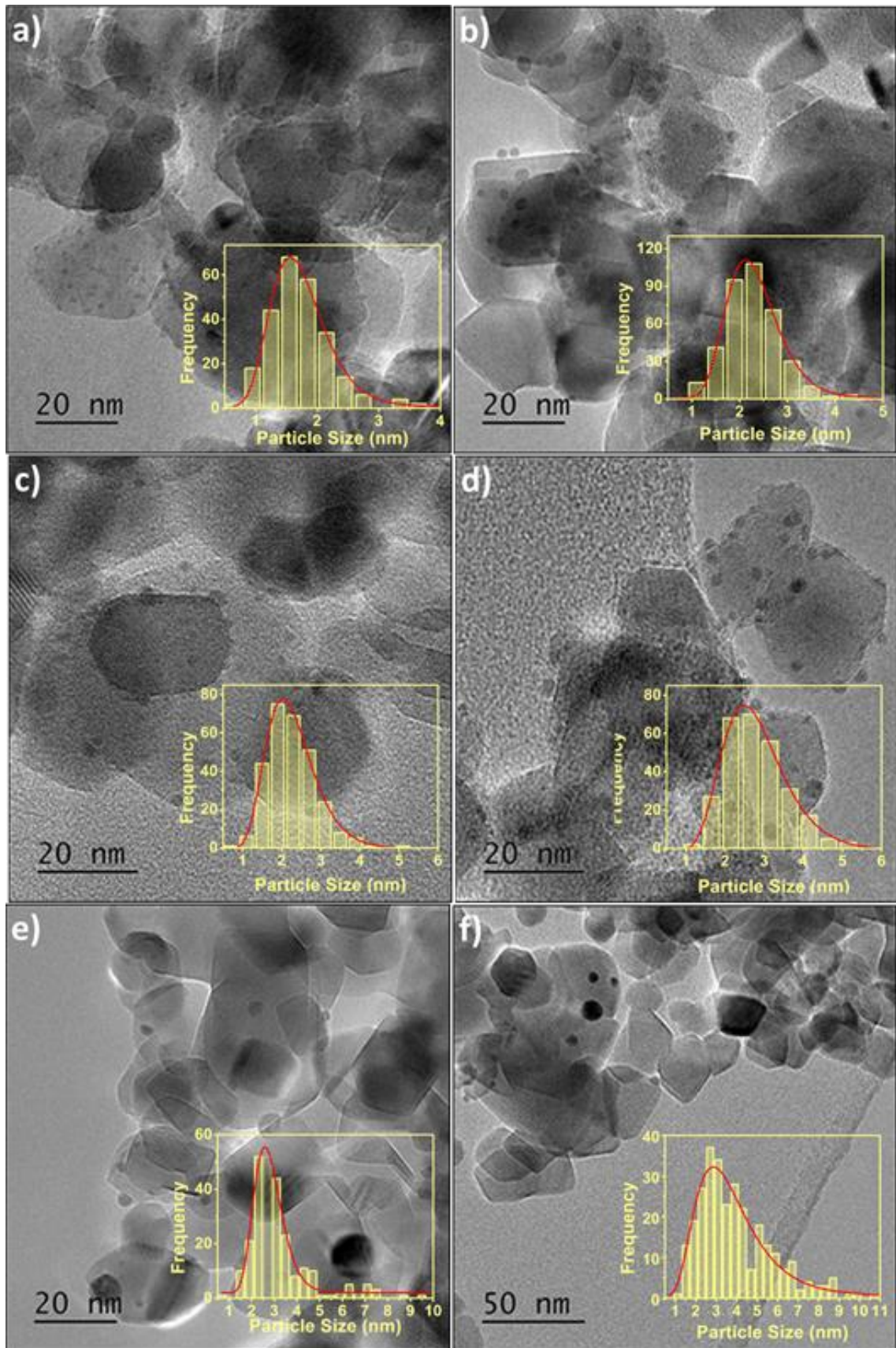
Figure 5.4 Representative TEM images and the corresponding NPs size distributions of a) Ag/TiO$_2$ b) Ag$_{0.13}$Pd$_{0.87}$/TiO$_2$ c) Ag$_{0.25}$Pd$_{0.75}$/TiO$_2$ d) Ag$_{0.5}$Pd$_{0.5}$/TiO$_2$ e) Ag$_{0.13}$Pd$_{0.78}$/TiO$_2$ and g) Ag$_{0.87}$Pd$_{0.13}$/TiO$_2$ catalysts.

5.3.5. X-ray photoelectron spectroscopy (XPS) analysis

XPS analysis was performed to analyse surface chemical composition and to quantify the oxidation state of prepared catalysts. Table 5.4 shows XPS data of Ag(3d) and Pd(3d) for mono- and bimetallic Ag and Pd nanoparticles supported on TiO_2 together with their mean particle size values obtained from TEM results. Figure 5.5(a and b) shows the corresponding XPS core level spectra of Ag(3d) and Pd(3d), respectively. The XPS results for Ag(3d) in the whole series of samples confirmed the presence of silver oxide at binding energy of (367.30-366.86 eV) which is in agreement with previous report [38]. No evidence for the Ag metallic state which expected to be at binding energy of 368.2 eV [39]. The absence of metallic Ag is mainly due to its oxidation during the drying step at 110 °C, which involves exposing the sample to air. Given the literature, it is very difficult to study the mixture of Ag oxides (i.e. Ag_2O and/or AgO) since their Ag3d peaks are so closely spaced and it's not an easy task to differentiate their peaks. However, the binding energy observed for Ag(3d) in this study for all samples is very close to the B.E of AgO (367.4 eV), while Ag_2O is at B.E of 367.8 eV [38].

The XPS spectra of Ag(3d) obtained for the monometallic Ag/TiO_2 catalyst, show two symmetric peaks with binding energies (B.E) centred at 367.3 eV and 373.7 eV, which correspond to $Ag3d_{5/2}$ and $Ag3d_{3/2}$ doublet transitions, respectively. These binding energies are very close to that reported for AgO (367.4 eV) with a small negative shift by (-0.1 eV).

In respect to the bimetallic Ag_xPd_{1-x}/TiO_2 catalysts, a downward shift in the binding energy of $Ag 3d_{5/2}$ peak was observed from 367.3 to 366.88 eV upon addition of Pd to the Ag samples (Table 5.4). It can be noticed from XPS data that the Ag(3d) peaks are further negatively shifted as Pd/Ag ratio increases, with the most pronounced shift occurring in the $Ag_{0.13}Pd_{0.87}/TiO_2$ catalyst (0.54 eV). This negative shift in binding energy can be attributed to the strong metal-metal interaction and hence synergistic effect between Pd and Ag, and thus suggesting the formation of the AgPd alloy. Similarly, this observation has been reported previously by Zhu *et al.,* [40]. Moreover, the spectra indicated that when Pd/Ag ratio is increased, the full width at half maximum (FWHM) of the Ag(3d) peaks is broadened (Figure 5.5 a) which can be attributed to the reduced size of the AgPd NPs with increasing Pd/Ag ratio. Such results are in a good agreement with TEM results (see Table 5.4) where the mean metal particle sizes of the supported metal nanoparticles are decreased with increasing Pd/Ag ratio.

For the monometallic (Pd/TiO_2) and bimetallic ($AgPd/TiO_2$) catalysts, the XPS data of Pd(3d) region indicate the predominate of both metallic (Pd^0) and oxidic (Pd^{II}) states of palladium with BE ranging from (334.7-334.2 eV) and from (336.6- 336.2 eV), respectively. However, only metallic (Pd^0) state of palladium is predominate in $Ag_{0.75}Pd_{0.25}/TiO_2$ and $Ag_{0.87}Pd_{0.13}/TiO_2$ catalysts without any evidence for PdO phases. The oxidation state of palladium on the surface of the supported bimetallic catalysts is presented in Table 5.4.

Table 5.4 XPS data of Ag(3d) and Pd(3d) for mono- and bimetallic Au and Pd nanoparticles supported on TiO_2 along with their mean particle size values obtained from TEM.

Catalyst	BE (eV)		Pd^0/Pd^{II} (%)	Particle size (nm)	Ag:Pd (%)
	Ag($3d_{5/2}$)	Pd($3d_{5/2}$)			
Ag/TiO_2	367.3(-0.1)	---		1.74	---
Pd/TiO_2	---	334.7(-0.7)	83/17	2.62	---
$Ag_{0.13}Pd_{0.87}/TiO_2$	366.9(-0.54)	334.5(-0.9)	85/15	2.24	5:95
$Ag_{0.25}Pd_{0.75}/TiO_2$	366.88(-0.52)	334.3(-1.1)	86/14	2.26	13: 87
$Ag_{0.5}Pd_{0.5}/TiO_2$	366.9(-0.5)	334.26(-1.14)	94/6	2.77	40:60
$Ag_{0.75}Pd_{0.25}/TiO_2$	367.05(-0.35)	334.22(-1.18)	100/0	3.17	66:34
$Ag_{0.87}Pd_{0.13}/TiO_2$	367.2(-0.2)	334.2(-1.20)	100/0	3.94	83:17

Note: BE of bulk AgO = 367.4eV [43] BE of bulk Pd^0 = 335.4 eV [42]

There is an evidence from Table 5.4 that the ratio of Pd^{II}/Pd^0 species increases with increasing the stoichiometric ratio of Pd/Ag in the bimetallic catalysts. As a result, the highest amount of Pd^{II} species (15%) was found in $Ag_{0.13}Pd_{0.87}/TiO_2$ catalyst, while the smallest amount of Pd^{II} species (6%) was observed in $Ag_{0.5}Pd_{0.5}/TiO_2$ catalyst. Moreover, it was found that there is a correlation between the mean particle size of bimetallic catalyst Ag_xPd_{1-x}/TiO_2 (obtained by TEM) and the extent of Pd^{II} (see Table 5.4), where the mean particle size was found to be smaller in the catalyst with more Pd^{II}. These results are in a good agreement with a recent study by Rogers *et al.,* [23] who synthesized small Pd NPs by sol immobilization method and found that the smallest Pd nanoparticles size (1.4 ± 0.4 nm) has the highest ratio of Pd^{II} (71%) and only 29% of Pd^0). This observation can be attributed to the fact that small Pd nanoparticles form an oxidic surface layer at room temperature when exposed to air, as has been reported from previous literature [41].

147

The binding energy of Pd3d$_{5/2}$ peak in monometallic Pd/TiO$_2$ catalyst (334.7 eV) is lower than that of bulk palladium (335.4 eV) [42]. This suggests the presence of strong metal-support interaction (SMSI) between palladium nanoparticles and the support (TiO$_2$). For bimetallic catalysts, the addition of Ag to the Pd in the bimetallic catalysts led to a further negative shift in binding energy of Pd 3d$_{5/2}$ peaks (334.5-334.2 eV), resulting in enhanced electronegativity of the nanoparticles(Figure 5.5 b), and thus reflecting electron transfer between Pd and Ag [40]. This observation is strongly suggesting that, in addition to the strong metal-support interaction (SMSI), there is an evidence for further metal-metal interaction in AgPd bimetallic system.

Regarding the surface composition, XPS data confirmed that AgPd metal loading and ratios which were found to be slightly in agreement with MP-AES analysis, Ag:Pd molar ratios are shown in Table 5.4. However, these data cannot be considered as a true representation of the real surface composition. This suggests that all the supported nanoparticles are highly confined and well distributed on the surface of the support with very small particle sizes.
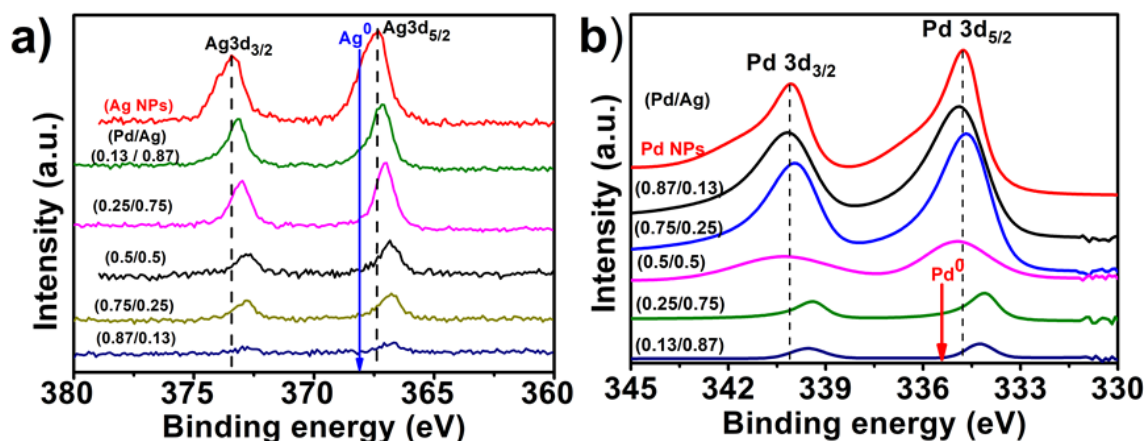
Figure 5.5 XPS core level spectra of a) Ag(3d) and b) Pd(3d) for monometallic (Ag/TiO$_2$ and Pd/TiO$_2$) and series of bimetallic Ag$_x$Pd$_{1-x}$ /TiO$_2$ catalysts; nominal Pd/Ag ratios are as indicated.

5.4. Catalytic reduction of 4-nitrophenol by NaBH₄ over Ag$_x$Pd$_{1-x}$/TiO₂ catalysts

Herein this Section, the reduction of 4-NP by NaBH₄ was used to evaluate the efficiency of monometallic Ag/TiO₂ and Pd/TiO₂ catalysts in addition to optimising the stoichiometric molar ratio between Ag and Pd in the bimetallic system (Ag$_x$Pd$_{1-x}$/TiO₂, where x = 0.13, 0.25, 0.5, 0.75 and 0.87) with high performance towards the probe reaction.

5.4.1. Activity testing

The catalytic performance of monometallic (i.e. Ag/TiO₂ & Pd/TiO₂) and bimetallic (i.e. Ag$_x$Pd$_{1-x}$/TiO₂) catalysts was tested in the reduction of 4-nitrophenol (4-NP) by NaBH₄ as reducing agent. The reaction was conducted under constant stirring (1000 rpm) and mild reaction conditions using water as the desired solvent, at temperature of 30 °C and atmospheric pressure. A large excess of NaBH₄ over 4-NP was used (NaBH₄/4-NP molar ratio = 30). This will simplify the reaction rate to follow pseudo first order reaction kinetics. Typically; 5 ml of NaBH₄ (0.03 M) is added into a 100 ml round bottom flask, as batch reactor, that contains the desired amount of catalyst and the aqueous solution of 4-NP (45 ml, 1.35×10^{-4} M, 4-NP/metal molar ratio = 13). The total volume of the reaction mixture was 50 ml. At different time interval (min), aliquot from the reaction mixture was then withdrawn using 1 ml syringe equipped with a filter (0.45 µm pore size) and transferred into the UV cuvette for a UV-Vis measurement. Subsequently, the UV-Vis spectra (in the range of 200 – 800 nm) were recorded and the concentration of 4-NP traced from the decay of the absorption band centred at 400 nm. Based on the calibration curve of standard solution of 4-NP, which previously described in Chapter 2, the molar extinction coefficient was estimated for 4-NP to be 18620 M^{-1} cm^{-1}. Finally, the concentration of 4-NP, as a function of time during the catalytic reaction, was calculated using the Beer's Lambert's law equation as discussed in Chapters 2 and 3.

5.4.2. Catalytic activity of monometallic Ag/TiO₂ & Pd/TiO₂ catalysts.

The catalytic activity of Ag/TiO₂ catalyst toward the reduction of 4-NP by NaBH₄ is shown in Figure 5.6. It can be seen that, there is a linear relationship between ln[4-NP]

and the time of reaction (min). This suggests that the reaction follows pseudo-first-order reaction kinetics. The apparent rate constant (K_{app}) of Ag/TiO$_2$ catalyst is 0.18 min^{-1}.

Comparing the activity of Ag/TiO$_2$ with monometallic Pd and Au supported on TiO$_2$, which previously studied in Chapter 3, it was found that Pd/TiO$_2$ catalyst exhibited the highest catalytic activity amongst the monometallic analogous of Au and Ag. The activity trends are in the following order; Pd/TiO$_2$ (0.20 min^{-1}) > Ag/TiO$_2$ (0.18 min^{-1}) > Au/TiO$_2$ (0.14 min^{-1}), however, the differences in the K_{app} values are slightly small particularly, between Ag/TiO$_2$ and Pd/TiO$_2$ catalysts. This activity trend agrees well with the results reported by Srisombat [44]. It's well know that Pd nanoparticles have the ability to adsorb hydrogen in many organic reactions [45,46]. So far, the highest activity observed for Pd/TiO$_2$ catalyst (with mean particle size = 2.6 nm) is expected due to the fact that Pd nanoparticles have active sites for hydrogen adsorption, and hence facilitate the removal of hydrogen from NaBH$_4$ which then can be used for the reduction of 4-NP.

The high activity of Ag/TiO$_2$ catalyst, compared to Au/TiO$_2$, could be correlated to the small mean particle size obtained for the former (1.7 vs 2.6 nm for Ag and Au, respectively). These results are in agreement with previous work done by Al-Marhaby *et al.,* [47] who demonstrated that the Ag NPs with smaller particle sizes have higher activity and hence interaction with 4-NP.
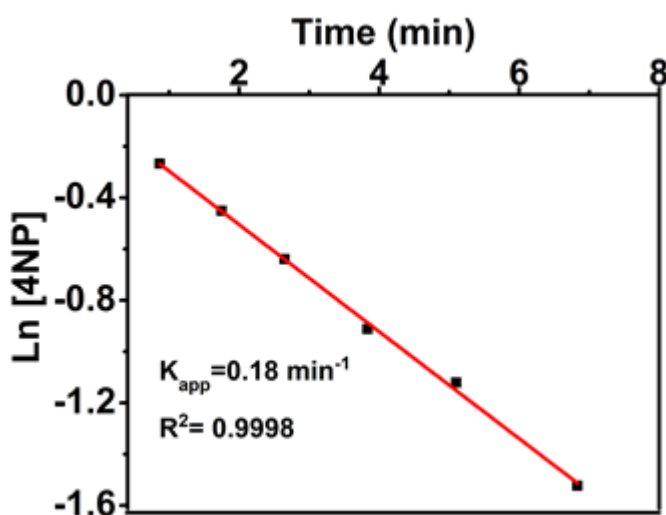
Figure 5.6 ln[4-NP] as a function of time plot for Ag/TiO$_2$. Reaction conditions: 4-NP/metal molar ratio = 13, NaBH$_4$ /4-NP molar ratio = 30, stirring rate = 1000 rpm and T = 30 ºC

5.4.3.　Catalytic activity of bimetallic Ag_xPd_{1-x}/TiO_2 catalyst series.

As we discussed previously in Section 5.4.2, monometallic Ag/TiO_2 and Pd/TiO_2 catalysts showed a promising activity towards the reduction of 4-NP by $NaBH_4$. According to the literature, we believe that bimetallic system containing both Ag and Pd supported on TiO_2 would have better activity than the monometallic analogous. Initially, we have prepared $AgPd/TiO_2$ catalyst (Ag:Pd molar ratio = 1:1) and then was tested in the reduction of 4-NP, under similar reaction conditions as in the preceding Section. The results showed that the prepared catalyst ($Ag_{0.5}Pd_{0.5}/TiO_2$) showed promising and higher activity with K_{app} value of 0.8 min^{-1} than monometallic Ag/TiO_2 and Pd/TiO_2 by a factor of ~ 4.4 and 4 respectively. However, we believe that the obtained performance could be further tuned up by optimizing the best stoichiometric ratio between Ag and Pd during the synthesis process. In this context, a series of bimetallic $AgPd/TiO_2$ catalysts with different Ag:Pd molar ratio were prepared (see Section 5.2.1) with a chemical formula of Ag_xPd_{1-x}/TiO_2, where, x = 0.13, 0.25, 0.75 and 0.87. The activity of the bimetallic catalysts was screened towards the reduction of 4-NP under the same reaction conditions conducted for monometallic Ag/TiO_2 and Pd/TiO_2 catalysts (see Section 5.4.1). The results of the catalytic reduction of 4-NP by $NaHB_4$ over Ag_xPd_{1-x}/TiO_2 catalysts are illustrated in Figure 5.7 and the obtained apparent rate constant values (K_{app}) are summarized in Table 5.5.
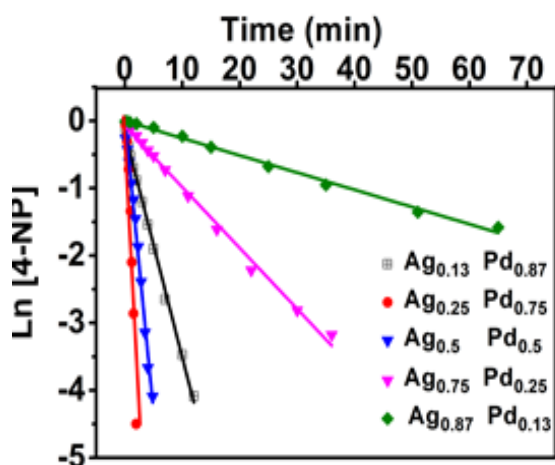
Figure 5.7 ln[4-NP] as a function of time for 4-nitrophenol reduction over the series of Ag_xPd_{1-x}/TiO_2. Reaction conditions: 4-NP/metal molar ratio = 13, $NaBH_4$ /4-NP molar ratio = 30, 1000 rpm, 30 ºC.T = 30 ºC

As can be seen from this Figure, the reaction over all catalysts follows a pseudo first order reaction kinetics. In addition, the data presented in Table 5.5, confirm that all bimetallic

catalysts have higher activity than monometallic analogous. As can be seen, the K_{app} values for bimetallic system (Ag_xPd_{1-x}/TiO_2) are in the arrange of 0.23 – 1.30 min^{-1}, while for Ag/TiO_2 and Pd/TiO_2 catalysts are 0.18 and 0.2 min^{-1}, respectively. Obviously, $Ag_{0.25}Pd_{0.75}/TiO_2$ catalyst with Ag:Pd molar ratio of 0.25 : 0.75 exhibited the highest activity (K_{app} = 1.3 min^{-1}) amongst all other bimetallic combinations. In contrast, bimetallic $Ag_{0.87}Pd_{0.13}/TiO_2$ catalyst, with the poorest palladium content (13 %), showed the lowest activity (K_{app} of 0.23 min^{-1}).

Table 5.5 Catalytic activity of Pd/TiO_2, Ag/TiO_2 and Ag_xPd_{1-x}/TiO_2 catalysts on the reduction of 4-NP by $NaBH_4$.

Catalyst	K_{app} (min^{-1})
Pd/TiO_2	0.20
$Ag_{0.13} – Pd_{0.87}/TiO_2$	0.35
$Ag_{0.25} – Pd_{0.75}/TiO_2$	1.30
$Ag_{0.5} – Pd_{0.5}/TiO_2$	0.8
$Ag_{0.75} – Pd_{0.25}/TiO_2$	0.27
$Ag_{0.87} – Pd_{0.13}/TiO_2$	0.23
Ag/TiO_2	0.18

To better understanding the effect of Ag/Pd ratio in the performance of the bimetallic system, a relationship between the apparent rate constant values (K_{app}) and the mean particle sizes are plotted against Pd content (%), in Ag_xPd_{1-x}/TiO_2 catalyst, and presented in Figure 5.8. As can be seen from this figure, a volcano shape is obtained with a highest activity observed for $Ag_{0.25}Pd_{0.75}/TiO_2$ catalyst. Initially, the activity was increased as the Pd to Ag molar ratio increases until reached a maximum value with the catalyst having Pd:Ag molar ratio of 0.75:0.25 (K_{app} = 1.3 min^{-1}). This was expected giving the fact that Pd is more active in this reaction than supported Ag NPs. Afterwards, a remarkable decrease in the catalyst's activity was observed upon increasing the Pd to Ag molar ratio from 0.75 to 0.87. As a result, the K_{app} value of the bimetallic catalyst with rich Pd content ($Ag_{0.13}Pd_{0.87}/TiO_2$) decreased to 0.35 min^{-1}.

In addition, and as can be seen from Figure 5.8, there is a reciprocal relationship between the K_{app} values and the mean sizes of supported NPs. Clearly, our results demonstrate that catalysts' activity increases with decreasing the mean particles size of the supported nanoparticles. The highest active catalyst ($Ag_{0.25}Pd_{0.75}/TiO_2$) have mean particle size of 2.26 nm, while the lowest active catalyst ($Ag_{0.13}Pd_{0.87}/TiO_2$) possess a mean value of ~ 4 nm. Similar observation, in regard to the particle size and their activity towards the reduction of 4-NP by $NaBH_4$, were recently reported by Rogers *et al.,* [23]. They prepared

1 wt.%Pd/TiO$_2$ catalyst using the same sol-immobilisation method, which is used here and found that catalysts with smallest mean particle size ($\sim$ 2.5 nm) showed the highest activity for the reduction of 4-NP by NaBH$_4$. It worth to mention here that, although Ag$_{0.25}$Pd$_{0.75}$/TiO$_2$ catalyst showed the highest activity (K$_{app}$ = 1.3 min^{-1}, 2.26 nm), it has relatively larger mean particle size than the less active Ag$_{0.13}$Pd$_{0.87}$/TiO$_2$ catalyst (K$_{app}$ = 0.35 min^{-1}, 2.24 nm). This suggests that there might be another factor which could be responsible for the observed activity such as synergistic effect between Ag and Pd and the metal/metal interfaces [48] which confirmed by XPS results.
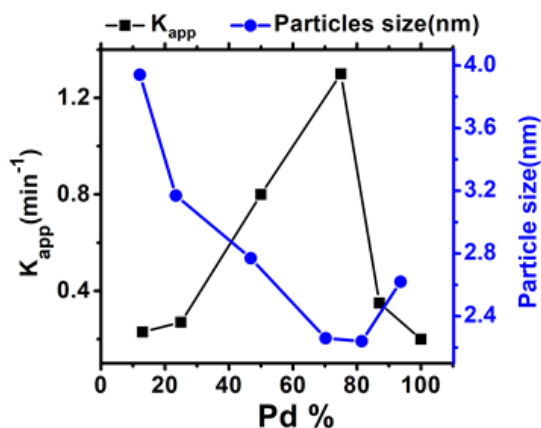
Figure 5.8 The apparent rate constant (K$_{app}$) and mean particle sizes against Pd content (%) in the series of Ag$_x$Pd$_{1-x}$/TiO$_2$ catalysts. Reaction conditions: 4-NP/metal molar ratio = 13, NaBH$_4$ /4-NP molar ratio = 30, stirring rate = 1000 rpm and T = 30 ºC.

5.5. Reduction of 4-Nitrophenol using formic acid as H donor

Over the last half a century, catalytic transfer hydrogenation has been shown to offer significant potential value in the field of organic and biochemistry [51]. More recently, the idea of employing chemical hydrides, e.g. borohydrides, hydrous hydrazine, and especially formic acid, for liquid phase storage of hydrogen under ambient conditions has been the subject of intense research interest [52].

Formic acid (FA) is a major product formed during biomass processing [53]. It has been considered as one of the most promising materials for hydrogen storage today due to its high volumetric hydrogen content, liquid state at room temperature, high stability, environmental safety, low toxicity [54]. Also, it can be used to generate different gaseous products (such as; H_2 and CO_2, etc.) by decomposition [55]. Furthermore, formic acid (and its salts) are able to donate hydrogen more easily than other potential hydrogen donors[56]. This results from the fact that a stable molecule such as CO_2, which has a very large negative enthalpy of formation released from the hydrogen donor during the transfer hydrogenation reaction. Simply stated, the hydrogen donation is irreversible. This is one of the major driving forces for the high reactivity of formats [55].

Formic acid has also been considered as a fuel in direct formic acid fuel cells (DFAFC) with its gravimetric hydrogen capacity of 4.4 wt%[54]. Hydrogen stored following formic acid decomposition can be released *via* a catalytic dehydrogenation reaction (Equation 5.1). However, the unwanted dehydration reaction (Equation 5.2) can also take place according to existing reaction conditions and catalyst selection. Increased heat and acidity generally promote dehydration reactions

$$HCOOH \rightarrow CO_2 + H_2 \qquad \Delta G = -48.4 \text{ kJ mol}^{-1} \qquad \text{(Eq. 5.1)}$$

$$HCOOH \rightarrow CO + H_2O \qquad \Delta G = -28.5 \text{ kJ mol}^{-1} \qquad \text{(Eq. 5.2)}$$
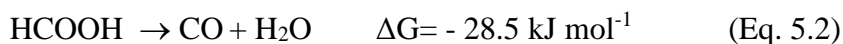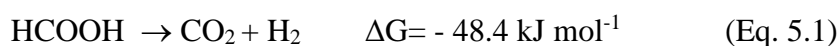
To close the cycle (Figure 5.9), CO_2 can be hydrogenated back to formic acid resulting in a CO_2 neutral process with a high selectivity and high catalytic activity [55]. A range of methods were used to close this loop for cheap and renewable production of hydrogen, compared to wind energy, such as electrolysis [57].

HCOOH

Hydrogen storage   Hydrogen delivery

H_2 H_2

CO_2
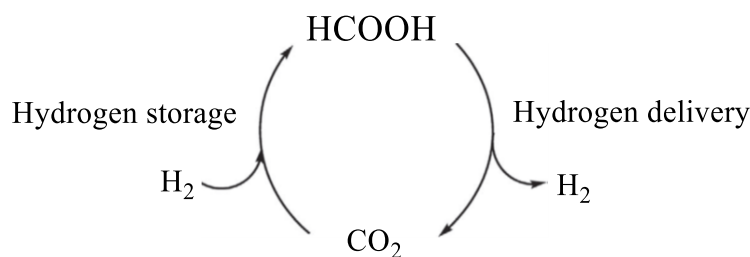
Figure 5.9 Formic acid/carbon dioxide cycle for hydrogen storage.

Formic acid has been employed as H-donor for different hydrogenation reactions [20–28]. However, to date the use of formic acid as reducing agent (H-donor) for reduction of 4- nitrophenol has not been thorough investigated and reported in the literature.

Gowda *et al.,* [51] reported the efficient catalytic transfer hydrogenation with formic acid using 10% Pd/C catalyst and it was shown the mild, simple and rapid reduction of nitro-group. They performed this reaction at room temperature for more than 50 different aromatic nitro compounds, including 4-nitrophenol. Their investigation showed that most of these compounds were converted to their corresponding amino in good yield. However, the method fails in case of halogen substituted aromatic nitro compounds and they attributed to the halide ion which may deactivate the Pd/C catalyst. The reduction time in most cases was in the range of 3 to 30 min, however, the reaction completion time for 2,2-dinitrodibenzyle was 60 min, while for 4-nitrophenol was 10 min with conversion yield of 91%. Furthermore, this investigation showed that using formic acid as H-donor for aromatic nitro compounds has several advantages such as; (i) selective reduction of aromatic nitro compounds in the presence of other reducible groups, (ii) rapid reaction, (iii) high yields of substituted anilines, and (iv) no pressure apparatus is needed (v) safety.

Subsequently, Javaid *et al.,* [58], investigated the reduction of 4-nitrophenol using aqueous formic acid under mild reaction conditions in catalytic tabular flow reactors. They modified the inner surface of the tubular reactors by adding a thin layer of Pd metal, a porous Pd and PdO layers. They demonstrated that the reduction of 4-NP was dependent

on the catalyst layer type, temperature, pH, concentration of formic acid, and residence time in the reactor. Furthermore, thier study showed that PdO provides more surface OH group than metallic Pd surface and hence providing more active sites with the substrate (4-NP). Furthermore, the study showed that 4-NP was reduced in transfer hydrogenation process and not by molecular H_2 generated from the dehydrogenation of formic acid. They validated their assumption by a control test in the absence of 4-NP resulting with no consumption of formic acid suggesting that the reduction of 4-NP was occurred *via* hydrogen transfer mechanism [58].

The reduction reaction of 4-NP with formic acid is:
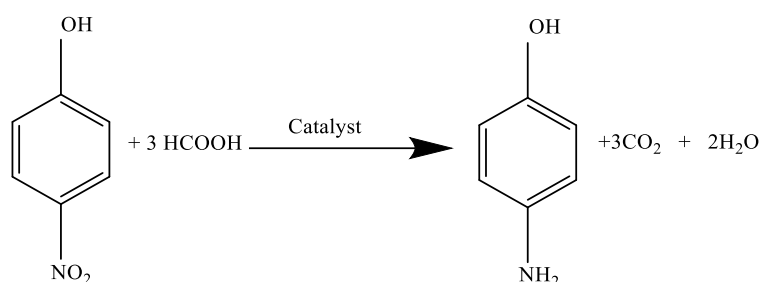
Scheme 5.1 Reduction of 4-NP using formic acid [58]

In this Section, formic acid as green reducing agent for the reduction of 4-nitrophenol is used instead of $NaBH_4$. Different mono metallic (Au, Pd and Ag) and bimetallic catalyst, namely, AuPd and AgPd supported on TiO_2 are examined as catalysts for the reduction of 4-NP using formic acid as hydrogen donor. In addition, the influence of formic acid concentration in the apparent rate constants and the effect of the bimetallic composition and optimum ratio have been studied with respect to the same reaction.

5.5.1. Catalytic reduction of 4-nitrophenol by formic acid (FA)

The reduction of 4-NP to 4-AP using formic acid was carried out in a glass reactor, described in detail in Chapter 2 (Section 2.4.1). The reaction was conducted under constant stirring (1000 rpm) and mild reaction conditions using water as solvent at 30 °C and atmospheric pressure. To maintain a pseudo-first order reaction kinetics, an excess of formic acid was used (formic acid/4-NP molar ratio =15-55, with an optimum value of 45). Typically; 5 ml of formic acid is added into a 100 ml round bottom flask, as batch reactor, that contains the desired amount of catalyst and the aqueous solution of 4-NP (45 ml, 1.35×0^{-4} M , 4-NP/metal molar ratio = 13). The total volume of the reaction mixture

was 50 ml. At different time interval (min), aliquot from the reaction mixture was then withdrawn using 1 ml syringe equipped with a filter (0.45 µm pore size) and transferred into the UV cuvette for a UV-Vis measurement. Subsequently, the UV-Vis spectra (in the range of 200 – 800 nm) were recorded and the concentration of 4-NP traced from the decay of the absorption band centred at 317 nm. Based on the calibration curve of standard solution of 4-NPwith formic acid, which previously described in Chapter 2, the molar extinction coefficient was estimated to be 9784 M^{-1} cm^{-1}. Finally, the concentration of 4-NP, as a function of time during the catalytic reaction, was calculated using the Beer's Lambert's law equation as discussed in Chapters 2 and 3.

 It is worth to mention here that, upon the addition of formic acid to the reaction mixture, the 4-NP peak remains unaltered at λ 317 and did not move to 400 nm, as we observed previously under basic conditions (i.e. when using $NaBH_4$ as a reducing agent), see Figure 5.10. Furthermore, the colour of 4-NP solution changed from pale yellow to colourless, which is also in contrast of the case of $NaBH_4$ (Figure 5.10a). This observation suggests that in the present of formic acid the nitrophenolate ions peak could not be observed because the formic acid acidifies the reaction medium (pH = 2.5), which decrease the rate of 4-NP ionization to 4-nitrophenolate ion, hence, no shift in the absorption band of 4-NP was observed [58]. In a control experiment, where 4-NP and formic acid are used in the absence of catalyst, no conversion of 4-nitrophenol was observed, indicating that 4-NP is not reduced by formic acid solely. However, a significant decrease of the peak at $\lambda = 317$ nm is observed in the presence of catalyst, along with the development of a peak at $\lambda = 300$ nm, indicating the formation of 4-AP. The presence of isosbestic points in the UV-

Figure 5.10 a) Image for colour change during catalytic reduction of 4-nitrophenol to 4-aminophenol by formic acid. b) An example for UV-Vis spectra collected during the catalytic reduction of 4-nitrophenol by formic acid using a Pd/TiO_2 catalyst.
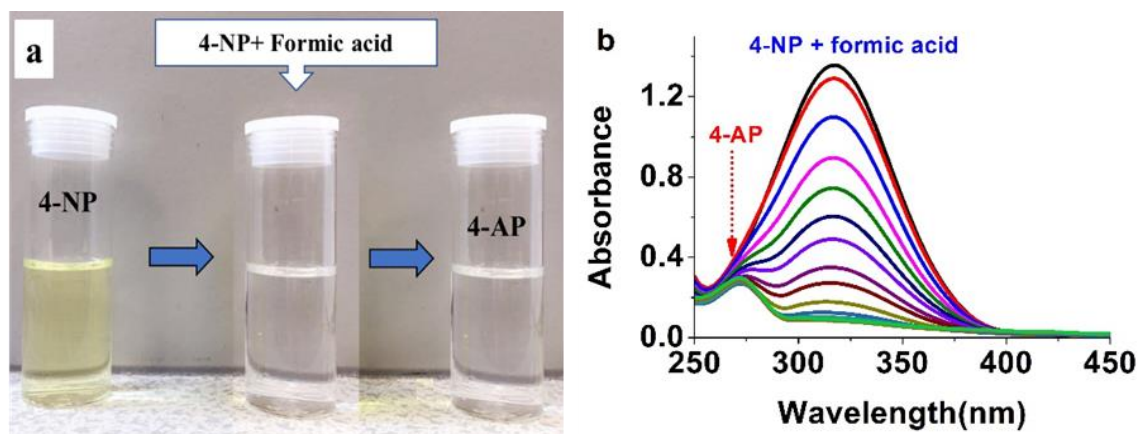
Vis spectra (Figure 5.10b) suggests that 4-AP is a sole product of the reaction, and consequently no side reaction occurs, which is in agreement with previous report [58]. In addition, the GC-MS signals were used to confirm that 4-AP is the sole product of this reduction (see appendix Figure A1).

5.5.2. Influence of formic acid concentration

The effect of formic acid (FA) concentration on the catalytic reduction of 4-NP was investigated initially. Higher concentration of formic acid is required to use in order to maintain the pseudo first-order reaction conditions, and then the apparent rate reaction constant (K_{app}) is dependent solely on the concentration of 4-NP. Here, concentration of 4-NP (1.35×0^{-4} M) and amount of catalyst (Pd/TiO$_2$, 4-NP/metal molar ratio = 13) were constrained to a constant value and the formic acid concentration was varied, FA/4-NP molar ratio = (15-55), as shown below in Figure 5.11.
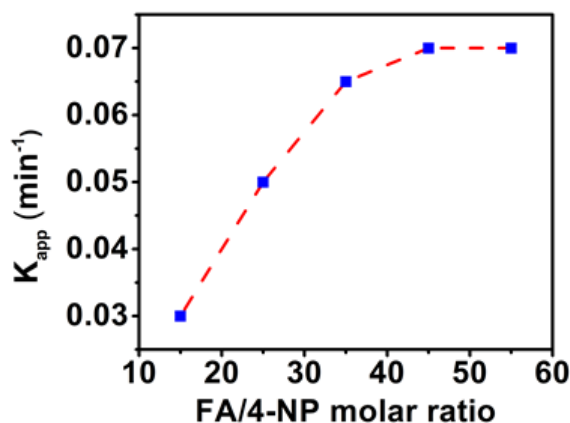
Figure 5.11 Effect of the concentration of formic acid on K_{app} for reduction of 4-NP over Pd/TiO$_2$. Reaction conditions: 4-NP/metal molar ratio = 13, stirring rate = 1000 rpm and T = 30 ºC, FA/4-NP molar ratio = (15-55) with a constant concentration of 4- NP[1.35×0^{-4} M].

 It could be shown that the apparent rate constant is increasing with an increasing concentration of formic acid until maximum value with a molar ratio of formic acid/4-NP = 45. Subsequently, further increase in the concentration of formic acid results in a flat plateau at higher concentration. The trend of the graph obtained from Figure 5.11 is similar to the graph reported by Suzuki *et al.,* [58] who studied the effect of formic acid concentration on the conversion of 4-NP at 30 °C. The nonlinear relationship between the K_{app} values and the formic acid concentration, in addition to the saturation at high concentrations, directly indicate that the reactants are competing for the reactive sites on the metal

surface. This means that there should be an optimal concentration where the reaction rate has reached a maximum value. Moreover, it becomes evident that this reaction follows a Langmuir-Hinshelwood mechanism. Therefore, a formic acid /4-nitrophenol molar ratio of 45 has chosen to be the optimum molar ratio in this work.

5.5.3. Catalytic activity of bimetallic Au_xPd_{1-x}/TiO_2

Monometallic Au and Pd nanoparticles supported on TiO_2 (i.e. Au/TiO_2 and Pd/TiO_2 catalysts) showed promising activity for the reduction of 4-NP by $NaBH_4$ (K_{app} = 0.14 and 0.2 min^{-1}, respectively), as described previously in Chapter 3. Moreover, the activity was further enhanced with bimetallic Au and Pd system (i.e. $AuPd/TiO_2$ catalyst, K_{app} = 0.38 min^{-1}) due to the synergistic effect in AuPd alloy with an optimum molar ratio of Au:Pd = 1:1. To further optimize the reaction conditions, we attempted, herein this Section, to explore the effect of reducing agent on this reaction by replacing $NaBH_4$ with an alternative renewable source such as formic acid (HCOOH) which is safe, easy to handle and requires no high pressure equipment. To best of our knowledge, using bimetallic combination of Au and Pd supported on TiO_2 as a catalyst together with formic acid, as a reducing agent, have not been reported before for the reduction of 4-NP. The lack of literature on use of this bimetallic system in this reaction may be due to the fact that Au NPs are not active in formic acid decomposition at mild reaction conditions [59–61].

Initial screening for the activity of monometallic Au/TiO_2 and Pd/TiO_2 catalysts for this reaction, using formic acid as a H-donor, showed that Au/TiO_2 catalyst is inactive, while Pd/TiO_2 is active with K_{app} = 0.07 min^{-1}, as shown in Figure 5.12 and Table 5.6. The catalytic activity of bimetallic Au and Pd system was also screened, focusing initially on a molar ratio of Au:Pd = 1:1, as it was the optimum molar ratio when using $NaBH_4$ as a reducing agent (described previously in Chapter 3). Although, monometallic Au supported nanoparticles was not active, interestingly, the activity of monometallic Pd/TiO_2 catalyst was further enhanced by a factor of ~ 6 (K_{app} = 0.4 min^{-1}) after adding Au as a second metal and mixed with Pd, to form AuPd alloyed nanoparticles (see Figure 5.12 and Table 5.6). This enhancement in activity of bimetallic $AuPd/TiO_2$ catalyst might be due to the synergistic effect between Au and Pd in the AuPd alloyed nanoparticles, as described and confirmed previously in Chapter 3.
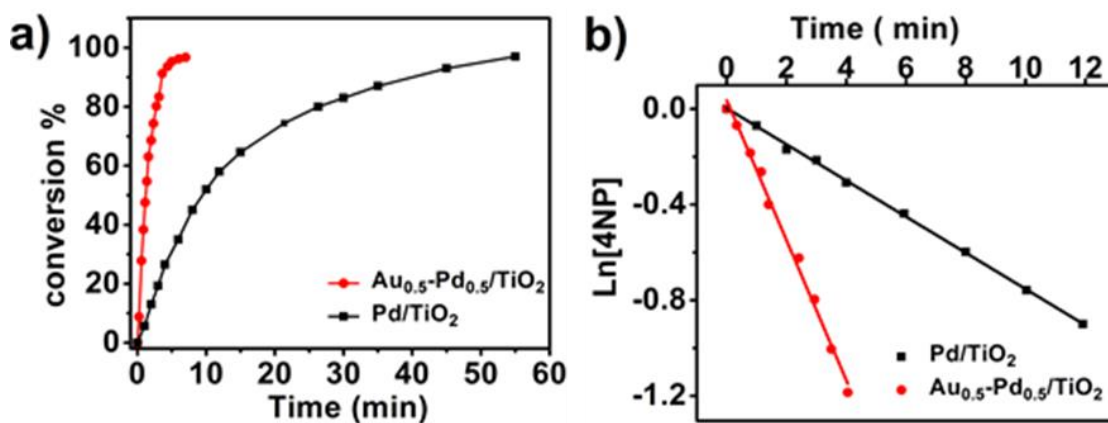
Figure 5.12 (a) Conversion (%) and (b) ln[4-NP] as a function of time (min) for the reduction of 4-NP by formic acid over Pd/TiO_2 and $Au_{0.5}Pd_{0.5}/TiO_2$ catalysts. Reaction conditions: 4-NP/metal molar ratio = 13, formic acid/4-NP molar ratio = 45, stirring rate = 1000 rpm and T = 30 °C.

To further optimize the composition and the molar ratio between Au and Pd nanoparticles towards the reduction of 4-NP by formic acid, we have examined the same Au_xPd_{1-x}/TiO_2 catalyst series that were tested in Chapter 3 using $NaBH_4$ as a reducing agent (i.e. Au_xPd_{1-x}/TiO_2, x = 0.13, 0.25, 0.5, 0.75, 0.87). As a result, a relationship between the apparent rate constant values (K_{app}) are plotted against Pd content (%), in Au_xPd_{1-x}/TiO_2 catalyst series, and presented in Figure 5.13 and data are summarized in Table 5.6. The results show clearly that the Au and Pd molar ratio can affect the apparent rate constant of the reduction of 4-NP by formic acid. As can be seen from this figure, a volcano shape, with the highest activity for $Au_{0.5}Pd_{0.5}/TiO_2$ catalyst, was also obtained as observed previously in Chapter 3 when $NaBH_4$ used as a reducing agent. The results showed that monometallic Au/TiO_2 catalyst and even after the inclusion of 13% Pd (i.e. $Au_{0.87}Pd_{0.13}/TiO_2$ catalyst) are inactive for this reaction. Subsequently, the bimetallic catalyst started to work after the inclusion of 25% of Pd (i.e. $Au_{0.75}Pd_{0.25}/TiO_2$ catalyst, K_{app} = 0.08 min^{-1}). Further addition of Pd content in the AuPd alloyed nanoparticles lead to an enhancement in the catalyst's activity reaching a maximum value at the top of the volcano shape with 50% of

Table 5.6 Catalytic activity of Pd/TiO_2, Au/TiO_2 and Au_xPd_{1-x}/TiO_2 catalysts on the reduction of 4-NP by formic acid.

Catalyst	K_{app} (min^{-1})
Pd/TiO_2	0.07
$Au_{0.13}Pd_{0.87}/TiO_2$	0.1
$Au_{0.25}Pd_{0.75}/TiO_2$	0.13
$Au_{0.5}Pd_{0.5}/TiO_2$	0.4
$Au_{0.75}Pd_{0.25}/TiO_2$	0.08
$Au_{0.87}Pd_{0.13}/TiO_2$	0
Au/TiO_2	0

160

Figure 5.13 K_{app} of 4-NP reduction by formic acid versus Pd molar ratio% in the series of Au_xPd_{1-x}/TiO_2 catalysts. Reaction conditions: 4-NP/metal molar ratio = 13, FA/4-NP molar ratio =45, stirring rate =1000 rpm, T= 30 ºC.

Pd content (i.e, $Au_{0.5}Pd_{0.5}/TiO_2$ catalyst, K_{app} = 0.4 min^{-1}). Afterwards, a remarkable decrease in catalyst's activity was observed whilst increasing the Pd content to 87% in $Au_{0.13}Pd_{0.87}/TiO_2$ catalyst, K_{app} = 0.1 min^{-1}.

The heterogeneous catalysis for the reduction of 4-NP by formic acid may occur in four steps: (i) adsorption of the reactant molecules (both 4-NP and formic acid) to the catalyst surface, (ii) diffusion of the molecules to the active site (AuPd alloyed nanoparticles) and formation of the surface adduct, (iii) reaction of the adduct to form the adsorbed product and (iv) finally desorption of the product (4-AP and CO_2). Thus, in our case the formic and 4-NP adsorbed on the catalyst surface undergoes intermolecular electron transfer through the catalyst followed by transfer of H_2 to 4-NP. The generated 4-AP and CO_2 then desorbed from the surface and then reoccupied by the fresh reactant molecules. In this way the metal surface is renewed for continuous reaction to occur. A suggested mechanism of this reaction over our bimetallic $AuPd/TiO_2$ catalyst can be illustrated in the following scheme representation (Figure 5.14):
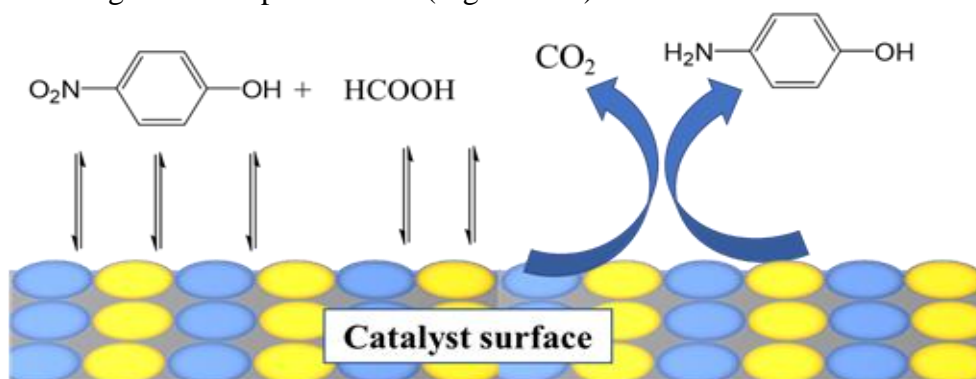
Figure 5.14 Schematic representation for the mechanistic of the 4-NP reduction by formic acid over supported nanoparticles.

The transfer of H_2 from formic acid to a nitro compound has frequently taken place where a base, such as triethylamine and NH_3, is present, and so adding bases is normally required for transfer hydrogenation [58]. The base-free catalytic transfer hydrogenation of a nitro compound demonstrated in our case is quite uncommon and may possibly be due to pH dependence of the electrostatic interaction between the catalytic surface and formic acid/format interfaces [58]. Formic acid dehydrogenation and subsequent reduction of the nitro group may be a pathway for this reaction.

To ensure that the nitro group is reduced by hydrogen generated by dehydrogenation of formic acid, we conducted a control test, in the absence of 4-NP, and we found that formic acid was consumed, and hydrogen was, subsequently, generated which might be responsible for the reduction of 4-NP [59–61]. However, we cannot exclude the second mechanism in which the reduction of nitro group can be taken place through the transfer hydrogenation process as reported previously by Javaid *et al.,* [58].

To further get insight into the mechanism and the role of Au and Pd nanoparticles, 50% of Au/TiO_2 and 50% of Pd/TiO_2 catalysts were physically mixed together and used for the reduction of 4-NP. The obtained results are presented in Figure 5.15. The results clearly demonstrated that there was a drop in the activity by nearly 60% compared to the activity of monometallic Pd/TiO_2 catalyst. This suggests that Au/TiO_2 alone is not active in the reaction and has no any promotion effect on the activity of Pd/TiO_2 in contrast it has a negative effect on the activity of Pd/TiO_2. This observation can explain the high activity of AuPd alloyed nanoparticles in the bimetallic system. The results suggest that there is no synergistic effect between the two pure metal in the case of physical mixing. It can be attributed to the fact that the individual Au and Pd nanoparticles, in the physical mixture, are segregated, while, the AuPd in the alloyed bimetallic catalyst are consistent of homogeneous random of AuPd alloy resulting a strong interaction between the two metals and hence the presence of a synergistic effect. Therefore, we can conclude that the high activity of Au/Pd bimetallic system was due to the synergistic effect of AuPd alloyed nanoparticles.
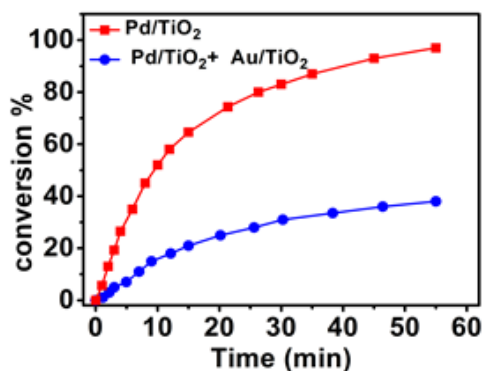
Figure 5.15 Conversion (%) as a function of time (min) for the reduction of 4-NP by formic acid over Pd/TiO_2 and physically mixed (Au/TiO_2 and Pd/TiO_2) catalysts. Reaction conditions: 4-NP/metal molar ratio = 13, formic acid/4-NP molar ratio = 45, stirring rate = 1000 rpm and T = 30 ºC.

5.5.4. Catalytic activity of bimetallic Ag_xPd_{1-x}/TiO_2

As we found previously, $Au_{0.5}Pd_{0.5}/TiO_2$ catalyst showed promising activity for the reduction of 4-NP by formic acid, as H-donor. The observed activity was correlated to the synergistic effect between Au and Pd in the alloyed nanoparticles. Herein this section we aimed to explore the activity of another bimetallic system, mainly AgPd alloyed nanoparticles supported on TiO_2 towards the reduction of 4-NP when formic acid used as H-donor. Initially, we have started to screen the activity of monometallic Ag/TiO_2 and Pd/TiO_2 catalyst towards the reduction of 4-NP by formic acid. Subsequently, a combination of bimetallic systems containing different stoichiometric ratios of Ag and Pd nanoparticles have been also tested for this reaction. The obtained results are summarized in Table 5.7. The obtained results indicated that, monometallic Ag/TiO_2 catalyst is not active for this reaction, which is very similar to the inactive Au/TiO_2 catalyst. The non-activity of supported Ag nanoparticles maybe due to its non-ability of formic acid dehydrogenation [17,62]. In contrast, monometallic Pd/TiO_2 catalyst exhibited promising activity (K_{app} = 0.07 min^{-1}).

To further optimize the composition and the molar ratio between Ag and Pd nanoparticles towards the reduction of 4-NP by formic acid, we have examined the same Ag_xPd_{1-x}/TiO_2 catalyst series that were tested in this Chapter using $NaBH_4$ as a reducing agent (i.e. Ag_xPd_{1-x}/TiO_2, x = 0.13, 0.25, 0.5, 0.75, 0.87). As a result, a relationship between the

163

apparent rate constant values (K_{app}) are plotted against Pd content (%), in Ag_xPd_{1-x}/TiO_2 catalyst series, and presented in Figure 5.16 and data are summarized in Table 5.7.

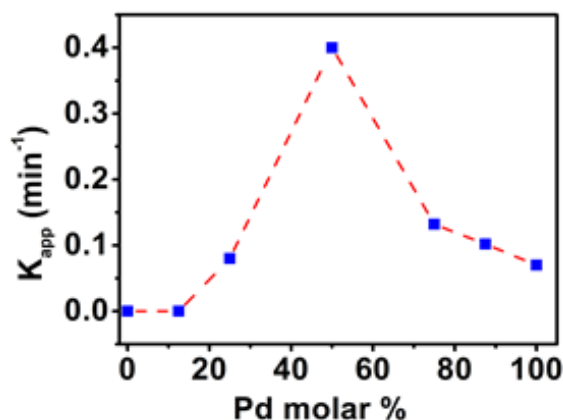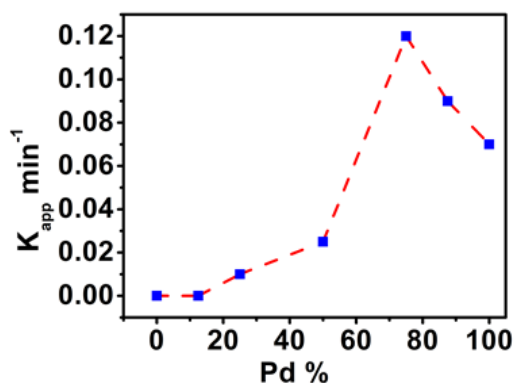Figure 5.16 K_{app} of 4-NP reduction by formic acid versus Pd molar ratio% in the series of Ag_xPd_{1-x}/TiO_2 catalysts. Reaction conditions: 4-NP/metal molar ratio = 13, FA/4-NP molar ratio =45, stirring rate =1000 rpm and T= 30 ºC.

Table 5.7 Catalytic activity of Pd/TiO_2, Ag/TiO_2 and Ag_xPd_{1-x}/TiO_2 catalysts on the reduction of 4-NP by formic acid.

Catalyst	K_{app} (min^{-1})
Pd/TiO_2	0.07
$Ag_{0.13}Pd_{0.87}/TiO_2$	0.09
$Ag_{0.25}Pd_{0.75}/TiO_2$	0.12
$Ag_{0.5}Pd_{0.5}/TiO_2$	0.02
$Ag_{0.75}Pd_{0.25}/TiO_2$	0.01
$Ag_{0.87}Pd_{0.13}/TiO_2$	0
Ag/TiO_2	0

The results show clearly that the Ag and Pd molar ratio can affect the apparent rate constant of the reduction of 4-NP by formic acid as H-donor. As can be seen from this figure, a volcano shape, with the highest activity for $Ag_{0.25}Pd_{0.75}/TiO_2$ catalyst, was also obtained as observed previously in this Chapter when $NaBH_4$ was used as a reducing agent. The results showed that monometallic Ag/TiO_2 catalyst and even after the inclusion of 13% Pd (i.e. $Ag_{0.87}Pd_{0.13}/TiO_2$ catalyst) are inactive for this reaction. Subsequently, the bimetallic catalyst started to work after the inclusion of 25% of Pd (i.e. $Ag_{0.75}Pd_{0.25}/TiO_2$ catalyst, K_{app} = 0.01 min^{-1}). Further addition of Pd content in the AgPd alloyed nanoparticles lead to an enhancement in the catalyst's activity reaching a maximum value at the top of the volcano shape with 75% of Pd content (i.e, $Ag_{0.25}Pd_{0.75}/TiO_2$ catalyst, K_{app} = 0.12 min^{-1}). Afterwards, a remarkable decrease in catalyst's activity was observed whilst increasing the Pd content to 87% in $Ag_{0.13}Pd_{0.87}/TiO_2$ catalyst, K_{app} = 0.09 min^{-1}. In summary, this trend in activity is very similar to our results, with the series of catalysts, when $NaBH_4$ was used as a reducing agent.

5.6. Reduction of 4-nitrophenol using hydrous hydrazine as H donor

Recent research has focused on the possibility of using sodium borohydride as a hydrogen source for the reduction of 4-NP to 4-AP under alkaline conditions [45–51]. However, employment of alternative sources of hydrogen, particularly, hydrous hydrazine, other than sodium borohydride for the reduction of 4-NP has been scarcely reported in the literature.

Hydrous hydrazine, such as hydrazine monohydrate, $H_2NNH_2 \cdot H_2O$, is a carbon-free chemical hydrogen storage material, existing in the liquid state over a wide range of temperature (213–392 K). In addition, it has a hydrogen content as high as 8.0 wt.% available for hydrogen release [70,71] which much higher than the hydrogen content of formic acid (4.4 wt.%). Hydrous hydrazine is much safer than pure hydrazine, which the latter is scientifically considered hazardous material [72]. Moreover, It is much cheaper than sodium borohydride and formic acid (according to Sigma-Aldrich prices by a factor of 7 and 1.4, respectively), and it is also relatively easy to produce. The basic source of hydrazine, nitrogen and hydrogen, are found abundantly in nature and there is no limit to compound recycling [73]. Hydrazine synthesis can also be carried out in conjunction with the mass-synthesis of ammonia and urea[74].

Catalytic decomposition of anhydrous hydrazine, in the presence of trace amount of transition metals, has been explored by various research groups [70,73,75,76] and it has been shown that hydrazine can be decomposed in two ways; (i) the complete decomposition to generate hydrogen and inert N_2 in gaseous states (Equation 5.3) and in this way, the *in situ* production of hydrogen gas on the active metal surface promotes reduction reactions. Hydrogen generated by this reaction can be utlised for the reduction process, circumventing the requirement for elaborate hydrogenation apparatus [77].

$$H_2NNH_2 \longrightarrow N_2(g) + 2H_2(g) \qquad \Delta H = \text{-95.4 kJ mol}^{-1} \qquad \text{(Eq. 5.3)}$$

(ii)The incomplete decomposition (Equation 5.4);

$$3H_2NNH_2 \longrightarrow 4NH_3 + N_2(g) \qquad \Delta H = \text{-157 kJ mol}^{-1} \qquad \text{(Eq. 5.4)}$$

Most of these reports on the decomposition of hydrazine show the presence of ammonia as a side-product, whereas the selective decomposition of hydrazine to exclusive hydrogen is scarce [70,73].

As hydrogen source, hydrous hydrazine has been widely used for many reactions [78–80]. Recently, using hydrous hydrazine as a hydrogen source for the reduction of 4-NP to 4-AP in alkaline solution has received more attention. Saleh and co- works [81] used hydrous hydrazine as the hydrogen donor for 4-NP reduction over Ni/SiO_2 and Ni/Al_2O_3 which prepared by impregnation method. Their findings indicated that the application of hydrous hydrazine as a hydrogen source proved highly effective for 4-NP reduction to 4-AP, with only H_2 and N_2 being produced from the catalytic decomposition of hydrazine hydrate, ammonia was not observed in this reduction system . This investigation demonstrated that Ni/Al_2O_3 catalyst had higher efficacy than Ni/SiO_2 for the reduction of 4-NP in the presence of hydrous hydrazine. In addition to all these observations, they proposed a possible mechanism for this reaction, taking into consideration the color change observed during the reaction. This proposed mechanism suggests that H_2 (produced from the decomposition of hydrazine over Ni metal) is firstly added to the nitro-group leading to the elimination of two water molecules and a rearrangement of the molecular structure to produce a green intermediate compound (A) (Scheme 5.2). The subsequent addition of a further H_2 molecule to the green intermediate leads to the generation of 4-aminophenol.
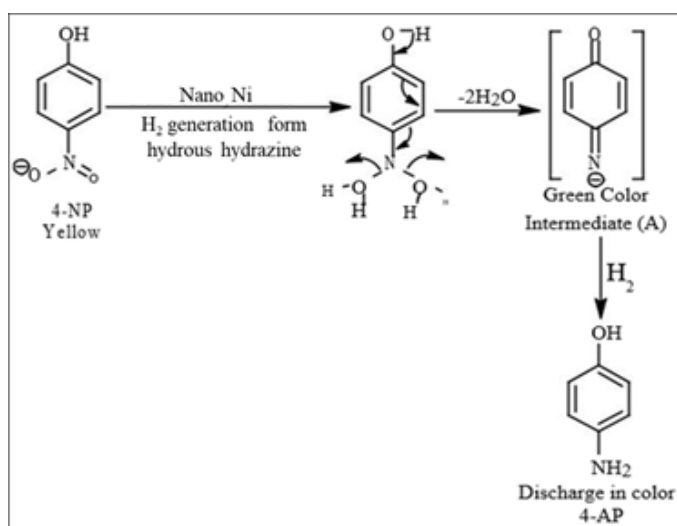
Scheme 5.2 Proposed mechanism for the reduction of 4-NP using hydrous hydrazine suggested by Saleh et.al [81].

Subsequently, the same group [82] extended their studies to demonstrate the influence of the bimetallic Ni/ Cu loaded on zeolites for reduction of 4-NP by using hydrous hydrazine as hydrogen source. The results of this work clearly demonstrated that bimetallic Ni/Cu catalysts showed superior catalytic activity relative to monometallic Ni loaded on the

same zeolites. Furthermore, they observed that whilst single metal copper is inactive in this hydrogenation process, it will, however, decompose hydrous hydrazine in the vicinity of highly active Ni metal in the same alloy, causing an increased generation of H_2 and consequently improved reaction rate.

Yazid *et al.,* [83] reported the reduction of 4-nitrophenol by hydrous hydrazine as the reducing agent over an Au/TiO_2 catalyst, which was prepared by the deposition-precipitation (DP) method at several pH levels. They demonstrated that the catalytic activity was dependent upon gold particle size, loading, distribution and the pH. Findings indicate that the smaller Au particles (4 -and 5 nm) constitute the most active catalytic particles in this reaction. Song *et al.,* [84] synthesized ZnO-loaded $Co_{0.85}Se$ nanocomposites *via* the hydrothermal process for the hydrous hydrazine decomposition and catalytic reduction of 4-nitrophenol. They demonstrated a remarkable performance for the decomposition of hydrous hydrazine and subsequent catalytic reduction of 4-NP relative to individual $Co_{0.85}Se$ or ZnO components. Yu *et al.,* [85] employed hydrazine as hydrogen donor and anhydrous ethanol as a solvent with Pd/ CSs for nitroaromatic reductions. They observed that Pd nanocrystals showed superior catalytic activity for transfer hydrogenation of nitroaromatics under ambient conditions. Furthermore, they observed that the palladium precursor, additive and metal loading all greatly influenced the size of loaded Pd nanoparticles and their subsequent catalytic activity. However, conversion of 4-NP to 4-AP was only 83.1 % over 22 h with 100 % selectivity to 4-aminophenol. In addition, this investigation studied the influence of solvent, reaction temperature and concentration of hydrous hydrazine on selectivity improvement.

Figueras *et al.,* [86] studied the reduction of aromatic nitro compounds with hydrous hydrazine at 333 K in the presence of the iron (III) oxide-MgO catalyst and methanol as solvent. The catalyst was found to be highly active and 100% selective and no dehalogenation or demethylation was observed. However, the reusability study of the catalyst showed that the catalyst became deactivated after each run. They restored the original activity for used catalyst by reactivated in nitrogen at 723 K. They concluded that the deactivation was attributed to the decrease in the surface area due to hydration of the catalyst by water in hydrous hydrazine and water formed in the reaction.

Selim and Fathy [87] studied the influence of catalyst loading and concentration of NaOH for reduction of 4-NP and using hydrous hydrazine as hydrogen donor under alkaline conditions at $80^{o}C$. They employed nanoparticle nickel supported on kaolin (5% Ni-K)

as a catalyst. Results indicated that increasing the weight of the catalyst from 0.2 g to 1 g dramatically decreased the time required for total reduction from 30 min to 3.66 min. Furthermore, they identified that higher concentrations of NaOH also led to a detectable reduction in the time required for complete reduction of 4-NP, but further increase led to increase in the time required for the reduction. This was attributed to the decrease in the mobility of the reactants to be in contact with the catalyst. This results in a good agreement with results recently reported by Dasgupta *et al.,* [77], who studied reaction mechanism and kinetics of the reduction of 4-NP to 4-AP using hydrazine as a hydrogen source at room temperature. This reaction was performed in aqueous alkaline solution, using NaOH and Ni–Pd bimetallic nanoparticles as a catalyst. The Ni–Pd was synthesised with varying compositions using the co-reduction method in the presence of PVP. They showed that the monometallic Pd and Ni NPs and the physical mixture of Ni and Pd NPs (at a ratio of 70:30) were inactive toward the catalytic conversion, whereas the activity with respect to the reduction of 4-NP, was significantly greater for the bimetallic catalyst. They referred the high activity to the synergistic effect in the bimetallic system and it was highly dependent on the ratio between Ni and Pd, the $Ni_{70}Pd_{30}$ nanocatalyst exhibited the highest activity for 4-NP reduction with constant rate 7.53×10^{-3} min^{-1}. In addition to all these observations, they studied the effect of pH and 4-NP, hydrazine and catalyst concentrations, and the results approved that the reduction follows the Langmuir–Hinshelwood mechanism where 4-NP reduction occurred through intermolecular electron transfer between N_2H_4 and 4-NP when both were adsorbed on the catalytic site[87].

The reduction of 4-nitrophenol with hydrous hydrazine is given by:
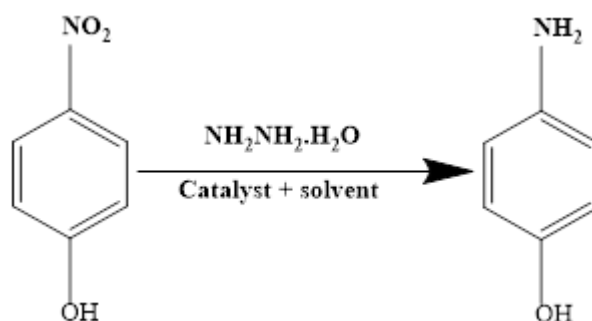
Scheme 5.3 Reduction of 4-NP using hydrous hydrazine.

In this Section, the utility of hydrous hydrazine (as an alternative source of hydrogen) is studied for this reaction (reduction of 4-NP) over $Au_{0.5}Pd_{0.5}/TiO_2$ and $Ag_{0.25}Pd_{0.75}/TiO_2$ catalysts, in addition to their monometallic analogous (Ag, Au and Pd). Moreover, the

reaction was optimized by varying different parameters that may influence this reaction (e.g., concentration of NaOH and N_2H_4 and pH of the reaction mixture) have been investigated.

5.6.1. Catalytic reduction of 4-nitrophenol by hydrous hydrazine

The reduction of 4-NP to 4-AP using hydrous hydrazine ($N_2H_4.H_2O$) was carried out in a glass reactor, described in detail in Chapter 2 (Section 2.4.1). The reaction was conducted under constant stirring (1000 rpm) and mild reaction conditions using water as solvent at 30 °C and atmospheric pressure. A large excess of hydrous hydrazine over 4-NP was used (Hydrous hydrazine /4-NP molar ratio =10-60, with an optimum value of 40), in order to maintain the pseudo first-order condition, and then the apparent rate reaction is dependent solely on the concentration of 4-NP [83]. The experimental conditions are the following: 4-nitrophenol and hydrous hydrazine were prepared in a 0.075 M NaOH solution to provide a basic and stable condition for the catalytic reaction. The basic condition was chosen because hydrous hydrazine reacts optimally at this environment (will be discussed in detail later in the next Section). The preparation of 4-NP in aqueous NaOH solution resulted in the shift of the absorbance peak of 4-NP from λ 317 nm to λ 400 nm. Furthermore, the colour of 4-NP solution changed from light yellow to dark yellow (Figure 5.17a), due to the formation of 4-nitrophenolate ions under alkaline conditions. This observation is similar to our observation when $NaBH_4$ used as reducing agent and also in good agreement with previous reports [77,88]. Typically; 5ml of hydrous hydrazine (0.06 M) is added into a 100 ml round bottom flask, as batch reactor, that contains the desired amount of catalyst and the basic solution of 4-NP (4-NP & NaOH. 0.75 M), (45ml, 1.35×10^{-4} M, 4-NP/metal molar ratio = 13). The total volume of the reaction mixture was 50 ml. At different time interval (min), aliquot from the reaction mixture was then withdrawn using 1 ml syringe equipped with a filter (0.45 µm pore size) and transferred into the UV cuvette for a UV-Vis measurement. Subsequently, the UV-Vis spectra (in the range of 200 – 800 nm) were recorded and the concentration of 4-NP traced from the decay of the absorption band of 4-nitrophenolate ion centred at 400 nm. Based on the calibration curve of standard solution of 4-NP, which previously described in Chapter 2, the molar extinction coefficient was estimated for 4-NP to be 17630 M^{-1} cm^{-1}. Finally, the concentration of 4-NP, as a function of time during the catalytic reaction, was calculated using the Beer's Lambert's law equation as discussed in Chapters 2 and 3.

Similar to NaBH$_4$, the colour of the final solution changes to be colourless (see Figure 5.17a), indicating the formation of 4-aminophenol. The presence of isosbestic points in the UV-Vis spectra (Figure 5.17b) suggests that 4-AP (at 297 nm) is a sole product of the reaction, and consequently no side reaction occurs, which is in agreement with previous report [58]. In addition, the GC-MS were used to confirm that 4-AP is the sole product of this reduction (see appendix Figure A1). In a control experiment, where 4-NP and hydrous hydrazine are used without using any catalyst, no conversion of 4-nitrophenol was observed, indicating that 4-NP is not reduced by only hydrous hydrazine. Also, when measured amount of Pd/TiO$_2$ catalyst alone was added to a basic solution of 4-NP (4-NP & NaOH), the absorbance at 400 nm did not change with time, indicating no reduction of 4-NP. It ensures that in the presence of   Pd/TiO$_2$ or hydrous hydrazine molecules alone cannot catalyse 4-NP reduction under the same experimental conditions as previous has been reported [77].

Figure 5.17 a) Image for colour change during preparation of 4-NP in NaOH aqueous solution and b) An example for UV-Vis spectra collected during the catalytic reduction of 4-nitrophenol by hydrous hydrazine using a Pd/TiO$_2$ catalyst.
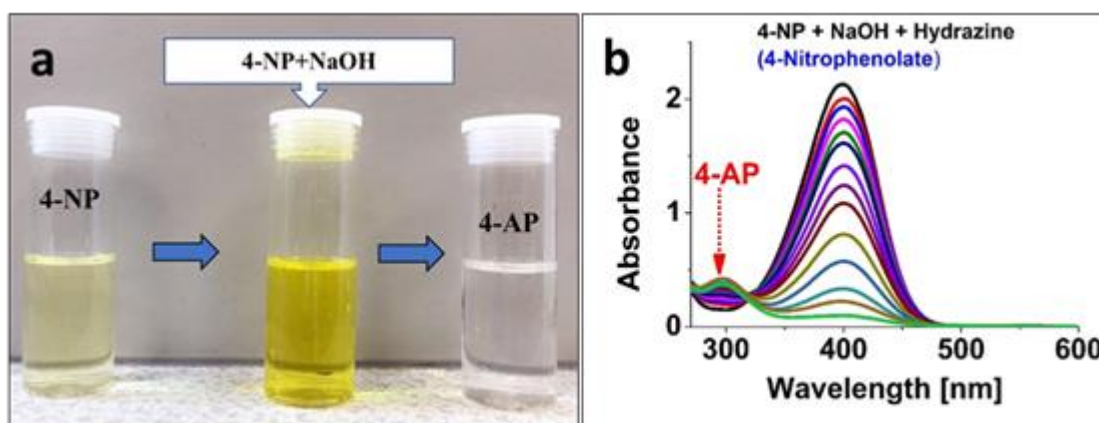
5.6.2.   Optimisation of reaction conditions

In this Section, the influence of concentration of both NaOH and hydrous hydrazine have been investigated and optimized for the reduction of 4-NP over Pd/TiO$_2$ catalyst. This study is important to explore the role of basic medium on the catalytic performance of the catalyst and also to maintain the pseudo first-order reaction kinetics which means that the apparent rate constant is dependent solely on the concentration of 4-NP.

5.6.3. Influence of NaOH concentration

The dependence of the apparent rate constant on the NaOH concentration was investigated and results are shown in Figure 5.18. Here, the amount of catalyst was fixed (5.2 mg of Pd/TiO_2) and the concentration of 4-NP and hydrous hydrazine were kept constant, ([4-NP] $=1.35\times10^{-4}$M & [hydrous hydrazine] $=0.05$ M), while the concentration of NaOH was varied in the range (0.025-0.1 M).
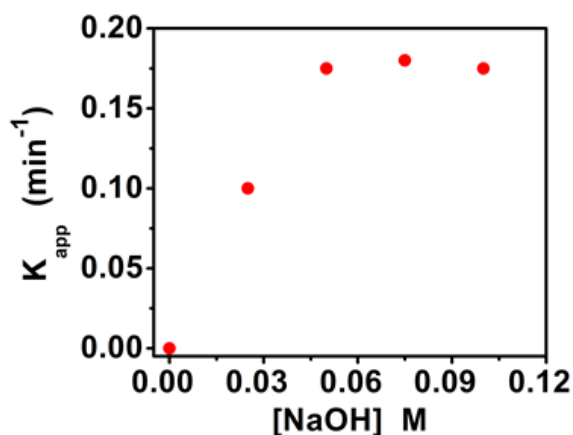
Figure 5.18 Effect of NaOH concentration on the apparent rate constants of 4-NP reduction by hydrous hydrazine over Pd/TiO_2 catalysts. Reaction conditions: 4-NP/metal molar ratio = 13, [hydrous hydrazine] $=0.05$ M, 30 °C, 1000 rpm, [NaOH]=(0.025-0.1M).

It was observed that the apparent rate constant for the reduction of 4-NP increases with increasing NaOH concentration and then reaches a plateau at concentration higher than 0.05 M of NaOH. At higher concentrations of NaOH the rate constant decreases because the surface is saturated with OH and these results in agreement with literature studies [77,87,88]

The influence of NaOH concentration in the catalytic reduction of 4-NP by hydrous hydrazine has been reported previously [77,87,88]. It was reported that NaOH can significantly enhance the reduction of 4-NP by hydrous hydrazine. The hydrolysis of hydrazine can be occurred when dissolved in water [111], as shown in the following equation;

$$N_2H_4 + H_2O \rightleftharpoons N_2H_5^+ + OH^- \qquad (Eq\ 5.3)$$
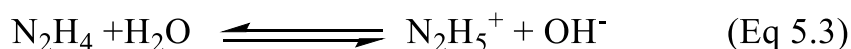
Protonated hydrazine ($N_2H_5^+$) is considered to be a weak reducing agent [123] compared to hydrazine (N_2H_4). Therefore, adding NaOH into hydrazine aqueous solution (N_2H_4 + H_2O) would supress the hydrolysis of hydrazine to form protonated hydrazine and thus

pushing the above equation to the left side, i.e. presence of hydrazine, which enhance the reduction of 4-NP. Therefore, in the present study a higher NaOH concentration was used for all experiments; [NaOH] = 0.075 M.

5.6.4. Influence of hydrous hydrazine concentration

To understand better the mechanism of the catalytic reduction of 4-NP with hydrous hydrazine and to maintain the pseudo first-order condition, the effect of hydrous hydrazine concentration on the catalytic reduction was studied and the obtained results are shown in Figure 5.19.
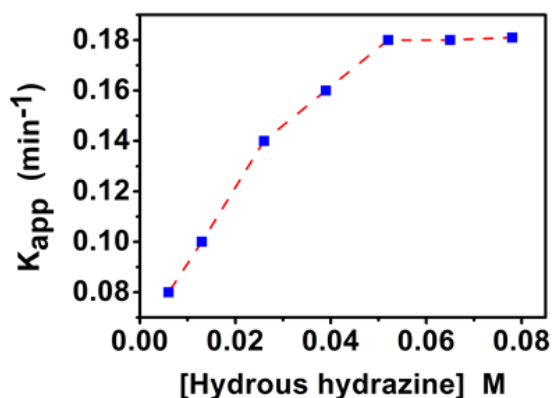
Figure 5.19 Effect of hydrous hydrazine concentration on the apparent rate constants of 4-NP reduction over Pd/TiO$_2$ catalysts. Reaction conditions: 4-NP/metal molar ratio = 13, [4-NP] =1.35×0^{-4} M , [NaOH]= 0.075 M, [hydrous hydrazine] = 0.006 - 0.08 M, stirring rate = 1000 rpm and T = 30 °C.

As shown in Figure 5.19, it is clear that hydrous hydrazine can significantly enhance the reduction of 4-NP. The apparent rate constant value increases with increasing hydrous hydrazine concentration and then reaches a plateau. The trend of the graph is similar to that obtained in previous research [77].

These observations firmly support the heterogeneous surface catalytic reaction for 4-NP reduction. The experimental results obtained are found to follow closely the Langmuir–Hinshelwood mechanism. According to experimental observations which is like the observations made with sodium borohydride and formic acid, we propose that the catalytic 4-NP reduction occurs when both the hydrous hydrazine molecule and 4-nitrophenolate ion are adsorbed on the active sites of the catalyst, in line with other reported study by Dasgupta *et al.,* [77]. They studied the reaction kinetics to elucidate the mechanism of catalytic reduction of 4-NP to 4-AP over Ni$_{70}$Pd$_{30}$ nano-catalyst using hydrous hydrazine as hydrogen source. Results of the kinetics analysis revealed that the

reduction follows the Langmuir–Hinshelwood mechanism where 4-NP reduction take place *via* intermolecular electron transfer between N_2H_4 and 4-NP when both were adsorbed on the catalytic site.

5.6.5. Catalytic activity of bimetallic $Au_{0.5}Pd_{0.5}/TiO_2$

To better understanding the role of reducing agent during the reduction of 4-NP, herein we focus on studying the reduction of 4-NP by hydrous hydrazine, as alternative reducing agent to $NaBH_4$ and/or formic acid, over monometallic Au/TiO_2 and Pd/TiO_2 catalysts. In addition, based on our previous work (Chapter 3), the reduction of 4-NP was also tested over the most active bimetallic $Au_{0.5}Pd_{0.5}/TiO_2$ catalyst. All activity testing was performed under the same reaction conditions which studied previously; ([4-NP] 1.35×0^{-4} M, 4-NP/metal molar ratio = 13, stirring rate = 1000 rpm and T = 30 °C). The obtained results are illustrated in Figure 5.20 and their corresponding K_{app} values are summarized in Table 5.8.

Table 5.8 Catalytic activity of Pd/TiO_2, $Au_{0.5}Pd_{0.5}/TiO_2$ catalysts on the reduction of 4-NP by hydrous hydrazine.

Catalyst	K_{app} (min^{-1})
Au/TiO_2	0
Pd/TiO_2	0.18
$Au_{0.5}Pd_{0.5}/TiO_2$	0.29
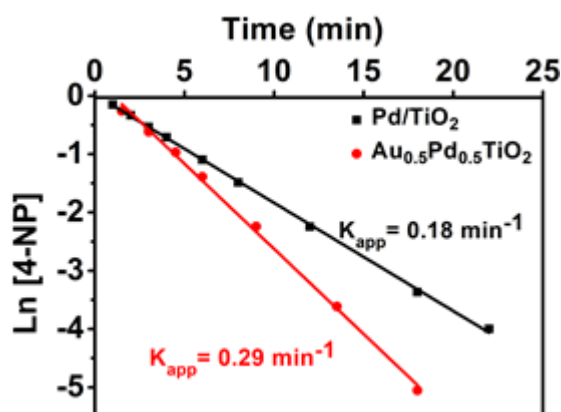
Figure 5.20 ln[4-NP] as a function of time for Pd/TiO_2 and $Au_{0.5}$-$Pd_{0.5}/TiO_2$ catalysts. Reaction conditions: 4-NP/metal molar ratio = 13, hydrous hydrazine/4-NP molar ratio = 40, [NaOH]=0.75 M, stirring rate = 1000 rpm and T = 30 °C.

The results clearly demonstrate that monometallic Au/TiO_2 catalyst is not active for the reduction of 4-NP by hydrous hydrazine, while Pd/TiO_2 is active ($K_{app} = 0.18$ min^{-1}) using the same experimental conditions. The activity is further increased when Au was added

as a second metal and mixed with the Pd to form AuPd alloyed nanoparticles (i.e. $Au_{0.5}$-$Pd_{0.5}/TiO_2$ catalyst, K_{app} = 0.29 min^{-1}) by a factor of 1.6 compared to Pd/TiO$_2$ catalyst (K_{app} = 0.18 min^{-1}). This remarkable enhancement in the catalyst's activity might be resulting from the synergistic effect between Au and Pd metals in the AuPd alloyed nanoparticles.

A summary of the catalytic activity of Pd/TiO$_2$ and $Au_{0.5}Pd_{0.5}/TiO_2$ in the reduction of 4-NP using different reducing agents is shown in Table 5.9.

Table 5.9 Catalytic activity of Pd/TiO$_2$ and $Au_{0.5}Pd_{0.5}/TiO_2$ catalysts in the reduction of 4-NP using different reducing agents. Results for NaBH$_4$ is obtained from Chapter 3.

Reducing agent	K_{app} min^{-1}	
	Pd/TiO$_2$	$Au_{0.5}Pd_{0.5}/TiO_2$
NaBH$_4$	0.20	0.38
Formic acid	0.07	0.40
Hydrous hydrazine	0.18	0.29

As can be seen from Table 5.9 that the activity of bimetallic $Au_{0.5}Pd_{0.5}/TiO_2$ catalyst is higher than monometallic Au/TiO$_2$ and Pd/TiO$_2$ analogous regardless the type of reducing agent, see K$_{app}$ value in Table 5.9. Thus, a synergistic effect between Au and Pd in the AuPd alloyed nanoparticles is the reason for the higher activity. However, the synergistic effect is more profound in formic acid than NaBH$_4$ taking the fact that Au/TiO$_2$ is not active with formic acid and hydrous hydrazine but active with NaBH$_4$ (see Table 5.9). The catalytic activity of $Au_{0.5}Pd_{0.5}/TiO_2$ catalyst, is very similar, when using formic acid and NaBH$_4$ as reducing agent. It is worth to note that in all reactions, an excess of reducing agent was added, so the difference in hydrogen capacity of these reducing agents is not considered as the main factor in this comparison. It seems that NaBH$_4$ is the best reducing agent with respect to the reactivity of mono and bimetallic catalysts. However practically, formic acid is much less toxic and cheaper than NaBH$_4$ [54].

5.6.6. Catalytic activity of bimetallic $Ag_{0.25}Pd_{0.75}/TiO_2$

The reduction of 4-NP by hydrous hydrazine was also studied using monometallic Ag/TiO_2 and Pd/TiO_2 catalysts, in addition to the most active bimetallic $Ag_{0.25}Pd_{0.75}/TiO_2$ system based on our previous work (see Sections 5.4.2 and 5.4.3) under the same reaction conditions: ($[4\text{-NP}] = 1.35 \times 10^{-4}$ M, 4-NP/metal molar ratio = 13, stirring rate = 1000 rpm and T = 30 °C). The obtained results are depicted in Figure 5.21 and the apparent rate constant values (K_{app}) are also summarized in Table 5.10.

Table 5.10 Catalytic activity of Pd/TiO_2 and $Ag_{0.25}Pd_{0.75}/TiO_2$ in the reduction of 4-NP using different reducing agents. Activity results for $NaBH_4$ and formic acid are obtained from Section 5.4.3 and Section 5.5.4, respectively.

Reducing agent	K_{app} min^{-1}	
	Pd/TiO_2	$Ag_{0.25}$-$Pd_{0.75}/TiO_2$
$NaBH_4$	0.20	1.3
Formic acid	0.07	0.12
Hydrazine	0.18	0.32
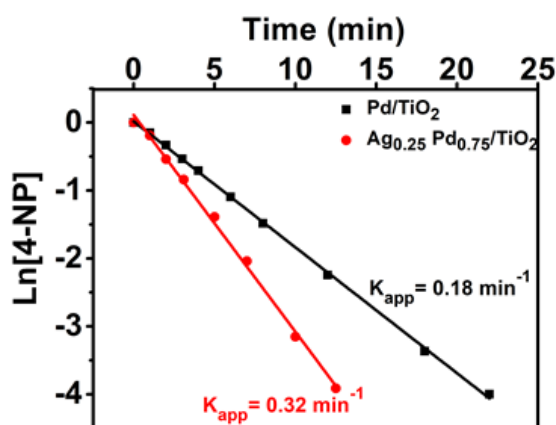
Figure 5.21 ln[4-NP] as a function of time for monometallic (Pd/TiO_2) and bimetallic ($Ag_{0.25}Pd_{0.75}/TiO_2$) catalysts. Reaction conditions: 4-NP/metal molar ratio = 13, hydrous hydrazine/4-NP molar ratio = 40, [NaOH] = 0.75 M, stirring rate = 1000 rpm and T = 30 ºC.

Similarly, Ag/TiO_2 catalyst was not active in this reaction, when hydrous hydrazine is used as the H-donor, while Pd/TiO_2 catalyst showed a promising activity with $K_{app} = 0.18$ min^{-1}. Moreover, the activity was further enhanced when bimetallic $Ag_{0.25}Pd_{0.75}/TiO_2$ was used as catalyst ($K_{app} = 0.32$ min^{-1}), which is higher than the activity of Pd/TiO_2 by a factor of 1.8. The highest activity observed over the bimetallic system ($Ag_{0.25}Pd_{0.75}/TiO_2$) could be explained by the synergistic effect of the AgPd alloyed nanoparticles. A

summary of the catalytic activity of Pd/TiO_2 and $Ag_{0.25}Pd_{0.75}/TiO_2$ catalysts for the reduction of 4-NP using different reducing agents is shown in Table 5.10.

It is evidenced that the synergistic effect between Ag and Pd is observed with $NaBH_4$, formic acid and hydrous hydrazine. The synergistic effect was significant in $NaBH_4$ than formic acid and hydrous hydrazine. Although, Ag/TiO_2 was active when using $NaBH_4$ as a reducing agent, it was inactive in the presence of formic acid and hydrous hydrazine.

So far, $Ag_{0.25}Pd_{0.75}/TiO_2$ catalyst, with the highest activity, could offer the easiest facile transfer of electrons from Ag to Pd and/or enhance hydrogen transfer to 4-NP [49].

Ag has a lower work function (4.64 eV) than Pd (5.00 eV) [50]. Therefore, electrons leave the Ag from a thus depleted region near a Pd/Ag interface into the Pd, which ends up with an electron-enriched region and this would be very easier when we have a very small particles' size.

The existence of these surplus/depletion electrons inside the metals facilitates the uptake/release of electrons by molecules that happen to be close to (on top of) these regions. The more interfaces there are, the more such electron rich/poor regions exist. This in turn increases the chances for randomly absorbed molecules to happen to be on-top of such regions. Therefore, these bimetallic interfaces can be expected to facilitate the metal's role as an electron relay system that opens up pathways for diverse intermediate steps in the reaction of adsorbed species. Meng and co-workers [49] have provided insights into the nature of such effects.

From the previous discussions, we can conclude that the bimetallic catalysts provide better catalytic activities than those of mono-metallic Ag and Pd catalysts due to possible electronic and synergetic effect, consistent with previous reports [16,48]. The fact that bimetallic nanostructures enhance the catalytic activity may be related to the presence of interfaces between Pd NPs and Ag NPs [48], which confirmed by XPS results.

Considering the highest activity of bimetallic $Au_{0.5}Pd_{0.5}/TiO_2$ and $Ag_{0.25}Pd_{0.75}/TiO_2$ catalysts in the presence of different reducing agents ($NaBH_4$, formic acid and hydrous hydrazine), it can be concluded that $Ag_{0.25}Pd_{0.75}/TiO_2$ was more active than $Au_{0.5}Pd_{0.5}/TiO_2$ catalyst by a factor of 3.4 and 1.1 when $NaBH_4$ and hydrous hydrazine were used as reducing agents, respectively. In contrast, when formic acid was used as alternative reducing agent, $Au_{0.5}Pd_{0.5}/TiO_2$ catalyst is more active than $Ag_{0.25}Pd_{0.75}/TiO_2$ catalyst by a factor of 3.3**,** as shown in Table 5.11.

Table 5.11 Activities' summary of bimetallic catalysts with optimized ratio in the reduction of 4-NP with different reducing reagents ($NaBH_4$, formic acid and hydrous hydrazine).

Reducing agent	K_{app} min^{-1}	
	$Au_{0.5}Pd_{0.5}/TiO_2$	$Ag_{0.25}Pd_{0.75}/TiO_2$
$NaBH_4$	0.38	1.3
Formic acid	0.40	0.12
Hydrous hydrazine	0.29	0.32

To better understand the reason for the high activity of $Ag_{0.25}Pd_{0.75}/TiO_2$ catalyst compared to $Au_{0.5}Pd_{0.5}/TiO_2$, we have focused on the result obtained by XPS and TEM analyses, which are summarized in Table 5.12. The greater activity of $Ag_{0.25}Pd_{0.75}/TiO_2$ catalyst can be linked to several factors such as particle size, synergistic effect and the structure of alloyed nanoparticles. According to our TEM results, the mean particle size of $Ag_{0.25}Pd_{0.75}/TiO_2$ and $Au_{0.5}Pd_{0.5}/TiO_2$ catalysts are 2.3($\pm$0.6) and 2.1($\pm$0.6) nm, respectively. It is obvious that there are no any significant differences in the mean particle sizes of the both two catalysts. In addition, surface oxidation state observed by XPS analysis could also be neglected as we use an excess of reducing agent and if there any oxidic species of both Au, Ag and/or Pd would eventually ended with a metallic state over all the nanoparticles, see Table 5.12 above. So far, there might be other factors that can help us understanding the differences in the catalysts' activity. From the XPS analysis, the binding energy of $Pd(3d_{5/2})$ in $Au_{0.5}Pd_{0.5}/TiO_2$ catalyst (BE = 334.69 eV) was shifted by -0.71 eV compared to metallic Pd bulk structure, while for $Ag_{0.25}Pd_{0.75}/TiO_2$ catalyst (BE = 334.3 eV) was shifted by -1.1 eV. So, it could be concluded that the interaction between Ag and Pd in the AgPd alloyed nanoparticles is stronger than the interaction between Au and Pd in the AuPd alloyed nanoparticles and hence the former has more synergistic effect than the later. This could be the main factor for the highest observed activity.

Table 5.12 Oxidation state for Pd(3d) XP spectra and mean particle size using TEM analysis for $Au_{0.5}Pd_{0.5}/TiO_2$ and $Ag_{0.25}Pd_{0.75}/TiO_2$ catalysts.

Catalyst	XPS: oxidation states of Pd(3d) region			TEM analysis: Particle size (nm)
	Pd^0 (%)	Pd^{II} (%)	BE (eV) for $Pd(3d_{5/2})$	
$Au_{0.5}Pd_{0.5}/TiO_2$	100	0	334.69 (-0.71)	2.1 ($\pm$0.6)
$Ag_{0.25}Pd_{0.75}/TiO_2$	87.5	13.5	334.3(-1.1)	2.3 ($\pm$0.6)

Note: BE of bulk Pd^0 = 335.4 eV [42]

To gain more insight into the structure–activity relationships and hence possible synergistic effect of alloyed nanoparticles in the bimetallic $Au_{0.5}Pd_{0.5}/TiO_2$ and $Ag_{0.25}Pd_{0.75}/TiO_2$ catalysts, characterization through high angle annular dark field (HAADF)- STEM microscopy was conducted. The obtained images together with their corresponding EDX mapping are presented in Figure 5.22. The results indicate the presence of single NPs along with random alloys on the surface of both bimetallic catalysts. Interestingly, $Ag_{0.25}Pd_{0.75}/TiO_2$ catalyst has rich population of nanoalloy with ratio around 87% which is higher than that observed for $Au_{0.5}Pd_{0.5}/TiO_2$ catalyst (~52 % AuPd alloy). This also could give us an explanation for the high activity and hence the synergistic effect in AgPd alloyed nanoparticles compared to AuPd alloyed system.
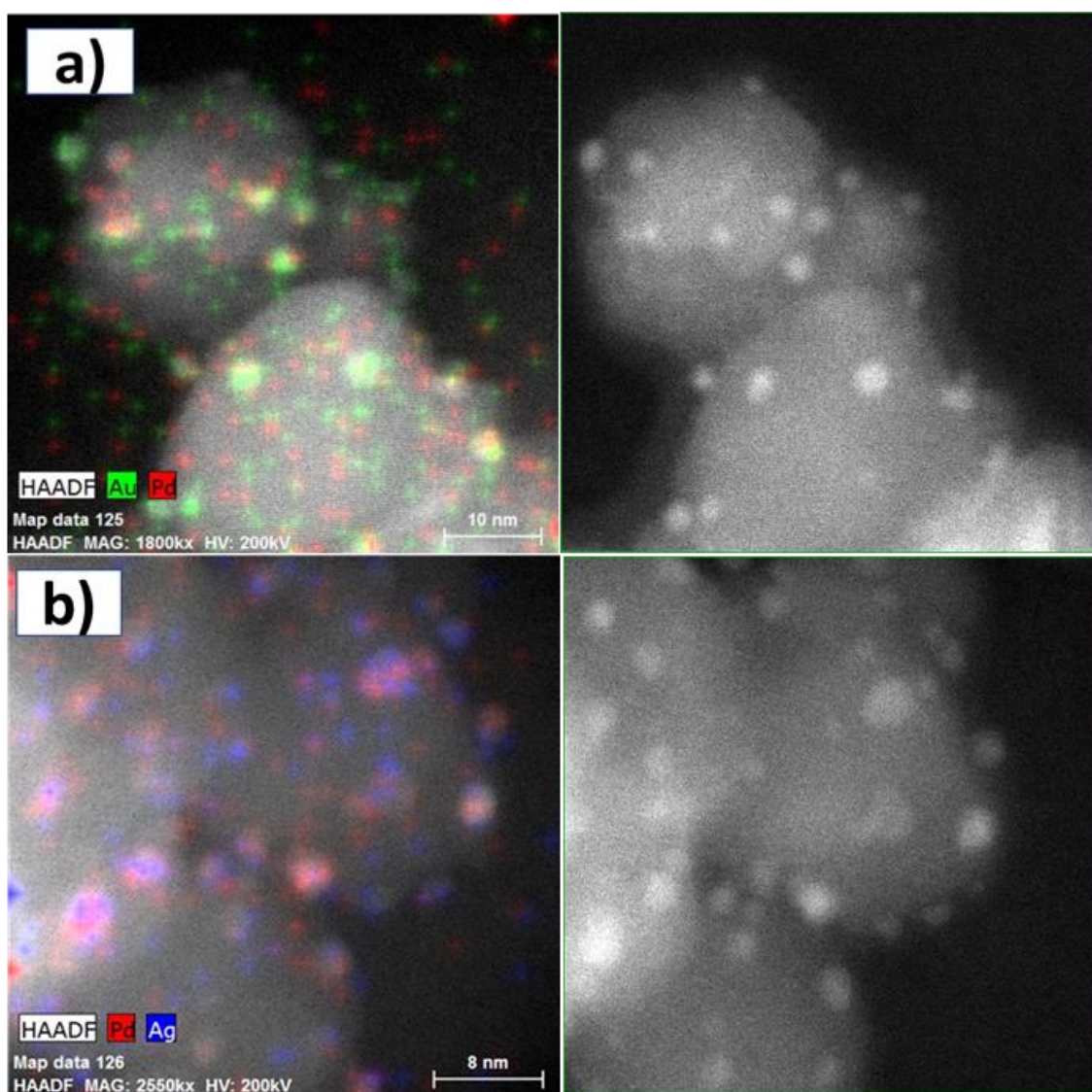
Figure 5.22 HAADF-STEM images and their corresponding EDX elemental mapping of NPs obtained for a) $Au_{0.5}Pd_{0.5}/TiO_2$ and b) $Ag_{0.25}Pd_{0.75}/TiO_2$.catalysts.

5.7. Reduction of different nitrophenols over Au$_{0.5}$Pd$_{0.5}$/TiO$_2$ and Ag$_{0.25}$Pd$_{0.75}$/TiO$_2$ catalysts.

To demonstrate the general applicability of the most active bimetallic catalysts (Au$_{0.5}$Pd$_{0.5}$/TiO$_2$ and Ag$_{0.25}$Pd$_{0.75}$/TiO$_2$) a range of different substrates were used as model reactions for catalytic testing. The catalytic reduction of additional nitrophenol isomers such as; 2-nitrophenol (2-NP), 3-nitrophenol (3-NP) was tested over these bimetallic catalysts. In addition, the reduction of other substrates including 4-nitroaniline (4-NA) and nitrobenzene (NB) were also conducted.

The hydrogenation of nitrophenol isomers (2-NP, 3-NP and 4-NP) was tested over the highest active bimetallic catalysts (Au$_{0.5}$Pd$_{0.5}$/TiO$_2$ and Ag$_{0.25}$Pd$_{0.75}$/TiO$_2$). The reason why we have decided to conduct the activity testing of all these isomers because the conjugation effect of the nitro group which might have an impact on the rate of the reaction. As shown in Scheme 5.4, the negative charge on the phenoxide ion in 2- and 4-nitrophenolate can be delocalized into the nitro group, stabilising the group, and hence would be less active for the reduction. In addition to the resonance effect, there is also an inductive effect, which is stronger in 2-nitrophenolate due to the shorter distance between the substituent group and the reacting group. The stronger inductive effect makes the nitrogen atom more positively charged, and therefore more reactive. In contrast, 3-nitrophenolate, there is no resonance stabilisation of the negative charge in to the nitro group, and only a small inductive effect. This also can be considered for other nitroarene derivatives such as 4-NA and NB, however, with different trend. The rate of hydrogenation for the nitrophenol isomers and other nitroarene derivatives can follow this order; 3-NP > 2-NP > 4-NP > 4-NA > NB [23,89].
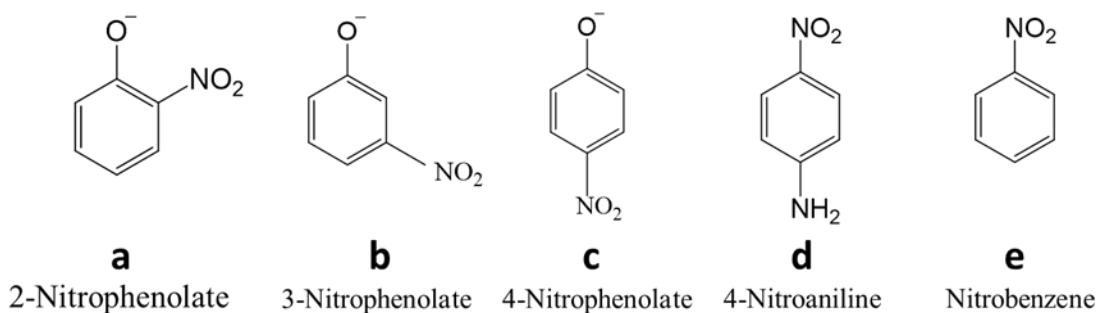
Scheme 5.4 Chemical structure of different nitroarenes: (a) 2-Nitrophenolate, (b) 3-Nitrophenolate, (c) 4-Nitrophenolate, (d) 4-Nitroaniline and (e) Nitrobenzene

Reactions were conducted under mild conditions and similar experimental procedures for the reduction of 4-NP, which described early in this Chapter. All catalytic activity testing was carried out in the presence of $NaBH_4$ as a reducing agent and under the following conditions: substrate/metal molar ratio = 30, $NaBH_4$/substrate molar ratio = 30, stirring rate = 1000 rpm and T= 30 °C. For each experiment, the UV-Vis spectra were recorded in the range of 200 – 800 nm. Then, the decrease in the absorption band of each substrate was traced together with the emerge of the new absorption band of the final product (i.e. the corresponding amino-product in our study). The obtained spectra are presented in Figure 5.23 (a, b, c, d and e) for 2-NP, 3-NP, 4-NP, 4-NA, and NB, respectively. The absorption band of 2-, 3- and 4-nitrophenol, in the presence of $NaBH_4$, are centred at 415, 394, 400 nm, and their corresponding amino products (i.e. 2-, 3- and 4-aminophenol) at 267, 269 and 300 nm respectively. In addition, the absorption bands of 4-nitroaniline and nitrobenzene are centred at 380 and 268 nm and their corresponding final products (4-phyenylenediamine and aniline) at 300 and 229 nm, respectively.
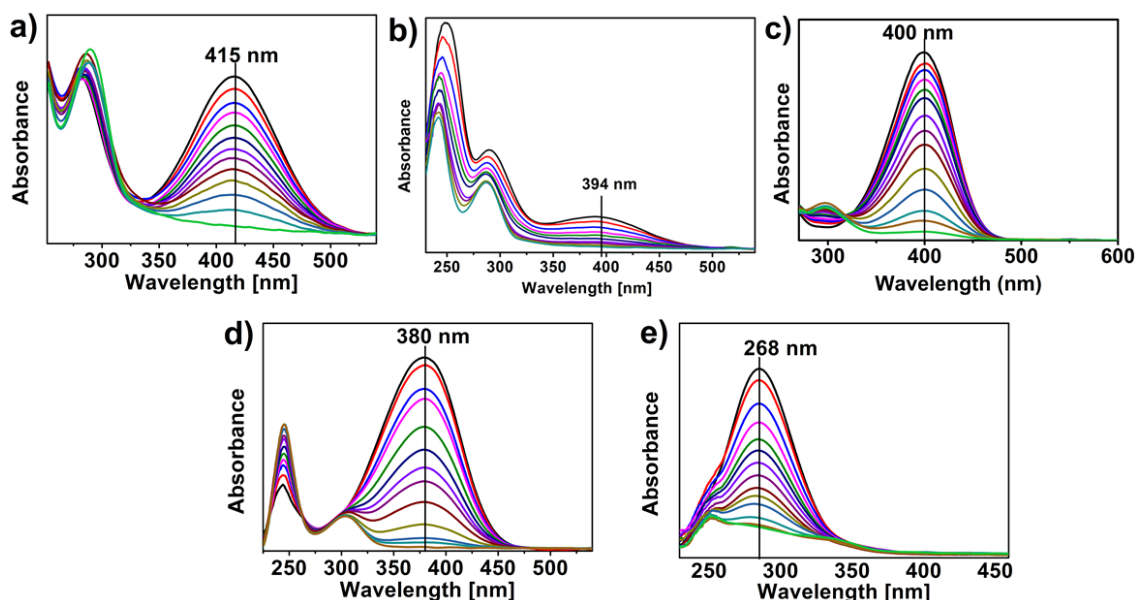
Figure 5.23 UV-Vis spectra for a) 2-NP, b) 3-NP, c) 4-NP, d) 4-NA and e) NB in the presence of $NaBH_4$.

The apparent rate constant values that extracted from the activity testing are summarized in Table 5.13. Generally, the results clearly demonstrate that both two bimetallic catalysts (i.e. $Au_{0.5}Pd_{0.5}$/TiO_2 and $Ag_{0.25}Pd_{0.75}$/TiO_2) are active towards the reduction of all substrates. However, $Ag_{0.25}Pd_{0.75}$/TiO_2 catalyst showed higher rates of the reaction than $Au_{0.5}Pd_{0.5}$/TiO_2 catalyst. As can be seen form Table 5.13, the apparent rate constant values

(K_{app}) for the reduction of 3-NP, 2-NP, 4-NP, 4-NA and NB substrates, over $Ag_{0.25}Pd_{0.75}/TiO_2$ catalyst, are 2.38, 1.26, 0.87, 0.45 and 0.22 min^{-1}, respectively, while over $Au_{0.5}Pd_{0.5}/TiO_2$ catalyst are 1.20, 0.78, 0.56, 0.25 and 0.09 min^{-1}, respectively. Based on our results and the discussion above, reactivity of reduction of nitroarene derivates was found the following order; 3-NP > 2-NP > 4-NP > 4-NA > NB, which are in the same trend as reported previously [23,89].

Table 5.13 Apparent rate constant values for the reduction of nitrophenol isomers, 4-nitroaniline and nitrobenzene in the presence of $Au_{0.5}Pd_{0.5}/TiO_2$ & $Ag_{0.25}Pd_{0.75}/TiO_2$ catalysts.

Substrate	K_{app} min^{-1}	
	$Au_{0.5}Pd_{0.5}/TiO_2$	$Ag_{0.25}Pd_{0.75}/TiO_2$
3-nitrophenol	1.20	2.38
2-nitrophenol	0.78	1.26
4-nitrophenol	0.56	0.87
4-nitroaniline	0.25	0.45
Nitrobenzene	0.09	0.22

Reaction conditions: substrate/metal molar ratio = 30, $NaBH_4$/substrate molar ratio = 30, stirring rate = 1000 rpm and T= 30 °C.

5.8. Catalyst reusability

One of the most important features for a heterogeneous catalyst is the ability to be recovered and recycled multiple times for the given reaction. The successful recovery and re-use thereafter are an essential feature of green chemistry. First, in order to confirm that the reaction is indeed catalysed by heterogeneous catalyst rather than homogeneous, leaching test was performed after the catalytic reduction of 4-NP. The reaction mixture was left to run for 1 min under standard conditions, then the supernatant solution was separated and allowed to run for additional 10 min. No further reaction was proceeded after removing the catalyst, suggesting that the absence of any leaching of the active components. This was confirming by the MP-AES elemental analysis and no traces of Ag and/or Pd species were detected after reaction above the detection limit of MP-AES which is 1 to 2 ppb.

To assess the reusability of $Ag_{0.25}$-$Pd_{0.75}$/TiO_2, the reduction of 4-NP reaction has been carried out for five times under the same experimental conditions and the results are shown in Figure 5.24.
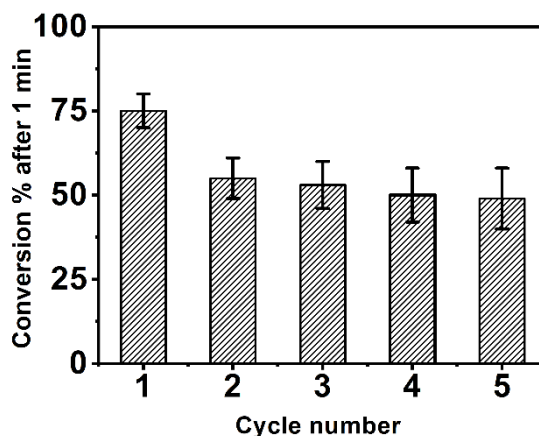
Figure 5.24 Reusability of $Ag_{0.25}Pd_{0.75}$/TiO_2 catalyst for the reduction of 4-NP. Reaction conditions: 4-NP/metal molar ratio = 5, $NaBH_4$/4-NP molar ratio = 30, stirring rate = 1000 rpm and T = 30 °C.

The standard procedure for studying reusability described in detail in Chapter 2 (Section 2.5). An excess $NaBH_4$ ($NaBH_4$ /4-NP molar ratio = 30) and a larger amount of the catalyst in the initial experiments (4-NP /metal molar ratio = 5) were used.

The results of reusability clearly showed a decrease in the catalytic activity after the 1st cycle, as can be seen from Figure 5.24, the conversion (%) dropped from 75% to 56%. However, the conversion (%) was decreased only from 65% to ~ 50% upon the fifth cycle.

To get insight into the reason for this remarkable drop in the catalyst's activity, XPS and TEM analyses were conducted on the fresh and used (5th cycle) catalysts. The XPS results showed that the surface composition (%) of metallic Pd on the fresh catalyst was 86%, while for the used catalyst increased to 100%. This is expected as we have used an excess of $NaBH_4$ (as a reducing agent) and this might be the reason for the reduction of surface Pd species throughout five cycles. Moreover, the TEM analysis performed on the fresh and used catalyst showed a remarkable growth of the mean particle size (from 2.26 to 2.55 nm), as well as an increase of the distribution of particles size from (1 – 4.5) nm to (1 – 6) nm, for the fresh and used catalysts, respectively, see Figure 5.25. The decrease in activity might be due to an increase of particles size and/or blocking of some active sites after the 1st cycle.
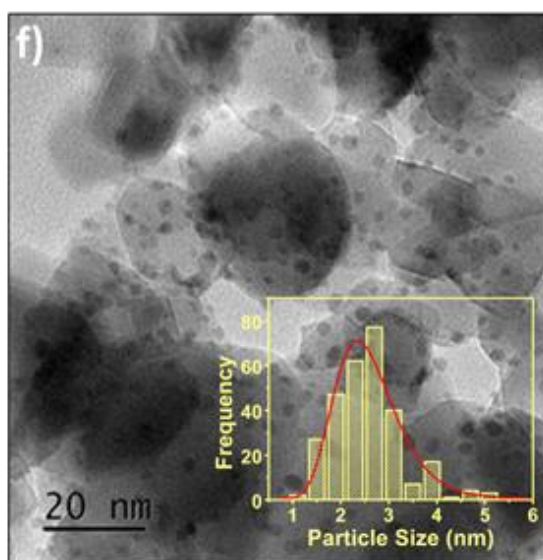
Figure 5.25 Selected TEM images and NPs size distributions histograms of reused $Ag_{0.25}Pd_{0.75}/TiO_2$ catalyst after 5 cycles.

5.9. Conclusions

Bimetallic of Ag and Pd alloyed nanoparticles supported on TiO_2 (Ag_xPd_{1-x}/TiO_2, where x = 0.13, 0.25, 0.5, 0.75 and 0.87) and their monometallic analogous (i.e. Ag/TiO_2 and Pd/TiO_2) were prepared *via* a sol immobilisation approach at room temperature using PVA and $NaBH_4$ as stabilizing and reducing agents, respectively. The electronic structure, chemical properties and the morphology of the prepared materials were probed using different complementary characterization techniques such as; UV-Vis spectroscopy, MP-AES, XRD, TEM, HAADF-STEM and XPS analyses.

Generally, each technique provided us with valuable piece of information and eventually by compiling these pieces together we gained a complete picture of our system. The UV-Vis spectroscopy during the synthesis protocol confirmed the full reduction of mono- and bimetallic nanoparticles. The actual metal loading, with high immobilisation and confinement with the support, are matched well with the nominated values, as confirmed by MP-AES analysis. This was further confirmed by the TEM results which showed that the sol-immobilization method was successfully achieved to prepare very small nanoparticles (< 4 nm) with narrow particle size distribution and these nanoparticles are well dispersed and confined onto TiO_2 support. Moreover, the results confirmed the successful preparation of alloyed nanoparticles with narrow particle size distribution. In addition, the XRD results were further proved the successful synthesis of very small supported nanoparticles (i.e. < 5 nm) and highly dispersed on TiO_2, as it could not detect any diffraction peak for any of the supported nanoparticles. The XRD results are in line with the UV-Vis spectroscopy and TEM analyses.

The activity of the supported nanoparticles was evaluated for the reduction of 4-nitrophenol (4-NP) to 4-aminophenol (4-AP) using $NaBH_4$ as reducing agents. All supported nanoparticles showed promising activity with good efficiency and reusability. The catalysis results showed that AgPd alloyed nanoparticles exhibited high activity and performance than monometallic analogous. The high catalytic activity of bimetallic supported nanoparticles, compared to monometallic analogous, claimed to the presence of synergistic effect due to the metal-metal interaction, in addition to strong metal-support interaction (SMSI), as evidenced by XPS and HAADAF-STEM analyses.

Moreover, the rate of the reaction depends, not only, on the successful preparation of AgPd alloyed nanoparticles with small particle sizes, but also on the molar ratio between

Ag and Pd in the formed alloy. Thus, it was found that the bimetallic $Ag_{0.25}Pd_{0.75}/TiO_2$ catalyst (i.e. Ag:Pd molar ratio = 25:75) showed the best performance amongst all other bimetallic combinations towards the reduction of 4-NP.

Furthermore, this work illustrates, for the first time, the use of formic acid and hydrous hydrazine as a source of hydrogen for the catalytic reduction of 4-NP to 4-AP over bimetallic $AuPd/TiO_2$ and $AgPd/TiO_2$ catalysts and monometallic analogous. Initially, a systematic study was carried out to optimise the reaction conditions by varying a arrange of experimental parameters such as; concentration of formic acid, hydrous hydrazine and NaOH. The results showed that only monometallic Pd/TiO_2 catalyst was active, while monometallic Ag/TiO_2 and Au/TiO_2 catalysts were not active for reduction of 4-NP when both formic acid and hydrous hydrazine were used as a H-donor.

For the bimetallic system, the results showed that $Ag_{0.25}Pd_{0.75}/TiO_2$ catalyst was more active than $Au_{0.5}Pd_{0.5}/TiO_2$ catalyst by a factor of 3.4 and 1.1 when $NaBH_4$ and hydrous hydrazine were used as reducing agents, respectively. However, when formic acid was used as alternative reducing agent, $Au_{0.5}Pd_{0.5}/TiO_2$ catalyst is more active than $Ag_{0.25}Pd_{0.75}/TiO_2$ catalyst by a factor of 3.3.

In addition, the generality of $Au_{0.5}Pd_{0.5}/TiO_2$ and $Ag_{0.25}Pd_{0.75}/TiO_2$ catalysts has been studied with various nitroarenes (e.g. 2-nitrophenol (2-NP), 3-nitrophenol (3-NP), 4-nitroaniline (4-NA) and nitrobenzene (NB). The results showed that, the reactivity of reduction of nitroarene derivates was in following order; 3-NP > 2-NP > 4-NP > 4-NA > NB.

5.10. References

[1]   F. de Oliveira, L. Nascimento, C. Calado, M. Meneghetti and M. da Silva, Catalysts, 2016, 6, 215–225.

[2]   F. Muench, M. Rauber, C. Stegmann, S. Lauterbach, U. Kunz, H. J. Kleebe and W. Ensinger, Nanotechnology, 2011, 22, 415602–415611.

[3]   E. E. Bedford, S. Boujday, C. M. Pradier and F. X. Gu, RSC Adv., 2015, 5, 16461–16475.

[4]   P. Zhao, X. Feng, D. Huang, G. Yang and D. Astruc, Coord. Chem. Rev., 2015, 287, 114–136.

[5]   A. Henglein, Chem. Rev., 1989, 89, 1861–1873.

[6]   J. Noh and R. Meijboom, Appl. Nanotechnol. Water Res., 2014, 333–406.

[7]   S. M. Rogers, C. R. A. Catlow, C. E. Chan-Thaw, D. Gianolio, E. K. Gibson, A. L. Gould, N. Jian, A. J. Logsdail, R. E. Palmer, L. Prati, N. Dimitratos, A. Villa and P. P. Wells, ACS Catal., 2015, 5, 4377–4384.

[8]   N. Dimitratos, A. Villa, L. Prati, C. Hammond, C. E. Chan-Thaw, J. Cookson and P. T. Bishop, Appl. Catal. A Gen., 2016, 514, 267–275.

[9]   A. R. Tao, S. Habas and P. Yang, Small, 2008, 4, 310–325.

[10]   S. Cattaneo, S. J. Freakley, D. J. Morgan, M. Sankar, N. Dimitratos and G. J. Hutchings, Catal. Sci. Technol., 2018, 1677–1685.

[11]   X. Du, J. He, J. Zhu, L. Sun and S. An, Appl. Surf. Sci., 2012, 258, 2717–2723.

[12]   W. Fang, Y. Deng, L. Tang, G. Zeng, Y. Zhou and X. Xie, J. Colloid Interface Sci., 2017, 490, 834–843.

[13]   J. Chang, C. Liu, J. Liu, Y. Zhou, X. Gao and S. Wang, Nano-Micro Lett., 2015, 7, 307–315.

[14]   J. Feng, C. Ma, P. J. Miedziak, J. K. Edwards, G. L. Brett, D. Li, Y. Du, D. J. Morgan and G. J. Hutchings, Dalt. Trans., 2013, 42, 14498–14508.

[15]   G. L. Brett, Q. He, C. Hammond, P. J. Miedziak, N. Dimitratos, M. Sankar, A. A. Herzing, M. Conte, J. A. Lopez-Sanchez, C. J. Kiely, D. W. Knight, S. H. Taylor and G. J. Hutchings, Angew. Chemie - Int. Ed., 2011, 50, 10136–10139.

[16]   A. Roy and T. Pal, New J. Chem., 2017, 41, 12278–12287.

[17]   S. Zhang, Ö. Metin, D. Su and S. Sun, Angew. Chemie - Int. Ed., 2013, 52, 3681–3684.

[18]   D. Sun, P. Li, B. Yang, Y. Xu, J. Huang and Q. Li, RSC Adv., 2016, 6, 105940–105947.

[19]   S. D. Oh, M. R. Kim, S. H. Choi, J. H. Chun, K. P. Lee, A. Gopalan, C. G. Hwang, K. Sang-Ho and O. J. Hoon, J. Ind. Eng. Chem., 2008, 14, 687–692.

[20]   M. T. Islam, R. Saenz-Arana, H. Wang, R. Bernal and J. C. Noveron, New J. Chem., 2018, 42, 6472–6478.

[21]   A. A. Ismail, A. Hakki and D. W. Bahnemann, J. Mol. Catal. A Chem., 2012, 358, 145–151.

[22]   P. Suchomel, A. Panacek, R. Prucek, R. Zboril and L. Kvitek, Nanocon 2013, 5th Int. Conf., 2014, 225–231.

[23]   S. Rogers, R. Catlow, D. Gianolio, P. Wells and N. Dimitratos, Faraday Discuss., 2018,208, 443–454.

[24]   D. K. Bhui, H. Bar, P. Sarkar, G. P. Sahoo, S. P. De and A. Misra, J. Mol. Liq., 2009, 145, 33–37.

[25]   K. L. Kelly, E. Coronado, L. L. Zhao and G. C. Schatz, J. Phycial Chem. B, 2003, 107, 668–677.

[26]   X. Z. Lin, X. Teng and H. Yang, Langmuir, 2003, 19, 10081–10085.

[27]   K. Stamplecoskie and J. Scaiano, J. Am. Chem. Soc., 2010, 132, 1825–1827.

[28]   A. Ahmad, P. Mukherjee, S. Senapati, D. Mandal, M. I. Khan and M. Sastry, Colloids Surfaces B Biointerfaces, 2003, 28, 313–318.

[29]   N. Edayadulla, N. Basavegowda and Y. R. Lee, J. Ind. Eng. Chem., 2015, 21, 1365–1372.

[30]   S. Deki, K. Akamatsu, Y. Hatakenaka, M. Mizuhata and A. Kajinami, Nanostructured Mater., 1999, 11, 59–65.

[31]   R. Sharma, D. P. Bisen, U. Shukla and B. G. Sharma, Resent Research in Science and Technology, 2012, 4 (8), 77–79.

[32]   B. Zhang, Y. Yuan, K. Philippot and N. Yan, Catal. Sci. Technol., 2015, 5, 1683–1692.

[33]   R. Su, R. Tiruvalam, Q. He, N. Dimitratos, L. Kesavan, C. Hammond, J. A. Lopez-Sanchez, R. Bechstein, C. J. Kiely, G. J. Hutchings and F. Besenbacher, ACS Nano, 2012, 6, 6284–6292.

[34]   R. Liang, RSC Adv., 2014, 4, 36959–36966.

[35]   S. Wang, M. Zhang and W. Zhang, ACS Catal., 2011, 1, 207–211.

[36]   H. Khojasteh, M. Salavati-Niasari, A. Abbasi, F. Azizi and M. Enhessari, J. Mater. Sci. Mater. Electron., 2016, 27, 1261–1269.

[37]   H. Rong, S. Cai, Z. Niu and Y. Li, ACS Catal., 2013, 3, 1560–1563.

[38]   X. Gao, H.-L. Feng, Z.-Y. Zhang and J.-M. Ma, J. Korean Phys. Soc., 2010, 56, 1176–1179.

[39]   C. Jia, P. Yang, J. Li, B. Huang and K. Matras-Postolek, ChemCatChem, 2016, 8, 839–847.

[40]   X. Y. Zhu, Z. S. Lv, J. J. Feng, P. X. Yuan, L. Zhang, J. R. Chen and A. J. Wang, J. Colloid Interface Sci., 2018, 516, 355–363.

[41]   P. P. Wells, E. M. Crabb, C. R. King, R. Wiltshire, B. Billsborrow, D. Thompsett and A. E. Russell, Phys. Chem. Chem. Phys., 2009, 11, 5773–5781.

[42]   M. Brun, A. Berthet and J. . Bertolini, J. Electron Spectros. Relat. Phenomena, 1999, 104, 55–60.

[43]   S. Zhang, B. Zhang, S. Li, Z. Huang, C. Yang and H. Wang, J. Adv. Ceram., 2017, 6, 1–10.

[44]   L. Srisombat, J. Nonkumwong, K. Suwannarat, B. Kuntalue and S. Ananta,

Colloids Surfaces A Physicochem. Eng. Asp., 2017, 512, 17–25.

[45]   N. Arora, A. Mehta, A. Mishra and S. Basu, Appl. Clay Sci., 2018, 151, 1–9.

[46]   Z. D. Pozun, S. E. Rodenbusch, E. Keller, K. Tran, W. Tang, K. J. Stevenson and G. Henkelman, J. Phys. Chem. C, 2013, 117, 7598–7604.

[47]   F. A. Al-Marhaby and R. Seoudi, World J. Nano Sci. Eng., 2016, 6, 29–37.

[48]   C. Yu, X. Guo, Z. Xi, M. Muzzio, Z. Yin, B. Shen, J. Li, C. T. Seto and S. Sun, J. Am. Chem. Soc., 2017, 139, 5712–5715.

[49]   J. Huang, S. Vongehr, S. Tang, H. Lu and X. Meng, J. Phys. Chem. C, 2010, 114, 15005–15010.

[50]   X. Li, Z. Zeng, B. Hu, L. Qian and X. Hong, ChemCatChem, 2017, 9, 924–928.

[51]   D. Channe Gowda and S. Gowda, Indian J. Chem. - Sect. B Org. Med. Chem., 2000, 39, 709–711.

[52]   M. Grasemann, G. Laurency, Energy Environ. Sci. 2012, 5, 8171 – 8181.

[]53   J. Li, Q.-L. Zhu and Q. Xu, Chim. Int. J. Chem., 2015, 69, 348–352.

[54]   J. Eppinger and K.-W. Huang, ACS Energy Lett., 2017, 2, 188–195.

[55]   F. Sa, F. Sánchez, D. Motta and N. Dimitratos, Appl. Petrochemical Res., 2016, 6, 269–277.

[56]   D. Zhang, F. Ye, T. Xue, Y. Guan and Y. M. Wang, Catal. Today, 2014, 234, 133–138.

[57]   M. Momirlan and T. . Veziroglu, Renew. Sustain. Energy Rev., 2002, 6, 141–179.

[58]   R. Javaid, S. I. Kawasaki, A. Suzuki and T. M. Suzuki, Beilstein J. Org. Chem., 2013, 9, 1156–1163.

[59]   Y. Du, Y. Bin Shen, Y. L. Zhan, F. Di Ning, L. M. Yan and X. C. Zhou, Chinese Chem. Lett., 2017, 28, 1746–1750.

[60]   Y. Huang, J. Xu, X. Ma, Y. Huang, Q. Li and H. Qiu, Int. J. Hydrogen Energy, 2017, 42, 18375–18382.

[61]   X. Yang, P. Pachfule, Y. Chen, N. Tsumori and Q. Xu, Chem. Commun., 2016, 52, 4171–4174.

[62]   H. Liu, X. Liu, Y. Yu, W. Yang, J. Li, M. Feng and H. Li, J. Mater. Chem. A, 2018, 2–7.

[63]   H. Lu, H. Yin, Y. Liu, T. Jiang and L. Yu, Catal. Commun., 2008, 10, 313–316.

[64]   T. L. Lai, K. F. Yong, J. W. Yu, J. H. Chen, Y. Y. Shu and C. Bin Wang, J. Hazard. Mater., 2011, 185, 366–372.

[65]   T. Ma, W. Yang, S. Liu, H. Zhang and F. Liang, Catalysts, 2017, 7, 38–48.

[66]   M. Li and G. Chen, Nanoscale, 2013, 5, 11919–11927.

[67]   T. Ma, F. Liang, R. Chen, S. Liu and H. Zhang, Nanomaterials, 2017, 7, 239–248.

[68]   J. A. Johnson, J. J. Makis, K. A. Marvin, S. E. Rodenbusch and K. J. Stevenson, J. Phys. Chem. C, 2013, 117, 22644–22651.

[69]   A. Fedorczyk, J. Ratajczak, O. Kuzmych and M. Skompska, J. Solid State Electrochem., 2015, 19, 2849–2858.

[70]   H. L. Jiang, S. K. Singh, J. M. Yan, X. B. Zhang and Q. Xu, ChemSusChem, 2010, 3, 541–549.

[71]   S. K. Singh and Q. Xu, J. Am. Chem. Soc., 2009, 131, 18032–18033.

[72]   E. Granot, B. Filanovsky, I. Presman, I. Kuras and F. Patolsky, J. Power Sources, 2012, 204, 116–121.

[73]   S. K. Singh and Q. Xu, Catal. Sci. Technol., 2013, 3, 1889–1900.

[74]   H. Hayashi, Res. Chem. Intermed., 1998, 24, 183–196.

[75]   M. Yadav and Q. Xu, Energy Environ. Sci., 2012, 5, 9698–9725.

[76]   P. Z. Li and Q. Xu, J. Chinese Chem. Soc., 2012, 59, 1181–1189.

[77]   D. Bhattacharjee, K. Mandal and S. Dasgupta, RSC Adv., 2016, 6, 64364–64373.

[78]   L. He, Y. Huang, X. Yan, L. Li, A. Wang, X. Wang, C. Mou and T. Zhang, Applied Catal. B, Environ., 2014, 147, 779–788.

[79]   G. Yao, F. Chen, Z. Huo and F. Jin, Int. J. Hydrogen Energy, 2016, 41, 9135–9139.

[80]   F. Chen, G. Yao, Z. Huo and F. Jin, RSC Adv., 2015, 5, 11257–11260.

[81]   M. M. Selim, I. H. Abd El Maksod and T. S. Saleh, Egypt. J. Chem., 2009, 52, 491–506.

[82]   I. Hamdy, A. El, T. S. Saleh and E. Z. Hegazy, J. Alloys Compd., 2010, 506, 923–927.

[83]   H. Yazid, R. Adnan and M. A. Farrukh, Indian J. Chem. - Sect. A Inorganic, Phys. Theor. Anal. Chem., 2013, 52, 184–191.

[84]   T. Xu, J. Zhang, J. Song, H. Niu, C. Mao, S. Zhang and Y. Shen, Applied Catal. A, Gen., 2016, 515, 83–90.

[85]   B. H. and S.-H. Y. Yong-Ming Lu, Hai-Zhou Zhu, Wei-Gu Li, J. Mater. Chem. A, 2013, 3783–3788.

[86]   P. S. Kumbhar, J. Sanchez-Valente and F. Figueras, Tetrahedron Lett., 1998, 39, 2573–2574.

[87]   N. A. Fathy, M. M. Selim and N. A. Fathy, Egypt. J. Chem., 2012, 55, 649–658.

[88]   H. Li, J. Liao and T. Zeng, Catal. Sci. Technol, 2014, 4, 681–687.

[89]   J. Sun, Y. Fu, G. He, X. Sun and X. Wang, Catal. Sci. Technol., 2014, 4, 1742–1748.

Chapter 6

Conclusions and future work

6.1. Conclusions

Reduction of 4-nitrophenol (4-NP), by a reducing agent, to produce 4-aminophenol has received great attention due to its potential applications in the fields of environmental sciences and organic synthesis. Especially, because of its important applications in the industry fields such as production of antipyretic drugs, analgesic, pesticides, corrosion inhibitors, dyestuff and photographic developers [1–3]. However, it is well-known that 4-NP, in the presence of wastewater, can cause environmental pollution that is of great public concern [4,5]. Therefore, the degradation of 4-NP into non-toxic, high valuable, molecules, and in turn benign, has become great interest of research in recent years [4,6]. Moreover, this reduction is currently considered as a benchmark model reaction to evaluate supported and/or unsupported nanoparticles as potential catalysts. Meanwhile, in this thesis the reduction of 4-nitrophenol with $NaBH_4$ has been chosen as model reaction to evaluate the catalytic performance of the synthesized catalysts. In addition, the ability to use different reducing agents such as; formic acid and hydrous hydrazine, as H-donors, have been also examined.

The aim of this thesis was divided into three objectives, first, investigating the activity of mono and bimetallic Au and Pd nanoparticles supported onto commercial TiO_2 (P25) on the reduction of 4-NP by $NaBH_4$ in aqueous phase under mild reaction conditions. This investigation includes performance optimization of the bimetallic catalysts by studying different molar ratio between Au and Pd metal precursors. Second, studying the effect of other catalyst's support (CuO and/or NiO) on the reduction of 4-NP by $NaBH_4$. These supports are catalytically active in the reduction reaction compared to the inactive TiO_2 support. Finally, the catalytic performance of the bimetallic supported active components (AuPd and AgPd) was compared and examined with different reducing agents (formic acid and hydrazine), in regard to $NaBH_4$, in the reduction of 4-NP.

First objective was addressed in Chapter 3 where mono and bimetallic Au and Pd nanoparticles supported on TiO_2 have been successfully synthesized using sol-immobilization method by using PVA as stabilizer and $NaBH_4$ as reducing agent. UV-Vis spectroscopy data confirmed the reduction of metal precursors and formation of metal nanoparticles before immobilization. MP-AES confirmed the actual loading of metal nanoparticles onto the support, which agreed well with the nominal values. The mean

particle size of all mono- and bimetallic supported nanoparticles were found to be between (2.07 ±0.4) and (3.2 ±1.10) nm. The catalytic activity of mono- and bimetallic supported nanoparticles were evaluated towards the reduction of 4-NP by $NaBH_4$. The reaction parameters have been optimized under kinetic regime control and found to be: 4-NP/metal molar ratio of 13, $NaBH_4$/4-NP molar ratio of 30, at 30 °C and at stirring rate of 1000 rpm. At the optimized parameters, the Pd/TiO_2 was found to be more active than the Au/TiO_2 catalyst. Nevertheless, all bimetallic catalysts of Au_xPd_{1-x}/TiO_2 system (x = 0.13, 0.25, 0.5, 0.75 and 0.87) showed higher activity compared with their monometallic counterparts. This result was evidenced due to the synergistic effect between Au and Pd supported alloyed nanoparticles. Amongst all molar ratios, the highest activity was obtained with the bimetallic catalyst with a (1:1) molar ratio of Au and Pd nanoparticles. Interestingly, $Au_{0.5}Pd_{0.5}/TiO_2$ has the smallest particle size with the narrowest particle size distribution amongst other bimetallic catalysts at different molar ratio. In addition, $Au_{0.5}Pd_{0.5}/TiO_2$ catalyst has the highest fractions of alloyed nanoparticles as confirmed by STEM-EDX analysis. $Au_{0.5}Pd_{0.5}/TiO_2$ catalyst was reused for four times with small loss in catalytic activity.

Second objective is addressed in Chapter 4, we have shown that commercial CuO and synthesized NiO supports are active in the reduction of 4-NP reaction using $NaBH_4$ as a reducing agent before using them to prepare mono and bimetallic AuPd supported nanoparticles. Significant observations were made upon studying the supports activity, such as the commercial NiO was found to be not active, while the NiO synthesized support, prepared in our lab, was active in the reduction reaction. The activity of synthesized NiO was attributed to the presence of $Ni(OH)_2$ on the surface which was confirmed by XPS and TGA analyses, while the commercial NiO has no surface $Ni(OH)_2$ species. Another interesting observation was made when CuO support was tested in the reaction where long induction period was observed (~ 1.5 min). The induction time might be related to changes in the oxidation state of Cu on the surface of CuO during the reaction as evidenced by XPS and XRD analyses of the used samples.

The catalytic activity of mono- and bimetallic AuPd alloyed nanoparticles supported onto NiO and CuO were studied and compared with the results obtained from Chapter 3 where TiO_2 was used as support. The molar ratio of bimetallic AuPd supported alloyed nanoparticles in this work was fixed at 1:1 based on the optimisation results from the previous work reported in Chapter 3. The catalytic activity of mono- and bimetallic

catalysts followed the same order as the remarkable activity of the corresponding supports (CuO $\gg$ NiO > TiO$_2$ (not active)) and were in an order of (Au/CuO $\gg$ Au/NiO > Au/TiO$_2$), (Pd /CuO $\gg$ Pd/NiO >Pd/TiO$_2$) and (AuPd/CuO $\gg$ AuPd/NiO > AuPd/TiO$_2$). The highest activity observed for AuPd/CuO catalyst was correlated, not only, to strong metal-support interaction (SMSI), but also to metal-metal synergism between Au and Pd in the AuPd alloyed nanoparticles, which evidenced by XPS and TEM analysis. In addition, the results suggested that the particle sizes of supported nanoparticles as well as the specific surface area of the prepared catalysts were not significant factors in the catalysts' activity as proved by TEM and BET surface area measurements. Catalysts supported onto CuO and NiO were reused for four times with small loss in their activities. Interestingly, the induction time was disappeared for CuO support after the third use, suggesting its reduction by NaBH$_4$ as evidenced from XPS analysis.

Third objectives were addressed in Chapter 5, Ag and Pd monometallic and a range of bimetallic AgPd alloyed nanoparticles supported on TiO$_2$ have been successfully prepared using sol-immobilization method. The catalytic activity of the synthesized catalysts was studied towards the reduction of 4-NP by NaBH$_4$. The Pd/TiO$_2$ catalyst appear to be more active than the Ag/TiO$_2$ one. All bimetallic AgPd/TiO$_2$ catalysts showed higher activity than their monometallic counterparts (Ag/TiO$_2$ and Pd/TiO$_2$) due to synergistic effect between Ag and Pd in the alloyed nanoparticles as evidenced by XPS and HAADAF-STEM analyses. A volcano shape in the activity profile of bimetallic systems with different molar ratio of Ag and Pd was observed with the highest activity of 0.25:0.75 molar ratio of Ag and Pd nanoparticles. As a result, the activity of the bimetallic AgPd systems was not correlated only to the successful preparation of AgPd alloyed nanoparticles with small particle sizes, but also to the optimized molar ratio between Ag and Pd in the formed alloy.

Furthermore, our work illustrated, for the first time, the use of formic acid and hydrous hydrazine as a source of hydrogen resulting from the catalytic decomposition of the two compounds, for the catalytic reduction of 4-NP to 4-AP over bimetallic AuPd/TiO$_2$ and AgPd/TiO$_2$ catalysts and monometallic analogous. A systematic study was performed by optimizing the reaction conditions by varying a arrange of experimental parameters such as; concentration of formic acid (formic acid/4-NP molar ratio = 40), hydrous hydrazine (hydrous hydrazine/4-NP molar ratio = 45) and [NaOH] = 0.075M). The results showed when formic acid and hydrous hydrazine were used as a H-donor, monometallic Ag/TiO$_2$

and Au/TiO$_2$ catalysts were not active, while monometallic Pd/TiO$_2$ catalyst was active for reduction of 4-NP.

For the bimetallic system, the results showed that both Ag$_{0.25}$Pd$_{0.75}$/TiO$_2$ and Au$_{0.5}$Pd$_{0.5}$/TiO$_2$ catalysts showed promising activity toward the reduction of 4-NP by formic acid and hydrous hydrazine. However, the activity of Ag$_{0.25}$Pd$_{0.75}$/TiO$_2$ was more active than Au$_{0.5}$Pd$_{0.5}$/TiO$_2$ catalyst by a factor of 3.4 and 1.1, when NaBH$_4$ and hydrous hydrazine were used as reducing agents, respectively. In contrast, and when formic acid was used as alternative reducing agent, Au$_{0.5}$Pd$_{0.5}$/TiO$_2$ catalyst was more active than Ag$_{0.25}$Pd$_{0.75}$/TiO$_2$ catalyst by a factor of 3.3. Finally, the activity of Au$_{0.5}$Pd$_{0.5}$/TiO$_2$ and Ag$_{0.25}$Pd$_{0.75}$/TiO$_2$ catalysts has been evaluated with various nitroarenes (e.g. 2-nitrophenol (2-NP), 3-nitrophenol (3-NP), 4-nitroaniline (4-NA) and nitrobenzene (NB). The results showed that, the ability to reduce nitroarene derivates was in following order; 3-NP > 2-NP > 4-NP > 4-NA > NB.

6.2. Future work

Our work in this study showed the superior activity of bimetallic AgPd and AuPd supported nanoparticles for the reduction of 4-NP compared to their monometallic analogous prepared *via* sol-immobilization method. Recent study on monometallic Pd supported nanoparticles (Pd/TiO$_2$) prepared by sol-immobilization approach [7] showed that the preparation temperature and solvent being used during the synthesis process have an impact on both the sizes and distribution of the supported nanoparticles. So far, preparing bimetallic supported nanoparticles using different solvents (ethanol and ethanol/water) and/or at lower temperature (< 30 °C) could be considered as future investigation.

Moreover, as demonstrated in this thesis, the activity of the bimetallic catalysts based on Pd is dependent on the type of the metal, therefore, alloying Pd nanoparticles with a second metal such as; Ir, Ni, Ru, Pt and Rh may lead to an improvement in catalytic activity.

Also, it was demonstrated in this study, practically in Chapter 5, that the type of the reducing agent is a very important factor in influencing catalytic activity. Therefore, using different reducing agent such as; Silyl hydrides [8] might enhance the catalyst's activity.

To understand better the reaction mechanisms and structure/activity relationships during reaction, it would be useful to perform *in situ/operando* studies such as EXAFS/XANES combined with UV-Vis and FT-IR. These studies would be helpful to monitor on line structural changes of the support/metal nanoparticle during reaction, monitor possible deactivation phenomena and poisoning effects. Moreover, the development of continuous flow cell to monitor the long-term stability of the synthesised catalysts would be highly desirable. Finally, the general application of the synthesised catalysts on a range of functionalised nitrophenols and nitroarenes compounds could be explored using formic acid, hydrous hydrazine as H-donors.

6.3. References

[1]   T. R. Mandlimath and B. Gopal, J. Mol. Catal. A Chem., 2011, 350, 9–15.

[2]   N. Arora, A. Mehta, A. Mishra and S. Basu, Appl. Clay Sci., 2018, 151, 1–9.

[3]   H. P. Karki, D. P. Ojha, M. K. Joshi and H. J. Kim, Appl. Surf. Sci., 2018, 435, 599–608.

[4]   S. Nag, A. Pramanik, D. Chattopadhyay and M. Bhattacharyya, Environ. Sci. Pollut. Res., 2018, 25, 2331–2349.

[5]   K. Ying Cai, Y. Sheng Liu, Y. Xu, H. Zhou, L. Zhang and Y. Cui, Bull. Chem. React. Eng. Catal., 2017, 12, 89–95.

[6]   D. Meziane, A. Benadda-Kordjani, G. Nezzal, S. Benammar and A. Djadoun, React. Kinet. Mech. Catal., 2017, 122, 1145–1158.

[7]   S. Rogers, R. Catlow, D. Gianolio, P. Wells and N. Dimitratos, Faraday Discuss., 2018, 208, 443-454.

[8]   H. K. Kadam and S. G. Tilve, RSC Adv., 2015, 5, 83391–83407.

Appendix

Figure A1 shows the GC-MS analysis [MS (top), while GC (bottom)] which was conducted on the reaction mixture after the catalytic reduction of 4-nitrophenol. The results clearly show that 4-AP is the sole product for this reaction as confirmed by the GC spectrum (only one peak could be detected at retention time of 18 s). For better illustration, enlargements of GC spectrum and MS signals are presented in Figures A2 and A3, respectively.
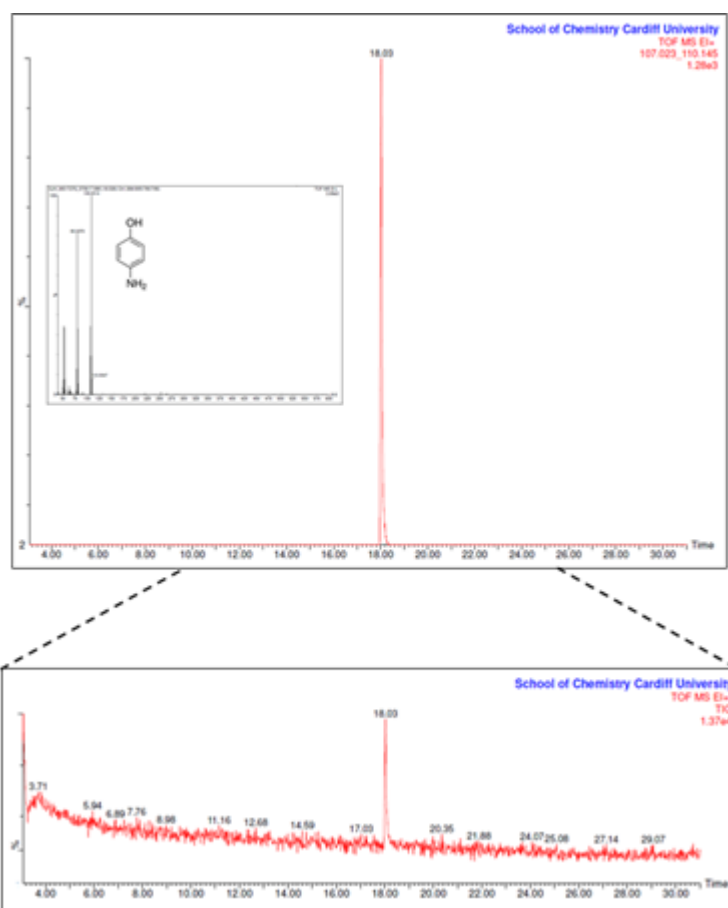

Figure A 1 GC-MS after the catalytic reduction of 4-nitrophenol with 4-AP as a sole product for this reaction.
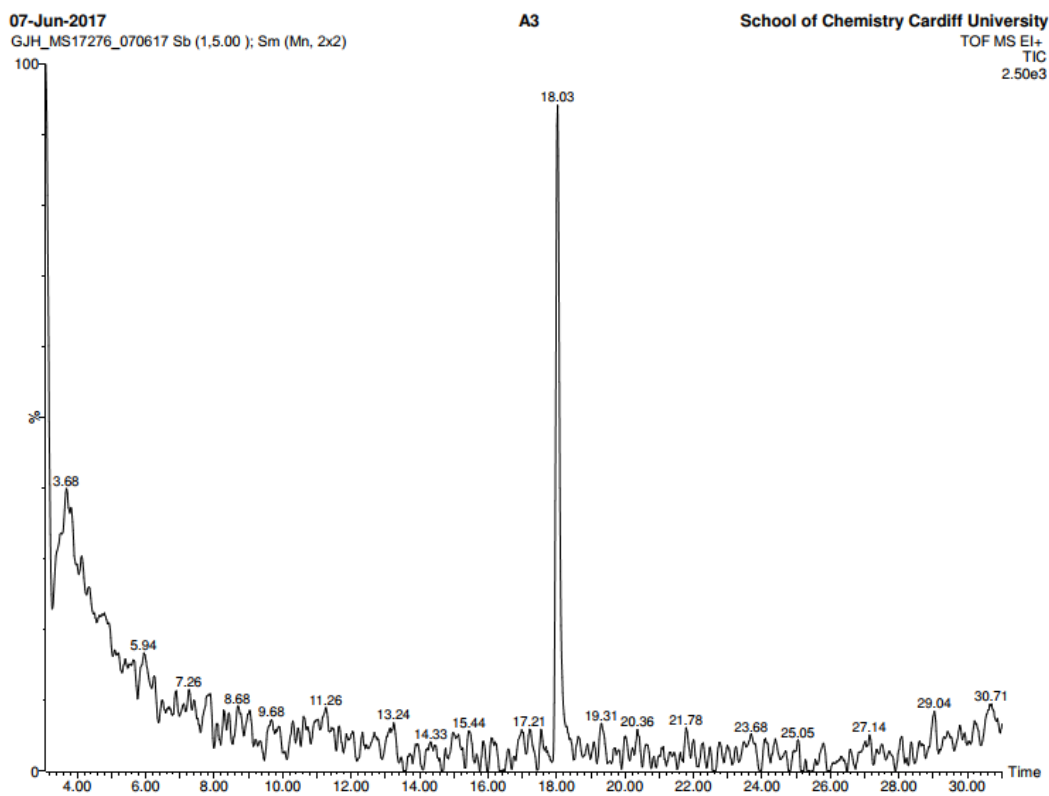
Figure A 2 Enlargement of GC spectrum presented in Figure A 1 above, suggesting that 4-AP is the sole product of the catalytic reduction of 4-NP by NaBH$_4$.
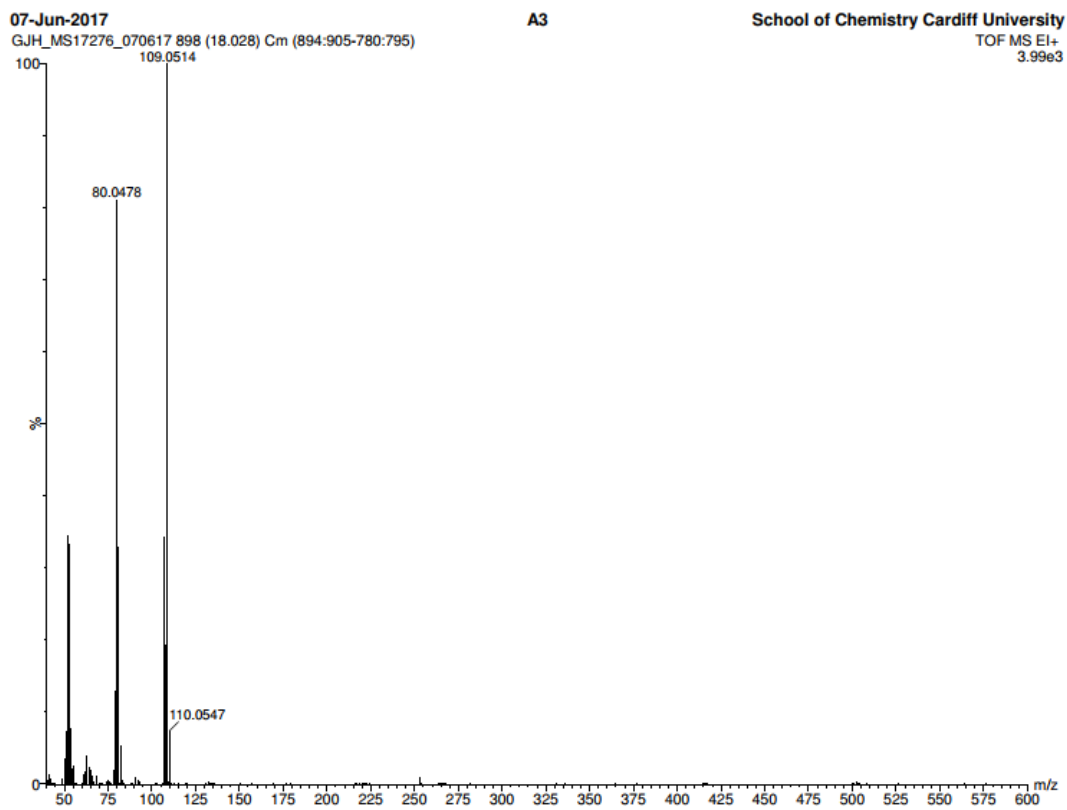
Figure A 3 Enlargement of the MS signals presented in Figure A 1 above.